# Exploring the Diverse Landscape of Layered Double Hydroxide-Based Nanomaterials

Trinity College Dublin
Coláiste na Tríonóide, Baile Átha Cliath
The University of Dublin

A thesis submitted to the School of Chemistry,

Trinity College Dublin, the University of Dublin

for the degree of Doctor of Philosophy

by

**Áine Coogan**

Under the supervision of Prof. Yurii K. Gun'ko

2024

# Declaration

I declare that this thesis has not been submitted as an exercise for a degree at this or any other university and it is entirely my own work. Due credit has been given to collaborators where appropriate.

I agree to deposit this thesis in the University's open access institutional repository or allow the Library to do so on my behalf, subject to Irish Copyright Legislation and Trinity College Library conditions of use and acknowledgement.

.....

Áine Coogan

# Summary

The overarching goal of this work was to prepare a range of layered double hydroxide-based two-dimensional nanomaterials, and explore how tuning their composition can lead to a diverse range of properties and applications.

Chapter 1 presents an introduction and brief review of the literature that is relevant to the experimental work presented in this thesis. This includes an introduction to nanomaterials, with a particular focus on two-dimensional nanomaterials, as well as their synthesis, structure, properties and applications. The structure and properties of layered double hydroxides are discussed, to highlight how their tunability results in their suitability as functional nanomaterials for a wide array of applications. A brief discussion on the history and theory of chirality in nanomaterials, nanomaterials as heterogeneous catalysts, nanomaterials as building blocks for nanofiltration membranes, and luminescent nanomaterials are also presented in this chapter.

Chapter 2 details all of the experimental work performed in this thesis, including all starting materials used, and detailed experimental procedures and methods for each chapter. Relevant theoretical backgrounds of the various instrumentation and characterisation techniques utilised throughout this project are also provided.

Chapter 3 focuses on the development of novel chiroptically active anisotropic

nanostructures derived from carbonate-intercalated copper-aluminium layered double hydroxide (CuAl-$CO_3$ LDH) nanosheets. It details the synthesis and characterisation of CuAl-$CO_3$ LDH nanosheets through a simple room-temperature aqueous co-precipitation approach. Then, the induction of chirality is explored in these materials through two distinct approaches – modified co-precipitation, and post-synthetic treatment, with both approaches resulting in the formation of nanostructures with chiroptical activity spanning the UV and visible spectrum. A discussion on the mechanism of chirality transfer is presented based on the experimental evidence.

Chapter 4 details the development of new photocatalytically active high-performance nanofiltration membranes made from CuAl-$CO_3$ LDH/partially oxidised boron nitride 2D nanocomposites. This project culminated in achieving state-of-the-art solvent flux rates, as well as near 100% retention values for model organic polluants, namely azo, thiazine and triarylmethane dyes. Notably, for the first time, photocatalytic degradation of Evans blue using LDH photocatalysts has been achieved, using visible-light sources. Furthermore, the idea of photocatalyst integration is introduced as a novel route to improving the anti-fouling properties of BNOx-based nanofiltration membranes.

Chapter 5 explores the development of photoluminescent LDHs *via* lanthanide doping, particularly trivalent europium and terbium doping in zinc-aluminium and magnesium-aluminium LDHs. An in-depth analysis of the structural and photophysical properties of these structures is provided. These LDHs are successfully implemented as luminescent turn-off nanosensors for the environmental detection of hexavalent chromium sources.

Finally, chapter 6 presents a conclusion of the entire body of work, outlining some of the key achievements of this research. An outline and plan for future work, as well as some preliminary results in this regard, are also discussed in this chapter.

# Acknowledgements

The first and arguably the most important 'thank you' of this thesis must go to my supervisor, Prof. Yurii Gun'ko. Just one week after stepping foot into his lab as a Senior Sophister student, and seeing the relationship he had with his group, I knew that was where I wanted to spend the next four years. Working under his guidance over the past four years has made the gruelling experience of getting a PhD enjoyable, which I previously thought was an impossible task. His constant support and encouragement, both in terms of applying for awards I had no business applying for, as well as giving me the creative freedom I needed to try anything I wanted in the lab, has shaped me into the researcher I am today. Without his wealth of knowledge and ideas on chemistry and nanomaterials, none of this work would be possible. Thanks to him, whenever I'm trying out a new synthesis, or working with a new material, I will always think 'can I make it chiral?'.

To the entire Gun'ko Group, past and present, thank you for your continuing support, both professionally and personally, over the past few years. I would like to give particular thanks to several Gun'ko group alumni. To Dr. Shelley Stafford, who mentored me as an undergraduate student, helped me to grow as a researcher, and encouraged me to stick around for a PhD - thank you. Secondly, I would like to thank Dr. Finn Purcell-Milton, who, during his time in the group was like a second supervisor to me. His constant wisdom and guidance, as well as bucket loads of patience when helping me with synthesis, is truly appreciated. Finally, I must thank Dr. Natalia García Doménech - my close collaborator, and even closer friend. I had a blast collaborating with her on the nanofiltration work, and am delighted that what started as a work relationship has blossomed into an amazing friendship. Thank you for keeping me sane amongst all the chaos of the past few years.

Next, I would like to thank my collaborators, without whom most of this work couldn't have gotten over the finish line. Firstly, thank you to Dr. Aran Rafferty for all of his work

on the porosity characterisation for the nanofiltration membranes. To Dr. Lucia Hughes and Dr. Tigran Simonian from Prof. Valeria Nicolosi's group – masters of the electron microscope, and fellow members of the NPCAM Class of 2019 – thank you both for coming to the rescue for SEM, TEM, EDX and EELS characterisation. To Valeria, thank you for your guidance and words of encouragement throughout this journey. To Tigran, perhaps more aptly described as a master of cheeky pints, thank you for also coming to the rescue in these past few months with liquid courage.

My research benefitted hugely from the extra hands I had throughout my four-year PhD journey, and I had the absolute pleasure of supervising five exceptional undergraduate research students and one secondary school student throughout that time: Seán, Amy, Kate, Quentin, Donagh and Dylan. I would like to especially thank one student in particular, Donagh Mc Ginley, whose drive, enthusiasm and research prowess really shone through, and who I have no doubt will become an exceptional researcher in his own right as he begins his PhD journey in London.

Despite the limited and ageing equipment in our department (and the occasional roof falling in), the technical support and training we have available to us is second-to-none. Our technical staff are literally, and figuratively, the glue that holds this crumbling place together. Thank you to Dr. Manuel Ruether, for training me on countless instruments, providing solid advice, and somehow managing to keep all of the equipment alive throughout the department – specifically for coming to the rescue whenever the CD spectrometer decided to take a nap in the middle of a measurement. A huge thank you also to Dr. Brendan Twamley, who made spending days on end in the TBSI basement (a.k.a. the pit of despair, his words not mine) doing pXRD so enjoyable with his chats, as well as consoling me when I had a terrible sample (there were many). Thank you also to all of the staff in the Advanced Microscopy Laboratory, particularly Dr. Megan Canavan, Clive Downing, and Dermot Daly, who were always there to help when I wanted to pretend that I was a microscopist for the day.

To the Chemistry Education and Public Engagement team – Dr. John O'Donoghue, Dr. Noelle Scully, Dr. Niamh McGoldrick, and Dr. Natalia García Doménech – thank you for introducing me to the weird and wonderful word of chemistry outreach. I really appreciate all the opportunities you gave me to work with the public, and to take regular breaks from the PhD. I think I've now met enough government ministers to last me a lifetime.

To my secondary school career guidance counsellor, who told me I wasn't the type of student that would be able to get the points to study Nanoscience in TCD, and to 'manage

my expectations' - thank you. Your lack of encouragement, and my stubbornness, made for a perfect combination in ensuring I got to where I wanted and needed to be.

I have to give a huge shoutout to my circle of friends, who distracted me from writing (which was sometimes appreciated, and other times less so). Thank to the 'Big Grippers' Kierain, Nick, Cathal and John, for helping me fulfill my dream of becoming the stereotypical STEM student-turned-hobby climber. To the 'nanos' - in particular Tigran, Seán, Richard, Dominik and Lucy - staying friends with you all and seeing your individual PhD journeys has been equal parts inspiring and reassuring. To everyone else, Conor, Stobie, Leannán, Craig, Lana, Eva, Tom, Hannah, the support over the years is so appreciated.

To Cathal, my rock, with a heart of gold and the patience of a saint. Thank you for the endless dinners and cups of tea over the last few months, the distractions I didn't know I needed, and the constant reassurance that I'll make it to the end. I love you.

Finally, to my family - I wouldn't be here without any of you. To my siblings, Stephen, Mary, Jane and Liam - coming home to visit on the weekends, even though I couldn't do it often enough, is what has kept me sane, especially over the last year. To Denise and Christy (a.k.a. Mammy and Daddy), thank you so much for everything you've done for me. From acting as a human alarm clock (because you knew an actual one would never wake me up), dragging me out of bed at 6.30 in the morning to make the commute up to Dublin, to the many dinners left in the microwave, you both made this all possible. It never mattered that you didn't have a clue what my research was about, your blind support was all I needed. I love you all, and this thesis belongs as much to you as it does to me.

***"We are the dust on the stained glass windows***
***Trying to comprehend the cathedral."***

**- Enter Shikari**

# Publications

**1)** Purcell-Milton, F.; Kuznetsova, V.A.; Bai, X.; **Coogan, Á.**; Martinez Carmona, M.; Garcia, J.A.; Bradley, A.L.; Gun'ko, Y.K. Chiroptically Active Quantum Nanonails, *Nanoscale Horizons*, **2024**, Advance Article.

**2)** Kuznetsova, V.A.; **Coogan, Á.**; Botov, D.; Gromova, Y.; Ushakova, E.; Gun'ko, Y.K. Expanding the Horizons of Machine Learning in Nanomaterials to Chiral Nanostructures, *Advanced Materials*, **2024**, *36*, 2308912.

**3)** **Coogan, Á.**; García Doménech, N.; Mc Ginley, D.; Simonian, T.; Rafferty, A.; Fedix, Q.; Donlon, A.; Nicolosi, V.; Gun'ko, Y.K. Layered double hydroxide/boron nitride nanocomposite membranes for efficient separation and photodegradation of water-soluble dyes. *Journal of Materials Chemistry A*, **2023**, *11*, 12266-12281

**4)** **Coogan, Á.**; Hughes, L.; Purcell-Milton, F.; Cardiff, S.; Nicolosi, V.; Gun'ko, Y.K. Two-Dimensional Chiroptically Active Copper Oxide Nanostructures. *The Journal of Physical Chemistry C*, **2022**, *126*, 18980–18987.

**5)** García Doménech, N.; **Coogan, Á.**; Purcell-Milton, F.; Casasín García, M.L.; Sanz Arjona, A.; Brunet Cabré, M.; Rafferty, A.; Mckelvey, K.; Dunne, P.W.; Gun'ko, Y.K. Partially oxidised boron nitride as a 2D nanomaterial for nanofiltration applications. *Nanoscale Advances*, **2022**, *4*, 4895–4904.

**6)** **Coogan, Á.**; and Gun'ko, Y.K. Solution-based "bottom-up" synthesis of group VI transition metal dichalcogenides and their applications. *Materials Advances*, **2021**, *2*, 146–164.

# Conference presentations

**2024 Chemical Nanoscience and Nanotechnology Annual Meeting, London, UK**
*Towards recyclable 2D material-based nanofiltration membranes for water purification*, January $16^{th}$, 2024 (Oral Presentation)

**2023 Materials Research Society Fall Meeting and Exhibit, Boston, MA, USA**
*Layered double hydroxide/boron nitride nanocomposite membranes for efficient separation and photodegradation of water-soluble dyes*, November $28^{th}$, 2023 (Poster presentation)

**2023 Materials Research Society Fall Meeting and Exhibit, Boston, MA, USA**
*Decomposition of layered double hydroxides for accessing chiral metal oxides*, November $28^{th}$, 2023 (Oral presentation)

**$16^{\mathbf{th}}$ International Conference on Materials Chemistry (MC16), Dublin, Ireland**
*Towards recyclable 2D material-based nanofiltration membranes for water purification*, July $5^{th}$, 2023 (Oral presentation)

**$16^{\mathbf{th}}$ International Conference on Materials Chemistry (MC16), Dublin, Ireland**
*Use of layered double hydroxides to access chiroptically active 2D metal oxides*, July $3^{rd}$, 2023 (Poster presentation)

**2022 Materials Research Society Fall Meeting and Exhibit, Boston, MA, USA**
*Towards recyclable nanofiltration membranes - oxidised boron nitride-layered double hydroxide hybrid membranes for water purification and photocatalysis*, November $29^{th}$,2022 (Poster presentation)

**2022 Materials Research Society Fall Meeting and Exhibit, Boston, MA, USA**
*Two-dimensional chiroptically active copper (II) oxide nanostructures from layered double hydroxides*, November $29^{th}$,2022 (Poster presentation)

**2022 Materials Chemistry Poster Symposium, London, UK**
*Synthesis of chiral copper (II) oxide nanosheets via treatment of layered double hydroxides*, November $17^{th}$,2022 (Poster presentation)

# Awards and Grants

**CAS Future Leaders Award - American Chemical Society and Chemical Abstracts Service - 2024**
Awarded to 35 exceptional early career researchers worldwide to attend leadership training at CAS headquarters and present their research at the ACS Fall 2024 meeting.

**Best Oral Presentation Award - Chemical Nanoscience and Nanotechnology Annual Meeting, Royal Society of Chemistry - 2024**
Awarded for the best oral presentation at the conference, as chosen by an experienced academic panel.

**Best Poster Award - MRS Fall Meeting and Exhibit, Materials Research Society - 2023**
Awarded to a selection of the best posters at the conference, as chosen by the meeting chairs.

**Researcher Development Award - Royal Society of Chemistry 2022 and 2023**
Financial support awarded to early career scientists to undertake activities to support their research careers.

**BOC Gases Bursary - BOC Gases and TCD School of Chemistry - 2023**
Awarded annually to three Ph.D. candidates in the department who are deemed to have made significant advances in their research.

**Best Poster Award - Materials Chemistry Poster Symposium, Royal Society of Chemistry - 2022**
Awarded to the best poster at the conference, as chosen by an experienced academic panel.

# Contents

# List of Figures

# List of Tables

# Commonly used abbreviations

•OH – hydroxyl radical

0D – zero dimensional

1D – one dimensional

2D – two dimensional

3D – three dimensional

BNOx – partially oxidised boron nitride

CD – circular dichroism

CPL – circularly polarised light

CuAl-$CO_3$ LDH – carbonate-intercalated copper-aluminium layered double hydroxide

CuO-D-Phe – D-Phenylalanine-functionalised copper oxide

CuO-L-Phe – L-Phenylalanine-functionalised copper oxide

D - dextrorotatory

DBTA – dibenzoyl tartaric acid

DR UV-Vis – diffuse reflectance ultraviolet-visible

EB – Evans blue

EDX – energy dispersive X-ray spectroscopy

EELS – electron energy loss spectroscopy

FT-IR – Fourier-transform infrared

HAADF-STEM – high-angle annular dark field scanning transmission electron microscopy

h-BN – hexagonal boron nitride

hTA – hydroxyterephthalic acid

IPD – intraparticle diffusion

IR - infrared

L - levorotatory

LCPL – left-handed circularly polarised light
LDH – layered double hydroxide
LDH/BNOx – layered double hydroxide/partially oxidised boron nitride nanocomposite
LMCT – ligand-to-metal charge transfer
LPE – liquid-phase exfoliation
MB – methylene blue
MO – methyl orange
MP - millipore
NF – nanofiltration
NIR – near-infrared
PDF – powder diffraction file
PFO – pseudo-first-order
Phe - phenylalanine
PL - photoluminescence
ppm – parts per million
PSO – pseudo-second-order
PVDF – polyvinylidene fluoride
pXRD – powder X-ray diffraction
R - rectus
RCPL – right-handed circularly polarised light
RhB – rhodamine B
RPM – revolutions per minute
S - sinster
SEM – scanning electron microscopy
STEM – scanning transmission electron microscopy
TA – terephthalic acid
TEM – transmission electron microscopy
TGA – thermogravimetric analysis
UN SDG – United Nations Sustainable Development Goals
UV-Vis – ultraviolet-visible
vdW – van der Waals

# Chapter 1

# Introduction

## 1.1 The United Nations Sustainable Development Goals

The United Nations Sustainable Development Goals (UN SDGs) are a set of 17 global objectives, which were adopted and endorsed in 2015 by all UN member states as part of the 2030 Agenda for Sustainable Development. Described by the UN as an 'urgent call for action', the SDGs address a broad spectrum of global challenges including poverty, climate change, and the health of our planet, serving as a roadmap to achieving peace, prosperity, and sustainability worldwide by 2030. An overview of the 17 SDGs is given in Figure 1.1.

Both chemists and materials scientists alike are poised to play a crucial role in achieving numerous SDGs through their expertise and innovation in the development and optimisation of novel materials.[1–3] There are several SDGs that are particularly relevant challenges for materials researchers to solve.


Figure 1.1: An overview of the 17 United Nations Sustainable Development Goals.[4]

SDG 6, which highlights issues with access to clean water and sanitation, is one in which materials science is expected to be hugely pivotal. Researchers are continuously developing new advanced materials for water filtration and purification, which have the potential to revolutionise water treatment processes.[5–7] Furthermore, the development of antimicrobial and antibacterial coatings by materials scientists can help mitigate bacterial growth on pipes and in water storage facilities, acting as another safeguard for water quality.[8–11] Novel materials for energy applications is perhaps one of the largest areas of research in materials science today, which will be hugely influential in working towards SDG 7, which focuses on affordable and clean energy. Research into novel energy materials is the main driving force behind the development of efficient and sustainable energy technologies, including new batteries, photovoltaics, hydrogen fuel cells, and other energy harvesting and storage systems.[12–14] SDG 13, which underscores the urgency of climate action, aligns very closely with these efforts, as we transition away from fossil fuels and towards greener, renewable and sustainable energy sources.

## 1.2 Nanoscience - a modern field?

Nanoscience is a diverse and rapidly evolving field, transcending the traditional barriers between the disciplines of biology, chemistry, physics, medicine, and engineering. It can generally be defined as the study of objects, materials and phenomena at the nanometre scale – that is, on the scale of one billionth of one metre.[15] In the public realm, nanoscience and nanotechnology are considered to be relatively new and often futuristic fields, and unfortunately, due in part to ineffective science communication and the structures of pay-walled scientific publishing, are poorly understood, often leading to negative connotations.[16] In most works of fiction, nanoscience is often seen as a force for evil, with 'nanobots' typically being the prime suspects in bringing about doomsday scenarios, as depicted in movies such as 'Star Trek: First Contact', and in novels such as Michael Crichton's 'Prey'. In parallel, this lack of understanding, and thus fear, of nanotechnology has led to numerous conspiracy theories, particularly in relation to Covid-19 vaccines.[17] These misconceptions, while rooted in fiction and disinformation, can unconsciously shape public perceptions of the field, and can hinder genuine appreciation and understanding of the immense positive potential offered by nanoscience.[18]

Within the scientific community, many people attribute the birth of the field to theoretical physicist and Nobel laureate Richard Feynman, who delivered his now famous lecture, entitled 'There's Plenty of Room at the Bottom', at the annual American Physical Society meeting in 1959.[19] His lecture was undoubtedly a catalyst in the surge in both research and public interest in the field, which has experienced a huge influx in interest in the past 25 - 30 years. However, nanotechnology has in fact, often unknowingly, been used in a variety of applications for centuries, from the carbon nanotubes in 17th century Damascus steel swords, to the vibrant reds and yellows in the stained glass windows of Medieval Europe, produced by gold and silver nanoparticles (Figure 1.2 (a,b)).[20–23]

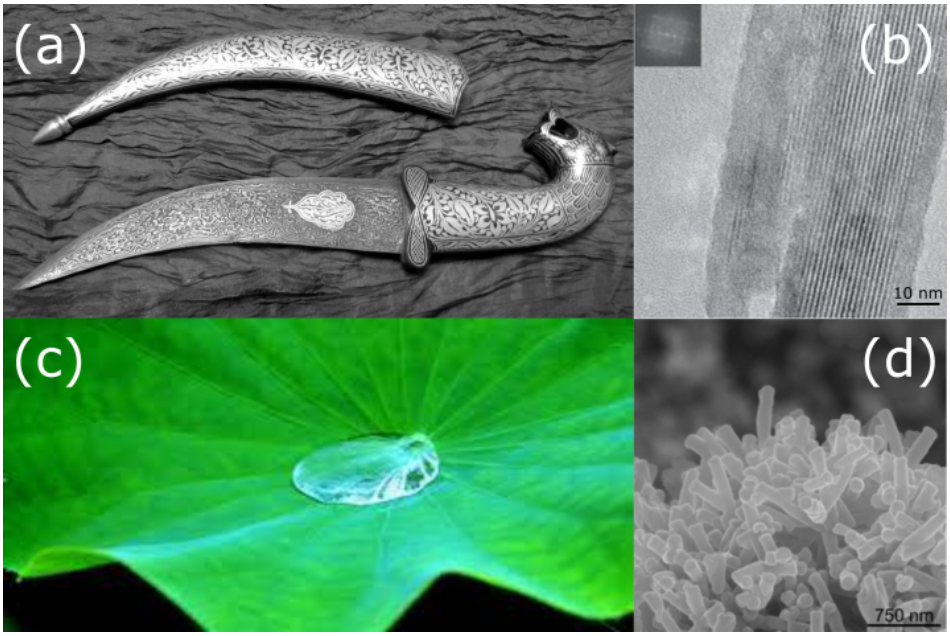


Figure 1.2: (a) Damascus steel blade. (b) TEM images depicting carbon nanotubes in Damascus steel. (c) Water droplet on Lotus leaf exhibiting hydrophobicity. (d) SEM image of Lotus leaf surface.[24–27]

In addition to man-made creations, many animals and plants also depend on nanoscience for survival. The leaf of the lotus flower exhibits a property called superhydrophobicity, due to its microscopic and nanoscopic features, which protects them from harsh environments (Figure 1.2 (c,d)). Water striders have evolved to be able run across water to avoid drowning, as the nanoscopic surface features on their legs increase their hydrophobicity.[28] These phenomena have, in turn, led nanoscientists to produce bio-inspired superhydrophobic coatings based on the lotus leaf and the water strider for numerous applications, including self-cleaning surfaces and microfluidic devices.[29,30]

## 1.3 What are nanomaterials?

Nanomaterials can be defined as materials which possess at least one dimension that measures less than 100 nanometres (nm).[31] These materials are typically sub-categorised in terms of dimensionality, being described with respect to the number of spatial dimensions of the object that are not on the nanoscale. The general shapes of nanomaterials that are accessible are three-dimensional (3D, e.g. polycrystals), two-dimensional (2D, e.g. nanosheets and nanofilms), one-dimensional (1D, e.g. nanowires and nanotubes) and zero-dimensional (0D, e.g. spherical nanoparticles and nanoprisms) (Figure 1.3).

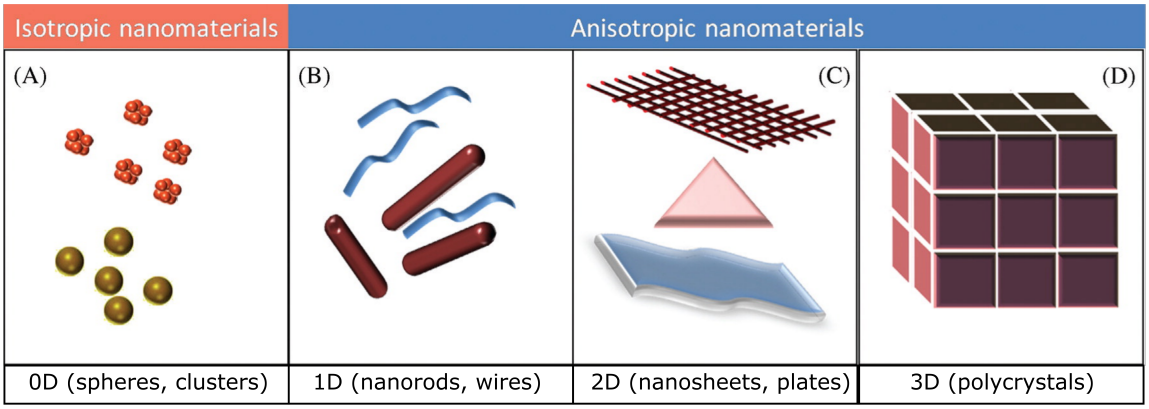


Figure 1.3: Classification of nanomaterials by dimensionality.[32]

On the nanoscale, many material properties become highly dependent on size, resulting in the emergence of a multitude of exotic properties.[33] Nanomaterials have exceptionally high surface-to-volume ratios in comparison to their bulk counterparts, as this ratio is inversely proportional to the length of the object, as demonstrated for a spherical object in Equation 1.1.

$$\frac{\text{surface area}}{\text{volume}} = \frac{4\pi r^2}{\frac{4}{3}\pi r^3} = \frac{3}{r} \tag{1.1}$$

Furthermore, as the size of the material is decreased, the percentage of atoms at the surface increases, and surface interactions become more dominant. Thus, a change in size of just a few nanometres can lead to vast changes in the behaviour and properties of nanomaterials, and this has been one of the main topics of study in the field for a number of years.[34] This anomalous size-dependent behaviour can both be as a result of surface effects, as well as quantum effects in the limit of very small nanoparticles. In fact, the importance of this phenomenon was given the highest form of recognition this year, with the 2023 Nobel Prize in Chemistry being awarded to Professors Moungi E. Bawendi, Louis E. Brus, and Alexei Ekimov, for the study of the quantum confinement phenomenon in quantum dots, a class of semiconducting nanomaterials which exhibit size-dependent luminescence emission.[35,36] This discovery has led to a number of real-world applications, with quantum dot LED-based displays being the primary example, leading to a global market share valued at over $5 billion USD in 2021.[37]

This size-property relationship is particularly evident in 2D materials, where control over the lateral size is vital for specific applications. For example, 2D material-based membranes consisting of nanosheets with larger lateral sizes are more likely to perform more efficiently, as they result in longer mass transport channels.[38,39] The thickness, or number of layers present in a 2D nanomaterial can also be hugely influential on their properties, for example in transition metal dichalcogenides (TMDs).[40] Bulk TMDs are indirect semiconductors, and they retain this property down to a thickness of two layers. They exhibit a tuneable bandgap which is dependent on the number of monolayers, and an indirect to direct bandgap transition on being reduced from the bulk to the monolayer.[41] Consequently, this results in Group VI monolayer TMDs such as $MoS_2$ and $WS_2$ being capable of exhibiting luminescence in the visible and near-IR regions region of the electromagnetic spectrum.[42]

These exceptional size-dependent properties, coupled with continuous advancements in nanoscale characterisation techniques, as well computational modelling and discovery of materials and their applications, have led to extensive research into nanomaterials in recent years.

## 1.4 Two-dimensional nanomaterials

Since the turn of century, research in the area of 2D nanomaterials has experienced a huge surge in interest, as proven in the data presented in Figure 1.4. Much of this can be traced back to 2004, when graphene was first isolated from graphite by Novoselov *et al.* by the method of mechanical exfoliation, for which he was awarded the Nobel Prize in Physics.[43,44]

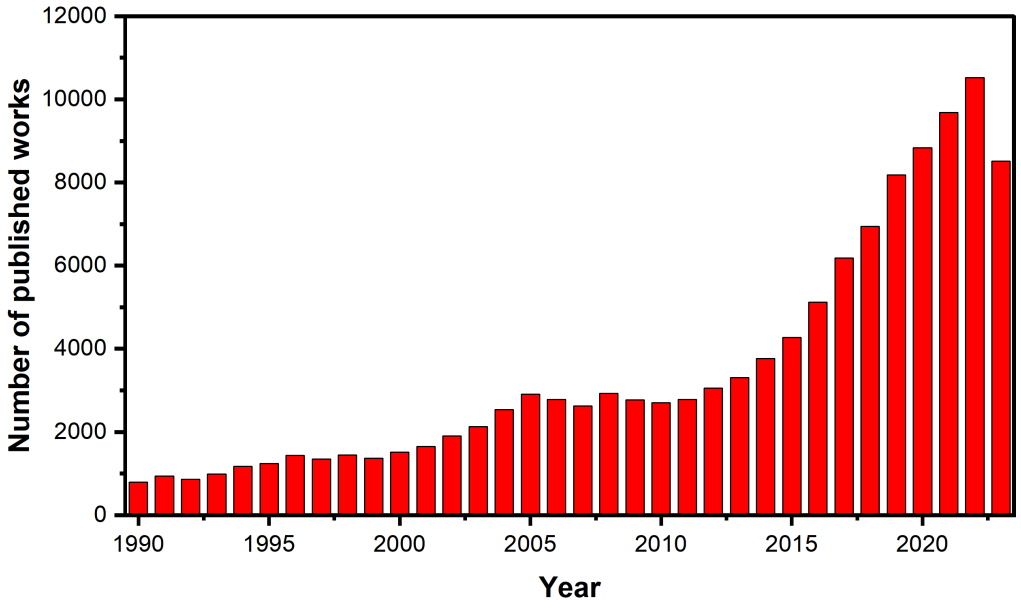


Figure 1.4: Number of publications on 2D materials, from the year 1990-2023, inclusive. Data obtained from Scopus

While this method produced high-quality samples of graphene, it was not scalable, thus limiting large-scale applications of the material.[45] In 2008, Coleman *et al.* reported liquid-phase exfoliation (LPE) of graphite, which opened the door for mass production of graphene through a facile, top-down approach.[46] This approach was later expanded upon by the same group, and was found to be effective in the exfoliation of a range of 2D materials, such as hexagonal boron nitride (h-BN) and TMDs, among others.[47]

2D nanomaterials, or more accurately quasi-2D materials, are typically characterised as having lateral dimensions of more than 100 nm, and thicknesses of a few nm. They can be more precisely categorised based on their structures, and can be distinguished as being derived from layered or non-layered materials. Moreover, within the regime of layered structures, further classifications can be made based on the interlayer interactions in these materials.

### 1.4.1 Types of 2D materials

#### Layered vs non-layered materials

2D materials are often classified in terms of the structure of their bulk counterparts, and whether these are layered, or non-layered.[48] Non-layered materials can be described as having strong isotropic chemical bonds – that is equal degrees of bonding - in all three dimensions. In the nano regime, 2D non-layered materials typically have a high degree of dangling bonds in the z-direction, leading to the formation of high-energy surfaces.[49] As such, their synthesis can be difficult, and often requires surface passivation *via* chemical functionalisation to yield colloidally stable structures. Some common examples of non-layered 2D materials include metals, metal oxides, and III-V semiconductors.[50–53] However, the majority of research conducted on 2D materials to date has been focused primarily

on layered materials.[54] Layered materials can be defined as having strong chemical bonds in the x- and y-directions (i.e. in-plane), and weaker interactions in the z-direction (i.e. out-of-plane).[55] Thus, the layers can be separated from one another with relative ease *via* physical and/or chemical methods to yield nanosheets or nanoplatelets. Some examples of 2D materials which are derived from naturally layered bulk structures include graphene, h-BN, TMDs, and LDHs.[56–58]

### Ionic vs van der Waals solids

Layered 2D materials can typically be further sub-categorised depending on the type of out-of-plane interactions, and are termed van der Waals (vdW) solids, and ionic solids.[59,60] vdW solids, such as TMDs, h-BN and graphene, typically have incredibly strong in-plane bonds, and weak vdW forces between the layers keep them bound together in the bulk. The vdW forces holding the sheets together can easily be disrupted, either mechanically or chemically, to obtain the 2D material.[61] Ionic solids, such as layered silicates, and layered double hydroxides (LDHs) consist of layers of counteranions 'sandwiched' between charged sheets, and are held together in the bulk by electrostatic interactions. A comparison between vdW and ionic solids is shown in Figure 1.5.

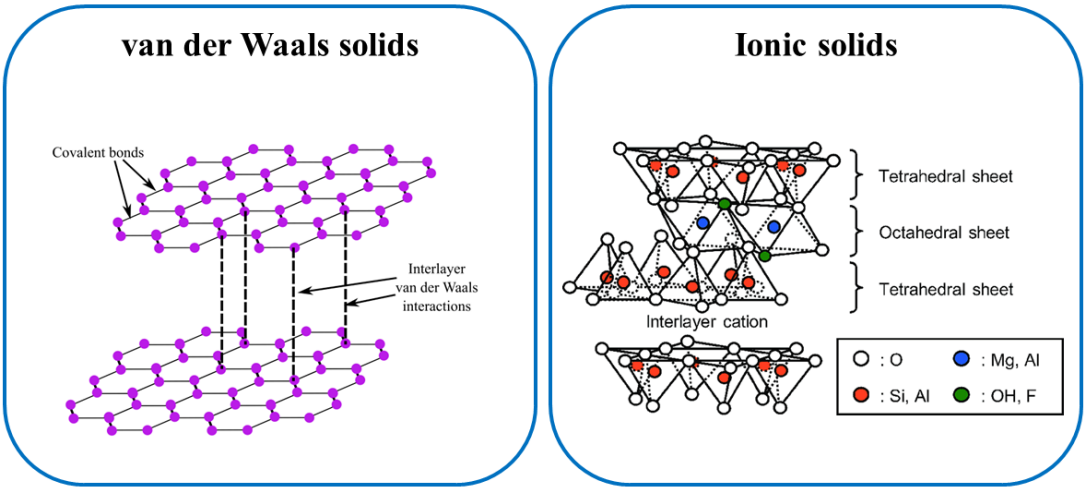


Figure 1.5: (left) The structure of graphite - a vdW solid from which graphene can be isolated. (right) The general structure of layered silicate - an ionic solid.[62]

### 1.4.2 Layered double hydroxides

Layered double hydroxides (LDHs) are a class of layered ionic materials, structurally consisting of positively charged brucite-like metal hydroxide sheets, intercalated with negatively charged counter ions.[63,64] Brucite is the mineral form of magnesium hydroxide, and consists of metal-centred, edge-sharing octahedral building blocks, with the hydroxide groups residing on the corners of the octahedra.[65] The first LDH - a carbonate-intercalated magnesium aluminium double hydroxide - was discovered in the $19^{th}$ century, and given the name hydrotalcite.[66] As such, LDHs are often referred to as hydrotalcite-like materials or anionic clays. In LDHs, the metal species is typically a mixture of divalent or trivalent cations, and to a lesser extent, monovalent cations in the case of Li-containing LDHs. The partial substitution of divalent $M^{2+}$ species such as $Cu^{2+}$, $Ni^{2+}$, $Mg^{2+}$, and $Zn^{2+}$ with trivalent

$M^{3+}$ species such as $Al^{3+}$, $Fe^{3+}$, $Cr^{3+}$, etc. in the $M(OH)_2$ brucite-like matrix results in an overall positive sheet charge.[67] The intercalation of anionic species into the LDH interlayer compensates for this positive charge, resulting in a more stable layered structure, that is held together by electrostatic interactions.[68] The most commonly reported intercalating anionic species in LDHs include carbonate ($CO_3^{2-}$)[69], nitrate ($NO_3^-$)[70], sulfate ($SO_4^{2-}$)[71] and halides (eg: $Br^-$, $Cl^-$, etc.)[72]. Water molecules also intercalate into the LDH interlayer space, and thus hydrogen bonding also plays a role in holding the sheets together.[73] The general formula for a LDH is shown in Equation 1.2:

$$[M^{2+}_{1-x}M^{3+}_x(OH)_2]^{x+}[A^{n-}]_{x/n} \cdot mH_2O \tag{1.2}$$

where $A^{n-}$ represents the intercalating, charge balancing ion, and $x$ is the fractional amount of trivalent cations in the structure. In general, a stable LDH structure is formed when $0.2 \leq x \leq 0.33$, and when the sizes of the anions are not too dissimilar. The general layered structure of a LDH is shown in Figure 1.6.

The unique properties and functionalities of LDH-based materials are a direct result of their distinct layered architecture. The partial substitution of $M^{2+}$ for $M^{3+}$ species results in the introduction of extra charge carriers, and as a result LDHs exhibit properties akin to p-doped semiconductors, where the $M^{3+}$ species acts as the dopant.[74] The variable and controllable composition of the double metal hydroxide sheets, including the relative amounts of the divalent and trivalent species, in addition to the elements used, results in high tunability of the bandgaps of these materials.[75]

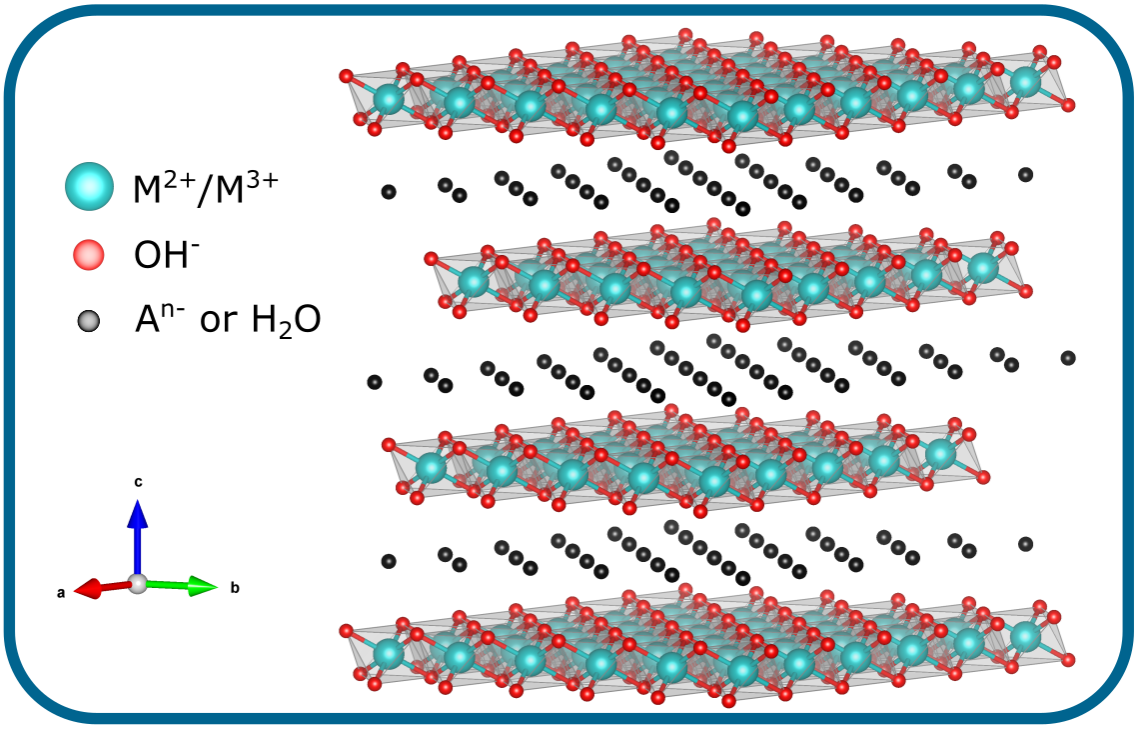


Figure 1.6: The general structure of a layered double hydroxide.

In comparison to altering the band structure of other, more traditional semiconducting nanomaterials, which typically requires complex defect engineering and doping, the bandgap of a LDH can be changed by simply altering the metal salt precursors used in synthesis.[76–78] As a result, a huge range of LDHs have been reported, ranging from narrow to wide bandgaps, with applications in this regard primarily focused on photocatalysis and electrocatalysis.[79–82]

In addition to the composition of the metal hydroxide sheets, the nature of the interlayer anion can also dictate many of the LDH properties.[80] For example, LDHs intercalated by carbonate anions have been reported to suppress the electron-hole recombination rate compared to other anions, thus improving their efficacy as photocatalysts.[83] Furthermore, the anions themselves are exchangeable, as they are held in the interlayer between cationic sheets by electrostatic interactions, and so can be replaced

in the interlamellar space by other species of interest.[84] As a result, a huge range of chemical species have been successfully introduced in the LDH interlayer, including amino acids[85], pharmaceutical compounds[86], and luminescent dyes[87]. This unique anion exchange capability serves as the basis of a wide variety of LDH applications, including catalysis[88], pollutant removal[89], energy storage[90], sensing[91], and drug delivery[92], to name a few. Thus, the inherent adaptability and tunability of LDHs make them a worthy focal point of materials science research. Some specific properties and applications of LDHs, as well as synthetic approaches, are discussed in more detail throughout this chapter.

### 1.4.3 Boron nitride

Crystalline boron nitride (BN) has four different structural polymorphs, which are analogous to carbon lattices, and can typically be split into either $sp^2$ or $sp^3$-bonded configurations, as shown in Figure 1.7. The $sp^3$-bonded phases, namely cubic (c-BN) and wurtzite (w-BN) are incredibly strong, non-layered materials, with c-BN being a structural analogue of diamond.[93] On the other hand, the $sp^2$-bonded hexagonal (h-BN) and rhombohedral (r-BN) are van der Waals layered materials with strong in-plane interactions and weak out-of-plane interactions, and thus can be exfoliated to obtain individual BN nanosheets. The primary structural difference between r-BN and h-BN is in the stacking pattern – h-BN stacks in an AB pattern, whereas r-BN stacks in an ABC pattern.[94] h-BN, which is analogous to graphite, is the most thermodynamically stable, and thus the most commonly used BN polymorph in both research and commercial applications.[95]

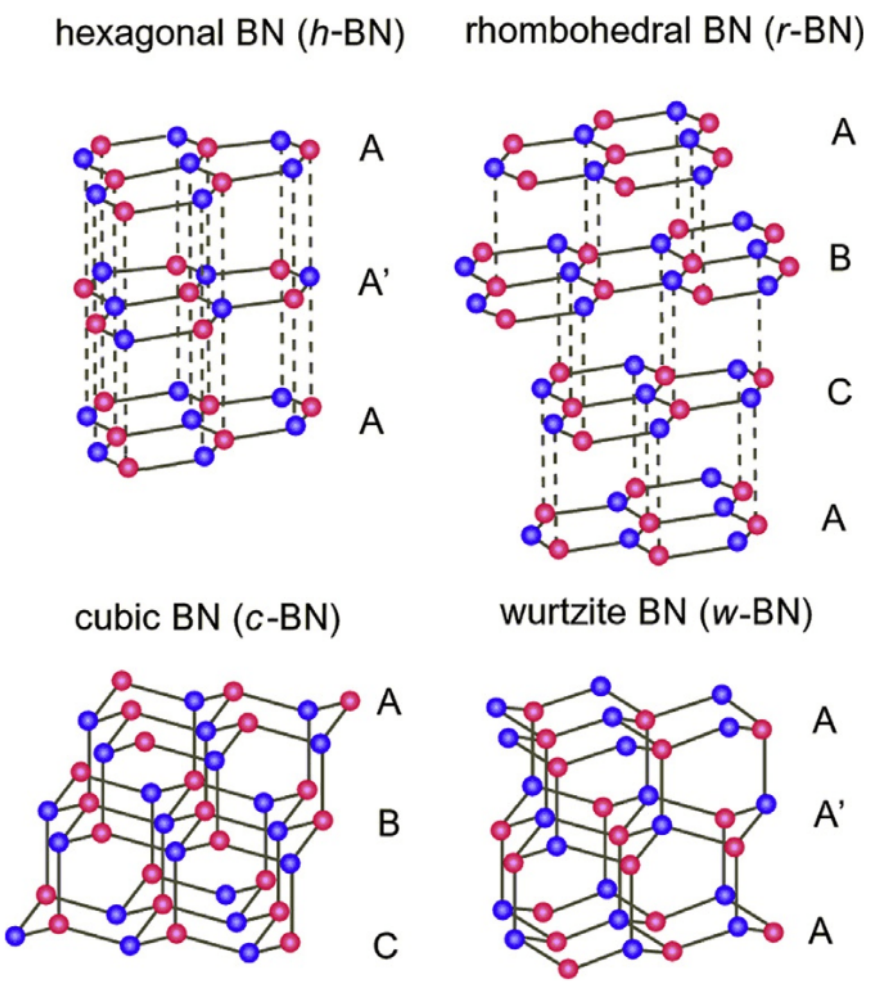


Figure 1.7: The four different polymorphs of boron nitride.[96]

Thus, individual sheets of h-BN are considered structural analogues of graphene, with alternating single and double boron-nitrogen bonds, earning it the nickname 'white graphene'.[97] Although it bears striking structural similarities to graphene, h-BN exhibits vastly different chemical and physical properties, including optical transparency due to its wide bandgap, electrical insulating properties, as well as excellent thermal and chemical stability.[98]

### 1.4.4 Preparation methods of 2D materials - 'top-down' vs 'bottom-up'

While a plethora of synthetic and preparation techniques for 2D materials exist, they can typically be categorised as either 'top-down' or 'bottom-up'. Here, an overview of common top-down and bottom-up synthetic methods, as well as synthetic strategies for producing LDHs in particular, are discussed.

#### Top-down methods

Top-down methods involve the exfoliation or etching of bulk materials to obtain thin layers of quasi-2D materials.[99] In the context of 2D materials, the term 'exfoliation' refers to a process whereby an external force is applied to cleave thin sheets, ranging from few-layers to monolayer, from a bulk material.[100] Undoubtedly, exfoliation is the most common method of preparing 2D materials. Generally, exfoliation processes utilise some external force (typically chemical, physical or a combination of the two) to overcome the energy of van der Waals interactions between sheets of a layered crystal, although in recent years much progress has been made on the exfoliation of non-van der Waals crystals, including layered ionic crystals, as well as non-layered, isotropic crystals.[101–103] While multiple types of exfoliation can be defined, the two most well-known methods are mechanical exfoliation and liquid-phase exfoliation.

Mechanical exfoliation, more often referred to as the 'Scotch tape method', involves the use of adhesive tape to peel thin layers from a bulk crystal of a layered material, such as graphite. In fact, this was how Nobel Laureate, Sir Kostya Novoselov, first isolated graphene from graphite.[43] The obtained 2D material can then easily be deposited on a

substrate. While this method was ideal for producing high-quality samples of graphene, its time-consuming, low-throughput nature, and thus lack of scalability, meant its use was limited to laboratory settings only. However, this 2D material production method has experienced somewhat of a revival in recent times, thanks to Prof. Andres Castellanos-Gomez, whose group recently developed a simple high-throughput mechanical exfoliation approach for vdW materials.[104]

Liquid-phase exfoliation (LPE) is a technique first reported and coined by Prof. Jonathan Coleman and his research group, paving the way for high-throughput and scalable production of vdW 2D materials. LPE is a solution-based technique, which involves breaking a vdW solid apart into individual layers in a given solvent using ultrasonic energy, either in an ultrasonication bath, or by using an ultrasonic tip. One of the early proposed mechanisms of LPE was that the energy cost of exfoliation is minimised when the surface energies of the nanosheet and the solvent are roughly equal, allowing for the identification of appropriate solvents.[47] More recently, reports have demonstrated that the actual mechanism is a more complex, multi-step mechanism, involving the formation of defect planes and ultrasonic energy-induced cleavage and 'unzipping' of the crystals.[105]

Although the method of LPE addresses the issue of scalability in the production of 2D materials, it does present other challenges. The best results from LPE are often obtained using high-boiling point organic solvents, such as $N$-methyl-2-pyrrolidone (NMP) and dimethylformamide (DMF), which are toxic and hard to remove from the end product.[106] However, the exfoliation of an array of 2D materials in green solvents, including water and ethanol, have gained significant traction in recent years.[107–109] Furthermore, LPE alone has relatively poor controllability over the number of layers and lateral sizes of nanosheets formed, often requiring further post-processing steps to achieve monodisperse samples.[110] Despite these challenges, LPE is still the preferred technique for producing large amounts of exfoliated 2D materials, such as h-BN, with relative ease.

### Bottom-up methods

An alternative approach to exfoliation for the production of 2D materials is controlled 'bottom-up' synthesis. Bottom-up synthesis refers to methods by which materials are produced by assembly of the individual atoms and molecules to produce the desired structures. In many cases, bottom-up synthetic approaches can address the shortfalls of LPE in terms of monodispersity of products, as well as eliminate the need for post-processing. Furthermore, both layered and non-layered materials are easily accessible *via* bottom-up approaches. Perhaps one of the most widely-known methods of 'bottom-up' synthesis is chemical vapour deposition, which can produce highly crystalline, defect-free large lateral size monolayers of many layered and non-layered materials.[111–113] The main drawback of this method is that it is very expensive, energy intensive, deals with harmful and often toxic chemical precursors, and shows low potential for commercial scalability.[114] Instead, solution-based bottom-up synthetic approaches may be a more viable option in terms of cost, accessibility and quality, as well as potential scalability.[115] In this regard, some of the most commonly reported approaches include hydro/solvothermal, hot-injection, and precipitation techniques.[116–118]

Hydro/solvothermal methods date back to the early 1900s in the works of Morey and Niggli, and are commonly used in the synthesis of a variety of nanomaterials.[119,120] They involve the synthesis of materials in closed vessels at high temperatures and pressures, carried out in water (hydrothermal) or other, non-aqueous solvents (solvothermal). The main variables in hydro/solvothermal reactions are the type of solvent, reaction time, and reaction temperature. While these methods have many advantages, including relatively low energy consumption and use of green solvents, the batch hydro/solvothermal process has traditionally been considered somewhat of an informational 'black box', as it is a closed system, and information can only be gained pre- and post-synthesis.[121] That

being said, synchroton studies have played a pivotal role in unraveling the intricacies of hydro/solvothermal synthetic approaches, with autoclave *in situ* diffraction studies being instrumental in understanding the hydro/solvothermal crystallisation of a range of materials, from LDHs, to zeolites, and beyond.[122–124]

The concept of hot-injection synthesis can be attributed to LaMer and Dinegar who, in the 1950s, proposed a set of conditions which are necessary to synthesise monodisperse colloidal solutions of nanoparticles.[125] Their theory involved a rapid nucleation step, followed by a slower step of controlled growth of nuclei to form larger particles.[126] This motivated some groups of researchers to develop a new method of synthesising colloidal QDs which involved the rapid injection of organometallic precursors into vessels at high temperatures containing coordinating ligands and solvents. This method, termed 'hot-injection', has become commonplace in the synthesis of QDs, and has also been transferred to the synthesis of 2D materials, mainly TMDs.[127,128] A number of parameters can be varied in the hot-injection approach, including temperature, reaction time, coordinating and non-coordinating solvents, and choice of precursors (elemental vs organometallic). While hot-injection allows for higher degrees of controllability over the reaction, and allows for information to easily be obtained at various reaction stages through taking aliquots for analysis, it also suffers from some drawbacks.[129] The main downside to hot-injection is that it is a very energy-intensive process, requiring high temperatures over lengthy timescales, and often utilises non-environmentally friendly, high boiling-point organic solvents.[130] Furthermore, the scalability of this process is still limited, and even successful large-scale hot-injection reactions can prove to be very costly and energy inefficient.[131]

Precipitation synthesis is a commonly reported nanomaterials synthesis technique, and is much simpler, greener, and more accessible than the previously mentioned bottom-up synthetic techniques.[132,133] Precipitation reactions involve the addition of metal precursors to a solvent, followed by the addition of a base to force the precipitation of nanoparticles out

of solution.[134] Co-precipitation is a specific subset of this reaction, in which multiple metal salts are precipitated out in conjunction with one another to produce a material composed of a mixture of the metals.[135] The main synthetic variables in these types of reactions are the atmosphere (inert vs. atmospheric conditions), pH, temperature, and the type of base used. For example, basic substances such as sodium citrate can be used both as base, as well as a stabiliser in the synthesis of magnetic ferrite nanoparticles.

(Co-)precipitation reactions are typically carried out at low temperatures ($< 120\ ^{\circ}C$), and very often at room temperature. In addition, (co-)precipitation reactions are often carried out in aqueous media or other benign solvents, which lends itself to a number of applications, including in medicine, and in environmental applications.[136] This technique has been used in the synthesis of a variety of nanomaterials, including magnetic nanoparticles (particularly ferrites), LDHs, and layered silicates.[137] The main benefits of this technique are that it is a very green and environmentally friendly process. (Co)-precipitation is incredibly simple, requires no specialised equipment or glassware, has huge potential for scalability, and is very energy efficient, often requiring no heat input or use of inert atmospheres.[117] However, due to the low temperatures involved, 2D materials synthesised using this approach are often multi-layered, and sometimes the bulk counterparts can instead be formed.[138] Furthermore, the number of 2D materials accessible *via* this approach is limited at this stage. Nevertheless, it is still a very useful, simple, and green technique for specific materials, including LDHs.

**Layered double hydroxides - synthetic approaches**

LDHs have been studied extensively since the 1940s, and as such there are a plethora of synthetic strategies that have been reported in the literature to date. Co-precipitation is the most commonly reported bottom-up synthetic method for LDHs, and the primary synthetic method employed throughout this thesis. A general schematic of the co-precipitation process for carbonated-intercalated copper-aluminium LDHs, as an example, is shown in Figure 1.8.

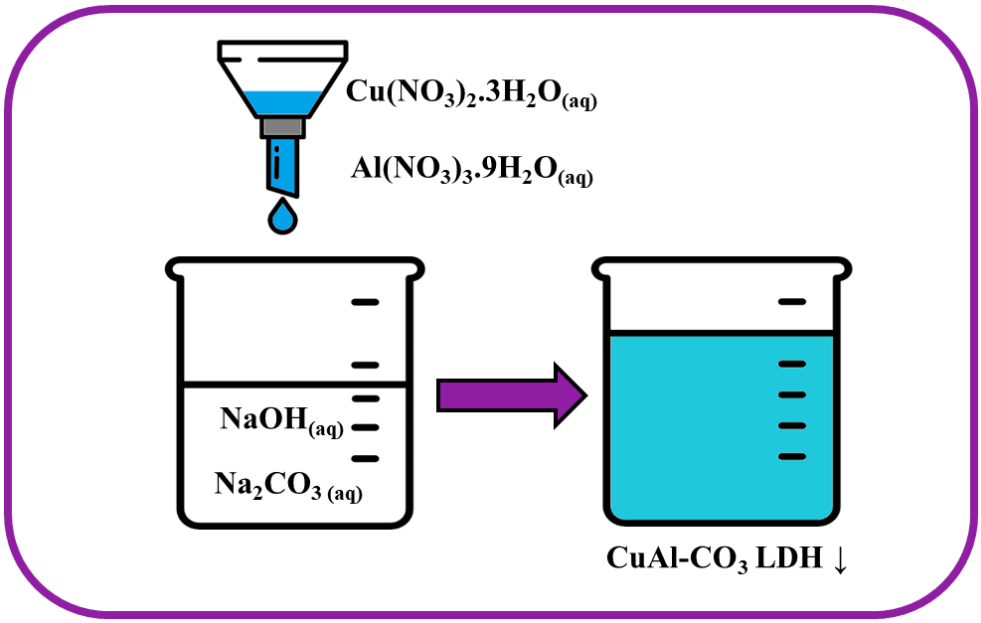


Figure 1.8: Schematic of a co-precipitation reaction for the formation of carbonate-intercalated copper-aluminium layered double hydroxides.

However, the co-precipitation approach, despite its simplicity and the formation of high purity LDH phases, has some disadvantages, including producing LDH particles with broad size distributions. Besides the co-precipitation method, numerous top-down and bottom-up approaches have been reported for the preparation of LDHs. The homogenous precipitation method, often called the 'urea method', is another commonly used approach for the bottom-up synthesis of LDHs.[139,140] Briefly, an aqueous solution of divalent and trivalent metal salts, along with urea, are added to a hydrothermal autoclave. Elevated temperatures are utilised

to drive the thermal hydrolysis of urea to form ammonium carbonate, increasing the pH of the solution and facilitating the precipitation of the hydroxides from the metal salts to form the LDH phase.[141] Other weak bases such as hexamethlyenetetramine are occasionally used in place of urea.[142,143] This method produces large LDH nanosheets with excellent crystallinity, but in the case of aluminium-containing LDHs has been shown to result in the formation of non-negligible amounts of undesirable side products, including amorphous aluminium oxides and hydroxides.[144]

Another bottom-up approach to LDH synthesis, which is most commonly used for Al-containing LDHs, is the sol-gel method. In this procedure, strong acids such as hydrochloric or nitric acid are used to drive the hydrolysis of organometallic precursors such as aluminium alkoxides. Salts containing the $M^{2+}$ species of choice are then added, and controlled condensation reactions result in LDH formation, rather than the formation of separate hydroxide phases.[145,146] As the mixture is aged, oligomerisation and polymerisation reactions result in the formation of a LDH gel with unique 'nanocapsule'-type morphologies. This approach has been found to be highly versatile in the production of numerous dimetallic and trimetallic LDHs.[147]

The reverse microemulsion approach to LDH synthesis was first introduced by the O'Hare group in 2005, and was developed further by the same group in subsequent years to produce monolayer LDHs.[148,149] This procedure involes introducing the traditional aqueous co-precipitation ingredients (e.g. metal salts, precipitating agent and anion source) into an oil phase containing surfactants, resulting in the formation of nano-sized aqueous droplets surrounded by surfactant dispersed in the organic phase. The co-precipitation reaction is then confined to the shape and size of these droplets, whose size can be controlled by varying the ratio of water to surfactant, resulting in the formation of highly monodisperse LDH NPs.[150] It is important to note that only the most common or noteworthy synthetic methods have been discussed here, but numerous alternative bottom-up synthetic approaches for

LDHs have been reported to date, including the salt-oxide method, oxidation approaches, and electrochemical deposition.[151,152]

In addition to bottom-up approaches, top-down, so-called 'delamination' methods are also widely used for producing LDH nanomaterials. However, in contrast to exfoliation of vdW materials, it is more difficult to achieve 2D materials from bulk LDH crystals due to their ionic nature.[153] Nevertheless, significant strides have been made in the delamination of LDHs, particularly by exploiting their anion exchange properties. Most of the reported delamination protocols involve the use of a surfactant and a highly polar solvent. First, anionic surfactant molecules are intercalated into the LDH interlayer space *via* anion exchange, which expands the $d$-spacing and thus weakens interlayer interactions between the brucite sheets. Dispersing this surfactant-intercalated LDH in a polar solvent leads to solvation of the hydrophobic tails of the surfactant molecules, causing delamination of the LDH into individual sheets.[153,154] A large variety of intercalates have been reported to be successful for inducing delamination, including sodium dodecyl sulfate, sodium 4-octylbenzenesulfonate and sodium dodecylbenzenesulfonate[154,155], as well as a range of amino acids.[156] Furthermore, numerous solvents have been utilised in delamination processes, including formamide[157,158], butanol[159], ethanol[160], N,N-Dimethylformamide[161] water[162], and even extending to non-polar solvents such as toluene and tetrachloromethane.[163]

## 1.5 Chirality in nanomaterials

Chirality is a term that refers to the asymmetry of molecules, in which a chiral molecule is non-superimposable on its mirror image form.[164] The first experimental observation of chirality can be traced back to the year 1812, when French physicist Jean-Baptiste Biot discovered that the plane of polarised light was observed to have been rotated with respect to the incident beam after passing through organic material.[165] In 1848, Louis Pasteur, fondly known as the 'father of chirality', made further strides in this area of optical asymmetry, reporting that crystals of tartaric acid were capable of this property of rotating the plane of polarised light, and that it was a result of asymmetry down to a molecular level.[166] This phenomenon was later termed 'chirality' by Lord Kelvin in the year 1893.[167] The ability of chiral molecules to interact anisotropically with circularly polarised light (CPL) is due to a property called circular birefringence, in which there are two distinct refractive indices in a given material – one value for right-handed CPL (RCPL), and another value for left-handed CPL (LCPL).[165]

These molecular isomers are termed enantiomers. While enantiomers exhibit many near-identical physical and chemical properties, they differ in how they interact with CPL. They can be labelled dextrorotatory ($D$) if they rotate the plane of polarised light clockwise, or levorotatory ($L$) if it is rotated anti-clockwise.[168] While this naming system is appropriate for describing the optical rotatory properties of a given molecule, it is not sufficient to describe the absolute configuration in terms of stereocentres. Carbon-based stereocentres are the most common type, and are typically defined as a carbon atom which has four different substituents bonded to it. The system used for assigning absolute configuration is based on Cahn-Ingold-Prelog (CIP) rules, and the letter $S$ (from the Latin sinister) is used to describe left-handed enantiomers, whereas the letter $R$ (from the Latin rectus) is used to describe right-handed enantiomers.

The phenomenon of chirality is evident all throughout nature, with some examples of biologically important chiral molecules including amino acids and DNA, as well as pharmaceutically important compounds. For example, chiral compounds such as penicillamine are used in the treatment of heavy metal poisoning and rheumatoid arthritis, and citalopram is used as a drug in the treatment of depression and anxiety. While it was once believed chirality was limited to organic systems, this was disproven by Alfred Werner in 1911, who described chirality in hexol, a cobalt-centred metal complex. Since then, chirality has been observed in numerous inorganic systems, and perhaps one of the biggest consequences of this was the emergence of the field of chiral nanomaterials. This field was pioneered by Prof. Yurii Gun'ko and his research group, dating back to the synthesis of chiral cadmium sulfide (CdS) QDs in 2007 by Moloney *et al*. A brief overview of the timeline of chirality, highlighting some key milestones, is shown in Figure 1.9.

It is important to note that the study of chirality in nanomaterials can often be much more complex than for organic molecules, as chirality must be considered on both the molecular scale, as well as the nano and microscale, and, as such, can not sufficiently be described by CIP rules. The most common way to observe chirality amongst these systems remains through monitoring the optical activity, although it has progressed from the times of Louis Pasteur. Nowadays, optical activity in nanomaterials is typically measured using circular dichroism (CD) spectroscopy, which analyses the asymmetry in the response of chiral materials to CPL. The absolute strength of the CD signal is typically reported in terms of the Kuhn anisotropy factor or $g$-factor, which normalises the CD response by its absorbance and is discussed in more detail in the Materials and Methods section. Depending on the type of chirality present, the $g$-factor can vary substantially.

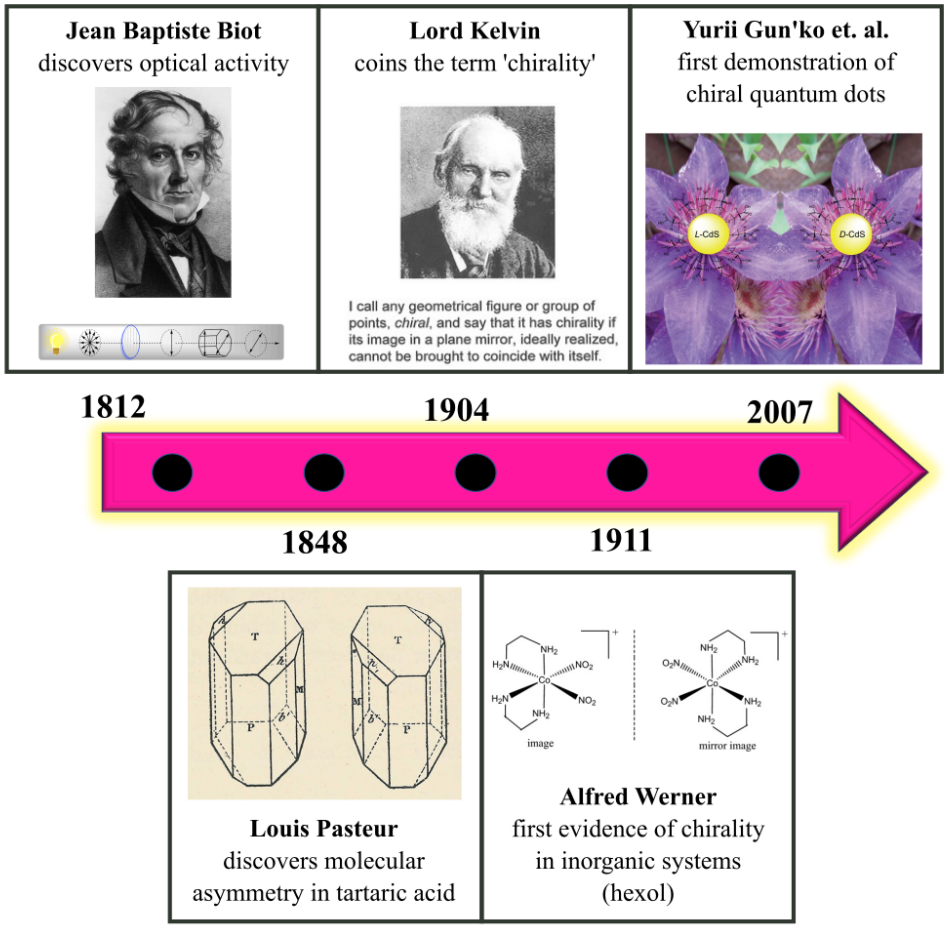


Figure 1.9: Some key milestones in the study of chirality.[169–174]

### 1.5.1 Common types of chirality observed in inorganic nanomaterials

Typically CD signals can be observed in nanomaterials through one of three types of nanoscale chirality, which can be categorised as intrinsic chirality, ligand-induced chirality, and chiral assembly or superstructure formation.[175,176] A visual overview of the types of chirality observed in nanomaterials is shown in Figure 1.10.

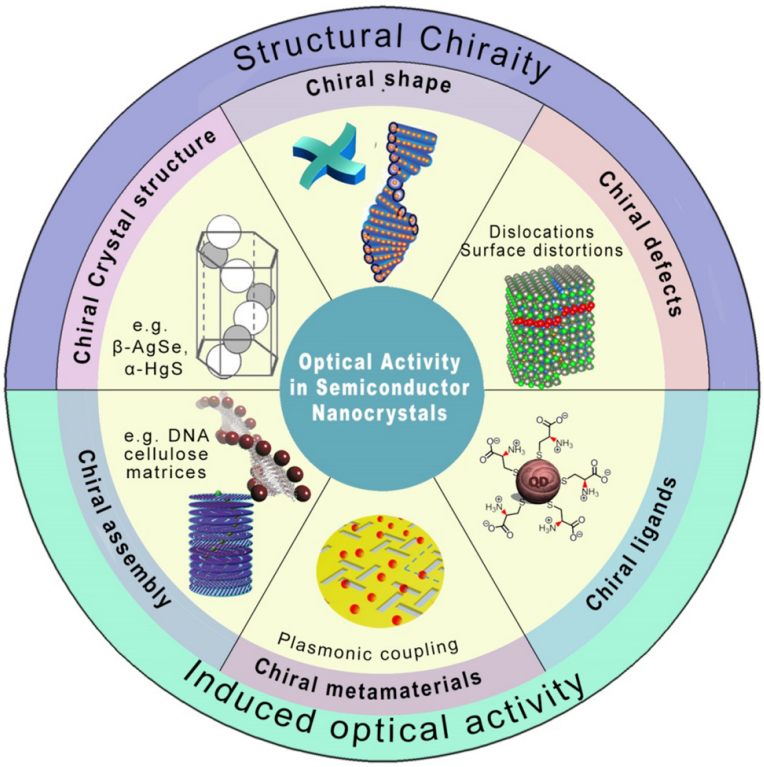


Figure 1.10: An overview of the main types of chirality observed in nanomaterials.[177]

### Intrinsically chiral nanoparticles

Nanoparticles (NPs) are not perfect or ideal geometric objects, and as such often have asymmetric faces, edges and vertices, as well as both surface and bulk defects and dislocations. Chiral arrangements of defects and/or distortions in the crystal lattice (e.g: screw dislocations) can often induce optical activity in NPs.[178–181] The use of chiral ligands, either *in situ* or by post-synthetic treatment, can result in the generation of chiral defects and distortions.[177,182]

Some materials, such as gold and copper, have high Miller-index facets with intrinsic chirality due to the presence of the chiral terraces, or kink sites.[183] Furthermore,

some materials possess intrinsically chiral crystal lattices, such as $\alpha$-HgS, selenium and tellurium.[184–186] Carbon nanotubes (CNTs) also possess intrinsic chirality, depending upon the direction in which a 2D nanosheet is rolled up to form the nanotube.[187]

### Ligand-induced chirality

The transfer of chirality from surface adsorbed chiral ligands to achiral inorganic nanomaterials is typically referred to as 'ligand-induced chirality'. This type of chirality is typically observed using chiroptical spectroscopy, with the appearance of new CD bands after ligand functionalisation indicative of successful chiral induction.[177,188] These new CD bands appear in the UV and visible regions of the electromagnetic spectrum due to the overlap of the electronic states of the chiral surface ligand with those of the nanomaterial. In particular, these bands typically appear in the plasmonic region for metal NPs, and in the range of excitonic transitions in semiconductor NPs.[184,189–191] Furthermore, if a chiral molecule has multiple anchor groups to a NP surface, the specific binding mode can affect the electronic overlap and thus the chiroptical properties, even inducing the opposite CD signal in the same enantiomer with a different binding mode.[192,193]

### Chiral assemblies and superstructures

Nanomaterials can also exhibit significant optical activity if the shape itself is chiral, or by assembling into structures. Chiral NP assemblies, which may be formed from achiral or chiral building blocks, are capable of exhibiting substantial optical activity.[194–196] This enhanced optical activity in chiral assemblies arises due to the strong electromagnetic coupling between the individual NPs, giving rise to an amplified chiral response.[197] A particularly intriguing aspect of chiral assembly is hierarchical or structural chirality, in

which the chirality of the individual particles is translated into chiral geometry of the assembled superstructure itself, which can strongly enhance the optical activity. This chiral nanostructural assembly is similar to the assembly of amino acids in proteins into alpha helices and beta sheets.[198,199]

### 1.5.2 Synthetic strategies for the production of chiral nanomaterials

Chiral nanomaterials can be prepared using a number of methods, including templating, external forces, and synthesis or treatment with chiral ligands. The resulting chiral nanomaterials can range from individual chiral NPs, to microscale chiral assemblies, to macroscale chiral superstructures. Undoubtedly, the most commonly reported method of chirality induction is through synthetic functionalisation of nanomaterials with chiral molecules, either *in situ*, or by post-synthetic treatment or ligand-exchange reactions.[200–204] External forces, which are intrinsically chiral, can also be used to induce the chiral assembly of either chiral or achiral constituent NPs, typically resulting in significant changes to the optical activity. These include the use of vortices, magnetic fields, and CPL to induce chirality.[205–207] The emerging area of light-driven chirality is of significant interest, with left- and right-handed CPL being capable of driving the synthesis and self-assembly of left- and right-handed chiral nanostructures.[208]

### 1.5.3 Chirality in layered double hydroxides - progress and opportunities

To date, much progress has been made in the immobilisation of chiral species, including amino acids, drugs, and DNA, in the LDH interlayer gallery. Aisawa *et al.* successfully intercalated amino acids in a range of LDH compositions, both through direct co-precipitation using amino acids as the interlayer ion[209], as well as calcination-rehydration methods to remove carbonate from the interlayer and replace it with the amino acid upon rehydration of the LDH.[210] Both anion exchange and direct co-preciptiation approaches have also been used for the insertion of DNA in the LDH interlayer.[211,212] Wei *et al.* reported the intercalation of L-Dopa - a drug used in treating the symptoms of Parkinson's disease - in a magnesium-aluminium LDH for drug delivery. The strong electrostatic host-guest interactions between the carboxylate group of L-Dopa and the positively charged LDH layers prevents the racemisation of L-Dopa, improving its efficacy in *in vitro* models.[213]

However, despite the strides made in using LDHs as hosts for chiral molecules, the study of chirality induction in LDHs is still in its infancy. Synthesis of LDHs in the presence of symmetry breaking agents, or by using chiral templates, has the potential to produce unique chiral morphologies such as chiral nanoflowers, as has been demonstrated for metal oxides[214,215], and twisted assemblies of nanosheets or nanoplatelets, as has been reported for a number of materials[216–218]. Furthermore, there is significant scope for induction of optical activity in transition metal-containing LDHs. Successful coupling of the electronic states of chiral molecules and transition metal-containing LDHs would lead to chiroptical activity in the UV and visible region, akin to that observed by transition metal oxide and hydroxide-based nanomaterials.[219,220] It is anticipated that progress in this relatively untapped area of research could lead to new, exotic applications of LDHs, from asymmetric catalysis, to CPL emitters, to building blocks of membranes for enantioselective separation, and beyond.

# 1.6 Photoluminescence

## 1.6.1 Fluorescence vs. phosphorescence

Photoluminescence is the term given to the radiative decay of an excited electronic state of a material, which is formed by the absorption of photons.[221] Radiative decay of the excited state can occur *via* one of two pathways: fluorescence or phosphorescence.[222] This depends on whether the emission occurs from a singlet or triplet excited state. A singlet ground state consists of two paired electrons with opposite spins as per the Pauli exclusion principle, and thus has a spin multiplicity of 1 ($2S + 1$, where $S = +\frac{1}{2} - \frac{1}{2} = 0$). A singlet excited state is formed when the promoted electron maintains the same spin orientation. Emission that occurs from decay of a singlet excited state is known as fluorescence and occurs on a short timescale – typically on the order of nanoseconds.[223]

Triplet excited states, on the other hand, consist of two unpaired electrons with the same spin, either both spin-up or both spin-down, and thus these states have a spin multiplicity of 3.[224] Electronic transitions between states of different multiplicities are technically forbidden according to the spin selection rule, as it involves the excited electron essentially reversing its spin. However, this transition is more favourable through the process of intersystem crossing if there is overlap between the vibrational energy levels of the singlet and triplet excited states. This phenomenon is known as spin-orbit coupling, and is most commonly observed in materials containing heavier atoms.[225] Emission resulting from the decay of a triplet excited state is termed phosphorescence, and has a much longer lifetime than fluorescence, typically on the order of microseconds to seconds.[226] Phosphorescence is a characteristic of many lanthanide complexes and lanthanide-doped materials.[227]

### 1.6.2 Lanthanide luminescence

Luminescence arises in lanthanides due to $f-f$ electronic transitions. Although these transitions are technically forbidden according to Laporte selection rules, they do occur in solid matrices due the effects of the surrounding crystal field, removing the degeneracy of the $f$-suborbitals.[228] This results in the emission spectra of the lanthanide ions consisting of a number of sharp distinct emission peaks in a relatively narrow wavelength range. A further hallmark of lanthanide emission spectra are their large Stokes shifts, which are beneficial for applications as fluorescent probes, as emission measurements are less prone to interference from the excitation source.[229,230]

The emission of lanthanides is typically described using term symbols $^{2S+1}L_J$, where $S$ is the total spin quantum number, $L$ is the orbital angular momentum quantum number, and $J$ is the total angular momentum quantum number. The various radiative transitions in $Eu^{3+}$ and $Tb^{3+}$ ions are summarised by the Jablonski diagram in Figure 1.11.

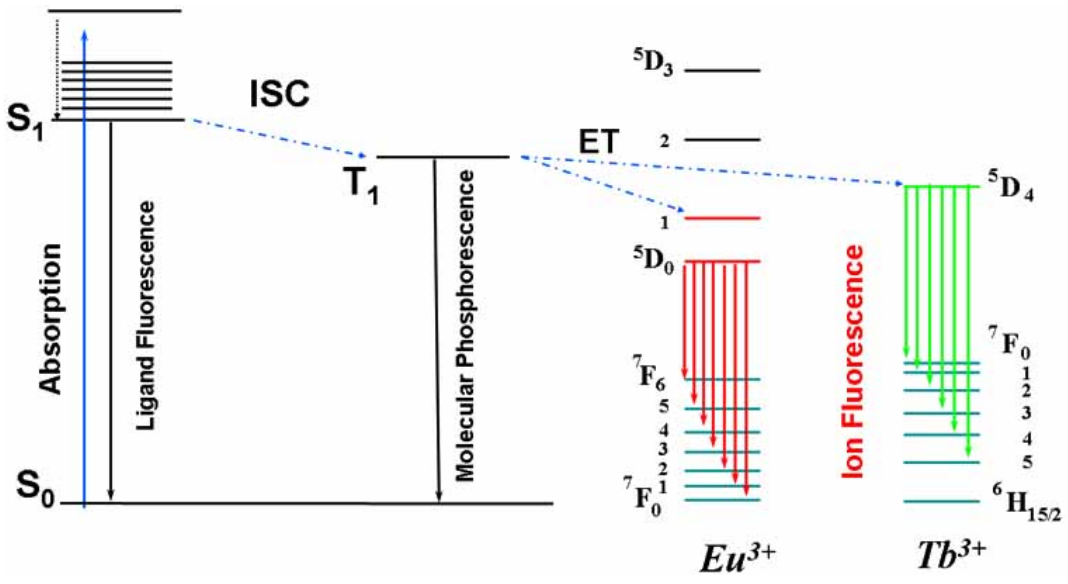


Figure 1.11: Jablonski diagram showing singlet to triplet conversion in $Eu^{3+}$ and $Tb^{3+}$ ions, and radiative decay of the triplet states.[231]

### 1.6.3 Layered double hydroxides as host matrices for lanthanide cations

Lanthanide luminescence is known to be highly sensitive to its environment, and the emission can be reduced or suppressed through various mechanisms, including solution quenching and self-quenching. In particular, self-quenching or 'concentration quenching' is a prevalent issue in lanthanide-based emissive materials. Concentration quenching mechanisms include both non-radiative cross-relaxation between adjacent lanthanide cations, and in the case of nanomaterials, energy transfer to the surface, further diminishing the emission intensity.[232] Doping of inorganic nanomaterials with lanthanide cations, particular $Eu^{3+}$ and $Tb^{3+}$ species, has been an incredibly important avenue of research in recent years.[233–237] This approach is based on the fact that the inorganic matrix can protect the lanthanide species from the surrounding environment, minimising solvent quenching. Furthermore, the use of small amounts of lanthanide dopants in inorganic nanostructures both minimises concentration quenching, as well as saves on cost, while preserving the unique luminescence behaviour. LDHs are an ideal candidate for lanthanide cation doping, as these trivalent species can seamlessly integrate into the LDH sheet structure, occupying the centre of the $M(OH)_6$ octahedra by replacement of either the $M^{2+}$ or $M^{3+}$ species, and as such, there have been numerous reports of trivalent europium and terbium-doped LDHs.[238–243] Thus, integration of lanthanide cations within LDH structures not only protects them from quenching, but also provides a stable framework to expand their applications, ranging from optoelectronics, to luminescent sensing, and beyond.

## 1.7 Nanofiltration for water purification

Nanofiltration (NF) is a membrane-based filtration technology that has performances that are considered somewhere between that of ultrafiltration (UF), which is effective for the separation of macromolecules, and reverse osmosis (RO), which in the ideal case, only permits passage of water through a membrane (Figure 1.12). NF is considered as striking the right balance between UF and RO, offering a higher degree of selectivity than UF, while operating at much lower pressures than RO, and thus minimising the energy consumption during the filtration process. The majority of publications on NF typically report operating pressures between 1 and 40 bar.[244]

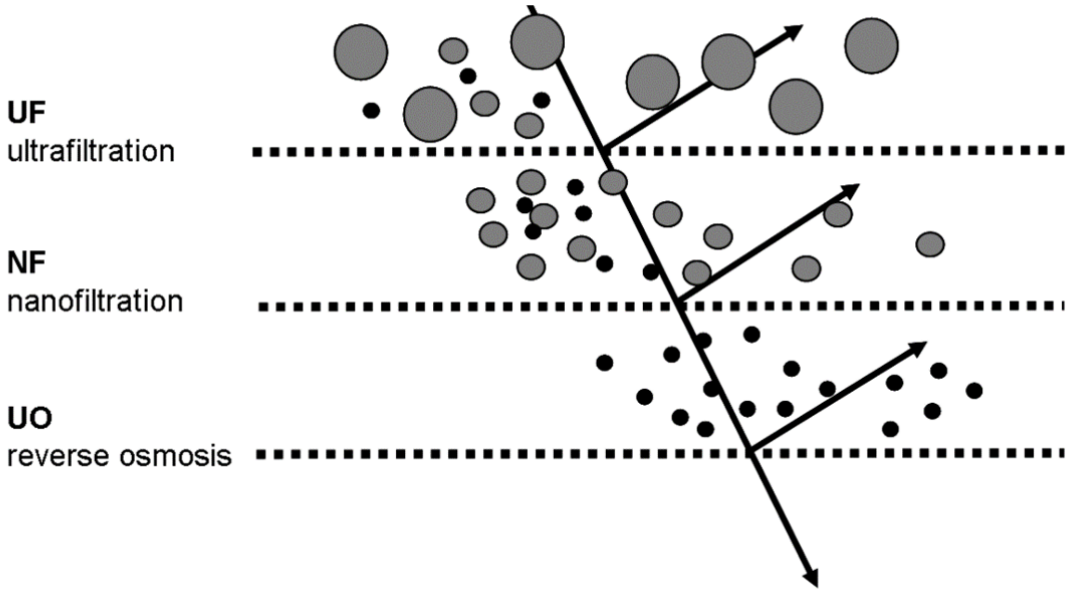


Figure 1.12: Comparison of ultrafiltration, nanofiltration and reverse osmosis filtration capabilities.[245]

NF membranes have traditionally been characterised in terms of their pore size, with typical NF membrane pore diameters lying in the region of 1-10 nm.[246] However, a more commonly used definition in recent years involves the size of molecules it is capable of

filtering from a given solvent. In this regard, NF is typically described, in terms of both molecular weights and molecular sizes, as a method of filtration that is capable of rejection of molecules with molecular weights as small as 200 Daltons, or down to a molecular size of 1 nm.[247–249] When analysing the performance of a given NF membrane, there are a number of key performance indicators that must be taken into consideration – these are retention, solvent flux and energy consumption. The ideal NF membrane will exhibit both excellent retention and solvent flux, and the design of these membranes to improve one of these characteristics must not come at the cost of the other.[250,251] Retention is the term used to describe the efficacy of a membrane in removing specific components from a mixture or solution. Retention can be calculated by comparing the concentration of the analyte in the permeate (i.e. after passing through the membrane) with the concentration of the analyte in the feed (i.e. before passing through the membrane), according to Equation 1.3:[251]

$$R_x(\%) = (1 - \frac{C_{P,x}}{C_{F,x}}) \times 100 \tag{1.3}$$

where:

$R_x$ is the retention (in %),

$C_{P,x}$ is the concentration of the analyte in the permeate, and

$C_{F,x}$ is the concentration of the analyte in the feed.

Solvent flux or permeation describes the rate at which a solvent can pass through the membrane during the filtration process. The flux depends on the working area of the membrane, and is calculated at a certain fixed pressure, according to Equation 1.4:[252]

$$J = \frac{V}{At} \tag{1.4}$$

where:

$J$ is the solvent flux (typically reported as L $m^{-2}$ $h^{-1}$),

$A$ is the working area of the membrane (typically in $m^2$),

$V$ is the volume of solvent (typically in L), and

$t$ is the time taken for the solvent to pass through the membrane (typically in h).

Solvent flux and applied pressure are key factors in NF energy consumption, both of which should be carefully controlled to maximise the efficiency of the filtration process.

The separation mechanism in NF membranes is highly complex and still widely debated, however a number of theories can serve as explanations. The simplest theory is a simple steric effect, based on size exclusion of the particles, blocking them from entering the smaller pores of the membrane.[253,254] However, this does not account for the anomalous behaviour of membranes with large pore sizes exhibiting high retentions for small molecules. Another common observation is the electrostatic effect, also known as the Donnan effect, by which charged membranes exhibit high retentions by attracting oppositely charged ions, or high rejections by repelling similarly charged ions.[255,256] However, there are also drawbacks to this theory, as there are numerous reports of charged NF membranes not exhibiting any preference for charged or uncharged analytes. Another emerging theory, which only applies to NF membranes made of materials which have delocalised $\pi$-systems (such as BN and graphene), is that organic compounds can be retained *via* $\pi-\pi$ interactions.[107,108] In reality, the mechanism of retention in NF is likely the result of a complex interplay between all of the aforementioned effects.

### 1.7.1 Layered double hydroxides for water purification - stand-alone sorbents and membrane building blocks

LDHs are highly promising materials, both as sorbents and as components in nanofiltration membranes, for advancing water purification technologies. Due to their positive sheet charge and flexible basal spacing, they are effective adsorbents for a vast range of anionic pollutants, through both electrostatically driven surface adsorption, as well as anion exchange. While there are hundreds of reports in the literature on LDHs as sorbents for pollutant removal, the two most commonly reported classes of pollutants as targets for removal by LDHs are organic pollutants such as dyes and pharmaceutical compounds, and metal oxyanions.[257,258]

Removal of anionic dyes from water is perhaps one of the most widely reported applications of LDHs. The removal process is usually dominated by electrostatically-driven surface adsorption, especially in the case of $CO_3^{2-}$-intercalated LDHs, as the strength of interaction between $CO_3^{2-}$ and the positively charged metal hydroxide sheets means that the anion is very difficult to exchange for the dye molecule.[259–261] However, in the case of LDHs where the intercalating anion is less tightly bound, such as $NO_3^-$ or $Cl^-$, anion exchange contributes significantly to the dye removal process.[262,263] LDHs have been successfully utilised as solid-phase and colloidal sorbents for numerous anionic dyes, including methyl orange[264,265], Evans blue[266,267], Congo red[268,269], and Sunset Yellow[270], among others. LDH sorbents can typically be reused numerous times, by washing with solvents, or by calcination and regeneration *via* the memory effect, albeit with varying success when it comes to maintaining stable removal efficiency over several cycles.[271,272] Furthermore, the formation of nanocomposites containing LDHs in conjunction with negatively charged materials can facilitate the tandem removal of both anionic and cationic species.[273,274]

Aside from their use as sorbents, the use of LDHs as building blocks for NF membranes has gained significant traction in recent times a result of their anion exchange capabilities and high adsorption capacities.[275] Furthermore, their aqueous phase synthesis and stability is advantageous for water purification applications, compared with other common 2D materials used for membranes such as MXenes, graphene oxide, and $MoS_2$.[276–278] Wang *et al.* reported the fabrication of amino acid-intercalated MgAl LDH membranes on anodic aluminium oxide templates, achieving up to 98% rejection of a range of anionic dyes. Amino acid-intercalation aided in the formation of expanded hydrophilic transport channels, resulting in high solvent flux rates.[279] LDHs have been also used to improve the performance of polymer membranes, while maintaining their desirable properties such as high mechanical strength, as reported by Li *et al.* for LDH/polyamide membranes for both desalination and dye removal.[280] Using LDHs, which are conducive to high solvent flux due to the abundance of hydrophilic hydroxyl groups on the surface, enables breakthroughs in the performance trade-off between solvent flux and pollutant rejection.

### 1.7.2 Challenges facing the widespread use of nanofiltration in water treatment systems

Membrane fouling can be defined as the accumulation of pollutants on the surface or in the pores of membranes, and is perhaps one of the main limitations in the expansion of the widespread application of NF in purification and separation technologies.[281,282] This is a particularly challenging problem in conventional filtration mode, in which the flow of the solvent is perpendicular to the orientation of the membrane. Fouling significantly reduces the performance of NF membranes, through reduction of the solvent flow rate, which results in increasing operational costs as higher pressures have to be used to force the solvent through the membranes. As a result, fouling can also lead to mechanical failure of

the membranes if they cannot sustain the increased pressures required to drive the solvent through the partially blocked pores.[283] Furthermore, the cost and complexity of NF acts as a significant barrier to its more widespread implementation, particularly in lower income countries where innovative solutions to water treatment are most urgently needed.[284,285] It is estimated that the costs of NF are approximately double that of UF.[286,287] Most cost analyses of nanofiltration systems that can be found in the literature have been conducted in high-income countries such as Sweden, Germany and the Netherlands, where the financial and economic barriers to implementing such systems are minimal.[288–290] Therefore, it is clear that simpler and more sustainable routes to NF membrane production are required to drive costs down and to drive the field forward, thus making a real impact in lower-income countries around the world where it matters the most.

## 1.8 Catalysis

The discovery of catalysis is most frequently, and incorrectly, attributed to Jöns Jakob Berzelius, who unquestionably was a pioneer in the field, and officially coined the term in the year 1836.[291] However, as is regrettably all too common throughout scientific history, it was, in fact, a woman, Elizabeth Fulhame, who invented and discovered the field of catalysis 42 years earlier, while a male contemporary received undue credit and acclaim.[292]


Figure 1.13: (Left) An artist's interepretation of Elizabeth Fulhame, a forgotten chemist and the true inventor of catalysis. (Right) Her only published book, which first introduces the concept of catalysis and, in particular, photoreduction.[293]

A catalyst can be officially defined as 'a substance that increases the rate of a reaction, without modifying the overall standard Gibbs energy change in the reaction', as per the International Union of Pure and Applied Chemistry.[294] The process that involves using a catalyst to speed up a reaction is known as catalysis. Catalysts can typically be categorised as either homogeneous, or heterogeneous. Homogeneous catalysts exist in the same phase as the reactants.[295] Perhaps the most industrially relevant example of homogeneous catalysis is the use of solutions of transition metal complexes in the catalytic hydrogenation of alkenes, with the products finding myriad applications in the raw chemical, pharmaceutical, and agricultural industries.[296] Another commonly known example of homogeneous catalysis, in which reactants and catalysts are both in the gas phase is the destruction of atmospheric ozone by UV light, which are catalysed by chlorofluorocarbons.[297] In contrast, heterogeneous catalysts exist in a different phase to that of the reactants, resulting in a boundary between the two phases at which reactions can occur.[298] The most well-known example of a heterogeneous catalytic reaction involves the catalytic converter of the internal combustion engine. Inside a catalytic converter, solid metal surfaces (traditionally precious metals such as platinum, rhodium and palladium) catalyse the conversion of toxic gases to more benign

gaseous products including $N_2$, $O_2$, $CO_2$ and water vapour.[299] A schematic comparison of homogeneous and heterogeneous catalysis is shown in Figure 1.14.

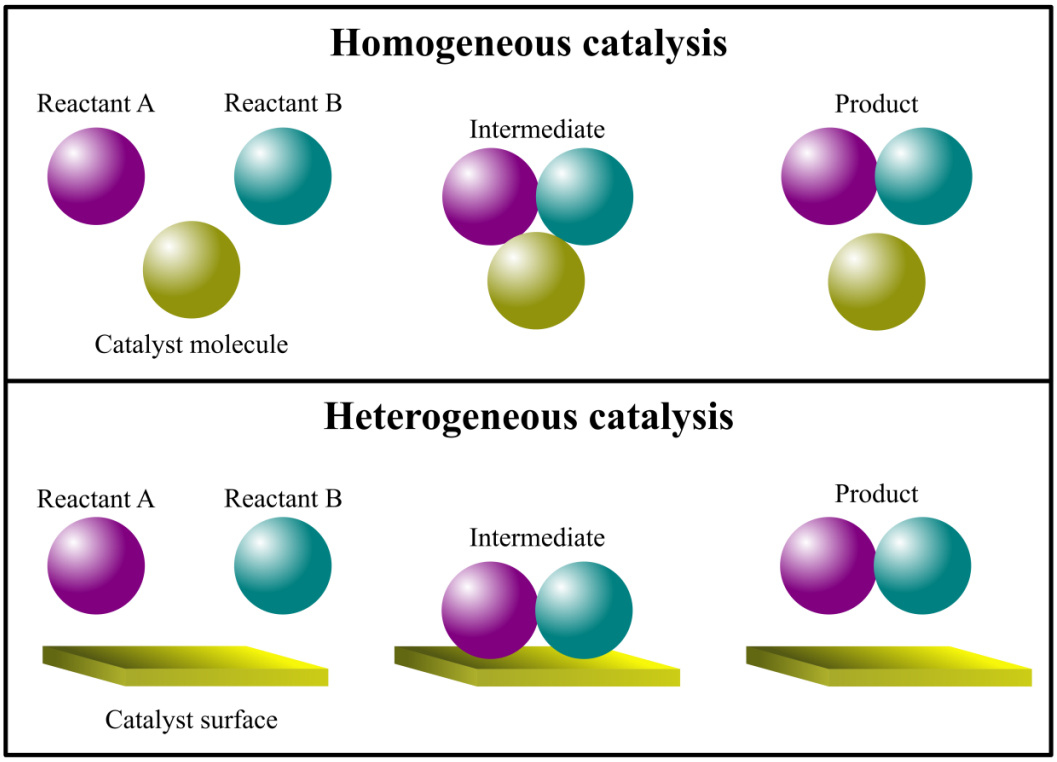


Figure 1.14: A comparison between homogeneous and heterogeneous catalysis.

### 1.8.1 Photocatalysis

Photocatalysis is a specific area of catalysis, that uses light (either UV or visible) to activate a catalyst, which then goes on to catalyse the chemical reaction. It is regarded as an effective means of utilising and converting solar energy.[300] Most nanomaterial-based heterogeneous photocatalysts are semiconducting materials, with metal oxides such as titanium dioxide ($TiO_2$) and zinc oxide (ZnO) being amongst the most commonly reported species.[301–304] When these materials absorb light, they generate electron-hole pairs which,

if the recombination rate is low enough, leads to redox reactions on their surfaces, as shown in the schematic in Figure 1.15.[305]

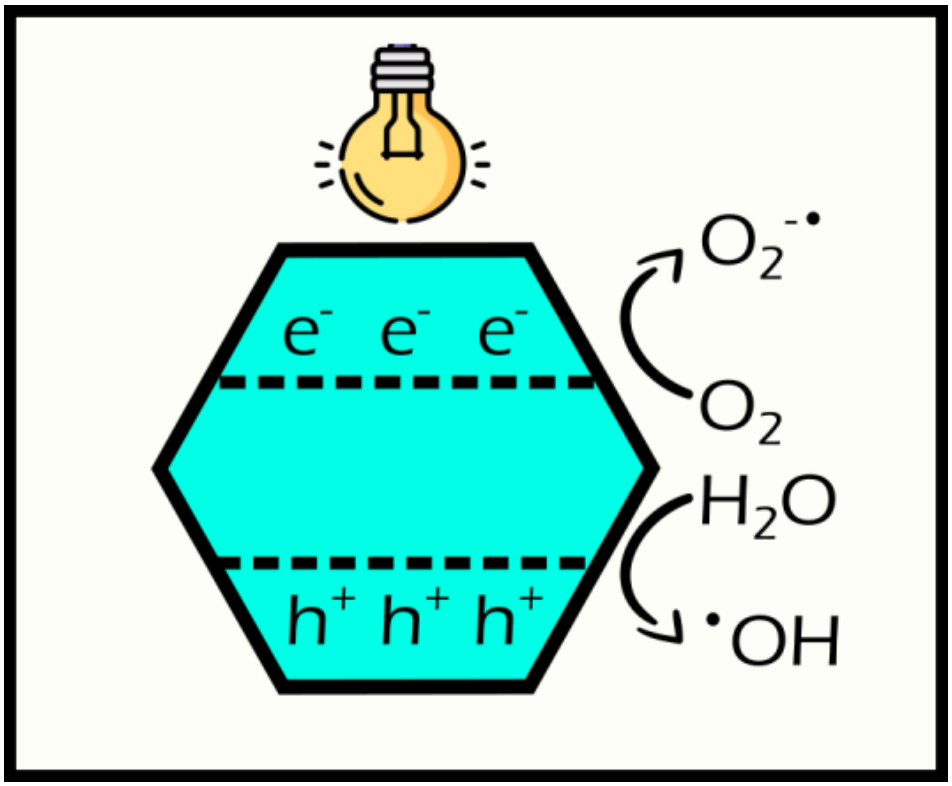


Figure 1.15: Schematic representation of the photogeneration of electrons and holes in a semiconducting nanomaterial, catalysing the formation of radical species in water.

Nanomaterials with an optical bandgap in the UV or visible regions of the electromagnetic spectrum are of significant interest as photocatalysts, specifically in the context of the global green energy transition.[306] The ability to harness sunlight for catalysing numerous of reactions, from the generation of sustainable fuels and feedstocks including hydrogen and ammonia, to the photodegradation of pollutants in environmental remediation applications, means photocatalysis plays a pivotal role in sustainability and green energy.

### 1.8.2 Fenton reactions

Fenton reactions are a specific subset of redox processes that are hugely exploited in the field of photocatalysis. They involve the redox reaction of a transition metal with variable valency to produce radical species, most notably hydroxyl radicals, from hydrogen peroxide.[307] While the iron-centred Fe(II)/Fe(III) redox pair was used for the discovery of the Fenton process, and thus is most commonly used, in recent years other transition metals such as copper, nickel, manganese and chromium have been used, and are dubbed 'Fenton-like' reactions.[308–312] The copper Fenton-like reaction involves cycling of the Cu(II)/Cu(I) redox pair, as shown in the schematic in Figure 1.16.

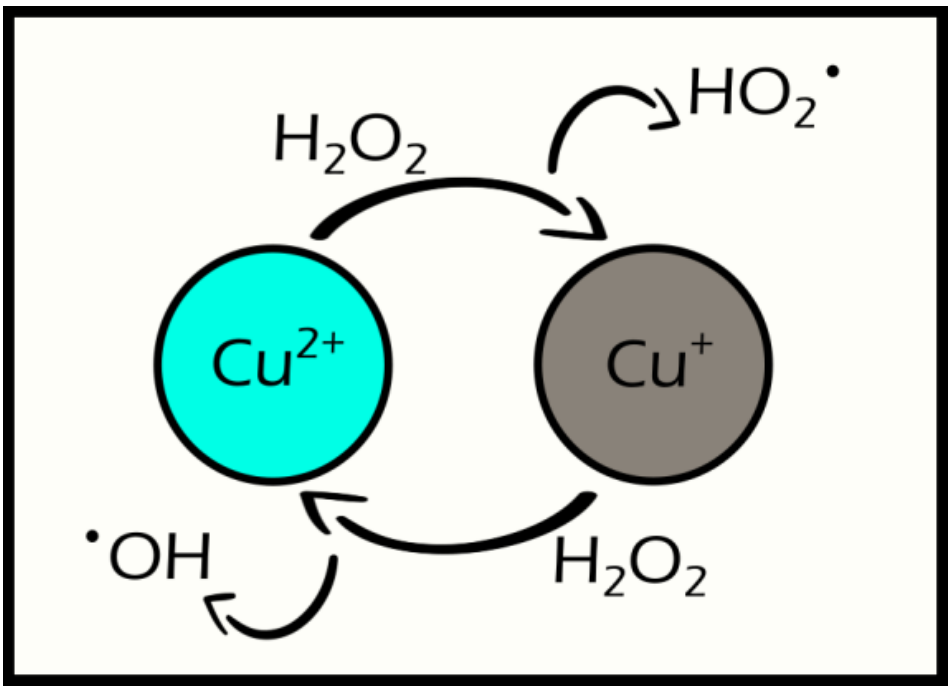


Figure 1.16: Schematic representation of the copper-centred Fenton-like reaction, leading to the production of radical species from hydrogen peroxide.

The Fenton reaction has been widely utilised by both chemists and materials scientists alike for applications in environmental remediation.[313,314] The generated hydroxyl radicals are highly reactive and can be used to photo-oxidise a range of organic pollutants including

dyes and pharmaceutical compounds, breaking them down into smaller, less harmful substances.[315] The real-world applications of this process range from water purification to decontamination of soil.[316,317]

### 1.8.3 Layered double hydroxides as heterogeneous photocatalysts

The unique characteristics of LDH nanosheets, including their high degree of compositional tunability, large surface-to-volume ratio, and ion exchange capabilities, make them viable candidates for heterogeneous photocatalysis. As discussed in Section 1.4.2, $M^{3+}$ doping in the extended $M(OH)_2$ sheets means they exhibit behaviour akin to p-type semiconductors. Thus, they can undergo photoinduced charge separation, with an excess of holes present, upon absorption of light above the bandgap energy.[318] The holes then proceed to react with water to form hydroxyl radicals, which are highly effective in the degradation of numerous organic pollutants. However, the high electron-hole recombination rates in LDHs remains a significant barrier to their photocatalytic efficiency, and thus LDHs are often presented as co-catalysts, forming heterojunctions with other semiconducting species, to boost this efficiency.[319–323]

The positive sheet charge of LDHs means they are efficient adsorbents for anionic pollutants, as previously discussed in Section 1.7.1, which, in combination with their large surface-to-volume ratio and charge carrier separation, can facilitate rapid photodegradation of anionic organic species.[324] Furthermore, LDHs which contain ions of Fe, Cu, Ni and Mn, among others, are capable of undergoing Fenton and photo-Fenton reactions which, in conjunction with their charge separation capabilities, can facilitate rapid photodegradation of organic pollutants.[325–327] The application of LDHs as heterogeneous photocatalysts has been widely reported for numerous reactions, including degradation of pollutants such as phenols and organic dyes[328,329], as well as for the hydrogen and oxygen evolution reactions.[330,331]

Thus, LDHs may serve as a key puzzle piece in solving many global issues relating to the UN Sustainable Development Goals, particularly SDG6, 7, 13, 14 and 15.

## 1.9 Aims of the Project

The overarching goal of this project is to develop new layered double hydroxide-based nanostructures and nanocomposites, and an exploration of their wide-ranging applications which arise from their unique structures and high degree of tunability *via* compositional variation. In particular, we aim to employ primarily green synthetic techniques for the synthesis of these materials, and examine their potential use where possible in various environmental applications. The applications of the prepared materials primarily involve photocatalysis, selective separation, and photoluminescent pollutant sensing. The main research and technical objectives of this work are as follows:

**1)** To synthesise a variety of layered double hydroxides using various metal salt species and co-precipitation reactions.

**2)** To characterise the resultant nanomaterials using various instrumental techniques, including pXRD, FT-IR, UV-Vis, CD, SEM, TEM, EDX, EELS, and PL.

**3)** To investigate the potential for chirality induction in copper-aluminium layered double hydroxides *via* one-pot synthesis, as well as post-synthetic treatment in the presence of chiral molecules.

**4)** To investigate the mechanism of chirality transfer in LDH-derived chiral metal oxides.

**5)** To test the potential of a variety of layered double hydroxides of various compositions for their ability to degrade organic pollutants *via* photocatalysis.

**6)** To investigate the potential use of copper-aluminium layered double hydroxides in nanofiltration membranes for the separation of a range of water-soluble dyes.

**7)** To optimise the nanofiltration performance of hybrid layered double hydroxide/partially oxidised boron nitride membranes and gain insights into the dye retention mechanisms.

**8)** To address the issue of fouling in partially oxidised boron nitride membranes *via* the use of copper-aluminium layered double hydroxides as novel photocatalytic anti-fouling components.

**9)** To synthesise a variety of phosphorescent rare-earth-doped layered double hydroxides and fully characterise them, including their photophysical properties and luminescent lifetimes.

**10)** To test phosphorescent rare-earth-doped layered double hydroxides in luminescent sensing applications, particularly for the sensing of dichromate in water.

It is anticipated that this work will contribute to the more wide-spread use of layered double hydroxides in a variety of applications, including sensing, nanofiltration, and other environmental applications. Finally, we also aim to shed light on the multifunctionality of this diverse class of nanomaterials with this work.

# References


(1) Dabarera, A.; Provis, J. L. *Materials and Structures/Materiaux et Constructions* **2023**, *56*, 1–4.

(2) Tundo, P.; Wissinger, J. *Chemistry International* **2022**, *44*, 35–37.

(3) Anastas, P.; Nolasco, M.; Kerton, F.; Kirchhoff, M.; Licence, P.; Pradeep, T.; Subramaniam, B.; Moores, A. *ACS Sustainable Chemistry and Engineering* **2021**, *9*, 8015–8017.

(4) Sustainable Development Goals launch in 2016 `https://www.un.org/sustainabledevelopment/blog/2015/12/sustainable-development-goals-kick-off-with-start-of-new-year/` (accessed 11/26/2023).

(5) Maletskyi, Z. *ACS Symposium Series* **2020**, *1348*, 3–35.

(6) Song, Y.; Phipps, J.; Zhu, C.; Ma, S. *Angewandte Chemie International Edition* **2023**, *62*, e202216724.

(7) Das, S.; O'Connell, M. G.; Xu, H.; Bernstein, R.; Kim, J. H.; Sankhala, K.; Segal-Peretz, T.; Shevate, R.; Zhang, W.; Zhou, X.; Darling, S. B.; Dunn, J. B. *ACS ES and T Engineering* **2022**, *2*, 2159–2173.

(8) Tabassum, H.; Ahmad, I. Z. *Letters in Applied Microbiology* **2022**, *75*, 731–743.

(9) Richter, A. P.; Brown, J. S.; Bharti, B.; Wang, A.; Gangwal, S.; Houck, K.; Hubal, E. A. C.; Paunov, V. N.; Stoyanov, S. D.; Velev, O. D. *Nature Nanotechnology* **2015**, *10*, 817–823.

(10) Imani, S. M.; Ladouceur, L.; Marshall, T.; Maclachlan, R.; Soleymani, L.; Didar, T. F. *ACS Nano* **2020**, *14*, 12341–12369.

(11) Papi, M.; Palmieri, V.; Bugli, F.; Spirito, M. D.; Sanguinetti, M.; Ciancico, C.; Braidotti, M. C.; Gentilini, S.; Angelani, L.; Conti, C. *Scientific Reports* **2016**, *6*, 1–7.

(12) Wang, Y.; Kavanagh, S. R.; Burgués-Ceballos, I.; Walsh, A.; Scanlon, D.; Konstantatos, G. *Nature Photonics* **2022**, *16*, 235–241.

(13) Ming, F.; Liang, H.; Huang, G.; Bayhan, Z.; Alshareef, H. N.; Ming, F; Liang, H; Huang, G; Bayhan, Z; Alshareef, H. N. *Advanced Materials* **2021**, *33*, 2004039.

(14) Xiao, F.; Wang, Q.; Xu, G. L.; Qin, X.; Hwang, I.; Sun, C. J.; Liu, M.; Hua, W.; wen Wu, H.; Zhu, S.; Li, J. C.; Wang, J. G.; Zhu, Y.; Wu, D.; Wei, Z.; Gu, M.; Amine, K.; Shao, M. *Nature Catalysis* **2022**, *5*, 503–512.

(15) Mulvaney, P. *ACS Nano* **2015**, *9*, 2215–2217.

(16) Murphy, F.; Alavi, A.; Mullins, M.; Furxhi, I.; Kia, A.; Kingston, M. *RSC Advances* **2022**, *12*, 11021–11031.

(17) No, COVID vaccines don't contain nanotechnology that can be programmed via 5G wireless networks — AP News `https://apnews.com/article/fact-check-covid-mrna-vaccine-nanotech-390958734912` (accessed 11/26/2023).

(18) Public perception of nanotechnology can quickly turn sour — Research — Chemistry World `https://www.chemistryworld.com/news/public-perception-of-nanotechnology-can-quickly-turn-sour/4015617.article` (accessed 11/26/2023).

(19) Feynman, R. *Caltech Engineering and Science* **1960**, *5*, 22–36.

(20) Reibold, M.; Paufler, P.; Levin, A. A.; Kochmann, W.; Pätzke, N.; Meyer, D. C. *Nature* **2006**, *444*, 286–286.

(21) Pérez-Villar, S.; Rubio, J.; Oteo, J. L. *Journal of Non-Crystalline Solids* **2008**, *354*, 1833–1844.

(22) Cionti, C.; Stucchi, M.; Meroni, D. *Journal of Chemical Education* **2022**, *99*, 1516–1522.

(23) Nanotechnology Through History: Carbon-based Nanoparticles from Prehistory to Today – Sustainable Nano `https://sustainable-nano.com/2013/06/17/nanotechnology-through-history-carbon-based-nanoparticles-from-prehistory-to-today/` (accessed 11/26/2023).

(24) Self-Cleaning Materials: Lotus Leaf-Inspired Nanotechnology - Scientific American `https://www.scientificamerican.com/article/self-cleaning-materials/` (accessed 11/26/2023).

(25) Forbes, P. *Scientific American* **2008**, *299*, 88–95.

(26) Organic material that mimics lotus leaves can repel water, biodegrade completely `https://www.firstpost.com/tech/science/organic-material-that-mimics-lotus-leaves-can-repel-water-biodegrade-completely-5939101.html` (accessed 11/26/2023).

(27) Cha, T. G.; Yi, J. W.; Moon, M. W.; Lee, K. R.; Kim, H. Y. *Langmuir* **2010**, *26*, 8319–8326.

(28) Wang, Q.; Yao, X.; Liu, H.; Quéré, D.; Jiang, L. *Proceedings of the National Academy of Sciences of the United States of America* **2015**, *112*, 9247–9252.

(29) Xu, Q.; Zhang, W.; Dong, C.; Sreeprasad, T. S.; Xia, Z. *Journal of The Royal Society Interface* **2016**, *13*, 20160300.

(30) Milionis, A.; Sharma, C. S.; Hopf, R.; Uggowitzer, M.; Bayer, I. S.; Poulikakos, D. *Advanced Materials Interfaces* **2019**, *6*, 1801202.

(31) ISO/TS 80004-1:2015(en), Nanotechnologies — Vocabulary — Part 1: Core terms `https://www.iso.org/obp/ui/#iso:std:iso:ts:80004:-1:ed-2:v1:en` (accessed 11/26/2023).

(32) Sajanlal, P. R.; Sreeprasad, T. S.; Samal, A. K.; Pradeep, T. *Nano Reviews* **2011**, *2*, 5883.

(33) Roduner, E. *Chemical Society Reviews* **2006**, *35*, 583–592.

(34) Roduner, E., *Nanoscopic Materials: Size-Dependent Phenomena and Growth Principles*; The Royal Society of Chemistry: Cambridge, UK, 2014.

(35) Press release: The Nobel Prize in Chemistry 2023 - NobelPrize.org `https://www.nobelprize.org/prizes/chemistry/2023/press-release/` (accessed 11/26/2023).

(36) Ekimov, A. I.; Efros, A. L.; Onushchenko, A. A. *Solid State Communications* **1985**, *56*, 921–924.

(37) Global Quantum Dots Market Report 2022 to 2027: Industry `https://www.globenewswire.com/en/news-release/2023/01/26/2595831/28124/en/Global-Quantum-Dots-Market-Report-2022-to-2027-Industry-Trends-Share-Size-Growth-Opportunities-and-Forecasts.html` (accessed 11/26/2023).

(38) Xiang, J.; Wang, X.; Ding, M.; Tang, X.; Zhang, S.; Zhang, X.; Xie, Z. *Chemosphere* **2022**, *294*, 133728.

(39) Han, D.; Dong, X.; Yu, G.; Gao, T.; Zhou, K. G. *Advanced Membranes* **2022**, *2*, 100045.

(40) Coogan, Á.; Gun'ko, Y. K. *Materials Advances* **2021**, *2*, 146–164.

(41) Mak, K. F.; Lee, C.; Hone, J.; Shan, J.; Heinz, T. F. *Physical Review Letters* **2010**, *105*, 136805.

(42) Splendiani, A.; Sun, L.; Zhang, Y.; Li, T.; Kim, J.; Chim, C.-Y.; Galli, G.; Wang, F. *Nano Letters* **2010**, *10*, 1271–1275.

(43) Novoselov, K. S.; Geim, A. K.; Morozov, S. V.; Jiang, D.; Zhang, Y.; Dubonos, S. V.; Grigorieva, I. V.; Firsov, A. A. *Science* **2004**, *306*, 666–669.

(44) The Nobel Prize in Physics 2010 - NobelPrize.org `https://www.nobelprize.org/prizes/physics/2010/summary/` (accessed 11/26/2023).

(45) Yi, M.; Shen, Z. *Journal of Materials Chemistry A* **2015**, *3*, 11700–11715.

(46) Hernandez, Y.; Nicolosi, V.; Lotya, M.; Blighe, F. M.; Sun, Z.; De, S.; McGovern, I. T.; Holland, B.; Byrne, M.; Gun'ko, Y. K.; Boland, J. J.; Niraj, P.; Duesberg, G.; Krishnamurthy, S.; Goodhue, R.; Hutchison, J.; Scardaci, V.; Ferrari, A. C.; Coleman, J. N. *Nature Nanotechnology* **2008**, *3*, 563–568.

(47) Coleman, J. N.; Lotya, M.; O'Neill, A.; Bergin, S. D.; King, P. J.; Khan, U.; Young, K.; Gaucher, A.; De, S.; Smith, R. J.; Shvets, I. V.; Arora, S. K.; Stanton, G.; Kim, H. Y.; Lee, K.; Kim, G. T.; Duesberg, G. S.; Hallam, T.; Boland, J. J.; Wang, J. J.; Donegan, J. F.; Grunlan, J. C.; Moriarty, G.; Shmeliov, A.; Nicholls, R. J.; Perkins, J. M.; Grieveson, E. M.; Theuwissen, K.; McComb, D. W.; Nellist, P. D.; Nicolosi, V. *Science* **2011**, *331*, 568–571.

(48) Tao, P.; Yao, S.; Liu, F.; Wang, B.; Huang, F.; Wang, M. *Journal of Materials Chemistry A* **2019**, *7*, 23512–23536.

(49) Zhou, N.; Yang, R.; Zhai, T. *Materials Today Nano* **2019**, *8*, 100051.

(50) Paton, L. A.; Harrison, W. T. A.; Paton, L. A.; Harrison, W. T. A. *Angewandte Chemie International Edition* **2010**, *49*, 7684–7687.

(51) Zhou, K.; Shang, G.; Hsu, H.-H.; Han, S.-T.; Roy, V. A. L.; Zhou, Y.; Zhou, K; Zhou, Y; Shang, G; Han, S.-T; Hsu, H.-H; Roy, V. A. L.; Watt, J. *Advanced Materials* **2023**, *35*, 2207774.

(52) Lu, F.; Wang, H.; Zeng, M.; Fu, L. *iScience* **2022**, *25*, 103835.

(53) Gutiérrez, H. R. *ACS Applied Nano Materials* **2020**, *3*, 6134–6139.

(54) Ma, H.; Xing, Y.; Cui, B.; Han, J.; Wang, B.; Zeng, Z.; *Chinese Physics B* **2022**, *31*, 108502.

(55) Bian, Z.; Miao, J.; Zhao, Y.; Chai, Y. *Accounts of Materials Research* **2022**, *3*, 1220–1231.

(56) Kobayashi, Y.; Kumakura, K.; Akasaka, T.; Makimoto, T. *Nature* **2012**, *484*, 223–227.

(57) Pumera, M.; Sofer, Z.; Ambrosi, A. *Journal of Materials Chemistry A* **2014**, *2*, 8981–8987.

(58) Yoo, M. S.; Lee, H. C.; Wolf, C.; Nguyen, N. N.; Park, D. H.; Kim, J.; Lee, E.; Chung, H. J.; Cho, K. *Chemistry of Materials* **2020**, *32*, 5142–5152.

(59) Tantis, I.; Talande, S.; Tzitzios, V.; Basina, G.; Shrivastav, V.; Bakandritsos, A.; Zboril, R.; Tantis, I; Talande, S; Shrivastav, V; Bakandritsos, A; Zboril, R; Tzitzios, V; Basina, G *Advanced Functional Materials* **2023**, *33*, 2209360.

(60) McKinney, R. W.; Gorai, P.; Manna, S.; Toberer, E.; Stevanović, V. *Journal of Materials Chemistry A* **2018**, *6*, 15828–15838.

(61) Ajayan, P.; Kim, P.; Banerjee, K. *Physics Today* **2016**, *69*, 38–44.

(62) Ino, K.; Udagawa, I.; Iwabata, K.; Takakusagi, Y.; Kubota, M.; Kurosaka, K.; Arai, K.; Seki, Y.; Nogawa, M.; Tsunoda, T.; Mizukami, F.; Taguchi, H.; Sakaguchi, K. *PLOS ONE* **2011**, *6*, e22582.

(63) Sharma, A.; Kumari, S.; Sharma, S.; Singh, T.; Kumar, S.; Thakur, A.; Bhatia, S. K.; Sharma, A. K. *Materials Today Sustainability* **2023**, *22*, 100399.

(64) Cavani, F.; Trifirò, F.; Vaccari, A. *Catalysis Today* **1991**, *11*, 173–301.

(65) Chakoumakos, B. C.; Loong, C. K.; Schultz, A. J. *Journal of Physical Chemistry B* **1997**, *101*, 9458–9462.

(66) Khan, A. I.; O'Hare, D. *Journal of Materials Chemistry* **2002**, *12*, 3191–3198.

(67) Yu, J.; Wang, Q.; O'Hare, D.; Sun, L. *Chemical Society Reviews* **2017**, *46*, 5950–5974.

(68) Pálinkó, I.; Sipos, P.; Berkesi, O.; Varga, G. *Journal of Physical Chemistry C* **2022**, *126*, 15254–15262.

(69) Sasai, R.; Sato, H.; Sugata, M.; Fujimura, T.; Ishihara, S.; Deguchi, K.; Ohki, S.; Tansho, M.; Shimizu, T.; Oita, N.; Numoto, M.; Fujii, Y.; Kawaguchi, S.; Matsuoka, Y.; Hagura, K.; Abe, T.; Moriyoshi, C. *Inorganic Chemistry* **2019**, *58*, 10928–10935.

(70) Marappa, S.; Radha, S.; Kamath, P. V. *European Journal of Inorganic Chemistry* **2013**, *2013*, 2122–2128.

(71) Jiang, X. X.; Xue, J. Y.; Zhao, Z. Y.; Li, C.; Li, F. L.; Cao, C.; Niu, Z.; Gu, H. W.; Lang, J. P. *RSC Advances* **2020**, *10*, 12145–12150.

(72) Nagendran, S.; Kamath, P. V. *European Journal of Inorganic Chemistry* **2013**, *2013*, 4686–4693.

(73) Sudare, T.; Yamaguchi, T.; Ueda, M.; Shiiba, H.; Tanaka, H.; Tipplook, M.; Hayashi, F.; Teshima, K. *Nature Communications* **2022**, *13*, 1–9.

(74) Chowdhury, P. R.; Verma, V.; Medhi, H.; Bhattacharyya, K. G. *ACS Omega* **2019**, *4*, 10599–10609.

(75) Xu, S. M.; Yan, H.; Wei, M. *Journal of Physical Chemistry C* **2017**, *121*, 2683–2695.

(76) Zhang, J.; Vallée, R. A.; Kochovski, Z.; Zhang, W.; Shen, C.; Bertram, F.; Pinna, N. *Angewandte Chemie International Edition* **2023**, *62*, e202305353.

(77) Chaves, A.; Azadani, J. G.; Alsalman, H.; da Costa, D. R.; Frisenda, R.; Chaves, A. J.; Song, S. H.; Kim, Y. D.; He, D.; Zhou, J.; Castellanos-Gomez, A.; Peeters, F. M.; Liu, Z.; Hinkle, C. L.; Oh, S. H.; Ye, P. D.; Koester, S. J.; Lee, Y. H.; Avouris, P.; Wang, X.; Low, T. *npj 2D Materials and Applications* **2020**, *4*, 1–21.

(78) Smith, A. M.; Nie, S. *Accounts of Chemical Research* **2010**, *43*, 190–200.

(79) Bian, X.; Zhang, S.; Zhao, Y.; Shi, R.; Zhang, T. *InfoMat* **2021**, *3*, 719–738.

(80) Zhao, X. J.; Zhu, Y. Q.; Xu, S. M.; Liu, H. M.; Yin, P.; Feng, Y. L.; Yan, H. *Physical Chemistry Chemical Physics* **2020**, *22*, 19758–19768.

(81) Zhang, G.; Zhang, X.; Meng, Y.; Pan, G.; Ni, Z.; Xia, S. *Chemical Engineering Journal* **2020**, *392*, 123684.

(82) Zhao, Y.; Jia, X.; Waterhouse, G. I.; Wu, L. Z.; Tung, C. H.; O'Hare, D.; Zhang, T. *Advanced Energy Materials* **2016**, *6*, 1501974.

(83) Baliarsingh, N.; Parida, K. M.; Pradhan, G. C. *Industrial and Engineering Chemistry Research* **2014**, *53*, 3834–3841.

(84) Prasanna, S. V.; Kamath, P. V. *Industrial and Engineering Chemistry Research* **2009**, *48*, 6315–6320.

(85) Tran, H. N.; Lin, C. C.; Chao, H. P. *Separation and Purification Technology* **2018**, *192*, 36–45.

(86) Kiani, M.; Bagherzadeh, M.; Ghadiri, A. M.; Makvandi, P.; Rabiee, N. *Scientific Reports* **2022**, *12*, 1–14.

(87) Lee, J. H.; Jung, D. Y.; Kim, E.; Ahn, T. K. *Dalton Transactions* **2014**, *43*, 8543–8548.

(88) Sadjadi, S. In *Encapsulated Catalysts*, Sadjadi, S., Ed.; Academic Press: 2017, pp 443–476.

(89) Guo, J. Y.; Zhao, X. J.; Zhang, W.; Jie, Y.; Xu, X. Y.; Lu, H.; Song, H. T.; Yan, H. *Applied Surface Science* **2023**, *637*, 157759.

(90) Hu, J.; Tang, X.; Dai, Q.; Liu, Z.; Zhang, H.; Zheng, A.; Yuan, Z.; Li, X. *Nature Communications* **2021**, *12*, 1–10.

(91) Vigna, L.; Nigro, A.; Verna, A.; Ferrari, I. V.; Marasso, S. L.; Bocchini, S.; Fontana, M.; Chiodoni, A.; Pirri, C. F.; Cocuzza, M. *ACS Omega* **2021**, *6*, 20205–20217.

(92) Shirin, V. K. A.; Sankar, R.; Johnson, A. P.; Gangadharappa, H. V.; Pramod, K. *Journal of Controlled Release* **2021**, *330*, 398–426.

(93) Meng, Y.; Mao, H. K.; Eng, P. J.; Trainor, T. P.; Newville, M.; Hu, M. Y.; Kao, C.; Shu, J.; Hausermann, D.; Hemley, R. J. *Nature Materials* **2004**, *3*, 111–114.

(94) Cazorla, C.; Gould, T. *Science Advances* **2019**, *5*, eaau5832.

(95) Pakdel, A.; Bando, Y.; Golberg, D. *Chemical Society Reviews* **2014**, *43*, 934–959.

(96) Zhang, X.; Meng, J. In *Ultra-Wide Bandgap Semiconductor Materials*, Liao, M., Shen, B., Wang, Z., Eds.; Materials Today; Elsevier: 2019, pp 347–419.

(97) Golberg, D.; Bando, Y.; Huang, Y.; Terao, T.; Mitome, M.; Tang, C.; Zhi, C. *ACS Nano* **2010**, *4*, 2979–2993.

(98) Pakdel, A.; Zhi, C.; Bando, Y.; Golberg, D. *Materials Today* **2012**, *15*, 256–265.

(99) Biswas, A.; Bayer, I. S.; Biris, A. S.; Wang, T.; Dervishi, E.; Faupel, F. *Advances in Colloid and Interface Science* **2012**, *170*, 2–27.

(100) Tao, H.; Zhang, Y.; Gao, Y.; Sun, Z.; Yan, C.; Texter, J. *Phys. Chem. Chem. Phys.* **2017**, *19*, 921–960.

(101) Mao, N.; Zhou, C. H.; Tong, D. S.; Yu, W. H.; Cynthia Lin, C. *Applied Clay Science* **2017**, *144*, 60–78.

(102) Kaur, H.; Coleman, J. N. *Advanced Materials* **2022**, *34*, 2202164.

(103) Puthirath Balan, A.; Radhakrishnan, S.; Woellner, C. F.; Sinha, S. K.; Deng, L.; Reyes, C. D. L.; Rao, B. M.; Paulose, M.; Neupane, R.; Apte, A.; Kochat, V.; Vajtai, R.; Harutyunyan, A. R.; Chu, C. W.; Costin, G.; Galvao, D. S.; Martí, A. A.; Van Aken, P. A.; Varghese, O. K.; Tiwary, C. S.; Malie Madom Ramaswamy Iyer, A.; Ajayan, P. M. *Nature Nanotechnology* **2018**, *13*, 602–609.

(104) Sozen, Y.; Riquelme, J. J.; Xie, Y.; Munuera, C.; Castellanos-Gomez, A. *Small Methods* **2023**, *7*, 2300326.

(105) Li, Z.; Young, R. J.; Backes, C.; Zhao, W.; Zhang, X.; Zhukov, A. A.; Tillotson, E.; Conlan, A. P.; Ding, F.; Haigh, S. J.; Novoselov, K. S.; Coleman, J. N. *ACS Nano* **2020**, *14*, 10976–10985.

(106) Xu, Y.; Cao, H.; Xue, Y.; Li, B.; Cai, W. *Nanomaterials* **2018**, *8*, 942.

(107) Doménech, N. G.; Coogan, Á.; Purcell-Milton, F.; García, M. L. C.; Arjona, A. S.; Cabré, M. B.; Rafferty, A.; Mckelvey, K.; Dunne, P. W.; Gun'ko, Y. K. *Nanoscale Advances* **2022**, *4*, 4895–4904.

(108) Doménech, N. G.; Purcell-Milton, F.; Arjona, A. S.; García, M.-L. C.; Ward, M.; Cabré, M. B.; Rafferty, A.; McKelvey, K.; Dunne, P.; Gun'ko, Y. K. *Nanomaterials* **2022**, *12*, 473.

(109) Fernandes, J.; Nemala, S. S.; Bellis, G. D.; Capasso, A. *Frontiers in Chemistry* **2022**, *10*, 878799.

(110) Backes, C.; Szydłowska, B. M.; Harvey, A.; Yuan, S.; Vega-Mayoral, V.; Davies, B. R.; Zhao, P. L.; Hanlon, D.; Santos, E. J.; Katsnelson, M. I.; Blau, W. J.; Gadermaier, C.; Coleman, J. N. *ACS Nano* **2016**, *10*, 1589–1601.

(111) Fu, Q.; Wang, W.; Yang, L.; Huang, J.; Zhang, J.; Xiang, B. *RSC Advances* **2015**, *5*, 15795–15799.

(112) Khan, M. H.; Liu, H. K.; Sun, X.; Yamauchi, Y.; Bando, Y.; Golberg, D.; Huang, Z. *Materials Today* **2017**, *20*, 611–628.

(113) Liu, W.; Li, H.; Xu, C.; Khatami, Y.; Banerjee, K. *Carbon* **2011**, *49*, 4122–4130.

(114) Dahmen, K.-H. In *Encyclopedia of Physical Science and Technology (Third Edition)*, Meyers, R. A., Ed., Third Edition; Academic Press: New York, 2003, pp 787–808.

(115) Alam, S.; Chowdhury, M. A.; Shahid, A.; Alam, R.; Rahim, A. *FlatChem* **2021**, *30*, 100305.

(116) Kwon, S. G.; Hyeon, T. *Small* **2011**, *7*, 2685–2702.

(117) Dong, H.; Koenig, G. M. *CrystEngComm* **2020**, *22*, 1514–1530.

(118) Huo, Y.; Xiu, S.; Meng, L. Y.; Quan, B. *Chemical Engineering Journal* **2023**, *451*, 138572.

(119) Dubois, T.; Demazeau, G. *Materials Letters* **1994**, *19*, 38–47.

(120) Morey, G. W.; Niggli, P. *Journal of the American Chemical Society* **1913**, *35*, 1086–1130.

(121) Ma, Z. Y.; Yu, Z. L.; Xu, Z. L.; Bu, L. F.; Liu, H. R.; Zhu, Y. B.; Qin, B.; Ma, T.; Zhan, H. J.; Xu, L.; Wu, H. A.; Ding, H.; Yu, S. H. *Matter* **2020**, *2*, 1270–1282.

(122) Walton, R. I.; O'Hare, D. *Journal of Physical Chemistry B* **2001**, *105*, 91–96.

(123) Hooper, D.; Barnes, P.; Cockcroft, J. K.; Jupe, A. C.; Jacques, S. D. M.; Bailey, S. P.; Lupo, F.; Vickers, M.; Hanfland, M. *Phys. Chem. Chem. Phys.* **2003**, *5*, 4946–4950.

(124) Mitchell, S.; Biswick, T.; Jones, W.; Williams, G.; O'Hare, D. *Green Chem.* **2007**, *9*, 373–378.

(125) Lamer, V. K.; Dinegar, R. H. *Journal of the American Chemical Society* **1950**, *72*, 4847–4854.

(126) Thanh, N. T.; Maclean, N.; Mahiddine, S. *Chemical Reviews* **2014**, *114*, 7610–7630.

(127) Murray, C. B.; Norris, D. J.; Bawendi, M. G. *Journal of the American Chemical Society* **1993**, *115*, 8706–8715.

(128) Yin, W.; Bai, X.; Chen, P.; Zhang, X.; Su, L.; Ji, C.; Gao, H.; Song, H.; Yu, W. W. *ACS Applied Materials and Interfaces* **2018**, *10*, 43824–43830.

(129) Soni, A. K.; Joshi, R.; Ningthoujam, R. S. In *Handbook on Synthesis Strategies for Advanced Materials : Volume-I: Techniques and Fundamentals*, Tyagi, A. K., Ningthoujam, R. S., Eds.; Springer: Singapore, 2021, pp 383–434.

(130) Bai, X.; Purcell-Milton, F.; Gun'ko, Y. K. *Nanomaterials* **2019**, *9*, 85.

(131) Timonen, J. V.; Seppälä, E. T.; Ikkala, O.; Ras, R. H. A.; Timonen, J. V. I.; Ikkala, O; Ras, R. H. A.; Seppälä, E. T. *Angewandte Chemie International Edition* **2011**, *50*, 2080–2084.

(132) Kahouli, M.; Barhoumi, A.; Bouzid, A.; Al-Hajry, A.; Guermazi, S. *Superlattices and Microstructures* **2015**, *85*, 7–23.

(133) Bitenc, M; Marinšek, M; Orel, Z. C. *Journal of the European Ceramic Society* **2008**, *28*, 2915–2921.

(134) Karpinski, P.; Wey, J. In *Handbook of Industrial Crystallization*, Myserson, A. S., Ed., 2nd edition; Butterworth-Heinemann: 2002, pp 141–160.

(135) Stafford, S.; Garcia, R. S.; Gun'ko, Y. K. *Applied Sciences* **2018**, *8*, 97.

(136) Stafford, S.; Garnier, C.; Gun'ko, Y. K. *Nanomaterials* **2018**, *8*, 1044.

(137) Thomas, J.; Thomas, N.; Girgsdies, F.; Beherns, M.; Huang, X.; Sudheesh, V. D.; Sebastian, V. *New Journal of Chemistry* **2017**, *41*, 7356–7363.

(138) Bukhtiyarova, M. V. *Journal of Solid State Chemistry* **2019**, *269*, 494–506.

(139) Wang, Y.; Ying, Z.; Gao, Y.; Shi, L. *Chemistry – A European Journal* **2024**, *30*, e202303025.

(140) Adachi-Pagano, M.; Forano, C.; Besse, J.-P. *Journal of Materials Chemistry* **2003**, *13*, 1988–1993.

(141) Costantino, U.; Marmottini, F.; Nocchetti, M.; Vivani, R. *European Journal of Inorganic Chemistry* **1998**, *1998*, 1439–1446.

(142) Iyi, N.; Matsumoto, T.; Kaneko, Y.; Kitamura, K. *Chemistry Letters* **2004**, *33*, 1122–1123.

(143) He, J.; Wei, M.; Li, B.; Kang, Y.; Evans, D. G.; Duan, X. In *Layered Double Hydroxides*, Duan, X., Evans, D. G., Eds.; Springer Berlin Heidelberg: Berlin, Heidelberg, 2006, pp 89–119.

(144) Staal, L. B.; Charan Pushparaj, S. S.; Forano, C.; Prevot, V.; Ravnsbæk, D. B.; Bjerring, M.; Nielsen, U. G. *Journal of Materials Chemistry A* **2017**, *5*, 21795–21806.

(145) Prinetto, F.; Ghiotti, G.; Graffin, P.; Tichit, D. *Microporous and Mesoporous Materials* **2000**, *39*, 229–247.

(146) Smalenskaite, A.; Kaba, M. M.; Grigoraviciute-Puroniene, I.; Mikoliunaite, L.; Zarkov, A.; Ramanauskas, R.; Morkan, I. A.; Kareiva, A. *Materials* **2019**, *12*, 3738.

(147) Prince, J.; Montoya, A.; Ferrat, G.; Valente, J. S. *Chemistry of Materials* **2009**, *21*, 5826–5835.

(148) Hu, G.; O'Hare, D. *Journal of the American Chemical Society* **2005**, *127*, 17808–17813.

(149) Hu, G.; Wang, N.; O'Hare, D.; Davis, J. *Chemical Communications* **2006**, 287–289.

(150) Hu, G.; Wang, N.; O'Hare, D.; Davis, J. *Journal of Materials Chemistry* **2007**, *17*, 2257–2266.

(151) Daniel, S.; Thomas, S. In *Layered Double Hydroxide Polymer Nanocomposites*, Thomas, S., Daniel, S., Eds.; Woodhead Publishing Series in Composites Science and Engineering; Woodhead Publishing: 2020, pp 1–76.

(152) Richetta, M.; Medaglia, P.; Mattoccia, A.; Varone, A.; Pizzoferrato, R. *Journal of Material Science & Engineering* **2017**, *06*, 360.

(153) Wang, Q.; O'Hare, D. *Chemical Reviews* **2012**, *112*, 4124–4155.

(154) Adachi-Pagano, M.; Forano, C.; Besse, J. P. *Chemical Communications* **2000**, 91–92.

(155) Singh, M.; Ogden, M. I.; Parkinson, G. M.; Buckley, C. E.; Connolly, J. *Journal of Materials Chemistry* **2004**, *14*, 871–874.

(156) Hibino, T. *Chemistry of Materials* **2004**, *16*, 5482–5488.

(157) Wu, Q.; Olafsen, A.; Vistad, Ø. B.; Roots, J.; Norby, P. *Journal of Materials Chemistry* **2005**, *15*, 4695–4700.

(158) Wang, J.; Huang, L.; Gao, Y.; Yang, R.; Zhang, Z.; Guo, Z.; Wang, Q. *Chemical Communications* **2014**, *50*, 10130–10132.

(159) Hidalgo, J. M.; Jiménez-Sanchidrián, C.; Ruiz, J. R. *Applied Catalysis A: General* **2014**, *470*, 311–317.

(160) Cermelj, K.; Ruengkajorn, K.; Buffet, J. C.; O'Hare, D. *Journal of Energy Chemistry* **2019**, *35*, 88–94.

(161) Gordijo, C. R.; Leopoldo Constantino, V. R.; de Oliveira Silva, D. *Journal of Solid State Chemistry* **2007**, *180*, 1967–1976.

(162) Hibino, T.; Kobayashi, M. *Journal of Materials Chemistry* **2005**, *15*, 653–656.

(163) Jobbágy, M.; Regazzoni, A. E. *Journal of Colloid and Interface Science* **2004**, *275*, 345–348.

(164) Ichiro Kishine, J.; Kusunose, H.; Yamamoto, H. M. *Israel Journal of Chemistry* **2022**, *62*, e202200049.

(165) Ayuso, D.; Ordonez, A. F.; Smirnova, O. *Physical Chemistry Chemical Physics* **2022**, *24*, 26962–26991.

(166) Vantomme, G.; Crassous, J. *Chirality* **2021**, *33*, 597–601.

(167) Kelvin, W. T., *The Molecular Tactics of a Crystal*; Clarendon Press: Oxford, UK, 1893.

(168) Rodger, A.; Nordén, B., *Circular dichroism and linear dichroism*; Oxford University Press: Oxford, UK, 1997, p 150.

(169) Trudel, J. In *The Biographical Encyclopedia of Astronomers*, Hockey, T., Trimble, V., Williams, T. R., Bracher, K., Jarrell, R. A., Marché, J. D., Ragep, F. J., Palmeri, J., Bolt, M., Eds.; Springer New York: New York, NY, US, 2007, pp 125–127.

(170) Moloney, M. P.; Gun'ko, Y. K.; Kelly, J. M. *Chemical Communications* **2007**, 3900–3902.

(171) Barron, L. D. *Chirality* **2012**, *24*, 879–893.

(172) Gal, J. *Helvetica Chimica Acta* **2019**, *102*, e1900098.

(173) Ernst, K. H.; Wild, F. R.; Blacque, O.; Berke, H. *Angewandte Chemie International Edition* **2011**, *50*, 10780–10787.

(174) 5.4: Optical Activity - Chemistry LibreTexts `https://chem.libretexts.org/Bookshelves/Organic_Chemistry/Organic_Chemistry_I_(Liu)/05%3A_Stereochemistry/5.04%3A_Optical_Activity`.

(175) Visheratina, A.; Kotov, N. A. *CCS Chemistry* **2020**, *2*, 583–604.

(176) Kuznetsova, V.; Coogan, Á.; Botov, D.; Gromova, Y.; Ushakova, E. V.; Gun'ko, Y. K. *Advanced Materials* **2024**, *36*, 2308912.

(177) Kuznetsova, V.; Gromova, Y.; Martinez-Carmona, M.; Purcell-Milton, F.; Ushakova, E.; Cherevkov, S.; Maslov, V.; Gun'ko, Y. K. *Nanophotonics* **2020**, *10*, 797–824.

(178) Maqbool, Q.; Jung, A.; Won, S.; Cho, J.; Son, J. G.; Yeom, B. *ACS Applied Materials and Interfaces* **2021**, *13*, 54301–54307.

(179) Shao, X.; Zhu, C.; Kumar, P.; Wang, Y.; Lu, J.; Cha, M.; Yao, L.; Cao, Y.; Mao, X.; Heinz, H.; Kotov, N. A.; Shao, X; Kumar, P; Wang, Y; Lu, J; Yao, L; Cao, Y; Kotov, N. A.; Cha, M; Zhu, C; Heinz, H; Mao, X *Advanced Materials* **2023**, *35*, 2206956.

(180) Milton, F. P.; Govan, J.; Mukhina, M. V.; Gun'ko, Y. K. *Nanoscale Horizons* **2015**, *1*, 14–26.

(181) Baimuratov, A. S.; Rukhlenko, I. D.; Gun'ko, Y. K.; Baranov, A. V.; Fedorov, A. V. *Nano Letters* **2015**, *15*, 1710–1715.

(182) Tang, B.; Wang, S.; Liu, H.; Mou, N.; Portniagin, A. S.; Chen, P.; Wu, Y.; Gao, X.; Lei, D.; Rogach, A. L. *Advanced Optical Materials* **2023**, 2301524.

(183) Shukla, N.; Gellman, A. J. *Nature Materials* **2020**, *19*, 939–945.

(184) Meng, D.; Li, C.; Hao, C.; Shi, W.; Xu, J.; Sun, M.; Kuang, H.; Xu, C.; Xu, L. *Angewandte Chemie* **2023**, *135*, e202311416.

(185) Kuno, J.; Miyake, K.; Katao, S.; Kawai, T.; Nakashima, T. *Chemistry of Materials* **2020**, *32*, 8412–8419.

(186) Londoño-Calderon, A.; Williams, D. J.; Schneider, M. M.; Savitzky, B. H.; Ophus, C.; Ma, S.; Zhu, H.; Pettes, M. T. *Nanoscale* **2021**, *13*, 9606–9614.

(187) Pierce, N.; Chen, G.; Rajukumar, L. P.; Chou, N. H.; Koh, A. L.; Sinclair, R.; Maruyama, S.; Terrones, M.; Harutyunyan, A. R. *ACS Nano* **2017**, *11*, 9941–9949.

(188) John, N.; Mariamma, A. T. *Microchimica Acta 2021 188:12* **2021**, *188*, 1–25.

(189) Lan, X.; Zhou, X.; McCarthy, L. A.; Govorov, A. O.; Liu, Y.; Link, S. *Journal of the American Chemical Society* **2019**, *141*, 19336–19341.

(190) Branzi, L.; Purcell-Milton, F.; Cressoni, C.; Back, M.; Cattaruzza, E.; Speghini, A.; Gun'ko, Y. K.; Benedetti, A. *Nanoscale* **2022**, *14*, 12174–12182.

(191) Branzi, L.; Kavanagh, A.; Back, M.; Speghini, A.; Gun'ko, Y. K.; Benedetti, A. *Chemical Communications* **2023**, *59*, 6024–6027.

(192) Kuznetsova, V. A.; Mates-Torres, E.; Prochukhan, N.; Marcastel, M.; Purcell-Milton, F.; O'Brien, J.; Visheratina, A. K.; Martinez-Carmona, M.; Gromova, Y.; Garcia-Melchor, M.; Gun'ko, Y. K. *ACS Nano* **2019**, *13*, 13560–13572.

(193) Choi, J. K.; Haynie, B. E.; Tohgha, U.; Pap, L.; Elliott, K. W.; Leonard, B. M.; Dzyuba, S. V.; Varga, K.; Kubelka, J.; Balaz, M. *ACS Nano* **2016**, *10*, 3809–3815.

(194) Zhang, X.; Xu, Y.; Valenzuela, C.; Zhang, X.; Wang, L.; Feng, W.; Li, Q. *Light: Science & Applications* **2022**, *11*, 1–29.

(195) Ma, W.; Xu, L.; Moura, A. F. D.; Wu, X.; Kuang, H.; Xu, C.; Kotov, N. A. *Chemical Reviews* **2017**, *117*, 8041–8093.

(196) Vila-Liarte, D.; Kotov, N. A.; Liz-Marzán, L. M. *Chemical Science* **2022**, *13*, 595–610.

(197) Zhao, L.; Zhou, Y.; Niu, G.; Gao, F.; Sun, Z.; Li, H.; Jiang, Y. *Particle and Particle Systems Characterization* **2022**, *39*, 1–18.

(198) Sang, Y.; Liu, M. *Chemical Science* **2022**, *13*, 633–656.

(199) Bi, Y.; Cheng, C.; Zhang, Z.; Liu, R.; Wei, J.; Yang, Z. *Journal of the American Chemical Society* **2023**, *145*, 8529–8539.

(200) Imanaka, Y.; Nakahodo, T.; Fujihara, H. *ChemistrySelect* **2017**, *2*, 5806–5809.

(201) Kurtina, D. A.; Grafova, V. P.; Vasil'eva, I. S.; Maksimov, S. V.; Zaytsev, V. B.; Vasiliev, R. B. *Materials* **2023**, *16*, 1073.

(202) Aoki, R.; Horiuchi, T.; Makino, S.; Sano, N.; Imai, Y.; Sogawa, H.; Sanda, F. *Polymer* **2023**, *265*, 125576.

(203) Jiang, S.; Song, Y.; Kang, H.; Li, B.; Yang, K.; Xing, G.; Yu, Y.; Li, S.; Zhao, P.; Zhang, T. *ACS Applied Materials and Interfaces* **2022**, *14*, 3385–3394.

(204) Coogan, Á.; Hughes, L.; Purcell-Milton, F.; Cardiff, S.; Nicolosi, V.; Gun'ko, Y. K. *The Journal of Physical Chemistry C* **2022**, *126*, 18980–18987.

(205) Toyoda, K.; Miyamoto, K.; Aoki, N.; Morita, R.; Omatsu, T. *Nano Letters* **2012**, *12*, 3645–3649.

(206) Jeong, K. J.; Lee, D. K.; Tran, V. T.; Wang, C.; Lv, J.; Park, J.; Tang, Z.; Lee, J. *ACS Nano* **2020**, *14*, 7152–7160.

(207) Kang, J. S.; Kang, S.; Suh, J. M.; Park, S. M.; Yoon, D. K.; Lim, M. H.; Kim, W. Y.; Seo, M. *Journal of the American Chemical Society* **2022**, *144*, 2657–2666.

(208) Kim, J. Y.; Yeom, J.; Zhao, G.; Calcaterra, H.; Munn, J.; Zhang, P.; Kotov, N. *Journal of the American Chemical Society* **2019**, *141*, 11739–11744.

(209) Aisawa, S.; Takahashi, S.; Ogasawara, W.; Umetsu, Y.; Narita, E. *Journal of Solid State Chemistry* **2001**, *162*, 52–62.

(210) Aisawa, S.; Kudo, H.; Hoshi, T.; Takahashi, S.; Hirahara, H.; Umetsu, Y.; Narita, E. *Journal of Solid State Chemistry* **2004**, *177*, 3987–3994.

(211) Choy, J. H.; Kwak, S. Y.; Park, J. S.; Jeong, Y. J.; Portier, J. *Journal of the American Chemical Society* **1999**, *121*, 1399–1400.

(212) Desigaux, L.; Belkacem, M. B.; Richard, P.; Cellier, J.; Léone, P.; Cario, L.; Leroux, F.; Taviot-Guého, C.; Pitard, B. *Nano Letters* **2006**, *6*, 199–204.

(213) Wei, M.; Pu, M.; Guo, J.; Han, J.; Li, F.; He, J.; Evans, D. G.; Duan, X. *Chemistry of Materials* **2008**, *20*, 5169–5180.

(214) Duan, Y.; Liu, X.; Han, L.; Asahina, S.; Xu, D.; Cao, Y.; Yao, Y.; Che, S. *Journal of the American Chemical Society* **2014**, *136*, 7193–7196.

(215) Yu, H.; Huang, H.; Liang, J.; Deng, J. *Nanoscale* **2018**, *10*, 12163–12168.

(216) Jana, S.; De Frutos, M.; Davidson, P.; Abécassis, B. *Science Advances* **2017**, *3*, e1701483.

(217) Pan, H.; Zhu, C.; Lu, T.; Lin, J.; Ma, J.; Zhang, D.; Zhu, S. *Chemical Communications* **2017**, *53*, 1868–1871.

(218) Sang, Y.; Liu, M. *Chemical Science* **2022**, *13*, 633–656.

(219) Li, Y.; Wang, X.; Miao, J.; Li, J.; Zhu, X.; Chen, R.; Tang, Z.; Pan, R.; He, T.; Cheng, J.; Li, Y; Pan, R; Cheng, J; Wang, X; Chen, R; Miao, J; Tang, Z; Li, J; Zhu, X; He, T *Advanced Materials* **2020**, *32*, 1905585.

(220) Delahaye, É.; Eyele-Mezui, S.; Diop, M.; Leuvrey, C.; Rabu, P.; Rogez, G. *Dalton Transactions* **2010**, *39*, 10577–10580.

(221) Empedocles, S.; Neuhauser, R.; Shimizu, K.; Bawendi, M. *Advanced Materials* **1999**, *11*, 1243–1256.

(222) McGown, L. B.; Nithipahkom, K. *Applied Spectroscopy Reviews* **2000**, *35*, 353–393.

(223) Phillips, D. *Proceedings of the Royal Society A: Mathematical, Physical and Engineering Sciences* **2016**, *472*, 20160102.

(224) El-Sayed, M. A. *Accounts of Chemical Research* **1968**, *1*, 8–16.

(225) Blume, M.; Watson, R. *Proceedings of the Royal Society of London. Series A. Mathematical and Physical Sciences* **1962**, *270*, 127–143.

(226) Baryshnikov, G.; Minaev, B.; Ågren, H. *Chemical Reviews* **2017**, *117*, 6500–6537.

(227) Brinen, J. S.; Halverson, F.; Leto, J. R. *The Journal of Chemical Physics* **1965**, *42*, 4213–4219.

(228) Bünzli, J.-C. G. In *Including Actinides*, Bünzli, J.-C. G., Pecharsky, V. K., Eds.; Handbook on the Physics and Chemistry of Rare Earths, Vol. 50; Elsevier: 2016, pp 141–176.

(229) Singha, D. K.; Majee, P.; Mondal, S. K.; Mahata, P. *European Journal of Inorganic Chemistry* **2016**, *2016*, 4631–4636.

(230) Singha, D. K.; Majee, P.; Mondal, S. K.; Mahata, P. *Polyhedron* **2019**, *158*, 277–282.

(231) Brunet, E.; Juanes, O.; Rodriguez-Ubis, J. *Current Chemical Biology* **2012**, *1*, 11–39.

(232) Johnson, N. J.; He, S.; Diao, S.; Chan, E. M.; Dai, H.; Almutairi, A. *Journal of the American Chemical Society* **2017**, *139*, 3275–3282.

(233) Mohammadian, E.; Rahimpour, E.; Alizadeh-Sani, M.; Foroumadi, A.; Jouyban, A. *Applied Spectroscopy Reviews* **2022**, *57*, 39–76.

(234) Wang, Z.; Song, Y.; Cai, X.; Zhang, J.; Tang, T.; Wen, S. *Royal Society Open Science* **2019**, *6*, 191077.

(235) Tu, D.; Zheng, W.; Huang, P.; Chen, X. *Coordination Chemistry Reviews* **2019**, *378*, 104–120.

(236) Gupta, S. K.; Sudarshan, K.; Kadam, R. M. *Materials Today Communications* **2021**, *27*, 102277.

(237) Syamchand, S. S.; Sony, G. *Journal of Luminescence* **2015**, *165*, 190–215.

(238) Pastor, A.; Chen, C.; de Miguel, G.; Martín, F.; Cruz-Yusta, M.; O'Hare, D.; Pavlovic, I.; Sánchez, L. *Chemical Engineering Journal* **2023**, *471*, 144464.

(239) Gao, X.; Hu, M.; Lei, L.; O'hare, D.; Markland, C.; Sun, Y.; Faulkner, S. *Chemical Communications* **2011**, *47*, 2104–2106.

(240) Chen, Y.; Zhou, S.; Li, F.; Wei, J.; Dai, Y.; Chen, Y. *Journal of Fluorescence* **2011**, *21*, 1677–1682.

(241) Chen, Y.; Bao, Y.; Wang, X. *Journal of Fluorescence* **2016**, *26*, 813–820.

(242) Curtius, H.; Ufer, K. *Clays and Clay Minerals* **2007**, *55*, 354–360.

(243) Chen, Y.; Li, F.; Zhou, S.; Wei, J.; Dai, Y.; Chen, Y. *Journal of Solid State Chemistry* **2010**, *183*, 2222–2226.

(244) García Doménech, N.; Purcell-Milton, F.; Gun'ko, Y. K. *Materials Today Communications* **2020**, *23*, 100888.

(245) Membrane Technology Principle `https://www.ps-prozesstechnik.com/en/membrane-technology/membrane-process-development/membrane-technology-principle.html` (accessed 11/26/2023).

(246) Sutariya, B.; Karan, S. *Separation and Purification Technology* **2022**, *293*, 121096.

(247) Hilal, N.; Al-Zoubi, H.; Darwish, N. A.; Mohammad, A. W.; Arabi, M. A. *Desalination* **2004**, *170*, 281–308.

(248) Chang, E. E.; Liang, C. H.; Huang, C. P.; Chiang, P. C. *Separation and Purification Technology* **2012**, *85*, 1–7.

(249) Yu, W.; Liu, T.; Crawshaw, J.; Liu, T.; Graham, N. *Water Research* **2018**, *139*, 353–362.

(250) Li, P.; Xie, H.; Bi, Y.; Miao, C.; Chen, K.; Xie, T.; Zhao, S.; Sun, H.; Yang, X.; Hou, Y.; Niu, Q. J. *Applied Surface Science* **2023**, *618*, 156650.

(251) Sorribas, S.; Gorgojo, P.; Téllez, C.; Coronas, J.; Livingston, A. G. *Journal of the American Chemical Society* **2013**, *135*, 15201–15208.

(252) Staszak, K. *Physical Sciences Reviews* **2017**, *2*, 20170142.

(253) Deen, W. M. *AIChE Journal* **1987**, *33*, 1409–1425.

(254) Boo, C.; Wang, Y.; Zucker, I.; Choo, Y.; Osuji, C. O.; Elimelech, M. *Environmental Science and Technology* **2018**, *52*, 7279–7288.

(255) Wang, X. L.; Tsuru, T.; Nakao, S. I.; Kimura, S. *Journal of Membrane Science* **1997**, *135*, 19–32.

(256) Li, J.; Xu, C.; Long, J.; Ding, Z.; Yuan, R.; Li, Z. *ACS Applied Nano Materials* **2022**, *5*, 7373–7381.

(257) Da Gama, B. M. V.; Selvasembian, R.; Giannakoudakis, D. A.; Triantafyllidis, K. S.; McKay, G.; Meili, L. *Molecules* **2022**, *27*, 4900.

(258) Johnston, A. L.; Lester, E.; Williams, O.; Gomes, R. L. *Journal of Environmental Chemical Engineering* **2021**, *9*, 105197.

(259) Zheng, Y. M.; Li, N.; Zhang, W. D. *Colloids and Surfaces A: Physicochemical and Engineering Aspects* **2012**, *415*, 195–201.

(260) Bhojaraj; Arulraj, J.; Kolinjavadi, M. R.; Rajamathi, M. *ACS Omega* **2019**, *4*, 20072–20079.

(261) Miyata, S. *Clays and Clay Minerals* **1983**, *31*, 305–311.

(262) Chen, Y.; Jing, C.; Zhang, X.; Jiang, D.; Liu, X.; Dong, B.; Feng, L.; Li, S.; Zhang, Y. *Journal of Colloid and Interface Science* **2019**, *548*, 100–109.

(263) Darmograi, G.; Prelot, B.; Layrac, G.; Tichit, D.; Martin-Gassin, G.; Salles, F.; Zajac, J. *Journal of Physical Chemistry C* **2015**, *119*, 23388–23397.

(264) Zaghouane-Boudiaf, H.; Boutahala, M.; Arab, L. *Chemical Engineering Journal* **2012**, *187*, 142–149.

(265) El Hassani, K.; Beakou, B. H.; Kalnina, D.; Oukani, E.; Anouar, A. *Applied Clay Science* **2017**, *140*, 124–131.

(266) Shamim, M.; Dana, K. *International Journal of Environmental Science and Technology* **2018**, *15*, 1275–1284.

(267) Kefif, F.; Ezziane, K.; Bahmani, A.; Bettahar, N.; Mayouf, S. *Bulletin of Materials Science* **2019**, *42*, 1–11.

(268) Bharali, D.; Deka, R. C. *Journal of Environmental Chemical Engineering* **2017**, *5*, 2056–2067.

(269) Chen, Y.; Chen, S.; Deng, Z.; Xu, X.; Qin, J.; Guo, X.; Bai, Z.; Chen, X.; Lu, Z. *International Journal of Environmental Science and Technology* **2023**, *20*, 10141–10152.

(270) De Sá, F. P.; Cunha, B. N.; Nunes, L. M. *Chemical Engineering Journal* **2013**, *215*, 122–127.

(271) Shabbir, R.; Gu, A.; Chen, J.; Khan, M. M.; Wang, P.; Jiao, Y.; Zhang, Z.; Liu, Y.; Yang, Y. *International Journal of Environmental Analytical Chemistry* **2022**, *102*, 1060–1077.

(272) Wang, X.; Zhou, W.; Wang, C.; Chen, Z. *New Journal of Chemistry* **2018**, *42*, 9463–9471.

(273) Taher, T.; Yu, Z.; Melati, E. K. A.; Munandar, A.; Aflaha, R.; Triyana, K.; Wibowo, Y. G.; Khairurrijal, K.; Lesbani, A.; Rianjanu, A. *Journal of Hazardous Materials Letters* **2024**, *5*, 100103.

(274) Mallakpour, S.; Azadi, E.; Dinari, M. *Carbohydrate Polymers* **2023**, *301*, 120362.

(275) Li, B.; Xu, X.; Yang, Z.; Lu, J.; Han, J. *ChemPlusChem* **2024**, *89*, e202300521.

(276) Yeh, C. N.; Raidongia, K.; Shao, J.; Yang, Q. H.; Huang, J. *Nature Chemistry* **2015**, *7*, 166–170.

(277) Wang, Z.; Von Dem Bussche, A.; Qiu, Y.; Valentin, T. M.; Gion, K.; Kane, A. B.; Hurt, R. H. *Environmental Science and Technology* **2016**, *50*, 7208–7217.

(278) Song, H.; Jiang, D. E. *Nanoscale* **2023**, *15*, 16010–16015.

(279) Wang, N.; Huang, Z.; Li, X.; Li, J.; Ji, S.; An, Q. F. *Journal of Materials Chemistry A* **2018**, *6*, 17148–17155.

(280) Li, B.; Yang, Z.; Dou, Y.; Zhang, J.; Lu, J.; Han, J.; Li, B; Yang, Z; Dou, Y; Zhang, J; Lu, J; Han, J *Angewandte Chemie International Edition* **2023**, *62*, e202304442.

(281) Li, Q.; Elimelech, M. *Environmental Science and Technology* **2004**, *38*, 4683–4693.

(282) Yu, H. B.; Zhang, X. Q.; Han, X.; Yang, Z. Z.; Zhou, Y. W.; Ding, W.; Du, M. X. *Water, Air, and Soil Pollution* **2022**, *233*, 1–9.

(283) Guo, W.; Ngo, H. H.; Li, J. *Bioresource Technology* **2012**, *122*, 27–34.

(284) Franke, V.; Ullberg, M.; Mccleaf, P.; Wålinder, M.; Hler, S. J. K.; Ahrens, L. *ACS EST Water* **2021**, *1*, 782–795.

(285) Epsztein, R. *Frontiers in Membrane Science and Technology* **2022**, *1*, 1048416.

(286) Shahkaramipour, N.; Tran, T. N.; Ramanan, S.; Lin, H. *Membranes* **2017**, *7*, 13.

(287) Zhang, R.; Liu, Y.; He, M.; Su, Y.; Zhao, X.; Elimelech, M.; Jiang, Z. *Chemical Society Reviews* **2016**, *45*, 5888–5924.

(288) Jafari, M.; Vanoppen, M.; van Agtmaal, J. M.; Cornelissen, E. R.; Vrouwenvelder, J. S.; Verliefde, A.; van Loosdrecht, M. C.; Picioreanu, C. *Desalination* **2021**, *500*, 114865.

(289) Lidén, A.; Persson, K. M. *Water* **2016**, *8*, 150.

(290) Gorenflo, A.; Velázquez-Padrón, D.; Frimmel, F. H. *Desalination* **2003**, *151*, 253–265.

(291) Ertl, G.; Freund, H. J. *Physics Today* **1999**, *52*, 32–38.

(292) Rayner-Canham, M.; Rayner, G. *History of Education* **2022**, *51*, 596–598.

(293) Brazil, R. *Chemistry World* **2022**.

(294) Laidler, K. J. *Pure and Applied Chemistry* **1996**, *68*, 149–192.

(295) Kumar, A.; Daw, P.; Milstein, D. *Chemical Reviews* **2022**, *122*, 385–441.

(296) Weber, S.; Stöger, B.; Veiros, L. F.; Kirchner, K. *ACS Catalysis* **2019**, *9*, 9715–9720.

(297) Washida, N.; Imamura, T.; Bandow, H. *Bulletin of the Chemical Society of Japan* **1996**, *69*, 535–541.

(298) Schlögl, R. *Angewandte Chemie International Edition* **2015**, *54*, 3465–3520.

(299) Farrauto, R. J.; Heck, R. M. *Catalysis Today* **1999**, *51*, 351–360.

(300) Wu, J.; Zheng, W.; Chen, Y. *Current Opinion in Green and Sustainable Chemistry* **2022**, *33*, 100580.

(301) Fujishima, A.; Honda, K. *Nature* **1972**, *238*, 37–38.

(302) Hoffmann, M. R.; Martin, S. T.; Choi, W.; Bahnemann, D. W. *Chemical Reviews* **1995**, *95*, 69–96.

(303) Tian, C.; Zhang, Q.; Wu, A.; Jiang, M.; Jiang, B.; Fu, H. *Chemical Communications* **2012**, *48*, 2858–2860.

(304) Nakata, K.; Fujishima, A. *Journal of Photochemistry and Photobiology C: Photochemistry Reviews* **2012**, *13*, 169–189.

(305) Klimov, V. I. *Journal of Physical Chemistry B* **2006**, *110*, 16827–16845.

(306) Feng, C.; Wu, Z.-P.; Huang, K.-W.; Ye, J.; Zhang, H.; Feng, C; Wu, Z.-P; Huang, K.-W; Zhang, H; Ye, J *Advanced Materials* **2022**, *34*, 2200180.

(307) Koppenol, W. H. *Free Radical Biology and Medicine* **1993**, *15*, 645–651.

(308) Meyerstein, D. *Nature Reviews Chemistry* **2021**, *5*, 595–597.

(309) Liang, X.; Zhong, Y.; He, H.; Yuan, P.; Zhu, J.; Zhu, S.; Jiang, Z. *Chemical Engineering Journal* **2012**, *191*, 177–184.

(310) Tušar, N. N.; Maučec, D.; Rangus, M.; Arčon, I.; Mazaj, M.; Cotman, M.; Pintar, A.; Kaučič, V. *Advanced Functional Materials* **2012**, *22*, 820–826.

(311) Torreilles, J.; Guerin, M. C.; Slaoui-Hasnaoui, A. *Free Radical Research Communications* **1990**, *11*, 159–166.

(312) Sutton, H. C.; Winterbourn, C. C. *Free Radical Biology and Medicine* **1989**, *6*, 53–60.

(313) Nogueira, R. F. P.; Trovó, A. G.; Silva, M. R. A. D.; Villa, R. D.; Oliveira, M. C. D. *Química Nova* **2007**, *30*, 400–408.

(314) Dihingia, H.; Tiwari, D. *Journal of Water Process Engineering* **2022**, *45*, 102500.

(315) Li, W.; Nanaboina, V.; Zhou, Q.; Korshin, G. V. *Water Research* **2012**, *46*, 403–412.

(316) Vorontsov, A. V. *Journal of Hazardous Materials* **2019**, *372*, 103–112.

(317) Yap, C. L.; Gan, S.; Ng, H. K. *Chemosphere* **2011**, *83*, 1414–1430.

(318) Fu, Y.; Ning, F.; Xu, S.; An, H.; Shao, M.; Wei, M. *Journal of Materials Chemistry A* **2016**, *4*, 3907–3913.

(319) Luo, Y.; Han, Y.; Hua, Y.; Xue, M.; Yu, S.; Zhang, L.; Yin, Z.; Li, X.; Ma, X.; Wu, H.; Liu, T.; Shen, Y.; Gao, B. *Chemosphere* **2022**, *309*, 136802.

(320) Sherryna, A.; Tahir, M.; Nabgan, W. *International Journal of Hydrogen Energy* **2022**, *47*, 862–901.

(321) Chen, J.; Wang, C.; Zhang, Y.; Guo, Z.; Luo, Y.; Mao, C. J. *Applied Surface Science* **2020**, *506*, 144999.

(322) Ning, F.; Shao, M.; Xu, S.; Fu, Y.; Zhang, R.; Wei, M.; Evans, D. G.; Duan, X. *Energy & Environmental Science* **2016**, *9*, 2633–2643.

(323) Zhang, M.; Luo, Z.; Zhou, M.; Zhang, G.; Alamry, K. A.; Taib, L. A.; Asiri, A. M.; Wang, X. *Applied Catalysis B: Environmental* **2017**, *210*, 454–461.

(324) Goh, K. H.; Lim, T. T.; Dong, Z. *Water Research* **2008**, *42*, 1343–1368.

(325) Bai, J.; Liu, Y.; Yin, X.; Duan, H.; Ma, J. *Applied Surface Science* **2017**, *416*, 45–50.

(326) Pelalak, R.; Hassani, A.; Heidari, Z.; Zhou, M. *Chemical Engineering Journal* **2023**, *474*, 145511.

(327) Wang, H.; Jing, M.; Wu, Y.; Chen, W.; Ran, Y. *Journal of Hazardous Materials* **2018**, *353*, 53–61.

(328) Zhang, L. H.; Li, F.; Evans, D. G.; Duan, X. *Industrial and Engineering Chemistry Research* **2010**, *49*, 5959–5968.

(329) El-Monaem, A.; M., E.; Elshishini, H. M.; Bakr, S. S.; El-Aqapa, H. G.; Hosny, M.; Andaluri, G.; El-Subruiti, G. M.; Omer, A. M.; Eltaweil, A. S. *npj Clean Water* **2023**, *6*, 1–24.

(330) Kaur, H.; Singh, S.; Pal, B. *Environmental Nanotechnology, Monitoring Management* **2021**, *16*, 100451.

(331) Segal, S. R.; Carrado, K. A.; Marshall, C. L.; Anderson, K. B. *Applied Catalysis A: General* **2003**, *248*, 33–45.

# Chapter 2

# Materials and Methods

## 2.1 Starting Materials

Copper nitrate trihydrate ($Cu(NO_3)_2{\cdot}3H_2O$, puriss, p.a. 99-104%) and aluminium nitrate nonahydrate ($Al(NO_3)_3{\cdot}9H_2O$, $\geq$ 98%) were purchased from Honeywell Fluka. Terbium nitrate hexahydrate ($Tb(NO_3)_3.6H_2O$, 99.9% (REO)) was purchased from Strem Chemicals, Inc. Europium nitrate hexahydrate ($Eu(NO_3)_3.6H_2O$, 99.9% (REO)), and D-phenylalanine (99%) were purchased from Alfa Aesar. Sodium dichromate ($Na_2Cr_2O_7$) was purchased from May and Baker. Zinc nitrate hexahydrate ($Zn(NO_3)_2{\cdot}6H_2O$, purum p.a., crystallized $\geq$ 99.0%), magnesium chloride hexahydrate ($MgCl_2 2.6H_2O$, BioXtra, $\geq$ 99.0%) L-Phenylalanine ($\geq$ 98%), Evans Blue ($\geq$ 75%), Methylene Blue ($\geq$ 82%), Rhodamine B base ($\sim$97%) and hydrogen peroxide ($H_2O_2$, 30% w/w) were purchased from Sigma Aldrich. Methyl Orange ($\geq$ 95%) was purchased from VWR International Ltd. Hexagonal boron nitride (h-BN) powder (particle size = 6-30 $\mu$M) and Durapore membrane filters (hydrophilic polyvinylidene fluoride (PVDF), 0.45 $\mu$m pore size and 47 mm diameter) were purchased from Merck. Sodium hydroxide (general purpose grade) was purchased from

Fisher Chemical. 400 mesh Cu-lacey carbon TEM grids were purchased from Ted Pella. Millipore water (MP $H_2O$) was supplied in-house using a Milli-Q system with resin filters operating at 18Ω. All materials were used as-obtained without further purification.

## 2.2 Experimental Procedures for Chapter 3

### 2.2.1 Co-precipitation synthesis of CuAl-$CO_3$ LDHs

This synthesis was modified slightly from previously published procedures.[1,2] $Na_2CO_3$ (0.81 g, 7.5 mmol) was added to a large beaker with 200 mL of MP $H_2O$. A few drops of 1 M NaOH solution were added to adjust the pH to 10. Separately, a metal salt solution was prepared by dissolving $Cu(NO_3)_2{\cdot}3H_2O$ (1.35 g, 5.58 mmol) and $Al(NO_3)_3{\cdot}9H_2O$ (2.1 g, 5.58 mmol) in 100 mL of MP $H_2O$. The metal salt solution was added dropwise to the $Na_2CO_3$ solution under magnetic stirring, also adding drops of 1 M NaOH solution as necessary to keep the pH $\geq$ 10. The mixture was left to stir for 4 h at room temperature, then left to age overnight. The resulting material was cleaned *via* centrifugation at 5000 RPM for 10 min, washing with MP $H_2O$ (3 times) and isopropanol (3 times). A small amount of the material was redispersed in ethanol, and the remaining material was dried in an oven at 80 °C overnight for further use. It is worth noting that this 1:1 metal salt ratio is less common in the literature, and in fact likely results in the formation of a product closer to a 2:1 Cu/Al ratio.

### 2.2.2 Chiral co-precipitation with Phe in situ

L- or D-Phe (0.307 g, 1.86 mmol) and $Na_2CO_3$ (0.135 g, 1.25 mmol) were added to a beaker with 125 mL of MP $H_2O$. A few drops of 1 M NaOH solution were added to adjust the pH to 10. Separately, a metal salt solution was prepared by dissolving $Cu(NO_3)_2.3H_2O$ (1.35 g, 5.58 mmol) and $Al(NO_3)_3{\cdot}9H_2O$ (2.1 g, 5.58 mmol) in 25 mL of MP $H_2O$. The metal salt solution was added dropwise to the Phe/$Na_2CO_3$ solution, adding drops of 1 M NaOH as necessary to keep the pH $\geq$ 10. The mixture was left to stir for 4 h at room temperature, then left to age overnight. The resulting material was cleaned *via* centrifugation at 5500 RPM for 10 min, washing with MP $H_2O$ (3 times) and isopropanol (3 times).

### 2.2.3 Chiral co-precipitation with DBTA in situ

L- and D-DBTA modified LDHs were prepared according to the protocol described in Section 2.2.2, with two modifications. L-/D-DBTA (0.67 g, 1.86 mmol) was used in place of L-/D-Phe, and the reaction was carried out at 35 °C to increase the solubility of DBTA in water.

### 2.2.4 Post-synthetic treatment of CuAl LDHs with phenylalanine

Dried CuAl LDHs (100 mg) were added to a round-bottomed flask with 50 mL of MP $H_2O$. Separately, 100 mg of L- or D-Phe was added to 50 mL of MP $H_2O$, adjusted to pH 10 using 1M NaOH. The L- or D-Phe solution was added dropwise to the LDH suspension. The mixture was left to stir for 4 hours, after which stirring was ceased and the mixture was left to age overnight. The resulting material was cleaned *via* centrifugation at 5000 RPM

for 10 mins, washing with MP $H_2O$ (3 times) and isopropanol (3 times). Some material was kept dispersed in ethanol for spectroscopic measurements, and the remainder of the material was dried in an oven at 80 °C for further use.

## 2.3 Experimental Procedures for Chapter 4

### 2.3.1 Co-precipitation synthesis of CuAl-$CO_3$ LDHs

This synthesis was carried out the same as described in Section 2.2.1, however centrifugal washing was carried out using MP $H_2O$ only (3 times).

### 2.3.2 Preparation of partially oxidised bulk BN by thermal oxidation

Bulk BN (5 g) was placed in a ceramic dish and placed in a furnace. The sample was heated in air at a rate of 5 °C to a target temperature of 1000 °C, and held for 30 minutes to produce bulk BNOx powder.

### 2.3.3 LDH/BNOx nanocomposite and membrane preparation

As-prepared CuAl-$CO_3$ LDH (60 mg) and BNOx (240 mg) were added to a round-bottomed flask with 100 mL of MP $H_2O$ and sonicated for 24 h to obtain the LDH/BNOx nanocomposite. Membranes were prepared by taking 50 mL of the suspension and passing it

through a PVDF template (pore size = 0.45 μm, diameter = 47 mm) by vacuum filtration operating at a pressure of 1 bar.

### 2.3.4 Nanofiltration performance tests - dye retention and solvent flux

Four water soluble dyes (Evans Blue, Methyl Orange, Methylene Blue, and Rhodamine B) were used for testing the retention of the LDH-BNOx membranes. The following concentrations were used, to ensure an average UV-Vis absorbance of 1 - 1.5 a.u., as shown in Table 2.1.

Table 2.1: Concentrations and corresponding absorbances at $\lambda_{max}$ of each dye.

| **Dye** | **Concentration (μM)** | $\lambda_{max}$ **(nm)** | **Abs (a.u.)** |
|---|---|---|---|
| Methyl Orange | 50 | 466 | 1.2 |
| Methylene Blue | 27 | 664 | 1.5 |
| Evans Blue | 15 | 606 | 1 |
| Rhodamine B | 20 | 558 | 1.5 |

20 mL of the dye solution was passed through the membrane using vacuum filtration operating at a pressure of 1 bar. A UV-Vis of the permeate was obtained. The permeate was further concentrated to obtain a 3 mL aliquot using rotary evaporation and re-dissolution to ensure a higher level of accuracy in the calculations, and a UV-Vis absorbance spectrum of the concentrated permeate was also obtained. The membrane retentions were calculated

according to Equation 2.1.

$$R_x(\%) = (1 - \frac{C_{P,x}}{C_{F,x}}).100 \tag{2.1}$$

where:

$R_x(\%)$ is the retention of the membrane,

$C_{P,x}$ is the concentration of the permeate, and

$C_{F,x}$ is the concentration of the feed solution,

However, as absorbance is directly proportional to concentration according to the Beer-Lambert law, the following form (Equation 2.2) can be derived, allowing retention to be calculated directly from the UV-Vis data:

$$R_x(\%) = (1 - \frac{A_{P,x}}{A_{F,x}}).100 \tag{2.2}$$

where:

$A_{P,x}$ is the concentration of the permeate, and

$A_{F,x}$ is the concentration of the feed solution.

Water permeance/flux measurements in our dead-end filtration system were carried out both for the PVDF template, as well as the LDH/BNOx membranes. This was conducted by recording the time taken for 20 mL of MP $H_2O$ to pass through the vacuum filtration system. The system was operating at a pressure of 1 bar, and the working area of the fritted glass filtration system is 9.6 x $10^{-4}$ $m^2$. Flux was calculated according to Equation 2.3:

$$F = \frac{V}{At} \tag{2.3}$$

where:

$F$ is the flux in L $m^{-2}$ $h^{-1}$,

$V$ is the volume of MP $H_2O$ in L,

$A$ is the working area of the filtration system in $m^2$, and

$t$ is the time taken for 20 mL of MP $H_2O$ to pass through the system.

### 2.3.5 Analysis of LDH/BNOx membrane dye adsorption kinetics

An as-prepared LDH/BNOx membrane was cut into two, with one half being placed in a clean, polycarbonate petri dish. 10 mL of the dye solution was added to the petri dish, and the petri dish was closed and placed in the dark. Regular aliquots were taken over the course of up to 6 hours for UV-Vis analysis and returned to the petri dish in a timely manner to minimise the light exposure time. The adsorption was modelled using pseudo-second order (PSO) kinetics, as shown in Equation 2.4, and described mathematically in more detail in Appendix C, and the Weber-Morris intra-particle diffusion (IPD) kinetic model, as shown in Equation 2.5. While the complex mathematics involved in the derivation of the Weber-Morris IPD model from Fick's laws of diffusion is far beyond the scope of this thesis, interested readers may refer to the cited literature.[3–5]

$$\frac{t}{q_t} = \frac{1}{k_2 q_2^2} + \frac{t}{q_2} \tag{2.4}$$

$$q_t = k_{IPD,i} t^{0.5} + c_i \tag{2.5}$$

where:

$q_t$ is the amount adsorbed at time $t$ (in mmol/g),

$q_2$ is the maximum adsorption capacity from the PSO model,

$k_2$ is the apparent PSO rate constant,

$k_{IPD,i}$ is the apparent IPD rate constant for stage $i$ in the IPD process, and

$c_i$ is the intercept of the plot of $q_t$ vs $t^{0.5}$ and corresponds to the thickness of the boundary layer. It is worth noting that the original Weber-Morris model does not include the $c_i$ term - this was added later by McKay *et al.*[6]

The second half of the membrane was used for the photocatalysis experiments, as described in Section 2.3.6.

### 2.3.6 Analysis of LDH/BNOx membrane photodegradation kinetics

An as-prepared LDH/BNOx membrane was cut into two, with one half being placed in a clean, polycarbonate petri dish. 10 mL of the dye solution was added to the petri dish, along with 10 µL of 30% w/w $H_2O_2$ solution. The open petri dish was placed under a Parkside (Lidl) 5 W COB LED lamp operating at maximum power. Aliquots were taken every 10 mins over the course of 120 mins for UV-Vis analysis and returned to the petri dish in a timely manner to maximise the light exposure time. The photocatalytic degradation measurements were performed in triplicate for each dye. The photodegradation process was

modelled using pseudo-first order (PFO) degradation kinetics, as described in Equation 2.6, and described mathematically in more detail in Appendix C.

$$ln(\frac{c_0}{c_t}) = k_1 t \tag{2.6}$$

where:

$c_0$ is the dye concentration before exposure to light,

$c_t$ is the dye concentration at a certain time $t$ after exposure to light, and

$k_1$ is the apparent PFO rate constant.

The values of $c_t$ were calculated by conversion of the absorbance values at $\lambda_{max}$ using the Beer-Lambert law. The second half of the membrane was used for the adsorption experiments, as described in Section 2.3.5.

### 2.3.7 Photodegradation control experiments

The experiment was performed as described in Section 2.3.6, with no membrane added as a photocatalyst, to determine the extent of dye photobleaching with $H_2O_2$ in the presence of visible light.

### 2.3.8 Hydroxyl radical probe experiments

The generation of hydroxyl radicals ($^{\bullet}$OH) by the LDH/BNOx nanocomposite were monitored using the terephthalic acid (TA) probe technique. 4 round-bottomed flasks were

filled with 10 mg of TA and 50 mL of 20 mM NaOH aqueous solution to aid with aqueous solubility. 30 mg of LDH/BNOx nanocomposite was added to each flask. One flask was placed under the LED lamp, and the second was placed in the dark. To the third and fourth flasks, 20 μL of $H_2O_2$ (30% (w/w)) was added. One of these was placed under the LED lamp, and the other was placed in the dark. The samples were left for three hours, after which the solids were removed by centrifugation at 15,000 RPM for 2 minutes. The supernatant was retained, and photoluminescence emission spectra of the fluorescent product, hydroxyterephthalic acid (hTA), were obtained using an excitation wavelength of 315 nm, an emission range of 350-500 nm, excitation and emission slit widths of 2.5 nm, 1 nm increments, and an integration time of 0.1 s.

## 2.4 Experimental Procedures for Chapter 5

### 2.4.1 Co-precipitation synthesis of Eu-doped MgAl LDHs

This synthesis was modified by us from a previously published procedure.[7] $Na_2CO_3$ (0.405 g, 3.75 mmol) was added to a beaker with 100 mL of MP $H_2O$. A few drops of 1 M NaOH solution were added to adjust the pH to 10 (Solution A). Separately, a mixed Mg/Al metal salt solution (solution B) was prepared by dissolving $MgCl_2.6H_2O$ (0.565 g, 2.79 mmol) and $Al(NO_3)_3.9H_2O$ (0.525 g, 1.40 mmol) to 50 mL of MP $H_2O$. Solution A was added dropwise to the $Na_2CO_3$ solution, adding drops of 1 M NaOH as necessary to keep the pH $\geq$ 10. Metal salt solution C was prepared by dissolving $Eu(NO_3)_3.6H_2O$ (0.124 g, 0.279 mmol) to 10 mL MP $H_2O$, and immediately added dropwise to solution A once all of solution B had been added, adding drops of 1 M NaOH as required to keep the pH $\geq$ 10. The mixture was left to stir for 4 h at room temperature, then left to age overnight. The resulting material

was cleaned *via* centrifugation at 5000 RPM for 10 min, washing with MP water (3 times) and isopropanol (3 times) and dried in an oven at 80 °C overnight for further use.

### 2.4.2 Co-precipitation synthesis of Tb-doped MgAl LDHs

This procedure was carried out as described in Section 2.4.1, with $Eu(NO_3)_3.6H_2O$ replaced by $Tb(NO_3)_3.6H_2O$ (0.126 g, 0.279 mmol).

### 2.4.3 Co-precipitation synthesis of Eu-doped ZnAl LDHs

This procedure was carried out as described in Section 2.4.1., with $MgCl_2.6H_2O$ replaced by $Zn(NO_3)_2.6H_2O$ (0.83 g, 2.79 mmol).

### 2.4.4 Co-precipitation synthesis of Tb-doped ZnAl LDHs

This procedure was carried out as described in Section 2.4.1, with $MgCl_2.6H_2O$ replaced by $Zn(NO_3)_2.6H_2O$ (0.83 g, 2.79 mmol), and $Eu(NO_3)_3.6H_2O$ replaced by $Tb(NO_3)_3.6H_2O$ (0.126 g, 0.279 mmol).

### 2.4.5 LDH quenching tests with dichromate

10 mg of as-prepared lanthanide-doped LDHs (MgAlEu, MgAlTb, ZnAlEu and ZnAlTb) were added to 10 mL of 2 mM $Na_2Cr_2O_7$ aqueous solution and sonicated for 10 minutes.

PL emission spectroscopy was conducted to examine the quenching, using an emission wavelength of 615 nm for Eu-doped LDHs, and 544 nm for Tb-doped LDHs. PL emission spectra for quenching studies were obtained using excitation and emission slit widths of 2 nm, a sample window of 10 ms, a flash count of 45, and an initial delay of 0.1 ms.

## 2.5 Instrumentation

### 2.5.1 UV-visible absorption spectroscopy

UV-visible absorption spectroscopy (UV-Vis) is a technique that examines how a material interacts with ultraviolet (UV) and visible light. In this technique, UV-visible light (typically in the 200-800 nm range) is generated from a broad band white-light source, that is then split into individual wavelengths using a monochromator. This light is then passed through the sample of interest, and a detector compares the intensity of the emergent beam at each wavelength (I) with that of the incident beam ($I_0$), which is reported as transmittance (T), according to Equation 2.7.

$$T = \frac{I}{I_0} \tag{2.7}$$

UV-Vis data is more often represented using the absorbance ($A$) parameter. Absorbance can be related to transmittance according to Equation 2.8.

$$A = -log_{10}T \tag{2.8}$$

Materials absorb certain wavelengths of light corresponding to specific electronic transitions, which can be visualised in UV-Vis spectroscopy as peaks in the absorbance (y-axis) versus wavelength (x-axis) graphical output.

The molar extinction coefficient is a measure of how strongly a sample absorbs at a given wavelength. It is a material property and is dependent on the composition and structure of the material. The absorbance of a sample is closely related to its concentration *via* the Beer-Lambert law, as shown in Equation 2.9.

$$A = \epsilon c l \tag{2.9}$$

where:

$A$ is the absorbance of the sample,

$\epsilon$ is the molar extinction coefficient,

$c$ is the molar concentration of the sample, and

$l$ is the path length

More accurately, it is the extinction ($E$) spectrum that is obtained from a UV-Vis spectrophotometer, which has contributions from both absorption and scattering effects. However, absorbance is - perhaps incorrectly - more commonly used, as scattering effects may be sufficiently miniscule that they can be neglected for solutions, as well as some colloidal solutions of sufficiently small nanoparticles. The Beer-Lambert law therefore does not hold for highly scattering samples, as the A $\approx$ E approximation begins to break down, which will be discussed in Section 2.5.2.[8]

All solution-based UV-Vis absorption measurements were acquired using an Agilent

Cary 60 Spectrophotometer with a wavelength range of 200-800 nm. Measurements were acquired using a 10 mm quartz cuvette with a UV-cutoff of 190 nm. Both HPLC ethanol and MP $H_2O$ were used as solvents, and are referenced throughout the thesis.

### 2.5.2 Diffuse reflectance UV-visible spectroscopy

Optical transmission measurements have contributions from both absorption and scattering effects. Scattering of light by small objects is generally described by Mie Theory, and for sufficiently small objects, the Rayleigh approximation is typically used, as described in Equations 2.10 and 2.11. It is important to note that this approximation assumes the scattering object is spherical.[9]

$$\epsilon = \alpha + \sigma \tag{2.10}$$

$$\sigma \propto \frac{D^6}{\lambda^4} \tag{2.11}$$

where $D$ is the diameter of the particle interacting with the light source, and $\epsilon$, $\alpha$ and $\sigma$ are the extinction, absorption, and scattering coefficients, respectively.

For molecular solutions and colloidal suspensions of sufficiently small nanoparticles, the scattering contributions can often be neglected. However, it is clear from Equation 2.11 that for larger nanomaterials, this cannot be the case. High aspect ratio anisotropic nanomaterials (1D and 2D materials) tend to scatter UV-visible light intensely, particularly at lower wavelengths, which can make solution-based measurements of these colloids difficult.

Often, the extinction curves of 2D materials are dominated by these scattering effects, and the intrinsic absorbance features and fine detail can become lost in the scattering background.[10]

Diffuse Reflectance (DR) UV-Vis spectroscopy is based upon the principle that rough or uneven surfaces exhibit diffuse reflection. When light is incident on a sample, there are typically two types of reflection which can occur - specular or diffuse. Specular reflection generally occurs when light is incident on a smooth, reflective surface, such as a mirror. This results in the angle of incidence being equal to the angle of reflection of the light beam. Diffuse reflection, on the other hand, occurs when a light in incident on a rough reflective surface, resulting in the reflected rays being scattered in all directions, as shown in Figure 2.1.

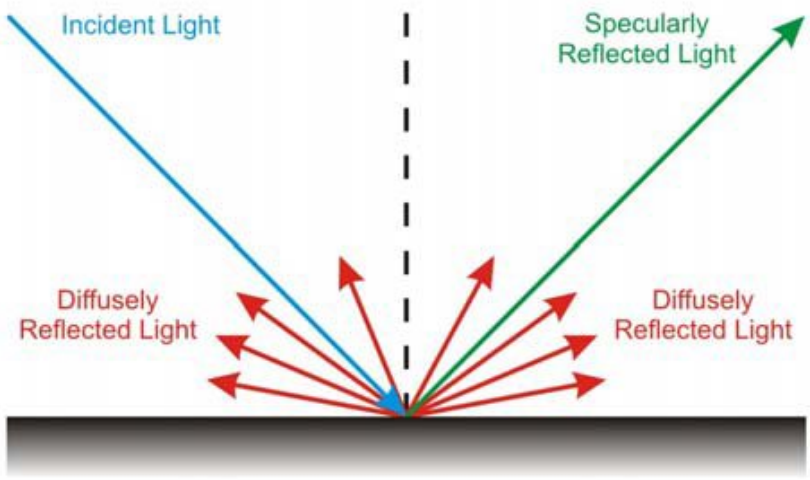


Figure 2.1: Specular vs. diffuse light reflection from a surface.[11]

Solid samples act as diffuse reflecting objects, which forms the basis for DR UV-Vis spectroscopy. The reflected light is then collected by a detector and gives a read out of reflectance vs. wavelength. DR UV-Vis instruments can also be operated in transmission mode if thin enough solid samples are used, for example thin films or drop-cast samples, allowing the absorbance to be calculated. The use of an integrating sphere is crucial for

these measurements. The inner surface of the integrating sphere is coated with a highly diffuse reflective material such as barium sulfate or InGaAs, and causes the transmitted light to undergo multiple diffuse reflections within the cavity, and ensures a uniform light distribution reaches the detector.[12]

All DR UV-Vis measurements were acquired using a Perkin Elmer Lambda 1050 UV-Vis-NIR spectrophotometer operating in transmission mode, with 150 mm InGaAs integrating sphere. Samples were prepared for DR UV-Vis by drop-casting some of the colloidal suspension onto a VWR super premium microscope slide cut to size, followed by solvent evaporation using a hot plate at 100 °C.

### 2.5.3 Circular dichroism spectroscopy

Circular dichroism (CD) spectroscopy is a technique used to study the chiral properties of molecules and materials, and is most often used in the study of biomolecules, such as proteins and nucleic acids.[13] It is also useful for the study of chiral nanomaterials, specifically those which exhibit chiroptical activity. CD can be defined as the difference in absorption of left- and right-handed circularly polarised light (CPL), as summarised in Equation 2.12.

$$\Delta A = A_l - A_r \tag{2.12}$$

where $A_l$ and $A_r$ are the absorbances of left- and right-handed CPL, respectively. CPL can be generated by passing horizontally and vertically polarised light through a quarter-wave plate, which results in the generation of two perpendicular light waves, with equal amplitudes, travelling 90 ° out of phase with respect to one another. As chiral molecules absorb left- and right-handed CPL to different extents, the resultant wave will be elliptically

polarised. For this reason, CD output on most spectropolarimeters is typically given in terms of ellipticity (θ).[14] Ellipticity (with units of mdeg) can be related to the difference in absorbance according to Equation 2.13.

$$\theta = 32980 \times \Delta A \tag{2.13}$$

A detailed derivation showing the origin of the conversion factor of 32980 is given in Appendix A. By definition, CD signals can only be observed if the sample absorbs in that region of the electromagnetic spectrum. Furthermore, a sudden change in CD response is often observed in the region of the absorbance maximum. For the purposes of comparing anisotropy and dissymmetry in materials independent of concentration, it is often useful to use a dimensionless quantity. For CD, this measure is the Kuhn anisotropy factor, more commonly referred to as the $g$-factor, which can be defined according to Equation 2.14.[15,16]

$$g = \frac{\Delta A}{A} \tag{2.14}$$

where $A$ is the UV-Vis absorbance intensity at a given wavelength. Combining Equations 2.13 and 2.14 allow us to calculate the $g$-factor directly from CD and UV-Vis absorbance spectra, according to Equation 2.15.

$$g = \frac{\theta}{32980 \times A} \tag{2.15}$$

CD spectra of nanomaterial colloidal dispersions were recorded using a Jasco J-815 spectropolarimeter, and a quartz cuvette with a UV cut-off of 190 nm, and a path length

of 10 mm. Both HPLC ethanol and MP $H_2O$ were used as solvents, and are referenced throughout the thesis.

### 2.5.4 Photoluminescence spectroscopy

Photoluminesence (PL) spectroscopy is a technique commonly employed in the study of the electronic and optical properties of materials. When light of sufficient energy is absorbed by a material, electrons can be promoted from the ground state to a higher electronic energy level, resulting in the formation of an excited state. This excited state is inherently unstable, and will eventually relax back to the ground state through a series of radiative and/or non-radiative relaxations, which are discussed in more detail in the Introduction chapter, and are summarised in the Jablonski diagram in Figure 2.2.

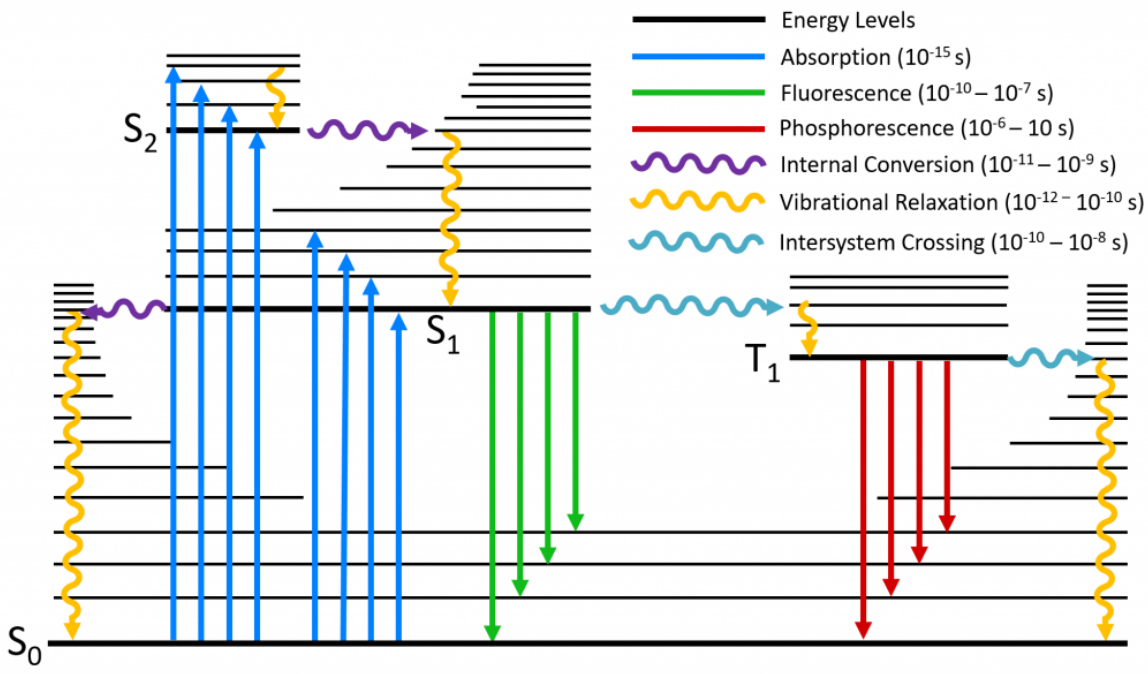


Figure 2.2: Jablonski diagram demonstrating absorption of energy, as well as radiative and non-radiative relaxation pathways within the electronic states of a molecule.[17]

The radiative relaxation pathways are studied using PL spectroscopy. Vibrational relaxation results in emission occurring from the lowest vibrational energy level of the excited state. Therefore, the emitted photon will typically have lower energy (and thus a longer wavelength) than the absorbed photon for a given transition. This phenomenon is known as the Stokes shift, as shown in Figure 2.3.

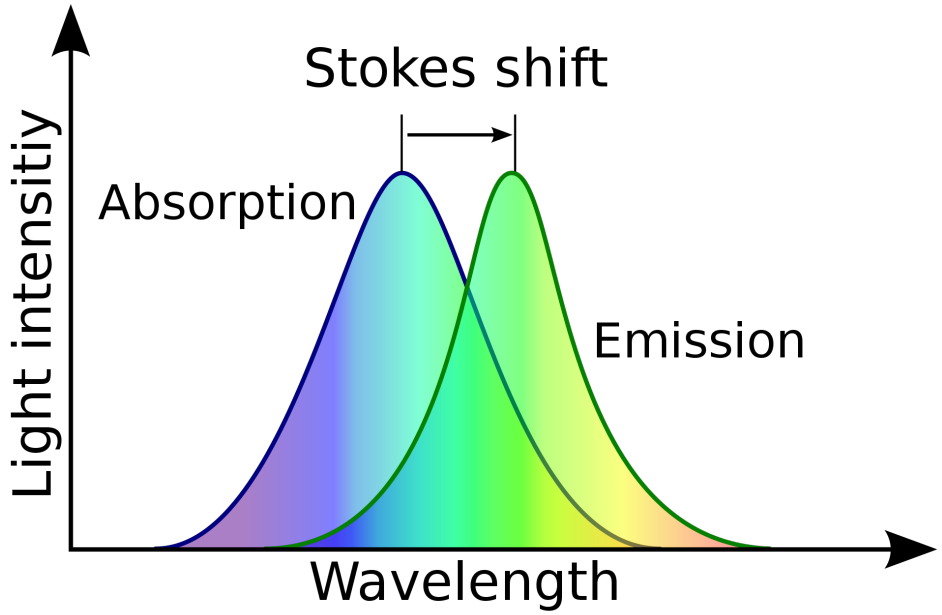


Figure 2.3: Superimposed PL excitation and emission spectra demonstrating the Stokes shift, whereby emission occurs at longer wavelengths than excitation.[18]

Photoluminescence spectrometers can be operated in both excitation and emission configurations, to record both types of spectra. Emission spectra are obtained by choosing a suitable fixed excitation wavelength, and scanning the emission over a given wavelength range using a monochromator. Conversely, excitation spectra are obtained by choosing a suitable fixed emission wavelength (typically that of the most intense emission band), and scanning the excitation over a given wavelength range.

PL excitation and emission measurements were performed using a Horiba Jobin Yvon Fluoromax-4, and a 10 mm quartz cuvette with a UV cut-off of 190 nm. Lanthanide-doped

samples were analysed in phosphorescence mode, whereas hydroxyl radical analysis was conducted in fluorescence mode. The specific excitation and emission wavelengths used will be referenced throughout the thesis.

### 2.5.5 Fourier transform infrared spectroscopy

Infrared (IR) spectroscopy is a non-destructive analytical technique which can be used to investigate the bonding in molecules and materials. Often referred to as vibrational spectroscopy, it is based on the fact that bonds can absorb radiation in the infrared region of the electromagnetic spectrum, causing the bonds to vibrate.

Absorption of infrared radiation by molecules causes transitions between vibrational energy states. In the simplest molecular case (i.e. a diatomic molecule), the bond can be treated as a simple harmonic oscillator, according to Equation 2.16.

$$\nu = \frac{1}{2\pi}\sqrt{\frac{k}{\mu}} \tag{2.16}$$

where:

$\nu$ is the frequency of the vibration,

$k$ is the force constant and

$\mu$ is the reduced mass and is given by $\mu = \frac{m_1 m_2}{m1+m_2}$, where $m_1$ and $m_2$ are the masses of the bonding atoms.

It is clear from Equation 2.16 that the vibrational frequency of any given bond depends both on the bond strength, as well as the masses of the bonding atoms. For example, higher bond orders, i.e., double and triple bonds, typically occur at higher frequencies than single

bonds, and bonds between heavier atoms, for example metal-oxygen bonds, typically appear at lower frequencies. Thus, IR spectroscopy can be used to identify specific functional groups in a given molecule. In the context of inorganic nanomaterials research, IR spectroscopy is most often used for determining successful surface functionalisation of materials with organic molecules, although it can be also used to probe metal-oxygen bonds. There are a number of different vibrations that can occur in molecules, including bending, stretching, and wagging, all of which have different frequencies associated with them and can be distinguished from another, even within the same molecule. Furthermore, for a band to be IR-active, there must be a change in the dipole moment of the molecule upon absorption of light.[19]

Fourier Transform IR (FT-IR) differs from more traditional, dispersive IR, in that instead of measuring just the dispersive IR transmission spectrum, a reference beam is combined with the beam transmitted through the sample to form an interference pattern, called an interferogram. The interferogram then undergoes Fourier transformation to generate a spectral output which is transmission as a function of wave frequency (typically given in wavenumbers – $cm^{-1}$). FT-IR is typically used over standard IR as it offers faster data acquisition and higher signal-to-noise ratios.[20]

FT-IR spectra were recorded using a PerkinElmer Spectrum 100 FT-IR with diamond UATR accessory.

### 2.5.6 Powder X-ray diffraction (pXRD)

X-ray diffraction is a non-destructive analytical technique that utilises X-rays to probe the crystal structure of a material. X-rays are generated by accelerating electrons towards a metal target (most commonly Cu in laboratory-based crystallographic applications). If the accelerated electrons have sufficient energy, they can displace electrons from the inner shells

of atoms of the target metal. An outer shell electron will relax back down to the inner shell to fill this vacancy, emitting characteristic X-rays. The most prominent emission lines are the $K_\alpha$, which arises due to an electronic transition from the $L$ to $K$ shell, and the $K_\beta$, which is a result of a transition from the $M$ to $K$ shell. The $K_\alpha$ emission is much more intense, and thus is more frequently used for X-ray diffraction studies. A second type of X-ray emission, known as Bremsstrahlung radiation, is also generated during this process, and occurs when high energy electrons are decelerated and deflected due to the influence of the positively charged atomic nucleus. Both the Bremsstrahlung and $K_\beta$ radiation can be filtered out of the signal, leaving behind just the $K_\alpha$ emission with a defined wavelength.

Diffraction is a phenomenon observed in electromagnetic radiation, by which the waves are bent or scattered by an obstacle or through an opening. Diffraction is most commonly observed when the wavelength of the electromagnetic radiation and the opening are comparable in size. X-ray wavelengths are on the order of angstroms (Å) – approximately 1.54 Å in the case of Cu $K_\alpha$ emission - which is comparable to the spacings between atomic planes, and thus they can be readily diffracted by periodic arrays of atoms, as is the case in crystals. Crystallographic planes are described in terms of Miller indices, denoted $(hkl)$. It is useful also to define $d_{hkl}$, the interplanar spacing between adjacent parallel planes of atoms in a crystal, which are described by Miller indices $(hkl)$.

Once the diffracted X-ray waves re-emerge from the sample, they can interfere either constructively or destructively. The conditions under which constructive interference occurs when X-rays are diffracted by a crystal are governed by Bragg's law, as shown in Equation 2.17 and Figure 2.4.

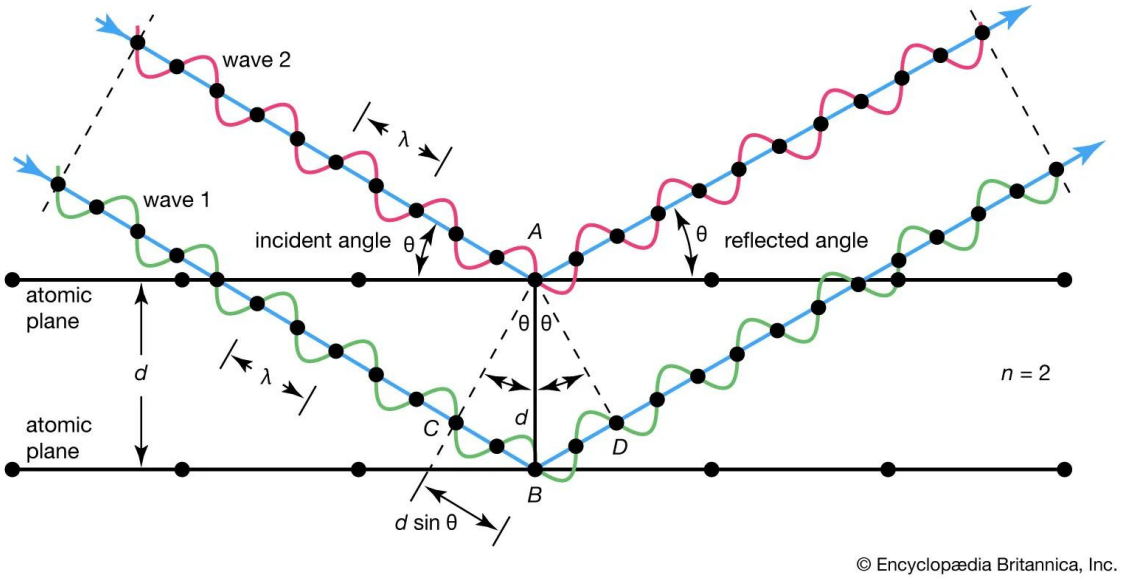


Figure 2.4: Bragg diffraction from periodic arrays of atoms in a crystal.[21]

$$n\lambda = 2d_{hkl}sin\theta \tag{2.17}$$

where:

θ is the angle of incidence,

$n$ is the order of diffraction (n = 1, 2, 3, etc.),

$d_{hkl}$ is the distance between Miller planes, and

$\lambda$ is the wavelength of the X-ray source.

The consequences of Bragg's law are therefore that constructive interference (and thus diffraction signals), can only appear at certain angles. Furthermore, Bragg's law allows one to estimate the spacing between crystallographic planes.

Powder X-ray diffraction (pXRD) varies slightly from the above case, as in a powder sample, tens of thousands of microcrystals are present in many different crystallographic

orientations, and thus diffracted beams emerge in many different directions. To be able to obtain reasonable intensities of diffraction events from powder samples, the Bragg-Brentano geometry is instead used, as shown in Figure 2.5. In this configuration, the sample is typically rotated to maximise the number of individual crystallites observed, resulting in a more reliable diffraction pattern.

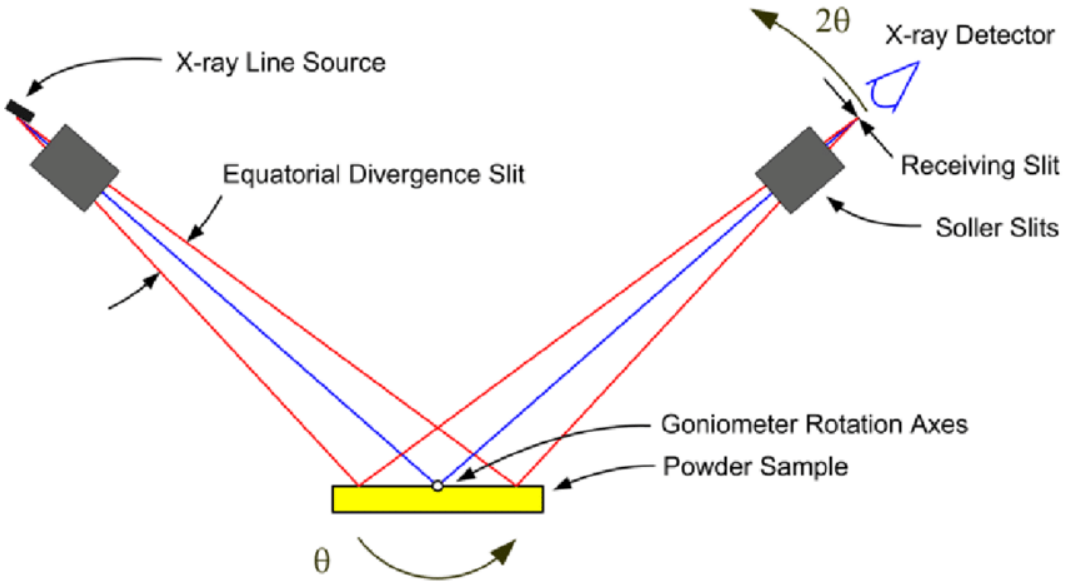


Figure 2.5: Illustration of Bragg-Brentano geometry for obtaining X-ray diffraction events from powder samples.[22]

pXRD measurements were obtained using a Bruker D2 Phaser ($2^{nd}$ Gen) benchtop diffractometer, and a Si low-background specimen holder. Measurements were performed using Cu $K_\alpha$ radiation ($\lambda = 1.54$ Å), in a typical 2θ range of 5-80°, with X-ray fluorescence correction. Powder samples were ground using a pestle and mortar immediately prior to measurements to minimise preferred orientation effects.

### 2.5.7 Electron microscopy and related techniques

Microscopy is an imaging technique which probes the interaction of a light beam with a given sample. The image resolution ($R$) of a microscope, and thus the minimum resolvable detail ($\delta$), which is inversely proportional to the resolution, is a function of the wavelength ($\lambda$) of incident light, and is derived from the classical Rayleigh criterion, according to Equation 2.18:

$$\delta = \frac{0.61\lambda}{NA} \tag{2.18}$$

where NA is the numerical aperture of the lens. For conventional optical microscopes, that operate using a visible light source ($\lambda \approx$ 400 – 800 nm), $\delta$ is limited to a range of approximately 200 – 400 nm. This level of resolution is too low for analysis of most microscopic and all nanoscopic objects.

Electrons can instead be used as a beam source to achieve higher resolution. Electrons exhibit wave-particle duality, as hypothesised by de Broglie, and the momentum ($p$) of an electron can be related to its momentum according to the de Broglie relation, as shown in Equation 2.19,

$$\lambda = \frac{h}{p} = \frac{h}{mv} \tag{2.19}$$

where:

$h$ is the Planck's constant,

$m$ is the electron mass, and

$v$ is the velocity.

High-voltages can be used to impart high kinetic energies on electrons through acceleration, according to Equation 2.20:

$$eV = \frac{mv^2}{2} \tag{2.20}$$

where:

$V$ is the accelerating voltage, and

$e$ is the electron charge.

The two above equations can be combined to give an expression for the wavelength in terms of the accelerating voltage, according to Equation 2.21.

$$\lambda = \frac{h}{\sqrt{2meV}} \tag{2.21}$$

Therefore, as the accelerating voltage is increased, the wavelength is decreased. Thus, by using electrons as a beam source, the resolution of a microscope can be greatly enhanced. For example, using an accelerating voltage of 100 kV gives a theoretical minimum resolvable distance in the picometer range. However this level of resolution is limited in practice by lens aberrations, and typically the highest achievable resolution on an uncorrected TEM is in the range of Å to nm depending on the performance of the lenses. Nevertheless, it is clear that using electrons as a beam source offers superior resolution compared to visible light, which is the basis for electron microscopy. Electron sources can either be thermionic (W and $LaB_6$ are typical examples) or field emission (either Schottky or cold field emission). Thermionic emission occurs by heating a metal to give electrons sufficient

energy to overcome the work function, whereas field emission exploits the fact that electric fields strengths are substantially higher at sharp points.

When electrons interact with a specimen, a large number of interactions can occur. These can include secondary electrons, diffracted or scattered electrons, as well as characteristic X-rays, as shown in Figure 2.6.[23] Depending on the generated signal one wishes to analyse, a number of techniques can be used, which will be discussed in the following subsections.

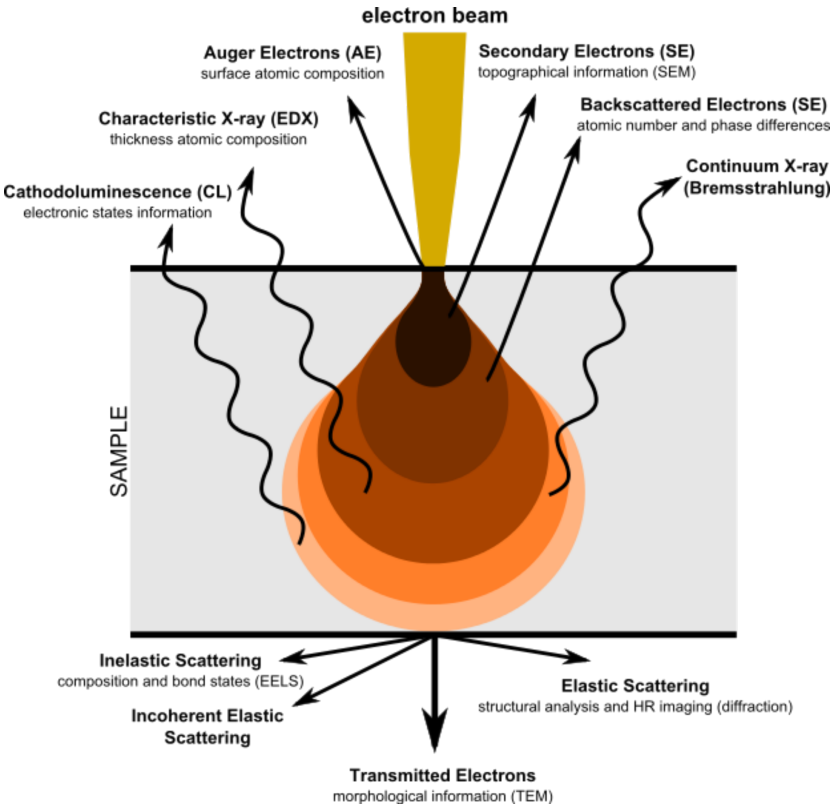


Figure 2.6: Schematic of the electron-specimen interaction volume, and variety of signals generated during as a result of this interaction.[23]

### Scanning electron microscopy (SEM)

Scanning electron microscopy (SEM) is a technique which involves scanning a focused electron beam across a sample, and analysing the back-scattered and secondary electrons to form an image of the surface. X-rays can also be generated through electrons interacting with the sample, which will be discussed in later subsections. The SEM column consists of an electron source (either thermionic or field emission), a series of electromagnetic lenses which converge and focus the beam, apertures which control the beam size, deflection coils which allow the beam to be rastered or scanned across the sample, and the detection and imaging system. SEM typically operates at relatively low accelerating voltages (typically 0.1 – 30 kV), limiting its maximum resolution to the order of 10s of nm. A schematic of a SEM column is shown in Figure 2.7.[24]

Backscattered electrons are the result of elastic scattering events between incident beam electrons and atomic nuclei. As such, they can give information on the variation in composition across a sample, as heavier elements are more efficient scatterers. Heavier elements therefore appear brighter in SEM images obtained using a backscattered electron detector.

In contrast, secondary electrons are the result of inelastic scattering events. Secondary electrons are low-energy electrons which are ejected from on or near the surface of the specimen, due to interaction of the primary electron beam with the atoms in the sample. As a result, secondary electron signals provide topographical information of a given sample.

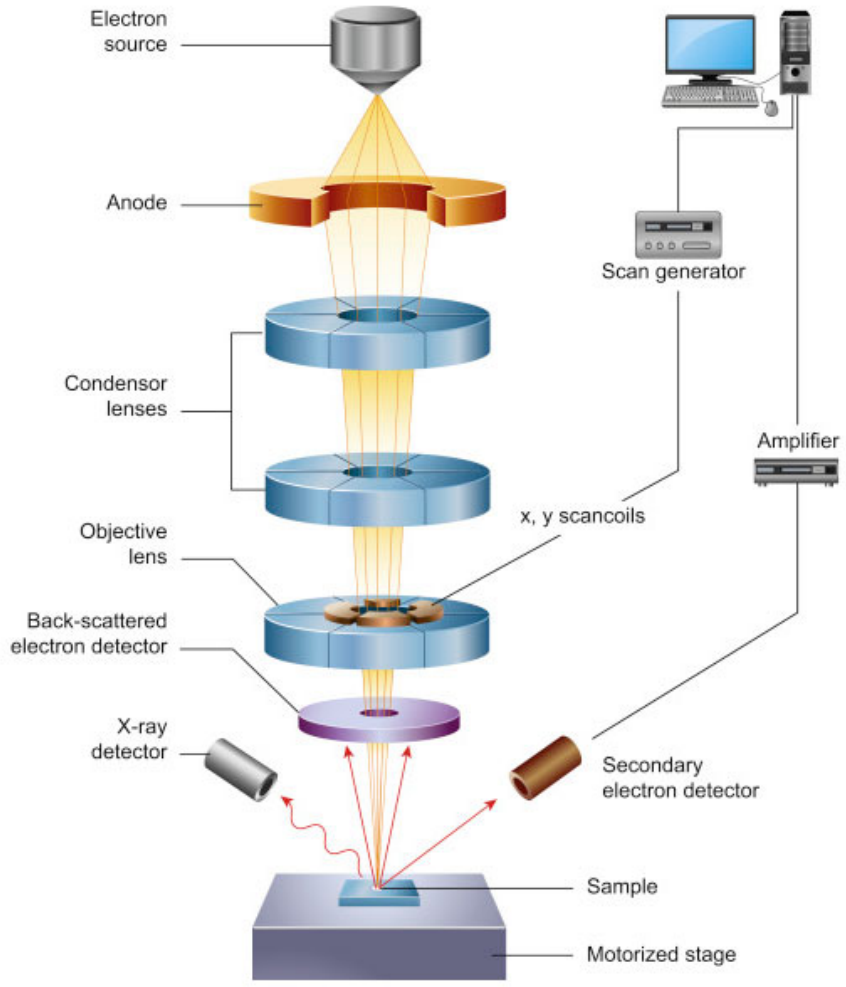


Figure 2.7: Schematic of a scanning electron microscope.[24]

SEM images were obtained using a Zeiss Ultra Plus Scanning Electron Microscope. Numerous SEM sample preparation methods were utilised in this work. In Chapter 4, Membrane samples were prepared for SEM by adhering a portion of the membranes to carbon tab-covered standard SEM and cross-section SEM stubs. In Chapter 5, some samples were prepared by sprinkling the dried, powdered material on a sticky carbon tab-covered standard SEM stub. All other SEM samples were prepared by drop-casting dispersed material in solvent of choice on a 400-mesh lacey carbon Cu TEM grid, followed by drying in vacuum overnight. SEM images in Chapter 3 were obtained by Dr. Lucia Hughes.

### Transmission electron microscopy (TEM)

Transmission electron microscopy (TEM) is an imaging technique which utilises the transmitted electrons to probe the structure and morphology of sufficiently thin nanomaterials. Much like in SEM, the TEM column consists of an electron gun, a series of electromagnetic lenses and apertures, and a camera and detector system. The accelerating voltage used for the electron beam is typically between 60 and 300 kV, allowing for much higher resolution (often atomic resolution) images to be obtained when compared with SEM. In traditional TEM mode, the illumination system is operated in a parallel beam configuration. TEM operated in parallel beam mode can also be used to obtain electron diffraction patterns, known as selected area electron diffraction (SAED). A schematic of a TEM is shown in Figure 2.8 (a). In contrast, scanning transmission electron microscopy (STEM) mode utilises the illumination system in a convergent beam configuration, and combines aspects of both SEM and TEM, as shown in Figure 2.8 (b). High-angle annular dark field STEM (HAADF-STEM) images can be obtained by using a detector to detect the higher angle scattered electrons, as shown in Figure 2.8 (c). The convergent beam is rastered across the sample, creating mass-thickness ($Z$) contrast images. In contrast to conventional TEM images, thicker areas, as well as areas containing atoms of heavier elements appear brighter in HAADF-STEM images.

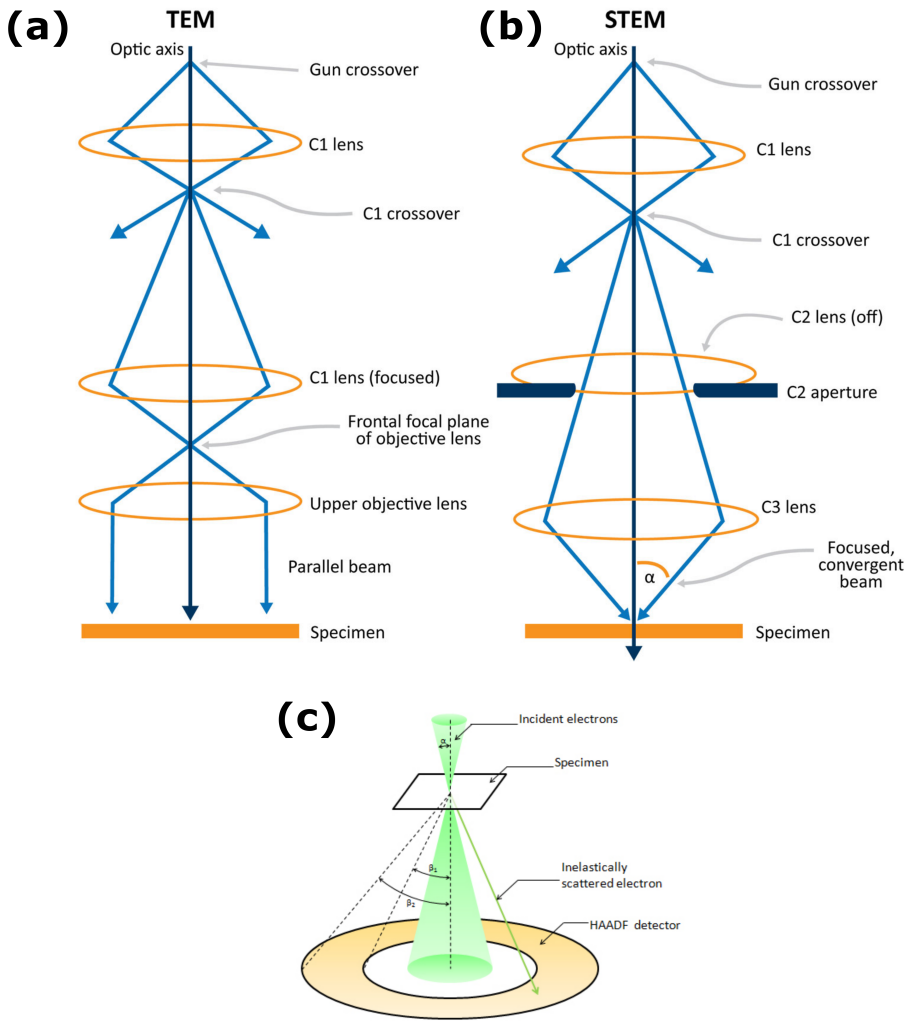


Figure 2.8: Schematics of TEM operating in (a) parallel beam mode and (b) convergent beam mode. (c) HAADF detector used in STEM mode.[25,26]

TEM imaging was performed using an uncorrected FEI Titan (scanning) transmission electron microscope (accelerating voltage = 300 kV). Samples were prepared for TEM *via* drop-casting of dispersed material in water or ethanol on 400-mesh lacey carbon Cu TEM grids, followed by drying in vacuum overnight. TEM and STEM imaging were conducted by Dr. Finn Purcell-Milton (Chapter 3), Dr. Lucia Hughes (Chapter 3) and Dr. Tigran Simonian (Chapter 4).

### Energy dispersive X-ray spectroscopy

Energy dispersive X-ray spectroscopy (EDX) is a technique commonly used in conjunction with electron microscopy to determine the elemental composition of a material. When high energy electrons interact with a specimen, they can force inner shell electrons in the atoms of the sample to be knocked out of their orbits and ejected from the sample, creating a hole in an inner shell. This electronic configuration is unstable, and thus an electron from a higher energy shell will relax back down to fill the hole, which is accompanied by the emission of electromagnetic radiation of an energy equal to the difference between the shells. This energy difference is on the order of keV, meaning that X-rays are generated during this process.

As atoms of each element have their own unique sets of energy levels, this means the generated X-rays are characteristic of the element from which they are emitted, and as such are typically referred to as characteristic X-rays. This phenomenon serves as the basis of EDX, and the frequencies (and thus energies) of the characteristic X-rays can be described by Moseley's law, as given in Equation 2.22.

$$\nu = \frac{E}{h} = A(Z - b)^2 \tag{2.22}$$

where:

$\nu$ is the frequency of the characteristic X-ray,

$E$ is the energy of the characteristic X-ray,

$h$ is Planck's constant,

$Z$ is the atomic number, and

$A$ and $b$ are constants that depend on the type of electronic transition.

The emitted characteristic X-rays are labelled using Siegbahn notation $X_y$, in which $X$ describes the shell the electron is being ejected from ($K$, $L$, $M$, etc.), and $y$ is the order of relaxation ($\alpha$ = relaxation across 1 shell, $\beta$ = relaxation across 2 shells). A schematic summarising this is shown in Figure 2.9.

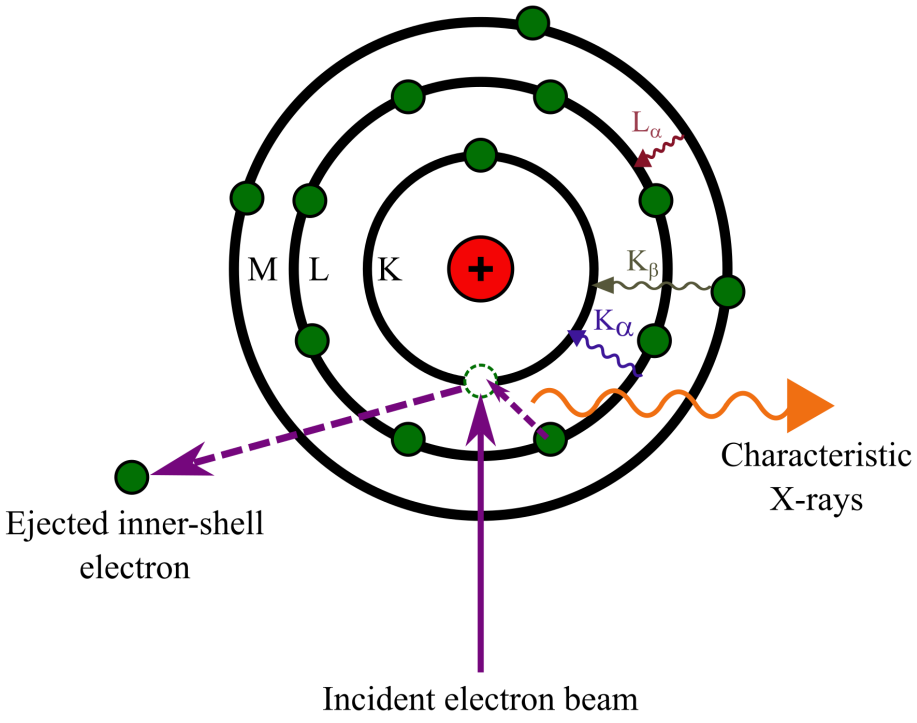


Figure 2.9: Schematic representing the working principle of EDX.

As high-energy incident electrons are capable of knocking inner-shell electrons out of orbit, EDX is typically carried out in conjunction with electron microscopy. The EDX detector equipped on an electron microscope measures the abundance or intensity of emitted X-rays as a function of their energy. A spectral output of counts versus X-ray energy is produced, which allows the determination of the elemental composition of a given sample. However, many standard EDX detectors cannot analyse elements lighter than sodium for a number of reasons, including the emitted X-ray energies, X-ray reabsorption, and detector sensitivity, so other techniques are preferred for lighter elements.

EDX spectroscopy and mapping were carried out by Dr. Tigran Simonian on the FEI Titan TEM using a beam current of approx. 500 pA, and a Bruker Quantax XFlash 6T-30 30 $mm^2$ EDX detector.

**Electron energy loss spectroscopy**

Electron energy loss spectroscopy (EELS) is a technique used in transmission electron microscopy to gain a huge number of insights into materials, including elemental compositions, electronic structures, and bonding characteristics. The technique involves analysing electrons that have lost energy after passing through a specimen, through inelastic interactions including plasmon and phonon excitations, inter and intra-band transitions, as well as inner shell ionisation events. For elemental analysis, the inner shell ionisations are the most important inelastic event, and the amount of energy lost after interaction with the sample is characteristic of the elements present.[27] EELS detectors are specifically designed to detect low energy losses, thus particularly useful for detection of lighter elements in a sample, where EDX may be less effective.

EELS was carried out by Dr. Tigran Simonian on the FEI Titan TEM using a beam current of approx. 500 pA, and a Gatan Tridium GIF system.

### 2.5.8 Thermogravimetric analysis

Thermogravimetric analysis (TGA) is a destructive analytical technique which can be used to study the thermal stability and decomposition profiles of a range of materials. It is typically used in materials science to study phase transitions, loss of solvent and other volatile components, as well as to determine the upper temperature limits under which materials can be safely used before degradation.

The components of a thermogravimetric analyser are as follows. A sample crucible is used to hold the sample during analysis, and is typically composed of a heat resistant material, such as ceramic. The sample crucible is loaded on to the arm of a precision balance, which monitors the mass of the sample over the course of the measurement, often down to a precision of a few micrograms. This is all moved into a furnace, which is controlled by external software to heat at a given rate within a certain range of time. A gas inlet is attached to the furnace, which allows for the thermal properties to be analysed under either inert or air atmosphere. A schematic of a typical TGA set up is shown in Figure 2.10.

There are three types of TGA that can be conducted - isothermal, quasistatic, and dynamic. In this work, dynamic TGA was conducted, which involves measuring the fluctuations in weight of a sample as the temperature is heated linearly over a certain timeframe. The produced output is a graph of the relative change in mass (typically given a percentage) as a function of temperature.[28]

TGA was carried out in this work using a Perkin Elmer Pyris 1 Thermogravimetric Analyser, a ceramic sample crucible, and under air atmosphere.

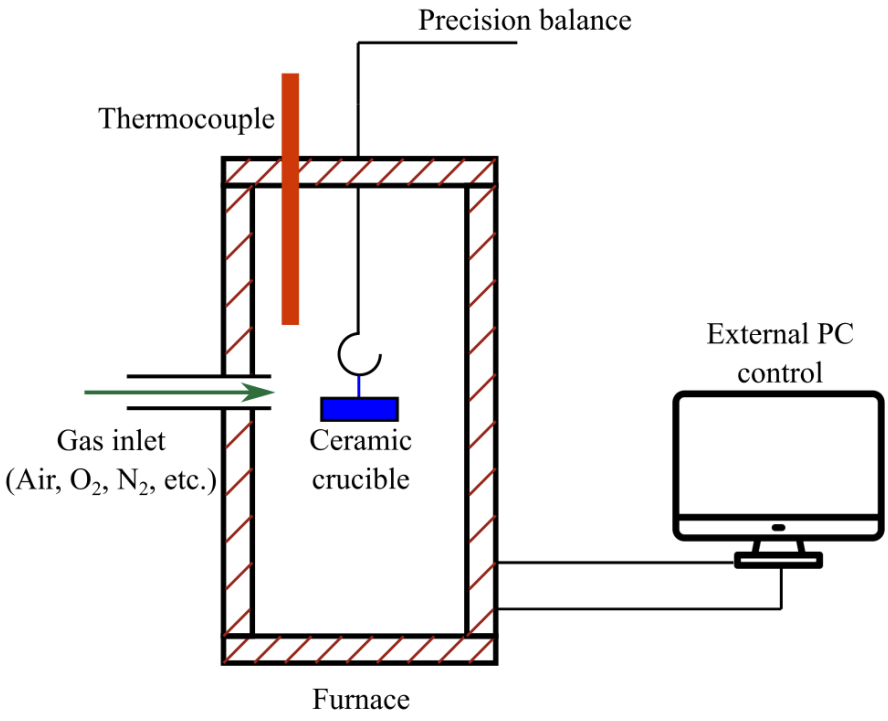


Figure 2.10: Schematic showing the working principles of TGA.

### 2.5.9 Mercury porosimetry

Mercury porosimetry is a destructive analytical technique, which can be used to study porous materials. It can be used to gain a wealth of information, including pore size and pore volume distribution, and thus is a very useful technique in the analysis of materials for both filtration and adsorption applications. Due to its exceptionally high surface tension, mercury is considered a non-wetting liquid for most solid materials. A non-wetting liquid can be described as one that creates a contact angle of 90-180° with a solid, as shown in Figure 2.11 in comparison with a wetting liquid, which creates a contact angle of less than 90°.[29]

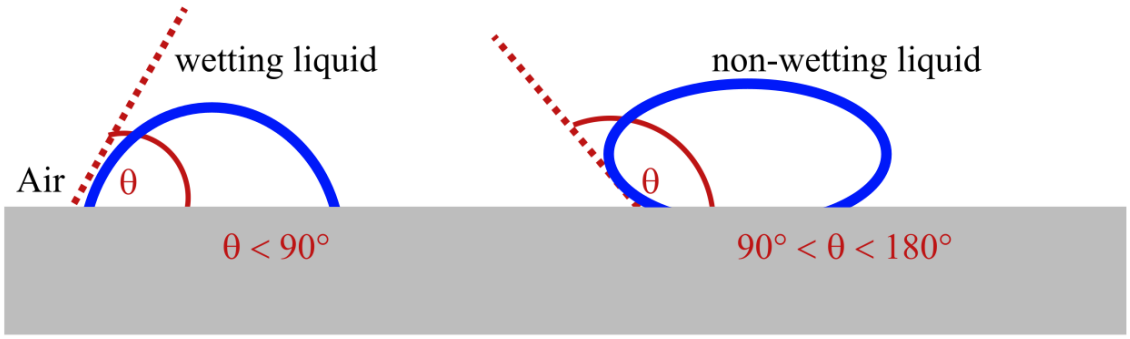


Figure 2.11: Wetting vs non-wetting liquids.

In essence, this means that mercury does not adhere to or spread across most solids. Instead, when it is contact with solids, it tends to bead up and form spherical droplets at the air-solid interface. Pressure can be used to force these droplets into small crevices, and gain information on their size, which is the working principle behind mercury porosimetry. Careful monitoring of the intrusion of mercury at different pressures allows for a pore size distribution to be determined. The pore size is inversely proportional to the applied pressure, i.e., higher pressure is required to force the mercury droplets into smaller pores, thus allowing the pore diameters and total pore volume to be estimated using this technique.[30]

Mercury porosimetry was performed in this work by Dr. Aran Rafferty, using an Autoscan-33 Porosimeter (Quantachrome, Hampshire, UK).

### 2.5.10 Zeta potentiometry

Zeta potentiometry is a non-destructive analytical technique that is commonly employed in materials research to investigate the surface charge of nanoparticles. However, the technique does not directly measure the surface charge of the particle, but instead measures the potential difference across the electrical double layer. When particles are

dispersed in a solvent, they can acquire a surface charge. This electric charge can arise for various reasons, including adsorption of ions from the surrounding medium, or indeed from ionisation of surface groups on the material. This phenomenon results in the formation of an electrical double layer surrounding the particle, consisting of an inner (Stern) layer and an outer (diffuse) layer, as shown in Figure 2.12.

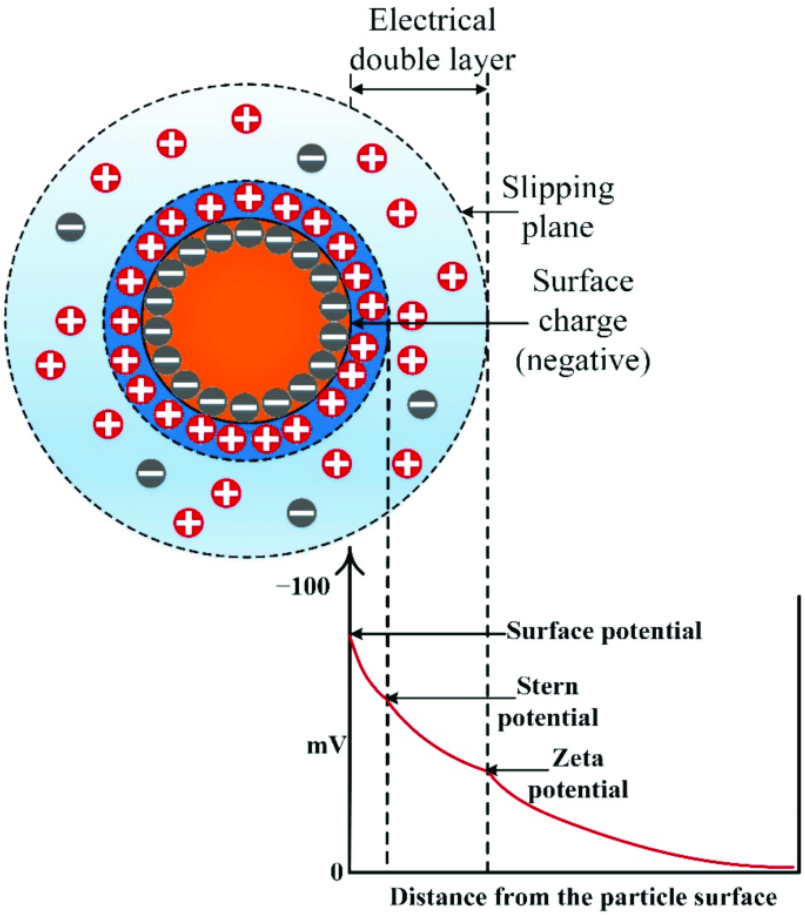


Figure 2.12: Schematic of the formation of an electrical double layer on a negatively charged nanoparticle in solution, as well as the relationship between the surface potential and zeta potential.[31]

The Stern layer resides closest to the NP surface and consists of a tightly bound ionic layer directly surrounding the particle. The ions in the Stern layer are considered to be essentially adsorbed to the particle surface, and thus move with the particle through the solution. The outer portion of the electrical double layer is called the diffuse layer, and

as the name suggests, consists of ions that are weakly bound to the particle. Both layers contribute to the zeta potential ($\zeta$), and $\zeta$ is typically defined as the electric potential at the interface of the electrical double layer and the dispersion medium.[32]

Aside from the sign of $\zeta$, i.e., whether it is positive or negative, the absolute value of $\zeta$ is also a useful measure in terms of the stability of a colloidal dispersion, and how resistant it is to flocculation or aggregation. Stability of colloidal suspensions are a result of electrostatic repulsion between individual particles, and thus, the higher the $|\zeta|$ value, the more stable the colloid. In numerical terms, generally any nanoparticle colloid that exhibits a value of $|\zeta| > 30$ mV is considered to be highly stable. A $|\zeta|$ value between 15-30 mV means the particles are partially stable, and may agglomerate, whereas a $|\zeta|$ value of $< 15$ mV means the colloid has low stability and is highly likely to aggregate.[33]

In practice, zeta potentiometry works by applying an electric field to a colloidal suspension, which causes the charged particles to move in response to the electric field. At the same time, a laser beam is directed through the sample, and detectors monitor the light scattered by the NPs in the colloidal suspension. The velocity of the particles can then be calculated by quantifying the Doppler shift in the scattered light, according to Equation 2.23.

$$v = c\frac{\Delta\lambda}{\lambda_0} \tag{2.23}$$

where:

$v$ is the velocity of the particle under the influence of the electric field,

$c$ is the speed of light,

$\delta\lambda$ is the wavelength shift, and

$\lambda_0$ is the wavelength of the light source.

Once $v$ is known, this allows for the electrophoretic mobility ($\mu_E$) to be calculated, according to Equation 2.24:

$$\mu_E = \frac{v}{E} \tag{2.24}$$

where $E$ is the electric field strength. Finally, $\zeta$ can be calculated from $\mu_E$ according to the Smoluchowski relation, as shown in Equation 2.25.[34]

$$\zeta = \frac{\eta \mu_E}{\epsilon} \tag{2.25}$$

where:

$\eta$ is the viscosity of the colloid, and

$\epsilon$ is the dielectric constant.

Zeta potential measurements were carried out using a Malvern Panalytical Zetasizer and disposable folded capillary zeta cells.

# References


(1) Berner, S.; Araya, P.; Govan, J.; Palza, H. *Journal of Industrial and Engineering Chemistry* **2018**, *59*, 134–140.

(2) Palza, H.; Delgado, K.; Govan, J. *Applied Clay Science* **2019**, *183*, 105350.

(3) Crank, J., *The mathematics of diffusion*, 2nd edition; Clarendon Press: Oxford, UK, 1975.

(4) Boyd, G. E.; Adamson, A. W.; Myers, L. S. *Journal of the American Chemical Society* **1947**, *69*, 2836–2848.

(5) Weber Jr., W. J.; Morris, J. C. *Journal of the Sanitary Engineering Division* **1963**, *89*, 31–59.

(6) McKay, G.; Otterburn, M. S.; Sweeney, A. G. *Water Research* **1980**, *14*, 15–20.

(7) Chen, Y.; Bao, Y.; Wang, X. *Journal of Fluorescence* **2016**, *26*, 813–820.

(8) Mamouei, M.; Budidha, K.; Baishya, N.; Qassem, M.; Kyriacou, P. A. *Scientific Reports* **2021**, *11*, 1–9.

(9) Van de Hulst, H. C., *Light Scattering by Small Particles (Dover Books on Physics)*, 2nd ed.; Dover Publications: 1981, p 496.

(10) Harvey, A.; Backes, C.; Boland, J. B.; He, X.; Griffin, A.; Szydlowska, B.; Gabbett, C.; Donegan, J. F.; Coleman, J. N. *Nature Communications* **2018**, *9*, 1–11.

(11) Básaca, L. C.; Rodríguez, J.; Sergiyenko, O. Y.; Tyrsa, V. V.; Hernández, W.; Hipólito, J. I.; Starostenko, O. *IEEE International Symposium on Industrial Electronics* **2010**, 1773–1778.

(12) Jacquez, J. A.; Kuppenheim, H. F. *Journal of the Optical Society of America* **1955**, *45*, 460–470.

(13) Rodger, A.; Nordén, B., *Circular dichroism and linear dichroism*; Oxford University Press: Oxford, UK, 1997, p 150.

(14) Circular Dichroism Spectroscopy - JASCO `https://jascoinc.com/learning-center/theory/spectroscopy/circular-dichroism-spectroscopy/` (accessed 10/12/2023).

(15) Paul, J.; Siegmann, K. *Chemical Physics Letters* **1999**, *304*, 23–27.

(16) Gui, L.; Hentschel, M.; Defrance, J.; Krauth, J.; Weiss, T.; Giessen, H. *ACS Photonics* **2019**, *6*, 3306–3314.

(17) Jablonski Diagram — What is it? — Edinburgh Instruments `https://www.edinst.com/us/blog/jablonski-diagram-2/` (accessed 11/25/2023).

(18) Stokes shift diagram - Wikimedia Commons (cepheiden) `https://commons.wikimedia.org/wiki/File:Stokes-Verschiebung.svg` (accessed 11/25/2023).

(19) Hasegawa, T. In *Quantitative Infrared Spectroscopy for Understanding of a Condensed Matter*; Springer: Tokyo, Japan, 2017, pp 37–46.

(20) Difference IR vs FTIR — Bruker `https://www.bruker.com/en/products-and-solutions/infrared-and-raman/ft-ir-routine-spectrometer/what-is-ft-ir-spectroscopy/difference-ir-vs-ftir.html` (accessed 11/25/2023).

(21) Bragg law — Definition, Equation, Diagram, Facts — Britannica `https://www.britannica.com/science/Bragg-law` (accessed 11/25/2023).

(22) Cline, J. P.; Mendenhall, M. H.; Black, D.; Windover, D.; Henins, A. *Journal of Research of the National Institute of Standards and Technology* **2015**, *120*, 173–222.

(23) SEM Signal - Electron Imaging - Advancing Materials https://www.thermofisher.com/blog/materials/sem-signal-types-electrons-and-the-information-they-provide/ (accessed 10/12/2023).

(24) Scanning Electron Microscopy - Nanoscience Instruments https://www.nanoscience.com/techniques/scanning-electron-microscopy/ (accessed 10/12/2023).

(25) Scanning Transmission Electron Microscopy - Nanoscience Instruments https://www.nanoscience.com/techniques/scanning-transmission-electron-microscopy/ (accessed 10/12/2023).

(26) high-angle annular dark-field scanning transmission electron microscopy, HAADF-STEM — Glossary — JEOL Ltd. https://www.jeol.com/words/emterms/20121023.031059.php#gsc.tab=0 (accessed 10/12/2023).

(27) Senga, R.; Suenaga, K. *Nature Communications* **2015**, *6*, 1–6.

(28) Prime, R. B.; Bair, H. E.; Vyazovkin, S.; Gallagher, P. K.; Riga, A. In *Thermal Analysis of Polymers: Fundamentals and Applications*; John Wiley Sons, Ltd: Hoboken, NJ, USA, 2008, pp 241–317.

(29) Karmakov, I. *Physics Education* **2000**, *35*, 435.

(30) Allen, T. In *Particle Size Measurement*; Springer: Dordrecht, Netherlands, 1990, pp 653–681.

(31) Sujith, S. V.; Kim, H.; Lee, J. *Metals* **2022**, *12*, 165.

(32) Hunter, R. J. In *Zeta Potential in Colloid Science: Principles and Applications*; Academic Press: Cambridge, MA, USA, 1981, pp 360–361.

(33) Carone, A.; Emilsson, S.; Mariani, P.; Désert, A.; Parola, S. *Nanoscale Advances* **2023**, *5*, 2017–2026.

(34) Sze, A.; Erickson, D.; Ren, L.; Li, D. *Journal of Colloid and Interface Science* **2003**, *261*, 402–410.

# Chapter 3

# Layered Double Hydroxide-Derived Chiroptically Active 2D Nanostructures

## 3.1 Introduction

The area of chiral inorganic nanostructures has experienced a huge surge in interest in recent years, and can be tracked back to 2007, the year in which Moloney *et al.* reported the first ever chiral quantum dot (Figure 3.1).[1] In the years since, much research has focused on the development of novel chiral inorganic nanostructures, due to their interesting properties and the abundance of potential applications, including as chiral sensors, catalysts, and metamaterials in advanced optical devices.[2–4] This area of research has focused on chirality induction in a wide variety of inorganic materials, such as spherical quantum dots, nanowires, tetrapods, and nanoflowers, among others.[1,5,6]

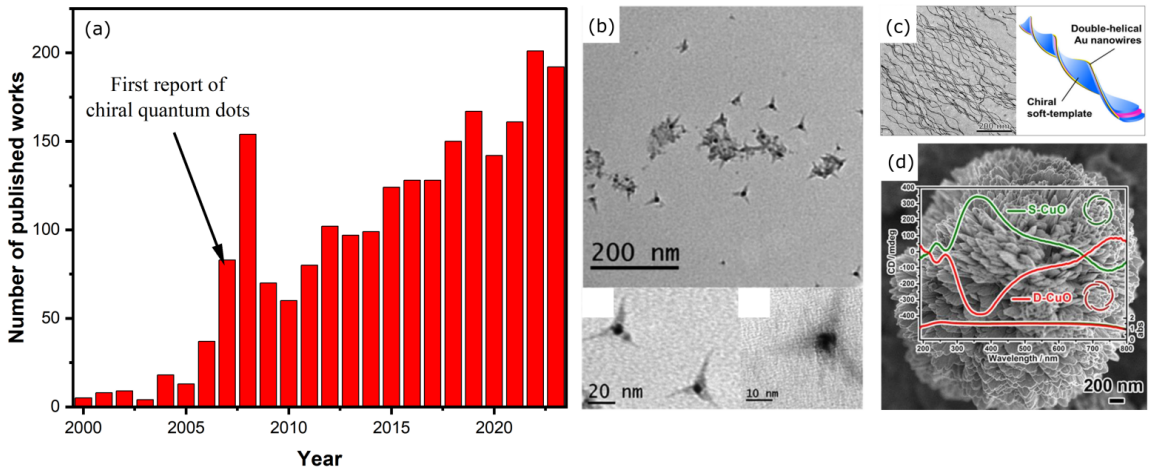


Figure 3.1: (a) Number of publications on chiral nanomaterials from 2000-2023. Data obtained from Scopus. (b-d) Various reported chiral inorganic nanostructures, including (b) tetrapods, (c) helical nanowires, and (d) nanoflowers.[5,7,8]

However, research on chiral 2D nanomaterials and their applications is still in the very early stages. This is despite the fact that these materials are expected to demonstrate unique properties due to their high aspect ratio, special electronic confinement and specific structural deformations of 2D nanosheets.[9] While there are several reports of chirality induction in 2D perovskites, research into other chiral 2D nanomaterials is limited.[10–13] For example, there is only one report on chiral graphene-based quantum dots, and one recent publication on the preparation of chiral 2D transition metal dichalcogenide (TMD) nanomaterials.[14,15] Induction of chirality in these colloidal 2D nanostructures can, in theory, be achieved by synthesis with the chiral ligand present *in situ*, or by relatively straightforward post-synthetic ligand exchange reactions, replacing the achiral species with the chiral molecule of choice.[16–18] It is anticipated that these chiral 2D nanomaterials may find applications in exciting and rapidly developing research areas such as biotechnology and nanomedicine, as chirality plays an integral role in chemical and biological recognition.[19]

Research on layered double hydroxides (LDHs) has experienced somewhat of a resurgence in recent years, due to the unique tunable properties, and ease of synthesis of

these materials, which gives rise to a vast number of applications, ranging from biomedical to catalysis.[20,21] In particular, LDHs are most commonly known for their anion exchange properties, which serves as the basis of many of their applications, particularly in energy storage and drug delivery.[22–24] This property means that they can host a wide variety of species in the interlayer spacing, including chiral molecules. However, despite the huge amount of research surrounding anion exchange in LDHs, the potential for induction of chirality in these materials, the effect of chiral ligands on LDH phase and structure, as well as subsequent circular dichroism studies, has not been explored to date.

Chiral copper oxide-based materials have been previously shown to find potential interesting applications in photonics (specifically nonlinear optics) and in medicine (e.g., the treatment of Parkinson's disease).[25,26] Based on these prospects, it is therefore worthwhile to explore new methods of synthesizing chiral metal oxides. While a small number of reports on the formation of chiral cupric and cuprous oxides do exist in the literature, they require elevated temperatures, in particular hydrothermal reaction conditions, to induce the transformation of copper hydroxide ($Cu(OH)_2$) to the oxide. Furthermore, additional surfactants and expensive symmetry-breaking agents have previously been required to achieve visible range chiroptical activity.[7,26]

## 3.2 Aims of this work

The main aim of this body of work was to develop new 2D chiroptically active nanostructures by induction of chirality in layered double hydroxides. In order to achieve this goal, the first step was the synthesis of carbonate-intercalated copper aluminium layered double hydroxide nanosheets using a room-temperature co-precipitation approach. The

resultant materials were characterised *via* pXRD, FT-IR, UV-Vis, TGA, and TEM to confirm the phase, chemical composition and morphology. We then planned to explore chirality induction in this material in two ways - the first by modifying the co-precipitation approach to include chiral ligands, and the second *via* post-synthetic treatment with chiral molecules. We aimed to prove the successful interaction of the chiral ligand with the layered double hydroxide using UV-Vis, pXRD and FT-IR studies. Furthermore, we aimed to analyse the induction of optical activity using CD, and to examine potential structural or 'macroscale' chirality using SEM and TEM.

## 3.3 Results and discussion

### 3.3.1 Synthesis of CuAl LDHs via co-precipitation

CuAl-$CO_3$ LDHs were synthesized *via* a modified and scaled-up version of the co-precipitation approach previously reported by Berner *et al.* as described in the Materials and Methods chapter.[27] Briefly, this synthetic procedure involved the dropwise addition of $Cu^{2+}$ and $Al^{3+}$ metal salts to a $Na_2CO_3$ solution, followed by a 24h ageing period. The mixture was kept at a pH of 10 throughout by the addition of 1M NaOH as required. The resultant material had a pale blue colour, which was consistent with previous reports in literature. Initially, pXRD was carried out on the resulting material, to confirm the formation of the LDH crystal structure, as shown in Figure 3.2. The most prominent diffraction peaks can be matched to the monoclinic phase of CuAl carbonate hydrotalcite (PDF 46-0099), with space group P2/m, confirming the successful formation of CuAl LDH. A monoclinic crystal structure is formed, as opposed to the more typical rhomohedral symmetry observed for LDHs, as a result of the formation of distorted $Cu(OH)_2$ octahedra due to the Jahn-Teller

effect of $Cu^{2+}$, as has been reported elsewhere.[27–30] The most notable reflections in the pXRD pattern are the (003), (006), and (009) reflections at $2\theta = 11.7°$, $23.5°$, and $35.2°$, respectively, representative of the formation of a hydrotalcite-like phase.[31] The reference pattern corresponds to a LDH structure with a Cu:Al ratio of 2.5:2, therefore the broad, low intensity feature situated between the (003) and (006) reflections may be due to the formation of amorphous aluminium-containing side products, as a result of the 1:1 molar ratio of $Cu^{2+}$:$Al^{3+}$ used in the synthesis. Furthermore, a $d_{(003)}$ basal spacing value of 7.55 Å was calculated, which is the expected value for a carbonate-intercalated CuAl LDH (CuAl-$CO_3$ LDH).[31]

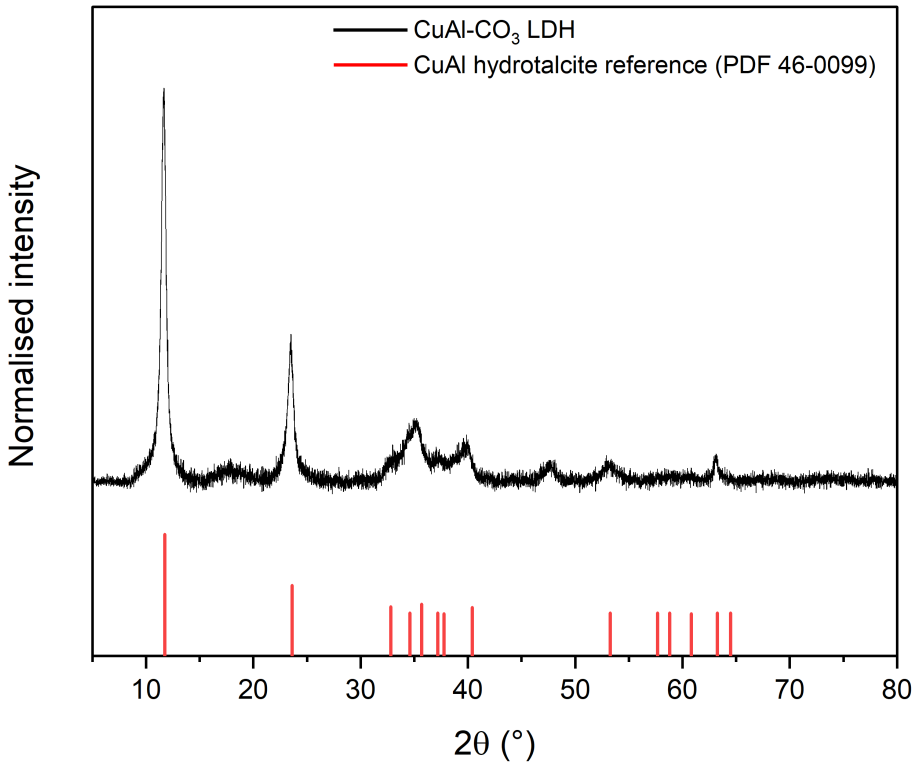


Figure 3.2: pXRD pattern of as-prepared CuAl-$CO_3$ LDH. Reference pattern of CuAl hydrotalcite is shown in red.

FT-IR analysis was also performed on the material, and a number of characteristic peaks are present which confirm the formation of CuAl-$CO_3$ LDHs, as shown in Figure 3.3. The most prominent bands present in the FT-IR spectrum are the hydroxyl band at 3400 $cm^{-1}$, which is indicative of O-H stretches within the metal hydroxide sheets, and the low-frequency bands at 680 and 440 $cm^{-1}$, which arise from vibrations of metal–oxygen bonds within the layers. Two further bands in the FTIR spectrum provide evidence on the intercalating species. The $v_3$ and $v_2$ vibrations of the carbonate anion are present at 1350 and 820 $cm^{-1}$, respectively, further supporting the formation of CuAl-$CO_3$ LDH.[32]

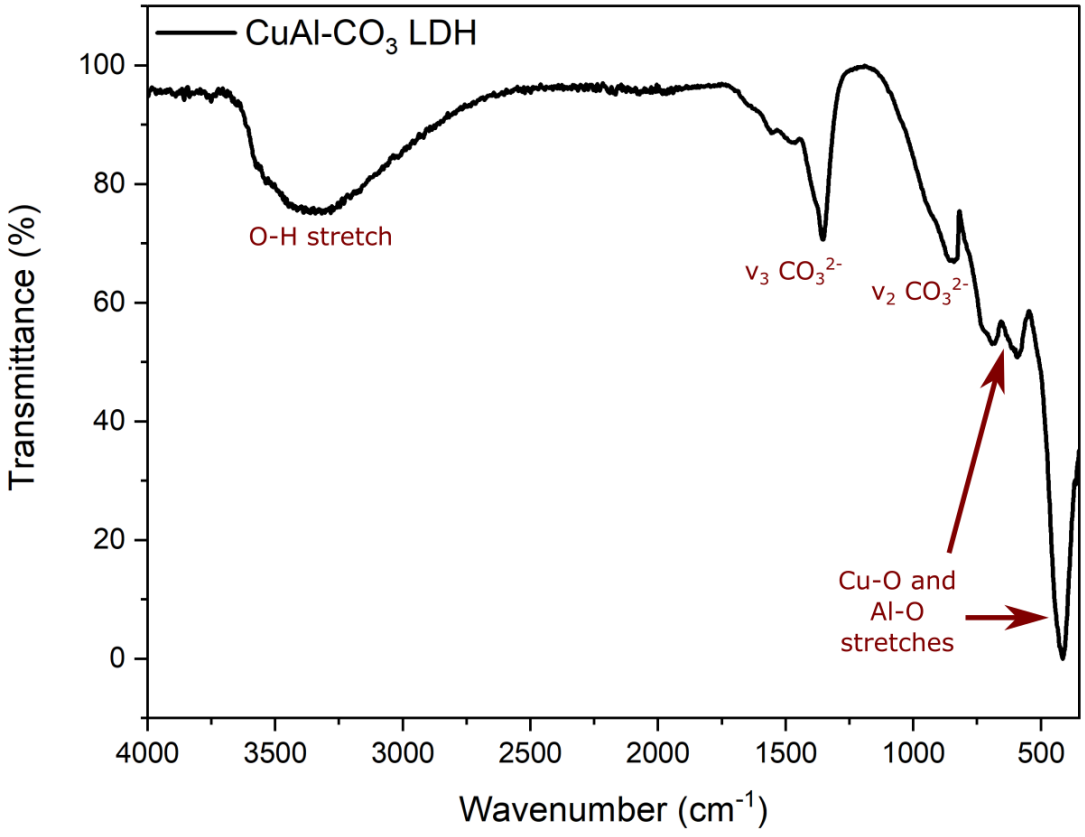


Figure 3.3: FT-IR spectrum of as-synthesised CuAl LDH.

Standard, liquid-phase UV-Vis spectroscopic studies were also performed on the sample in an ethanol dispersion, as shown in Figure 3.4 (a). The UV-Vis spectrum depicts

a broad, featureless absorption profile. However, the prominent blue colour of the product indicated that there should be an absorption band in the red region of the visible spectrum. It is likely that the absorption features were masked by strong scattering effects, which is characteristic of nanosheets in colloidal dispersions. Therefore, it was decided to conduct diffuse-reflectance (DR) UV-Vis on a solid sample of the material, as shown in Figure 3.4 (b). DR UV-Vis allows for scattering contributions to the extinction spectra to be subtracted, and the resultant spectrum is a more accurate depiction of the true absorption profile.

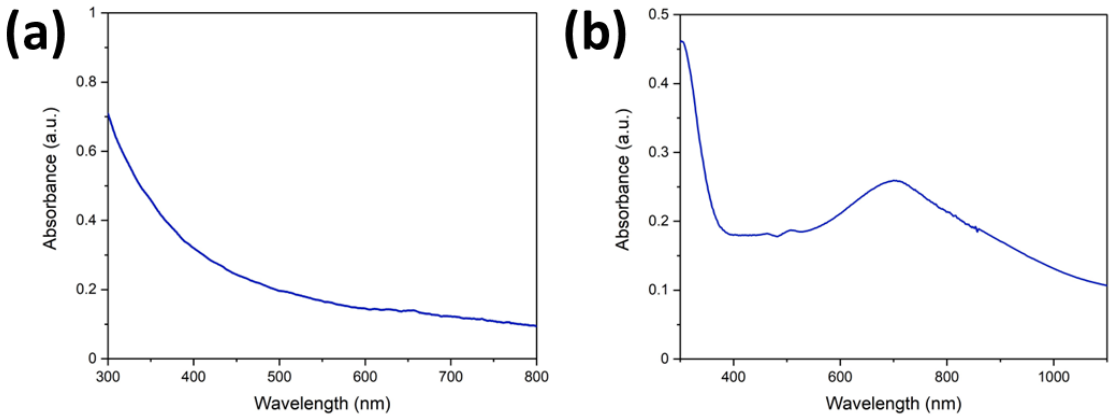


Figure 3.4: a) (a) Standard liquid-phase UV-Vis absorbance spectrum acquired using ethanol as solvent, and (b) solid-state DR UV-Vis spectrum of CuAl-$CO_3$ LDH.

The DR UV-Vis reveals an absorption profile indicative of the formation of CuAl-$CO_3$ LDH, with several distinct bands due to the presence of $Cu^{2+}$. The two main absorption features appear at roughly 475 and 700 nm. These bands can be assigned to $O^{2-}$ to $Cu^{2+}$ ligand to metal charge transfer (LMCT) and $Cu^{2+}$ $d-d$ transitions, respectively. The strong absorption band approaching 300 nm can be attributed to the microscope slide used as solid support (Appendix B, Figure B1).[33,34]

Thermogravimetric analysis (TGA) was also conducted on the sample, to assess the thermal stability of the material, and ensure that the drying step at 70 °C has no significant impact on the product. The TGA and differential TGA curves are shown in Figure 3.5.

Initially, a small amount of mass is lost ($< 2\%$) due to removal of surface adsorbed water. After this initial dehydration step, there are three main stages of mass loss that can be identified in the TGA curve. Stage 1, which has an onset at 148 °C, can be attributed to water loss from the LDH interlayer spacing. This step occurs at a temperature higher than the boiling point of water due to stabilisation by being trappped in the LDH interlayer. Roughly 13% of the LDH mass is lost during this phase. Complete thermal stability of the LDH up to a temperature of 148 °C therefore confirms that the drying step has no effect on the synthesised material.

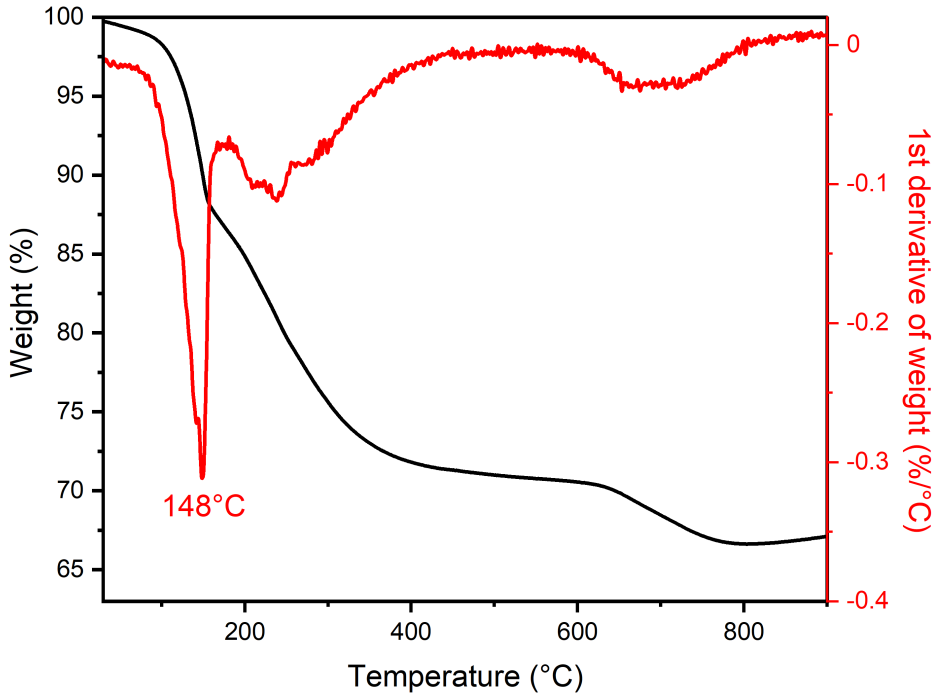


Figure 3.5: TGA (black) and differential TGA (red) curves of CuAl LDH acquired in air.

Stage 2, occurring between 200-550°C, can be attributed to dehydroxylation of the LDH sheets, and destruction of the LDH structure to form amorphous mixed metal oxides. Stage 3, the final stage, occurs between 550-800°C, and can be attributed to decomposition

of the carbonate anions which were present in the interlayer of the LDH.[35]

After initial characterisation confirmed the phase of the material, TEM was conducted on the CuAl-$CO_3$ LDH by Dr. Finn Purcell-Milton to examine the morphology. More specifically, this was to confirm the formation of LDH nanosheets, rather than bulk LDH, which can sometimes occur under mild co-precipitation conditions such as those presented here. TEM and STEM imaging both confirm the formation of LDH nanosheets, with an average lateral size of 126 $\pm$ 37 nm, as shown in Figure 3.6. The microscopy images clearly depict a material with a 2D nanosheet morphology, with some nanosheets observed to be folding or scrolling, which is a common consequence of drying effects on TEM grids. The size distribution analysis can be found in Appendix B (Figure B2).

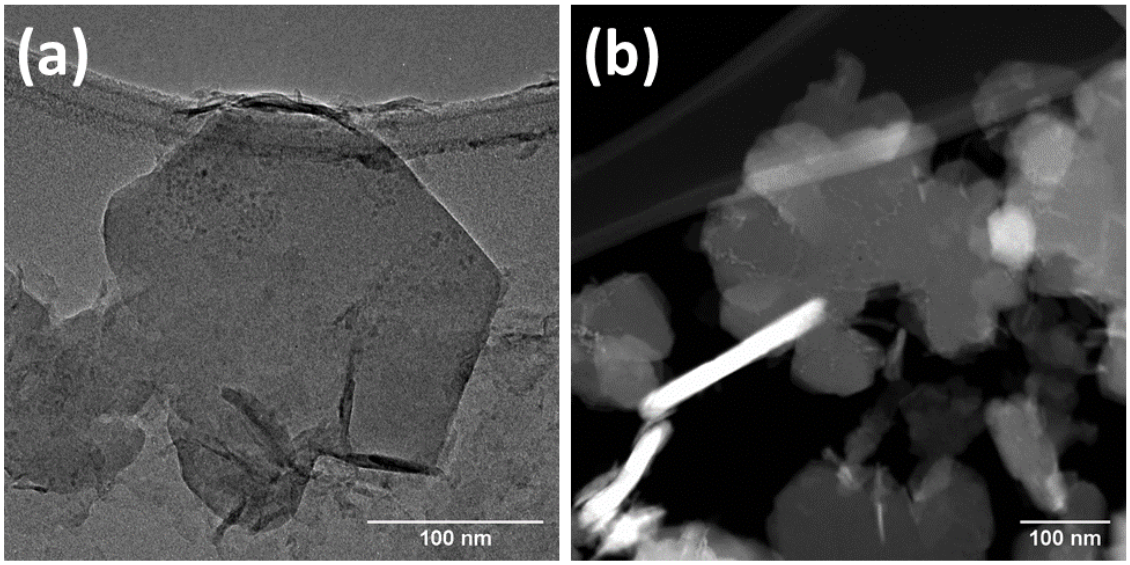


Figure 3.6: (a) TEM and (b) HAADF-STEM images of CuAl-$CO_3$ LDHs nanosheets prepared *via* co-precipitation.

Therefore, the thorough characterisation of the as-synthesised material *via* pXRD, FT-IR, TGA, UV-Vis and TEM confirms the successful formation of CuAl-$CO_3$ LDH nanosheets *via* the co-precipitation approach.

### 3.3.2 Chiroptically active LDH-derived nanostructures via modified co-precipitation

Following successful formation of CuAl-$CO_3$ LDHs *via* the co-precipitation approach, it was decided to modify the procedure by using chiral molecules in place of $Na_2CO_3$ as the intercalating agent, to investigate if chirality induction was possible by introducing chiral molecules into the interlayer spacing *in situ*. While a number of reports exist on the incorporation of chiral molecules into the LDH interlamellar space, to the best of our knowledge no reports of the chirality transfer from a chiral molecule to the LDH structure in the literature. In studies where chiral molecules were successfully intercalated into the LDH interlayer space, researchers typically used circular dichroism (CD) or vibrational CD to confirm the presence of the chiral molecule, but no chirality transfer from the organic molecule to the inorganic LDH matrix was observed.[36–38] Induction of chirality in nanomaterials, particularly the induction of chiroptical activity, is most commonly investigated by CD spectroscopy. An obvious sign of induction of chirality in a nanomaterial would be the appearance of new CD bands across the UV-Visible spectrum, distinct from that of the chirality inducing agent (i.e. chiral molecules).

For this initial study of chirality induction in CuAl LDHs, phenylalanine (Phe) and dibenzoyl tartaric acid (DBTA) were chosen as candidates. The structures of these molecules are shown in Figure 3.7 with stars indicating the stereocentres in each of the molecules. Phe, like all amino acids, is zwitterionic. When dissolved in water, the amino acid group is protonated, and the carboxylic acid group is deprotonated, leading to a molecule with positively and negatively charged functional groups, but the overall molecule remains charge neutral.[39] As Phe has a $pK_a$ of 2.2, and an isoelectric point ($pI$) of 5.48, then under basic conditions, a large proportion of the molecules in solution exist with the carboxyl group in deprotonated form, leading to an overall negative charge on the molecule.[40] Additionally,

DBTA is a diprotic acid, with predicted $pK_{a1}$ and $pKa_{a2}$ of - 6.6 and 2.8 respectively.[41] Therefore, a DBTA solution should consist of mostly deprotonated and, thus, negatively charged molecules at pH 10, which is the pH condition under which the LDHs are formed in this work. When molecules with an overall negative charge are accommodated in the LDH interlayer space, this typically leads to more stable nanostructures, as they counteract the positive charge of the LDH nanosheets. Therefore, it was decided to proceed with the modified co-precipitation approach, as described in the Materials and Methods sections 2.2.2 and 2.2.3.

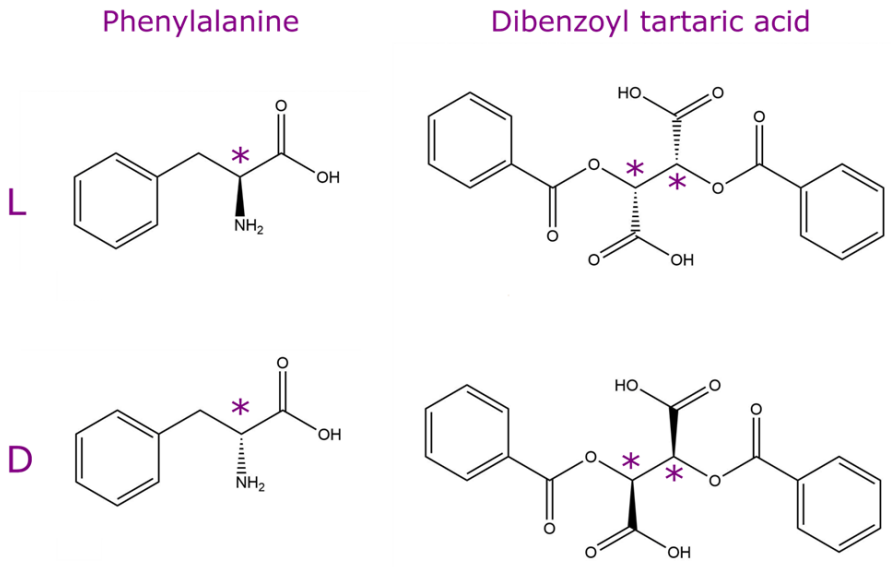


Figure 3.7: Structures of enantiomers of phenylalanine (left) and dibenzoyl tartaric acid (right).

CD spectroscopic studies were conducted to investigate potential chirality induction in the LDHs by the intercalation of chiral molecules. As shown in Figure 3.8, it is evident that chiroptical activity has indeed been induced in both cases. For both Phe and DBTA modification, the CD signal covers a wide wavelength range, spanning from the UV to the onset of the NIR region of the electromagnetic spectrum. Furthermore, the observed signals are completely distinct from that of Phe and DBTA molecules, which is a strong indicator

of ligand-induced chirality in the material (see Appendix B, Figure B3-B4). In addition, mirror images of the CD spectra are obtained when functionalisation is carried out with the opposite enantiomer, and Cotton effects are present, with the CD signals alternating between positive and negative values.[42]

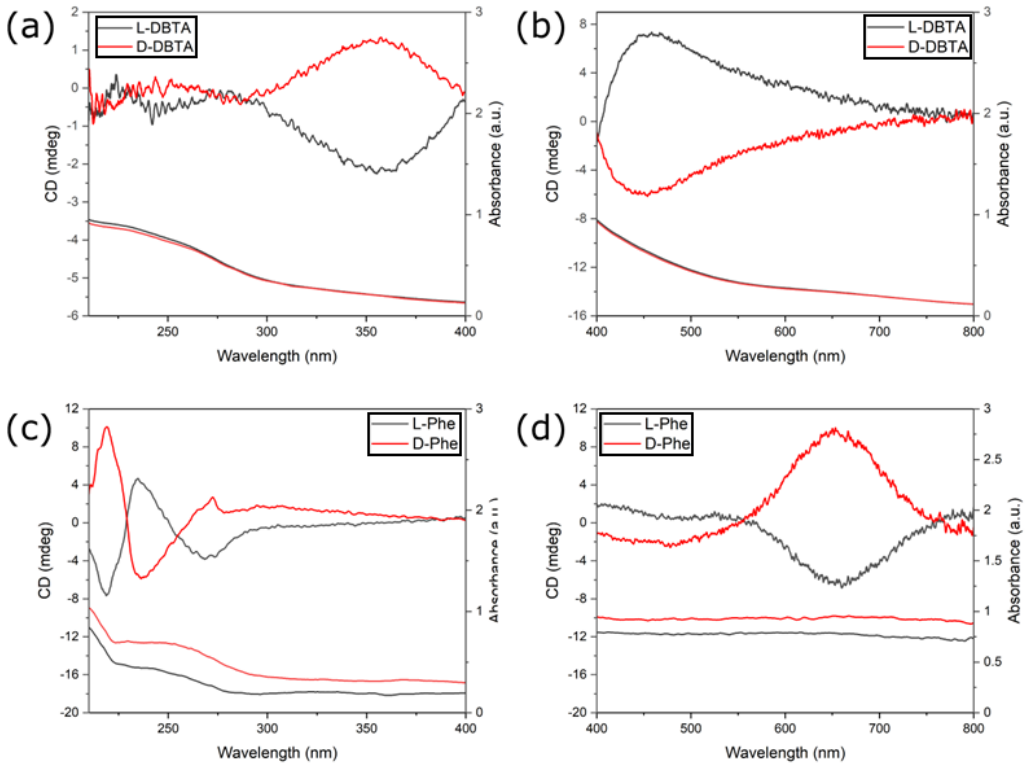


Figure 3.8: CD and UV-Vis absorption spectra of products of (a,b) L-DBTA and (c,d) L-Phe-modified CuAl LDH co-precipitation reaction. Spectra were acquired using ethanol as solvent.

However, it is important to note the CD signal in both Phe-LDH and DBTA-LDH samples were much weaker in the 400-800 nm region, requiring much higher concentrations of samples for analysis, due to the low absorbance of the material in that region of the spectrum. To allow for analysis of the CD response in the full 210-800 nm region, the anisotropy *g*-factor spectrum was generated for the DBTA-modified product, which allows us to evaluate the intrinsic chirality of the product (Figure 3.9).

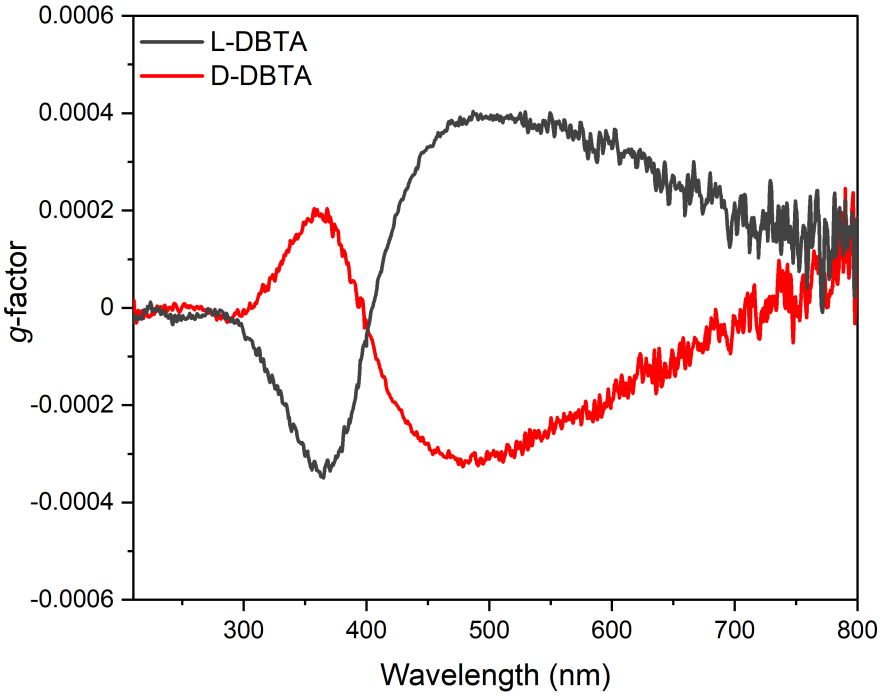


Figure 3.9: *g*-factor spectra of products of DBTA-modified CuAl LDH co-precipitation reaction.

Maximum *g*-factor values of -3.5 x $10^{-4}$ at 360 nm, and 4 x $10^{-4}$ at 480 nm were obtained in the case of the L-DBTA-LDH sample, which is in within the expected range for nanomaterials exhibiting ligand-induced chirality.[4] However, a significant degree of scattering was observed in the Phe-LDH samples, as shown in Figure 3.8 (d), which complicated the interpretation of the results. As the contribution of light-scattering on CD spectra is poorly understood, and the *g*-factor calculation is based on absorbance values, a reliable *g*-factor spectrum could not be obtained for the Phe-LDH product. Solid-state CD measurements would be required for more accurate *g*-factor measurements in this instance, which we did not have access to at the time of writing.

Subsequent to CD spectroscopic analysis, TEM and STEM were conducted by Dr. Finn Purcell-Milton on the resultant materials to examine their morphology, as shown in Figure 3.10.

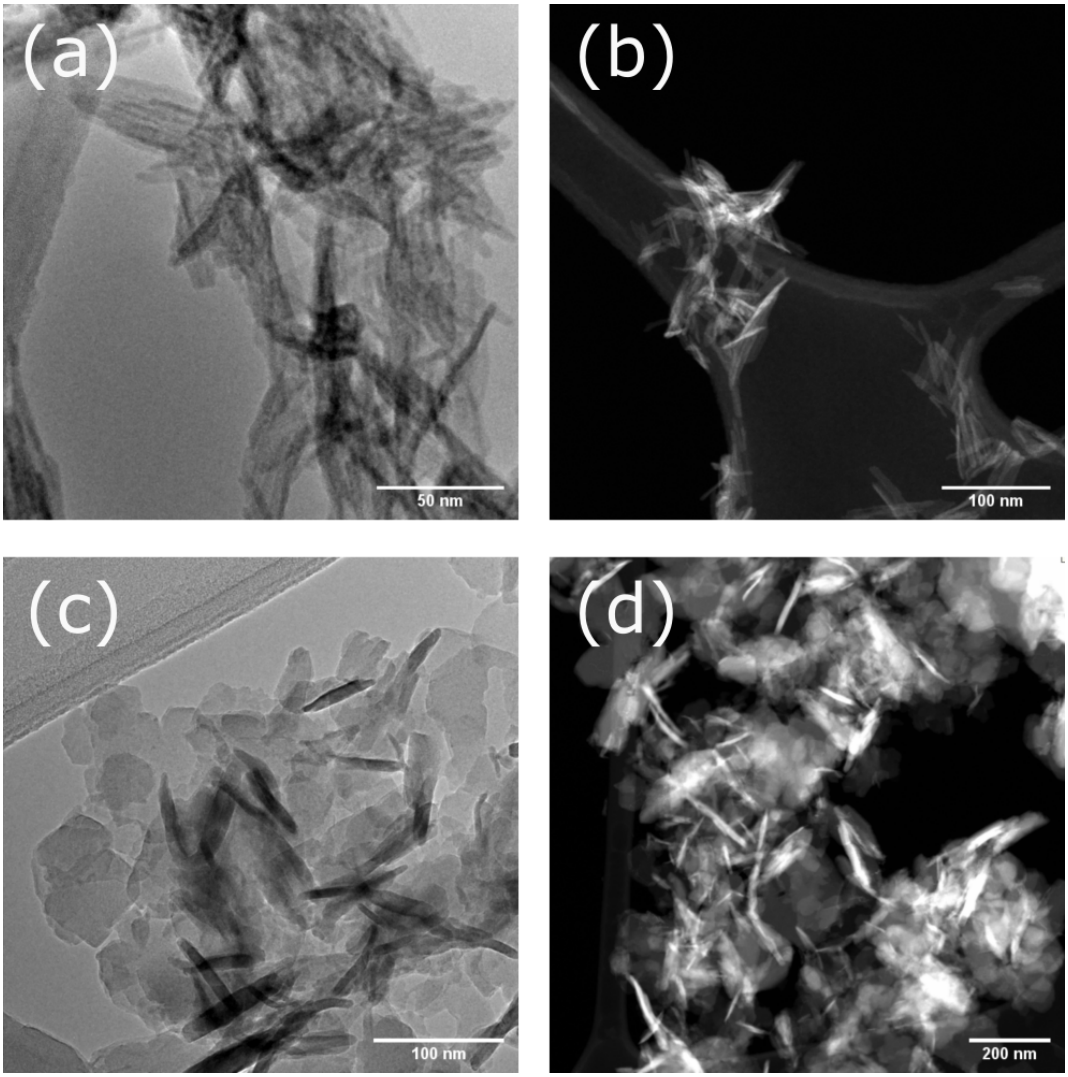


Figure 3.10: TEM (a,c) and STEM (b,d) images of L-Phe (a,b) and L-DBTA (c,d)-modified co-precipitation reaction products.

It can be observed that the products of the L-Phe modified co-precipitation reaction exhibit a needle or scroll-like morphology (Figure 3.10 (a,b)), in stark contrast to the nanoplate morphology exhibited by CuAl-$CO_3$ LDH. This distinct morphological transformation may be indicative of a change in phase. Furthermore, the nanoparticles resulting from the DBTA-modified co-precipitation, as shown in Figure 3.10 (c,d) are highly polydisperse and exhibit a number of shapes, including plates, and rod-like particles. This may be a sign that the reaction is producing a mixture of products. To investigate this

further, pXRD was conducted on both products, as shown in Figure 3.11.

One of the most straight-forward methods of detecting a change in the interlayer spacing of LDHs, as would be observed in the case of successful chiral molecule intercalation, is by monitoring the 2θ position of the (003) reflection. If the (003) reflection appears at lower values of 2θ than expected, this indicates an increase in the interlayer spacing. However, pXRD analysis of the resulting Phe-LDH and DBTA-LDH proved to be more complex than anticipated.

In the case of Phe-LDH (Figure 3.11 (a)), pXRD analysis revealed the unsuccessful formation of a hydrotalcite-like phase. The majority of the reflections in the pXRD pattern can be indexed to copper-phenylalanine (Cu-$(Phe)_2$), a chiral metal complex. Additionally, a low intensity CuAl LDH (003) diffraction peak is present at $2\theta = 11.7^{\circ}$. This is indicative of two competing reactions taking place - the first is the LDH co-precipitation, whereas the second is the metal complex precipitation, which has been reported elsewhere using similar reaction conditions to those used here.[43] It is clear that the metal complex formation dominates here. Therefore, while chiroptically active anisotropic nanostructures were indeed produced, they were a different species than expected.

A similar phenomenon was observed for the DBTA-LDH species, whereby a multicomponent mixture was produced, this time consisting primarily of copper oxide and copper hydroxide, as well as CuAl LDH. Furthermore, the products exhibited poor crystallinity, as evidenced by the broad peaks present in the pXRD pattern. Therefore, due to the low level of control of the modified co-precipitation reaction, evidenced by the side-reactions, coupled with the modest CD signals observed, it was decided to develop a new approach, as will be discussed in Section 3.3.3.

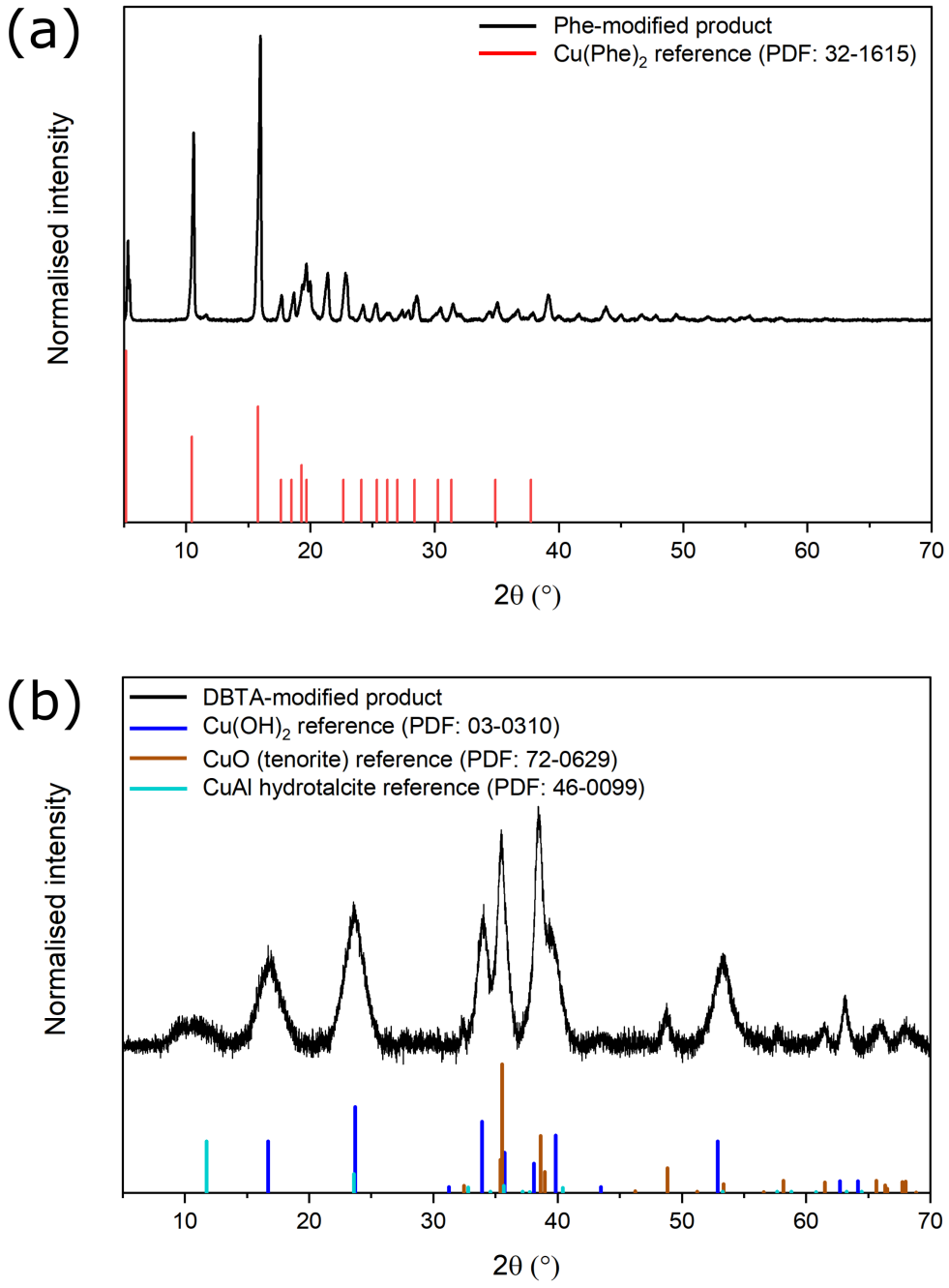


Figure 3.11: pXRD pattern of (a) L-Phe modified, and (b) L-DBTA modified co-precipitation reaction products. Reference patterns are provided for copper-L-phenylalanine (red), copper hydroxide (blue), copper oxide (brown) and copper aluminium layered double hydroxide (turquoise).

### 3.3.3 Preparation of chiroptically active LDH-derived CuO nanostructures via post-synthetic treatment

Due to the lack of synthetic control observed in the modified co-precipitation reaction, an alternative, post-synthetic treatment approach was developed. As-prepared CuAl LDHs (as discussed in Section 3.3.1) were treated with L- and D-Phe in the presence of NaOH. A gradual colour change from light blue to dark brown was observed, indicative of the formation of copper oxide species. pXRD was performed on the resultant samples to determine the phase of the resultant material, and it was confirmed that copper (II) oxide (CuO) was formed, as shown in Figure 3.12. From this point on, the L- and D-Phe modified products will be referred to as CuO-L-Phe, and CuO-D-Phe, respectively.

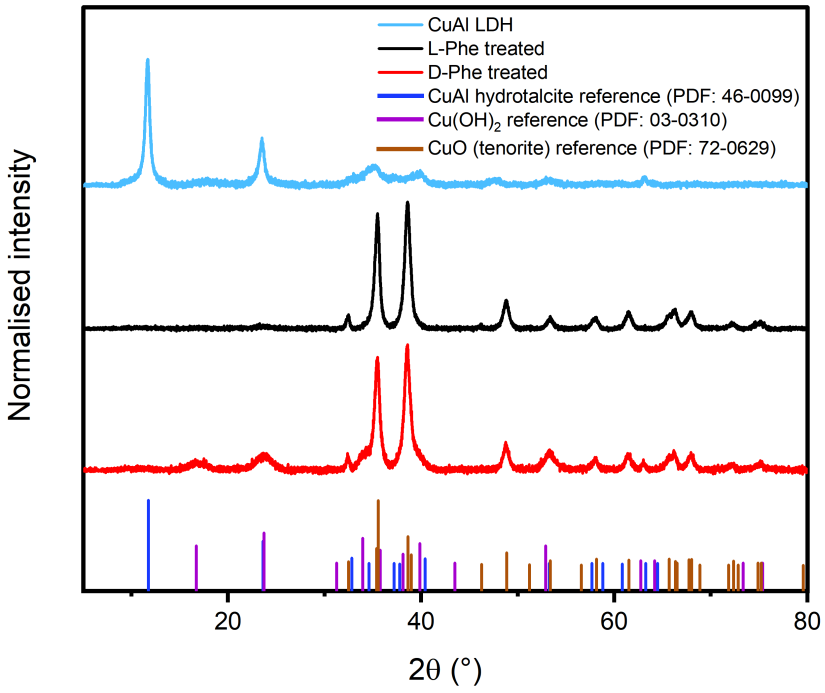


Figure 3.12: pXRD patterns of CuAl LDHs (light blue), CuO-L-Phe (black) and CuO-D-Phe (red). Reference pattenrs of CuAl hydrotalcite, $Cu(OH)_2$ amd CuO are given in dark blue, purple, and brown, respectively.

The pXRD analysis reveals a phase change from CuAl hydrotalcite to copper (II) oxide (CuO/tenorite) on reaction between LDH and L-/D-Phe. The diffraction peaks in both products can be indexed to the monoclinic tenorite (CuO) phase (PDF 80-0076, C2/c space group) as shown by the presence of the distinctive CuO (002) and (111) reflections at $2\theta = 35.6^{\circ}$ and $38.8^{\circ}$, respectively.[44] Two low-intensity reflections are also present in the pXRD patterns of the CuO-based materials corresponding to (020) ($2\theta = 16.7^{\circ}$) and (021) ($2\theta = 21^{\circ}$) reflections of $Cu(OH)_2$ (PDF 72-0140).[45] The presence of these reflections gives an insight into the mechanism of formation of CuO from CuAl-$CO_3$ LDH, which will be discussed in later sections.

FT-IR was also conducted on the resultant CuO materials to determine whether L- and D-Phe were present in the final product, as shown in Figure 3.13. The FT-IR spectra of CuO-L-Phe and CuO-D-Phe have some distinct differences from that of their CuAl-$CO_3$ LDH precursors. The disappearance of the 1350 $cm^{-1}$ band, previously assigned to $v_3$ $CO_3^{2-}$ vibrations, is observed, indicating the displacement or removal of carbonate anions from the LDH interlayer. The appearance of new vibrational bands around 3500 $cm^{-1}$, which can be assigned as N–H stretches, are indicative of the presence of the phenylalanine ligands in the final product.[46]

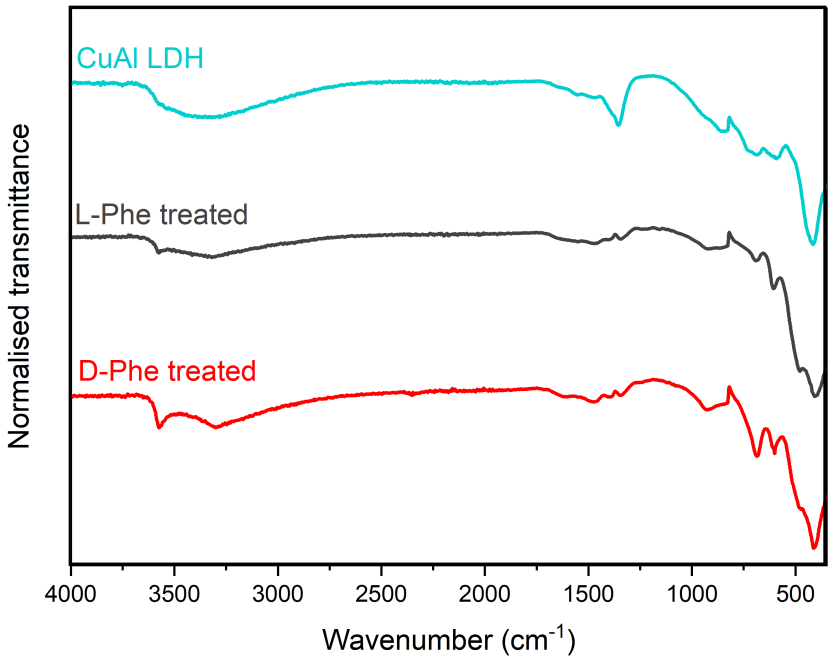


Figure 3.13: FT-IR spectra of CuAl LDH (blue), CuO-L-Phe (black) and CuO-D-Phe (red).

Once it had been confirmed that Phe was present in the final product, CD spectroscopy was once again conducted to determine whether the presence of Phe upon degradation of CuAl-$CO_3$ LDH to CuO had the effect of inducing chirality in the material. As can be observed from the CD spectra in Figure 3.14, it is evident that this post-synthetic approach was successful in inducing chirality and, more specifically, chiroptical activity. The observed CD spectra of the resultant materials are very distinct from those of phenylalanine and extend far beyond the range of signal that would be observed by the initial chiral molecule itself (Appendix B, Figure B3).

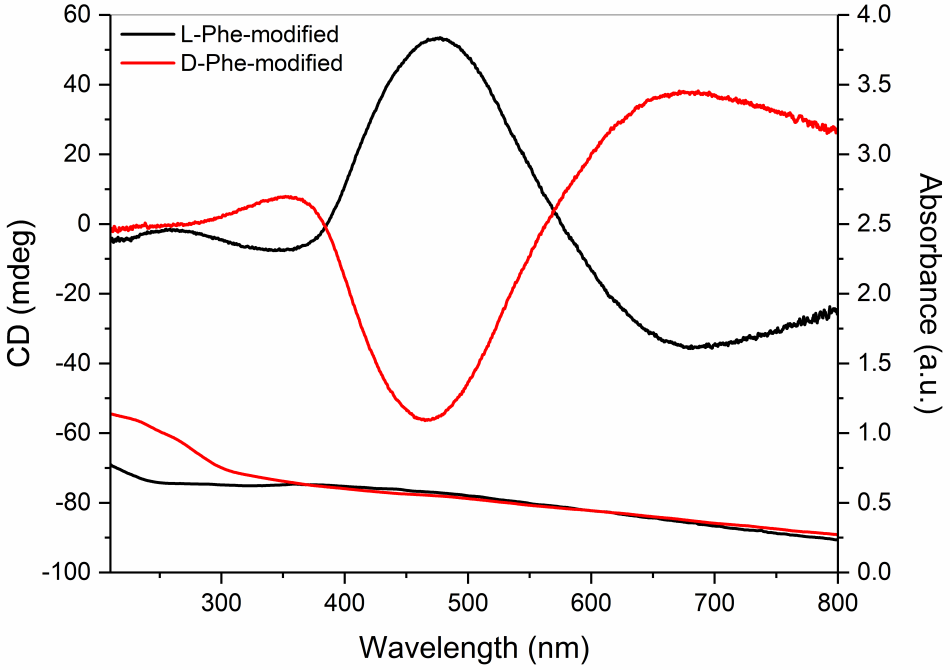


Figure 3.14: Combined UV-Vis (bottom) and CD (top) spectra of CuO-L-Phe (black) and CuO-D-Phe (red). Spectra were acquired using ethanol as solvent.

A high intensity CD signal is observed, and mirror images of the spectra are obtained when functionalised with the opposite enantiomer. Multiple CD absorption features are present throughout the spectra, with wavelengths ranging from UV to NIR, and the Cotton effect is present, with the CD signal alternating between positive and negative values. UV-Vis spectroscopy also demonstrates a significant enhancement in absorption of the CuO-Phe species compared to the CuAl LDH starting material (Appendix B, Figure B5).

The position of the CD bands is also noteworthy. The absolute maxima in CD intensity occur around 475 nm and 700 nm, which correspond with the absorption features observed previously in the DR UV-Vis spectrum (Figure 3.4 (b)). Therefore, the strong CD signal seen throughout the visible region with distinct bands at 475 and 700 nm, coupled with

the significant increase in absorption over time, points toward chirality being induced in the material *via* direct interaction between phenylalanine ligands and the Cu(II) sites in the LDH. In particular, the most intense CD band occurs in the region of the $O^{2-}$ to $Cu^{2+}$ LMCT band in the DR UV-Vis, indicating binding of Phe to $Cu^{2+}$ sites *via* the carboxyl group. The *g*-factor spectra of both CuO-L-Phe and CuO-D-Phe were also calculated, demonstrating anisotropy values more than an order of magnitude higher than the previous *in situ* samples, with values of up to 0.0035 observed for the 700 nm band associated with $Cu^{2+}$ $d-d$ electronic transitions (Figure 3.15).

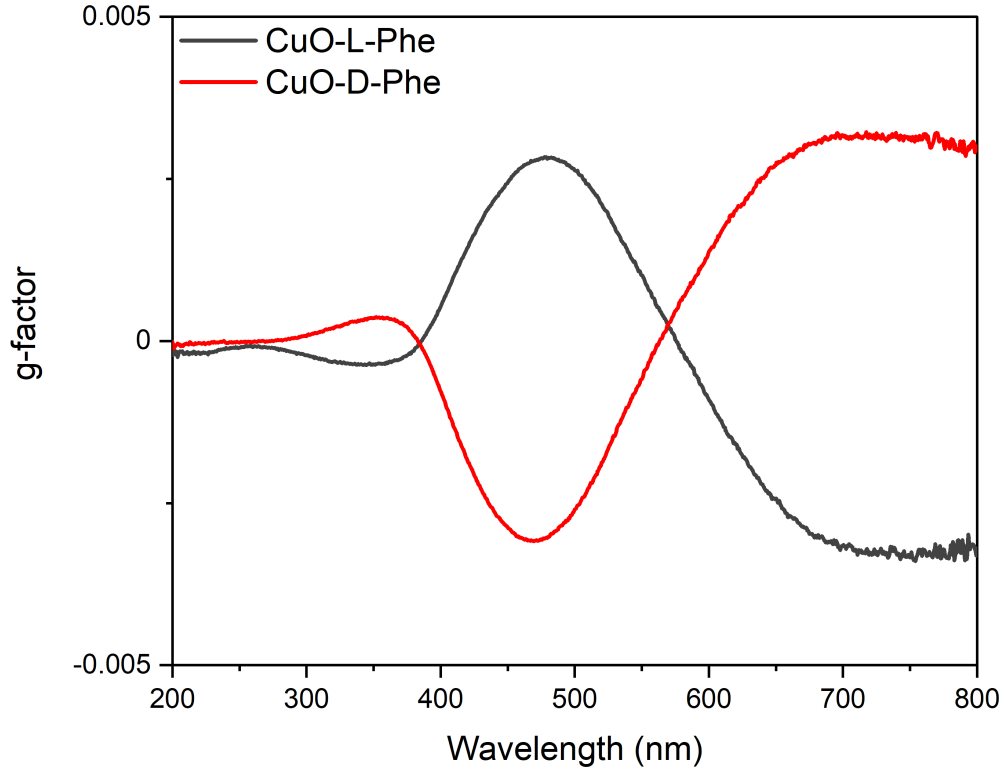


Figure 3.15: *g*-factor spectrum of CuO-L-Phe (black) and CuO-D-Phe (red)

This *g*-factor value is an order of magnitude higher than what would typically be expected for typical ligand-induced chirality transfer ($\approx 10^{-4}$), therefore it is likely there is another contributing factor to the high CD intensity, which will be discussed in later sections. It is important to note that CD spectra of these materials were re-recorded using water as a solvent, and there was no difference in the CD signal peak position or intensity (Appendix B, Figure B6). This confirms that the chirality has not arisen due to any transient solvent effects.

A time-dependent study was carried out to monitor the evolution of the CD signal over the duration of the reaction. The post-synthetic treatment was carried out as normal, with aliquots being taken from the reaction vessel for analysis at time intervals of 1, 2, 3, and 4 hrs. Stirring was ceased after 4 hours, the solution was left to age overnight, and one further aliquot was taken from the mixture 24 hrs after initiation of the reaction. The solid material was separated from solution by centrifugation at 5500 RPM for 10 minutes and no further cleaning was carried out. UV-Vis absorption measurements (Appendix B, Figure B7) show a steady, significant increase in absorption in the 300-800 nm region over time. CD measurements, as seen in Figure 3.16, also show a steady progression of the CD signal over time. It is worth noting that the phenylalanine ligand peak is present at roughly 215 nm in these spectra, however it is clear from previous CD studies that any excess free ligand is readily removed during the centrifugation process. This time-dependent analysis reveals an increase in the intensity of the CD signal over time, likely due to the replacement of carbonate by phenylalanine in the interlayer of the LDH, and subsequent interaction with the Cu(II) sites resulting in ligand-induced chirality. This increase in intensity is accompanied by a redshift in the CD bands, which is indicative of an increase in the anisotropy of the material.

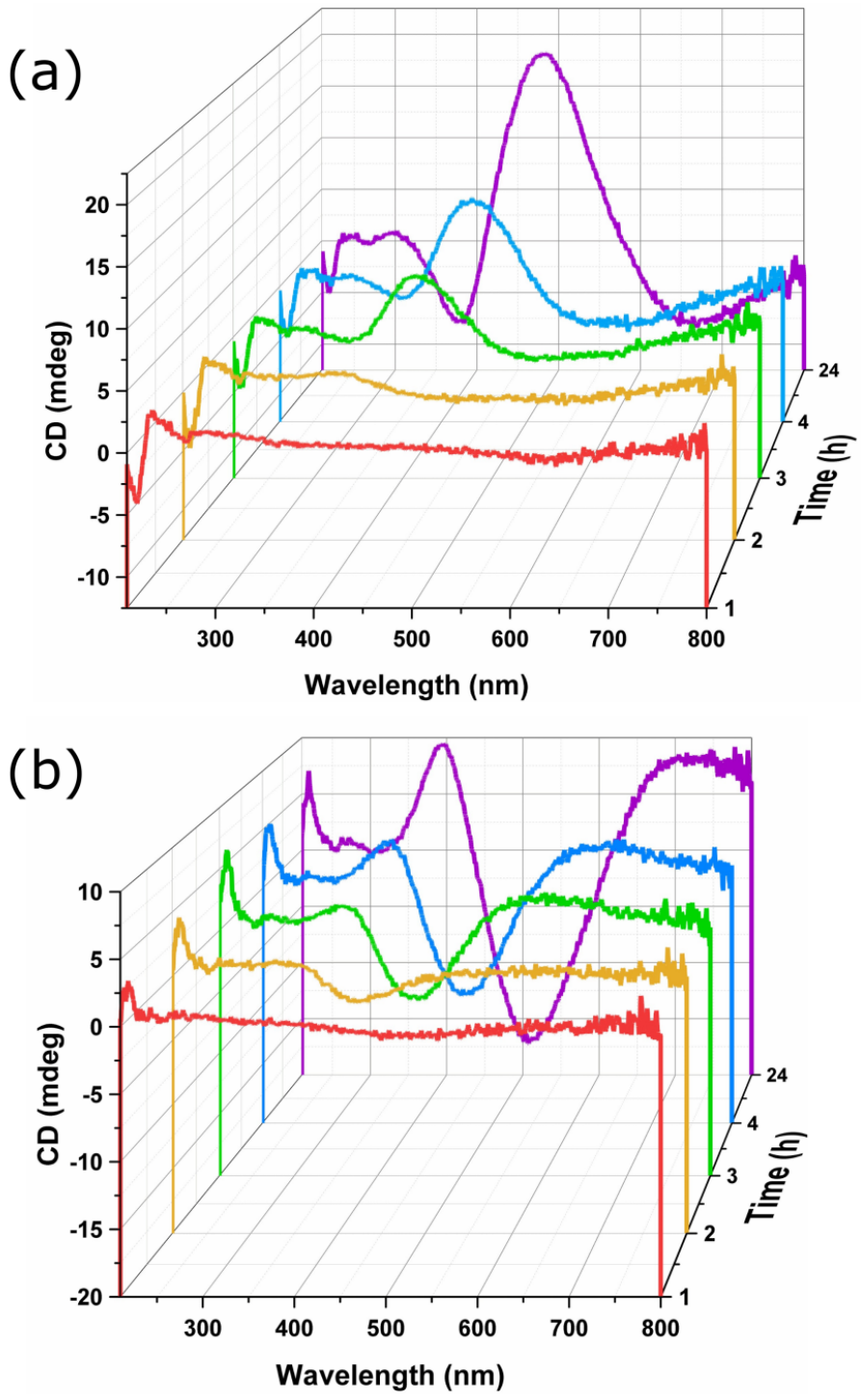


Figure 3.16: Time-dependent CD spectra in ethanol showing formation of (a) CuO-L-Phe and (b) CuO-D-Phe.

pXRD analysis of the time-dependent study, as shown in Figure 3.17, reveals a simultaneous decrease in hydrotalcite-like CuAl LDH assigned reflections, and an increase in intensities of CuO (tenorite) reflections over time, representing a gradual conversion from CuO to CuAl LDH. Reflections corresponding to copper-L-phenylalanine (Cu-(L-Phe)$_2$) and copper-D-phenylalanine (Cu-(D-Phe)$_2$) are also present in the pXRD time-study data, most notably the (100), (200) and (300) reflections at $2\theta = 5.3^\circ$, $10.6^\circ$ and $16.0^\circ$, respectively (PDF: 32-1615).

FT-IR analysis of the time-dependent study also points towards the formation of this Cu-(Phe)$_2$ complex as an intermediate product in this reaction, and serves as further proof that there is direct interaction between Cu(II) sites and phenylalanine ligands, causing the chirality transfer (Appendix B, Figure B8). Additionally, it can be deduced that due to the absence of Cu-(Phe)$_2$ reflections in pXRD data in the final product (Figure 3.12), it is clear that this species eventually gets converted to CuO-Phe or is readily washed out by centrifugation. Therefore, it can be said definitively that the observed CD signal is due to successful ligand-induced chirality in the CuO-Phe species.

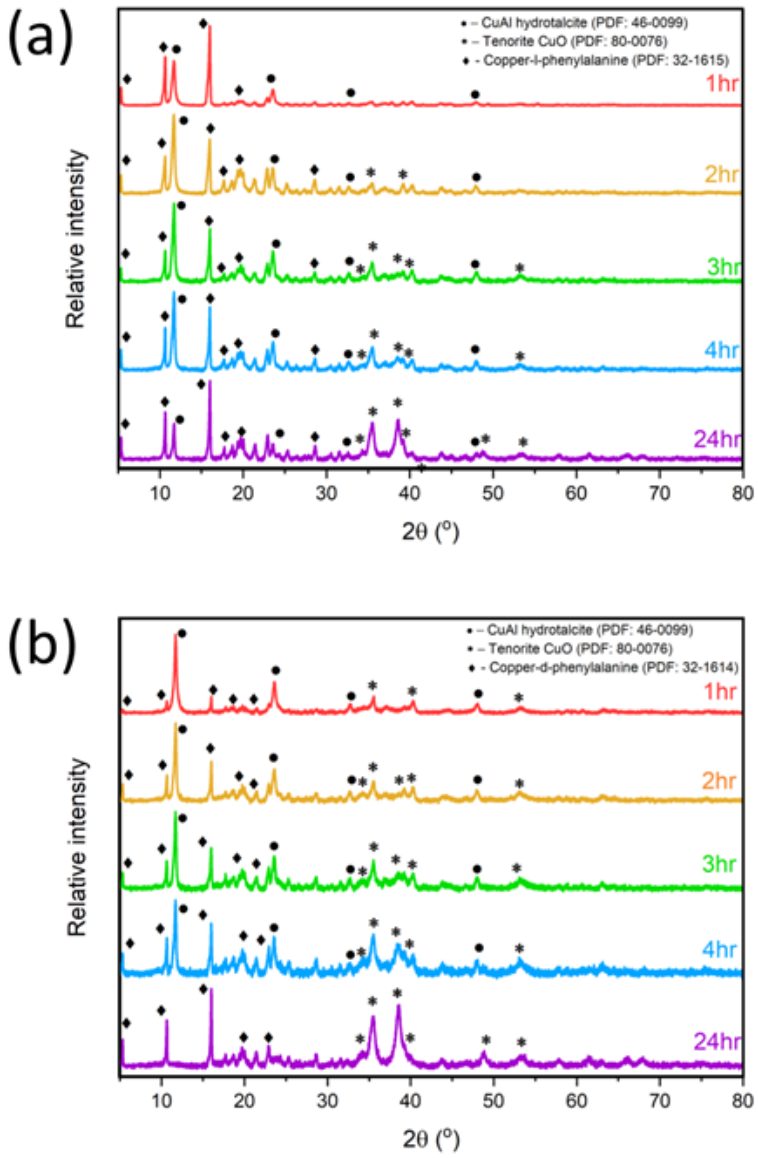


Figure 3.17: Time-dependent pXRD patterns of LDH-derived chiral CuO microstructures obtained *via* post-synthetic functionalisation of CuAl-$CO_3$ LDHs with (a) L-Phe, and (b) D-Phe.

To determine if any morphological change accompanied the phase change, SEM was conducted on the resultant CuO-Phe materials by Dr. Lucia Hughes. Representative SEM images of the CuO-L-Phe and CuO-D-Phe are shown in Figure 3.18, indicating that the chiral CuO structures exhibit a nanosheet cluster-like morphology.

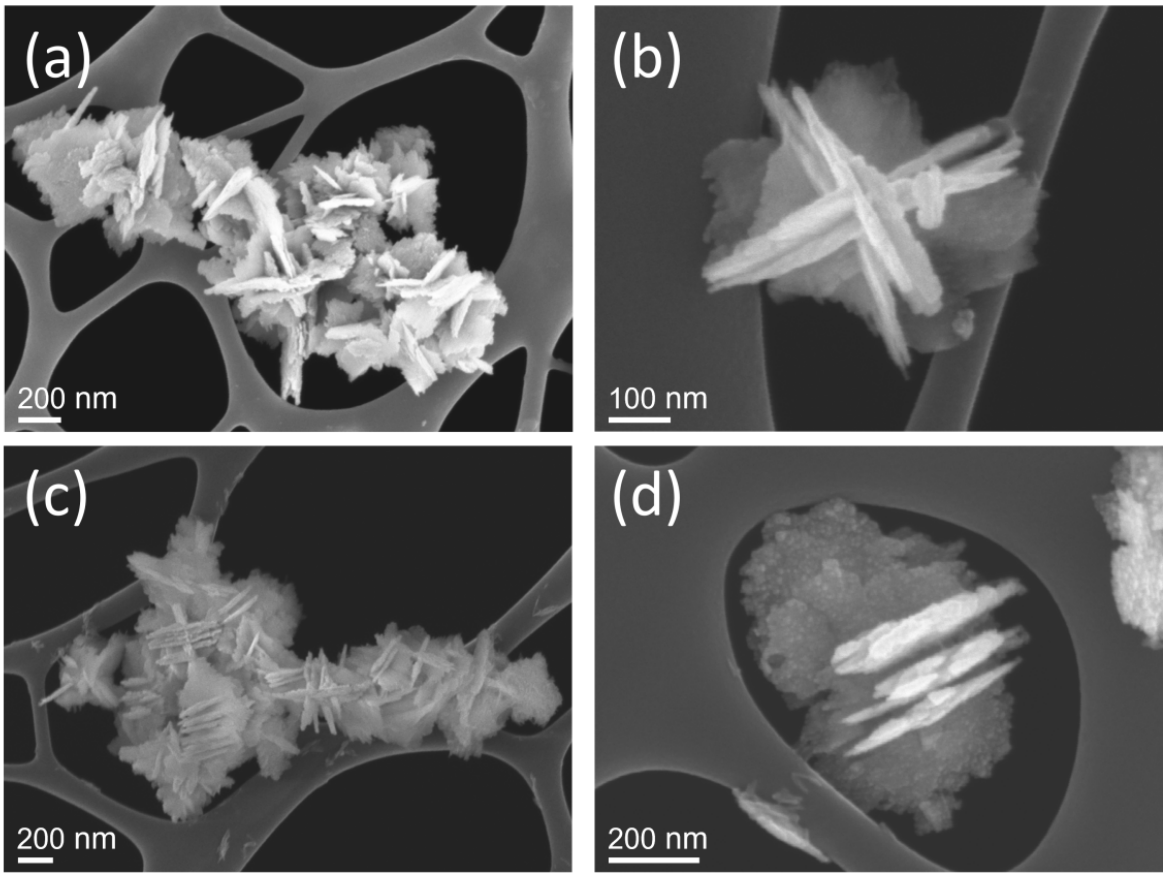


Figure 3.18: SEM images of (a,b) CuO-L-Phe and (c,d) CuO-D-Phe nanosheet clusters.

It is clear that the sample is predominately made up of clusters, which consist of sheets oriented at varying angles with respect to the electron beam. TEM was conducted by Dr. Lucia Hughes on the samples to further support this, confirming that the lateral size of the sheets is on the order of hundreds of nm, whereas the thickness is an order of magnitude lower (Figure 3.19).

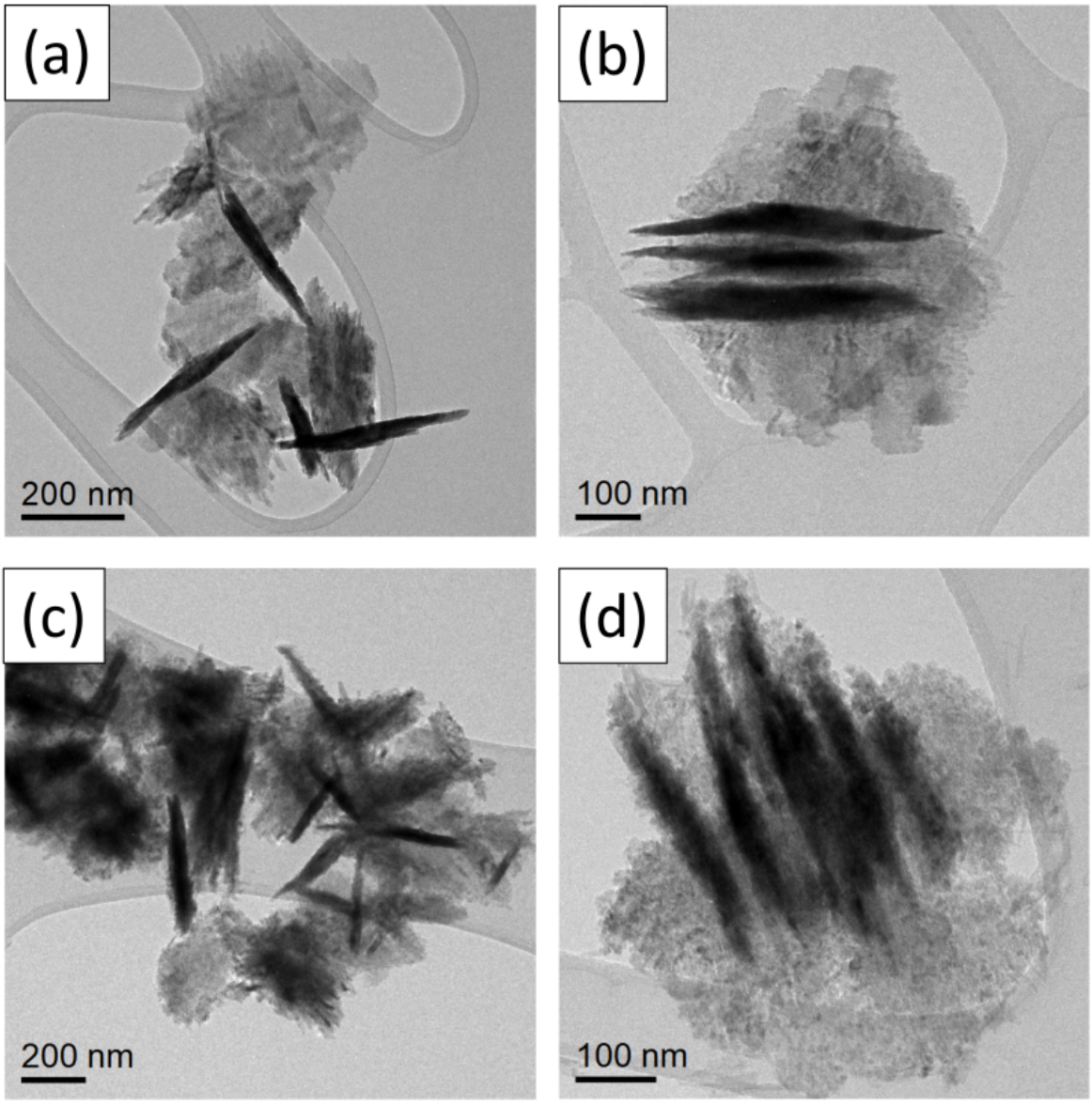


Figure 3.19: TEM images of (a,b) CuO-L-Phe and (c,d) CuO-D-Phe nanosheet clusters.

To support the phase and analysis of the resultant material, high resolution TEM (HRTEM) imaging was conducted by Dr. Lucia Hughes to investigate the crystallinity of the nanosheet clusters. The lattice fringes in the HRTEM images in Figure 3.20 (a,b) can be indexed to the (001) and (110) planes of the CuO phase, further supporting the pXRD analysis and the formation of the CuO tenorite crystal structure (PDF (80-0076)).

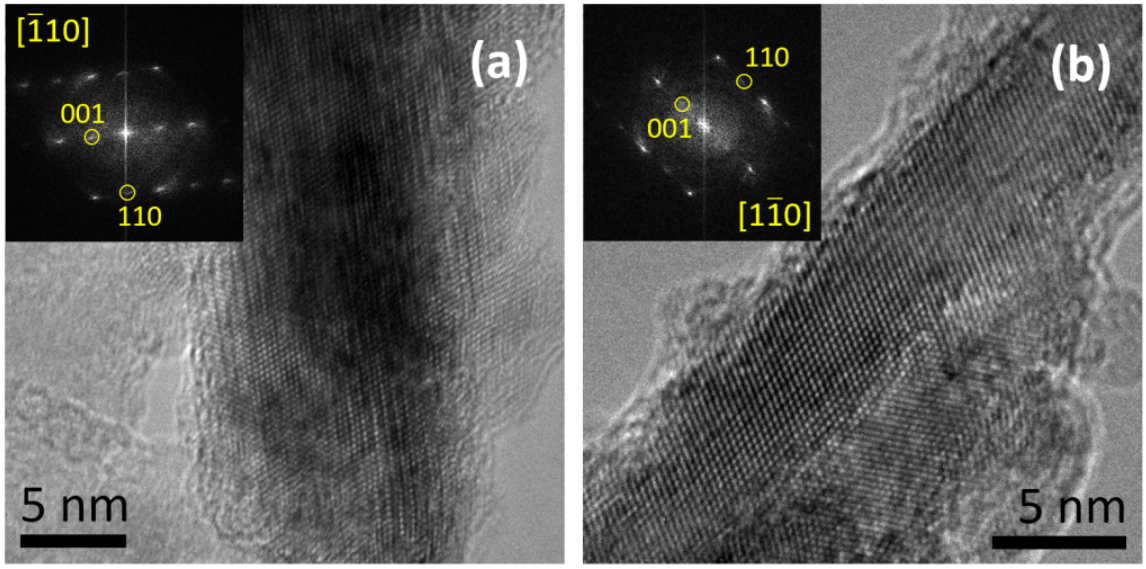


Figure 3.20: HRTEM images of (a) CuO-L-Phe and (b) CuO-D-Phe. The corresponding fast Fourier transforms (FFT) of the HRTEM images are shown in the insets, with the zone axis and main reflections denoted.

Furthermore, EDX mapping of the chiral CuO product shown in Figure 3.21 and corresponding spectra (Appendix B, Figure B9-B10) confirm its chemical composition. By combining the HRTEM crystallographic analysis with the EDX elemental analysis, it is clear that there are no remaining signatures of the LDH in the phenylalanine-treated samples.

pXRD, EDX, and HRTEM all confirm that the final product is CuO, and that there is no indication of the presence of aluminium within the chiral nanostructures. This is despite the fact that the solution-based degradation of CuAl LDHs has been reported to yield $Al(OH)_3$ as a product.[47] Therefore, the generated $Al(OH)_3$ must be playing another role. This, along with the presence of trace amounts of $Cu(OH)_2$ in the product, as indicated by pXRD, gives us an insight into the mechanism of formation of chiral CuO from achiral LDH precursors, which is discussed below in Section 3.3.4.

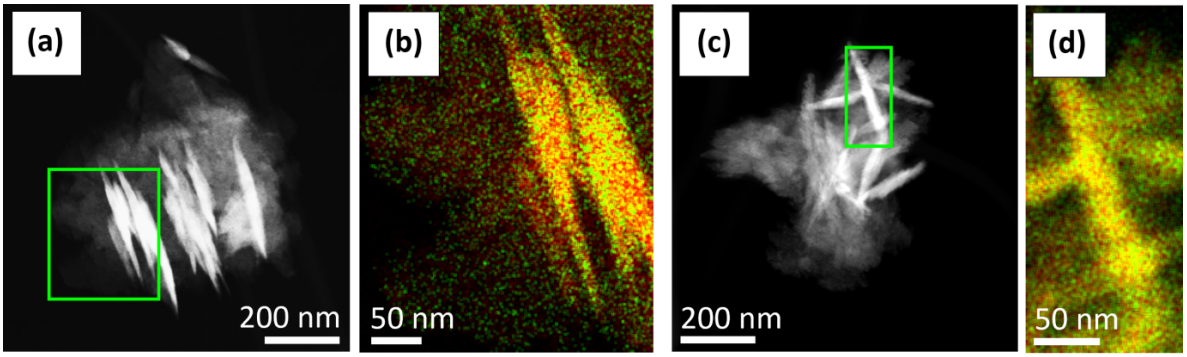


Figure 3.21: STEM image and corresponding EDX maps of highlighted region of interest of (a, b) CuO-L-Phe and (c, d) CuO-D-Phe. The O-K and Cu-L signals are mapped in green and red, respectively.

### 3.3.4 Proposed mechanism of CuAl LDH to chiral CuO evolution

Phenylalanine is known to form covalent bonds with $Cu^{2+}$ *via* both the amino and carboxyl groups. This proceeds by initial formation of a Cu–$(Phe)_2$ complex which, in the presence of $OH^-$ ions, is converted into $Cu(OH)_2$–Phe.[26] The Cu–O–Al bridging bonds in the LDH must be broken to form this species, and thus, covalent Phe interactions with the LDH forces decomposition into its constituent hydroxides, $Cu(OH)_2$ and $Al(OH)_3$. This phenomenon was supported by a visual analysis in our case, whereby it was observed that upon addition of the Phe/NaOH solution to the CuAl dispersion, a deeper blue colour is initially formed, indicative of the formation of $Cu(OH)_2$ (Figure 3.22 (b)). $Cu(OH)_2$ is metastable and, in sufficiently basic solutions, dissolves to form the $Cu(OH)_4{}^{2-}$ ion, finally precipitating out as the more stable CuO at room temperature in aqueous solutions.[48] This is observed in our case by the deep brown colour that forms as the reaction proceeds (Figure 3.22 (c)).

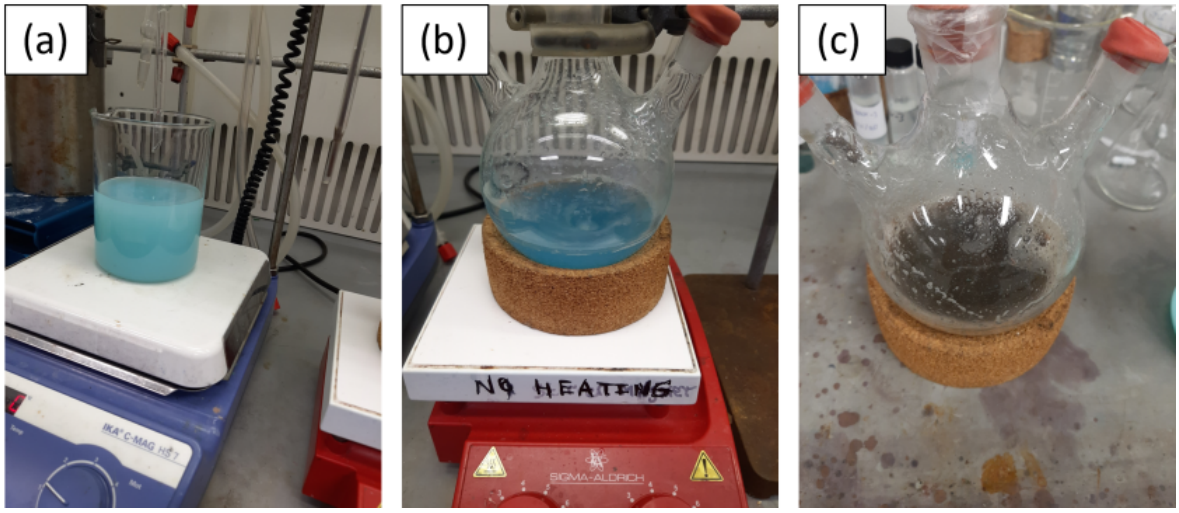


Figure 3.22: Images of reaction mixture (a) before, (b) immediately after, and (c) 24 h after addition of phenylalanine.

The amphoteric $Al(OH)_3$ generated in the LDH breakdown reacts with excess NaOH present in solution to form sodium tetrahydroxoaluminate ($NaAl(OH)_4$), which forms strongly basic aqueous solutions. Previous reports in the literature have theorized that when aluminium ions are present in sodium hydroxide solutions of pH 10 or above, the only aluminium-containing species present is the $Al(OH)_4^-$ ion.[49] $NaAl(OH)_4$ is water-soluble, whereas $Al(OH)_3$ should form a precipitate and crash out with the CuO in the centrifugation cleaning step. The formation of $NaAl(OH)_4$ therefore is consistent with experimental observations, as no Al-containing species are present after cleaning according to pXRD and EDX data. Therefore, the provision of a basic initial reaction medium, as well as the presence of $Al^{3+}$ in the LDH, both seem to be integral in forming the chiral copper oxide, by reacting to increase the concentration of $OH^-$ in solution, therefore driving the rapid, room-temperature, base-assisted transformation to CuO.[50]

We propose that the clusters of CuO nanosheets observed under SEM and TEM are the result of self-assembly of chiral CuO nanosheets into superstructures. Further electron microscopy images of these clusters are provided in the Appendix (Figure B11).

The formation of copper oxide clusters has been reported previously for $Cu_{1-x}O$ spherical NPs using phenylalanine as a ligand. As phenylalanine binds to the nanosheets through both the carboxyl and amine groups, the nonpolar, hydrophobic aromatic ring of the phenylalanine protrudes out from the nanosheet into the polar reaction medium. The phenyl moieties of adjacent phenylalanine ligands bound to different nanosheets attract one another through hydrophobic, π-π interactions, as is the case in folding of proteins, which may be the origin of the organization of CuO-Phe nanosheets into superstructures.[51,52] A schematic of this process is shown in Figure 3.23.

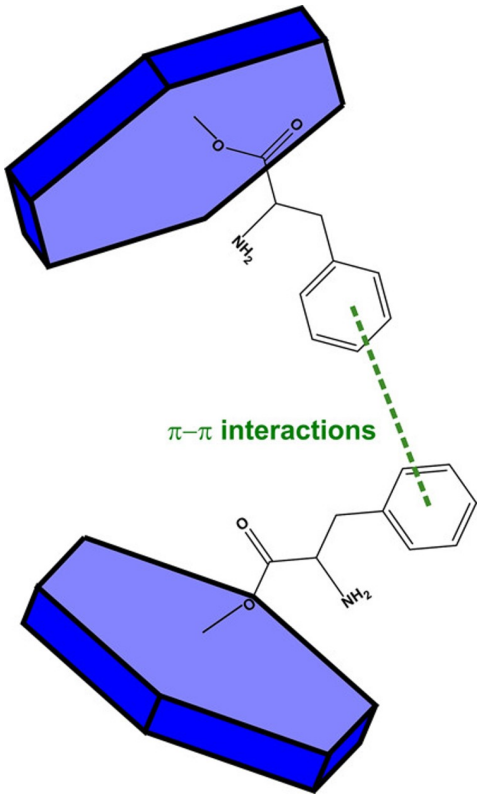


Figure 3.23: Schematic representation of π-π interactions between phenylalanine ligands on adjacent randomly oriented nanosheets, the driving force behind self-assembly of these chiral nanosheets into clusters and superstructures.

Self-assembly and self-organization of nanomaterials typically results in enhanced chiroptical activity, therefore the formation of these nanosheet clusters is likely a dominant factor in producing the strong CD signals and g-factor values displayed by these materials.[6,53]

An article from Prof. Nicola Pinna's group, published a number of months after our work, performed experimental and computational investigations on chirality transfer in similar CuO superstructures, and supports the conclusions derived from the work presented in this chapter.[54,55]

Therefore, the presented evidence supports towards the following theory: replacement of the carbonate anion in the LDH interlayer by phenylalanine and its subsequent binding to Cu(II) sites breaks the Cu–O–Al bridging bonds in the LDH structure, which leads to decomposition into the constituent hydroxides, $Cu(OH)_2$ and $Al(OH)_3$. The formation of $NaAl(OH)_4$ *in situ* due to the liberation of $Al(OH)_3$ upon breakdown of the LDH, and the inclusion of NaOH during the reaction, increases the abundance of free $OH^-$ in solution and is the driving force behind the room temperature transformation from $Cu(OH)_2$ to CuO. The binding of phenylalanine to the $Cu^{2+}$ sites, and its presence upon transformation from $Cu(OH)_2$ to CuO, leads to self-assembly of the nanosheets and a strong enhancement of the chiroptical activity.

## 3.4 Conclusions

CuAl-$CO_3$ LDH nanosheets were successfully synthesised *via* a room-temperature aqueous co-precipitation route. The material was fully characterised and used for investigations of chirality induction. In this work, we have pursued the induction of chirality in 2D materials *via* two distinct routes. Firstly, a modified co-precipitation approach was employed using two different chiral molecules. While chiroptical activity was induced, a low level of synthetic control was achieved, producing multiple products. A second approach was then developed to produce LDH-derived chiral CuO nanosheet clusters *via* an aqueous

post-synthetic treatment in the presence of sodium hydroxide and chiral ligands. Through CD and UV–Vis absorption studies, we provide evidence that the origin of chiroptical activity in the CuO nanostructures is a direct result of interaction between the Cu(II) sites and phenylalanine. Time-dependent XRD and FT-IR reaction studies serve as further proof of the interaction between Cu(II) and phenylalanine ligands *via* the formation of a $Cu(Phe)_2$ complex as an intermediate product. Time-dependent CD studies show that a steady increase in intensity and red-shift of the CD signal correlated with the formation of these chiral CuO structures, and the presence of phenylalanine on the surface drives the assembly of nanosheets into clusters. Thus, for the first time we have demonstrated that chiral 2D CuO nanostructures can be produced from initial layered hydroxide precursors *via* simple base-assisted decomposition in the presence of chiral ligands. This body of work is summarised by the graphic in Figure 3.24.

This unique approach could be potentially used for the preparation of other new metal oxide 2D nanostructures. We believe that these new chiroptically active copper oxide nanostructures may find a range of potential applications including in chiral sensing, asymmetric catalysis and enantiomeric resolution. In particular, we would like to explore the potential of chiral 2D copper oxide nanostructures as building blocks for new laminar membranes, which could be of particular interest to biopharmaceutical industries for enantioselective separation and purification of various chiral molecules and biomolecules.

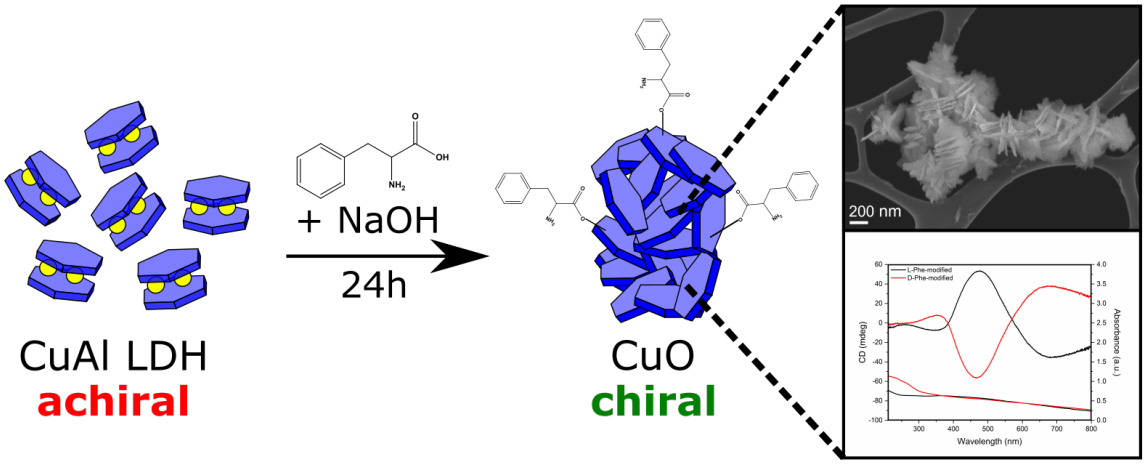


Figure 3.24: Graphical summary of the main findings and work of this chapter.

# References


(1) Moloney, M. P.; Gun'ko, Y. K.; Kelly, J. M. *Chemical Communications* **2007**, 3900–3902.

(2) Liu, J.; Yang, L.; Qin, P.; Zhang, S.; Kin Lam Yung, K.; Huang, Z.; Liu, J. J.; Yang, L; Qin, P; Huang, Z. F.; Zhang, S. Q.; L Yung, K. K. *Advanced Materials* **2021**, *33*, 2005506.

(3) Gui, L.; Hentschel, M.; Defrance, J.; Krauth, J.; Weiss, T.; Giessen, H. *ACS Photonics* **2019**, *6*, 3306–3314.

(4) Kuznetsova, V.; Gromova, Y.; Martinez-Carmona, M.; Purcell-Milton, F.; Ushakova, E.; Cherevkov, S.; Maslov, V.; Gun'ko, Y. K. *Nanophotonics* **2020**, *10*, 797–824.

(5) Govan, J. E.; Jan, E.; Querejeta, A.; Kotov, N. A.; Gun'ko, Y. K. *Chemical Communications* **2010**, *46*, 6072–6074.

(6) Kehoe, D.; Mates-Torres, E.; Samokhvalov, P.; García-Melchor, M.; Gun'ko, Y. K. *Journal of Physical Chemistry C* **2022**, *126*, 434–443.

(7) Duan, Y.; Liu, X.; Han, L.; Asahina, S.; Xu, D.; Cao, Y.; Yao, Y.; Che, S. *Journal of the American Chemical Society* **2014**, *136*, 7193–7196.

(8) Nakagawa, M.; Kawai, T. *Journal of the American Chemical Society* **2018**, *140*, 4991–4994.

(9) Shen, B.; Kim, Y.; Lee, M.; Shen, B; Lee, M; Kim, Y *Advanced Materials* **2020**, *32*, 1905669.

(10) Trujillo-Hernández, K.; Rodríguez-López, G.; Espinosa-Roa, A.; González-Roque, J.; Gómora-Figueroa, A. P.; Zhang, W.; Halasyamani, P. S.; Jancik, V.; Gembicky, M.; Pirruccio, G.; Solis-Ibarra, D. *Journal of Materials Chemistry C* **2020**, *8*, 9602–9607.

(11) Ahn, J.; Lee, E.; Tan, J.; Yang, W.; Kim, B.; Moon, J. *Materials Horizons* **2017**, *4*, 851–856.

(12) Jana, M. K.; Song, R.; Liu, H.; Khanal, D. R.; Janke, S. M.; Zhao, R.; Liu, C.; Valy Vardeny, Z.; Blum, V.; Mitzi, D. B. *Nature Communications* **2020**, *11*, 1–10.

(13) Ma, S.; Jung, Y.-K.; Ahn, J.; Kyhm, J.; Tan, J.; Lee, H.; Jang, G.; Lee, C. U.; Walsh, A.; Moon, J. *Nature Communications* **2022**, *13*, 1–10.

(14) Suzuki, N.; Wang, Y.; Elvati, P.; Qu, Z. B.; Kim, K.; Jiang, S.; Baumeister, E.; Lee, J.; Yeom, B.; Bahng, J. H.; Lee, J.; Violi, A.; Kotov, N. A. *ACS Nano* **2016**, *10*, 1744–1755.

(15) Purcell-Milton, F.; McKenna, R.; Brennan, L. J.; Cullen, C. P.; Guillemeney, L.; Tepliakov, N. V.; Baimuratov, A. S.; Rukhlenko, I. D.; Perova, T. S.; Duesberg, G. S.; Baranov, A. V.; Fedorov, A. V.; Gun'ko, Y. K. *ACS Nano* **2018**, *12*, 954–964.

(16) Riccardi, L.; De Biasi, F.; De Vivo, M.; Bürgi, T.; Rastrelli, F.; Salassa, G. *ACS Nano* **2019**, *13*, 7127–7134.

(17) Branzi, L.; Purcell-Milton, F.; Cressoni, C.; Back, M.; Cattaruzza, E.; Speghini, A.; Gun'ko, Y. K.; Benedetti, A. *Nanoscale* **2022**, *14*, 12174–12182.

(18) Coogan, Á.; Gun'ko, Y. K. *Materials Advances* **2021**, *2*, 146–164.

(19) Liu, P.; Hou, J.; Zhang, Y.; Li, L.; Lu, X.; Tang, Z. *Inorganic Chemistry Frontiers* **2020**, *7*, 2560–2581.

(20) Yan, L.; Gonca, S.; Zhu, G.; Zhang, W.; Chen, X. *Journal of Materials Chemistry B* **2019**, *7*, 5583–5601.

(21) Xu, Z. P.; Zhang, J.; Adebajo, M. O.; Zhang, H.; Zhou, C. *Applied Clay Science* **2011**, *53*, 139–150.

(22) Luengo, C. V.; Crescitelli, M. C.; Lopez, N. A.; Avena, M. J. *Journal of Pharmaceutical Sciences* **2021**, *110*, 1779–1787.

(23) Wang, N.; Huang, Z.; Li, X.; Li, J.; Ji, S.; An, Q. F. *Journal of Materials Chemistry A* **2018**, *6*, 17148–17155.

(24) Gerlach, P.; Douard, C.; Gaalich, I.; Athouël, L.; Sarmet, J.; Leroux, F.; Tavoit-Gueho, C.; Stevens, P.; Toussaint, G.; Brousse, T. *Journal of The Electrochemical Society* **2023**, *170*, 070505.

(25) Boltaev, G. S.; Ganeev, R. A.; Krishnendu, P. S.; Zhang, K.; Guo, C. *Scientific Reports* **2019**, *9*, 1–8.

(26) Hao, C.; Qu, A.; Xu, L.; Sun, M.; Zhang, H.; Xu, C.; Kuang, H. *Journal of the American Chemical Society* **2019**, *141*, 1091–1099.

(27) Berner, S.; Araya, P.; Govan, J.; Palza, H. *Journal of Industrial and Engineering Chemistry* **2018**, *59*, 134–140.

(28) Boulahbal, A. I.; Santamaría, L.; Azizi, A.; Boutahala, M.; Korili, S. A.; Gil, A. *Minerals Engineering* **2023**, *204*, 108413.

(29) Halcrow, S. M. A.; Halcrow, M. A. *Chemical Society Reviews* **2013**, *42*, 1784–1795.

(30) Dai, R.; Liu, B.; Zhang, Y.; Pedersen, J. N.; Zhang, X.; Dong, M.; Guo, Z. *Journal of Environmental Chemical Engineering* **2021**, *9*, 106390.

(31) Zhang, L. H.; Li, F.; Evans, D. G.; Duan, X. *Industrial and Engineering Chemistry Research* **2010**, *49*, 5959–5968.

(32) Stoylkova, T.; Chanev, C. *Reaction Kinetics, Mechanisms and Catalysis* **2016**, *117*, 47–58.

(33) Velu, S.; Suzuki, K.; Hashimoto, S.; Satoh, N.; Ohashi, F.; Tomura, S. *Journal of Materials Chemistry* **2001**, *11*, 2049–2060.

(34) Li, Y.; Li, Y.; Huang, L.; Bin, Q.; Lin, Z.; Yang, H.; Cai, Z.; Chen, G. *Journal of Materials Chemistry B* **2013**, *1*, 1256–1262.

(35) Theiss, F. L.; Ayoko, G. A.; Frost, R. L. *Journal of Thermal Analysis and Calorimetry* **2013**, *112*, 649–657.

(36) Aisawa, S.; Chida, C.; Ida, H.; Sang, J.; Hirahara, H.; Sato, H. *Applied Clay Science* **2023**, *244*, 107108.

(37) Sato, H.; Takimoto, K.; Kawamura, I.; Aisawa, S. *Bulletin of the Chemical Society of Japan* **2019**, *92*, _eprint: https://academic.oup.com/bcsj/article-pdf/92/10/1779/56299631/bcsj.20190161.pdf, 1779–1784.

(38) Sato, H.; Kawamura, I. *Biochimica et Biophysica Acta (BBA) - Proteins and Proteomics* **2020**, *1868*, 140439.

(39) Mossou, E.; Teixeira, S. C.; Mitchell, E. P.; Mason, S. A.; Adler-Abramovich, L.; Gazit, E.; Forsyth, V. T. *Acta Crystallographica Section C: Structural Chemistry* **2014**, *70*, 326–331.

(40) Amino Acids Reference Chart `https://www.sigmaaldrich.com/IE/en/technical-documents/technical-article/protein-biology/protein-structural-analysis/amino-acid-reference-chart` (accessed 09/11/2023).

(41) ContaminantDB: Dibenzoyl-L-tartaric acid `https://contaminantdb.ca/contaminants/CHEM017386` (accessed 09/11/2023).

(42) Berova, N.; Polavarapu, P. L.; Nakanishi, K.; Woody, R. W. Comprehensive Chiroptical Spectroscopy, Hoboken, 2011.

(43) Yao, Y.; Hou, H.; Liu, X.; Meng, K.; Qiu, J.; Wang, L.; Zhu, J. *Waste and Biomass Valorization* **2020**, *11*, 6967–6979.

(44) Tan, J.; Dun, M.; Li, L.; Zhao, J.; Li, X.; Hu, Y.; Huang, G.; Tan, W.; Huang, X. *Sensors and Actuators, B: Chemical* **2017**, *252*, 1–8.

(45) Marathey, P.; Khanna, S.; Patel, R.; Mukhopadhyay, I.; Ray, A. **2021**, 1383–1391.

(46) Mohamed, M. E.; Mohammed, A. M. *International Letters of Chemistry, Physics and Astronomy* **2013**, *15*, 1–17.

(47) Britto, S.; Vishnu Kamath, P. *Journal of Solid State Chemistry* **2009**, *182*, 1193–1199.

(48) Cudennec, Y.; Lecerf, A. *Solid State Sciences* **2003**, *5*, 1471–1474.

(49) Panias, D.; Asimidis, P.; Paspaliaris, I. *Hydrometallurgy* **2001**, *59*, 15–29.

(50) Zheng, L.; Liu, X. *Materials Letters* **2007**, *61*, 2222–2226.

(51) Park, J. I.; Nguyen, T. D.; De Queirós Silveira, G.; Bahng, J. H.; Srivastava, S.; Zhao, G.; Sun, K.; Zhang, P.; Glotzer, S. C.; Kotov, N. A. *Nature Communications* **2014**, *5*, 1–9.

(52) Hunter, C. A.; Singh, J.; Thornton, J. M. *Journal of Molecular Biology* **1991**, *218*, 837–846.

(53) Tan, C.; Qi, X.; Liu, Z.; Zhao, F.; Li, H.; Huang, X.; Shi, L.; Zheng, B.; Zhang, X.; Xie, L.; Tang, Z.; Huang, W.; Zhang, H. *Journal of the American Chemical Society* **2015**, *137*, 1565–1571.

(54) Zhang, J.; Vallée, R. A.; Kochovski, Z.; Zhang, W.; Shen, C.; Bertram, F.; Pinna, N. *Angewandte Chemie International Edition* **2023**, *62*, e202305353.

(55) Coogan, Á.; Hughes, L.; Purcell-Milton, F.; Cardiff, S.; Nicolosi, V.; Gun'ko, Y. K. *The Journal of Physical Chemistry C* **2022**, *126*, 18980–18987.

# Chapter 4

# Towards Recyclable 2D Material-Based Nanofiltration Membranes for Water Purification

## 4.1 Introduction

According to a report published by UNICEF and the WHO in 2019, one third of the world's population does not have access to clean, safe drinking water.[1] Dyes, surfactants and heavy metals leached into wastewater from the textile industry are a leading cause of water pollution.[2] The release of these dyes into wastewater streams can have numerous detrimental effects to humans, as well as aquatic flora and fauna. This dye pollution has a significant negative impact on biodiversity in our waterways. The high absorption coefficients of these dyes in the visible light region hinders photosynthesis, as light cannot penetrate the water efficiently.[3] Additionally, many of the dyes used industrially can be carcinogenic and mutagenic, causing long-term damage when ingested by aquatic life, as well as by humans.[4]

Azo dyes such as Evans Blue are a major concern, with up to 50% of the dye used in the dyeing process being released into wastewater, due to inadequate binding to textiles.[5,6] The toxicity of thiazine and triarylmethane dyes also present a significant risk.[7,8] Innovative methods of water filtration and treatment are therefore urgently needed in order to achieve United Nations Sustainable Development Goal 6 - which is access to clean water for all by 2030. Nanofiltration (NF) is increasingly being explored as an effective method of water purification.[9,10] However, many existing NF membranes suffer from significant and rapid fouling, restricting their lifetime significantly.[11] To contribute to and develop a greener, more circular economy and society, the methods we use for water treatment must be sustainable. Reusable, recyclable NF membranes have the opportunity to be game-changers in this area, and significant research has been conducted in recent years on approaches to anti-fouling and fouling-resistant NF membranes.[12–14]

2D nanomaterials, such as boron nitride, graphene and transition metal dichalcogenides are increasingly being explored as exciting candidates for new NF membranes.[15–18] Exceptional adsorption capacities can be achieved by 2D material-based membranes, due to their high surface-to-volume ratios, allowing more surface area for interaction with contaminants.[19] The stacking of nanosheets when forming membranes results in the formation of nano-porous channels, often allowing for more rapid solvent transport and higher selectivity.[20] Our previous work demonstrated the potential of partially oxidised boron nitride (BNOx) as a nanomaterial for high-performance NF membranes.[21] BNOx can be produced by partial oxidation and hydroxylation of the edges of BN sheets, which can be achieved by simple thermal oxidation at 900 °C, endowing BNOx with a partially negative surface charge.[22] The introduction of these OH groups has been demonstrated to have no reduction in the NF performance of the exfoliated material when compared with pristine BN. However, the major drawback of these membranes at present is that they are vulnerable to fouling, and must be disposed of after a single use, or alternatively

require very extensive cleaning using aggressive and environmentally harmful chemicals.

In recent years, there has been a resurgence in the study of LDHs, owed in part to their semiconductor nature.[23] The use of LDHs can be advantageous over other traditional 2D nanomaterials, due to their high scalability, low cost and ease of synthesis, as well as high bandgap tunability through variation of the metal cations, as well as the intercalating species.[24] Due to these interesting and unique properties, many recent reports have examined the applications of LDHs in heterogeneous catalysis, specifically as electrocatalysts and photocatalysts.[25–27] In particular, numerous reports of the design of transition-metal based LDHs for photodegradation of dyes in water remediation applications have emerged in recent years.[28–31] Furthermore, there exists an extensive body of literature on the study of LDHs for water remediation[32], both as stand-alone sorbents[30,33–36], as well *via* incorporation of LDHs into composite sorbents and filtration membranes.[37,38] Photocatalytically active nanomaterials may present an innovative route to achieve anti-fouling behaviour in NF membranes. Despite this, to the best of our knowledge, no reports exist of exploiting the photocatalytic activity of LDHs for use as anti-fouling additives in NF membranes.

Herein, we present the development of new, high-performance hybrid CuAl-$CO_3$ LDH/BNOx NF membranes for efficient separation and visible-light-driven photocatalytic degradation of several dyes – Evans Blue, Methyl Orange, Methylene Blue and Rhodamine B. We believe this innovative route to anti-fouling represents a significant step forward in advanced sustainable nanofiltration research.

## 4.2 Aims of this section of work

The main goal of this work was to develop new, multifunctional hybrid CuAl-$CO_3$ LDH/BNOx nanocomposite membranes, with both separation and photocatalytic modalities. We aimed to introduce catalytic functionality into previously developed in-house BNOx NF membranes *via* the addition of CuAl-$CO_3$ LDHs, with the end goal of achieving recyclable NF membranes. Firstly, we planned to full characterise optimised LDH/BNOx membranes *via* pXRD, FT-IR, zeta potential, SEM, TEM, EDX, EELS and mercury porosimetry to determine their properties. Then, we planned to test the LDH/BNOx nanocomposite membranes for their nanofiltration performance using a number of water-soluble dyes with various sizes and charges – namely Evans blue, methyl orange, methylene blue and rhodamine B. In addition, we planned to assess the photocatalytic activity of the membranes to determine the feasibility of the introduction of photocatalysts as a route to anti-fouling in NF membranes. Our final objective was to discuss and gain some insights into the mechanical stability of the membranes, and investigate the mechanism of photodegradation in the hybrid membrane.

## 4.3 Results and discussion

### 4.3.1 Characterisation of LDH/BNOx nanocomposite material and membranes

Partially oxidised BN (BNOx) was chosen over BN to fabricate the NF membranes due to the negative surface charge which arises as a consequence of the introduction of -OH groups during the thermal oxidation process, as previously reported by our group.[21] BNOx therefore has the ability to participate in attractive electrostatic interactions with LDHs, which should result in a uniform, electrostatically-stabilised nanocomposite. LDH nanosheets have an intrinsic positive surface charge, due to the doping of $M^{3+}$ species in the $M(OH)_2$ units.[39] CuAl-$CO_3$ in particular was chosen for this study as it has previously been reported in literature to exhibit photodegradation of azo dyes such as methyl orange (MO), and presents less risk for water treatment than more photoactive Cr-containing LDHs, which can sometimes be prone to oxidative leaching of $Cr^{6+}$.[40] Zeta potential ($\zeta$) measurements of as-prepared CuAl-$CO_3$ LDH and exfoliated BNOx were carried out in aqueous solution (pH 7) to confirm the presence of these complementary surface charges, and average values of $\zeta_{BNOx}$ = -30.7 mV and $\zeta_{LDH}$ = +33.6 mV were obtained (Figure 4.1).

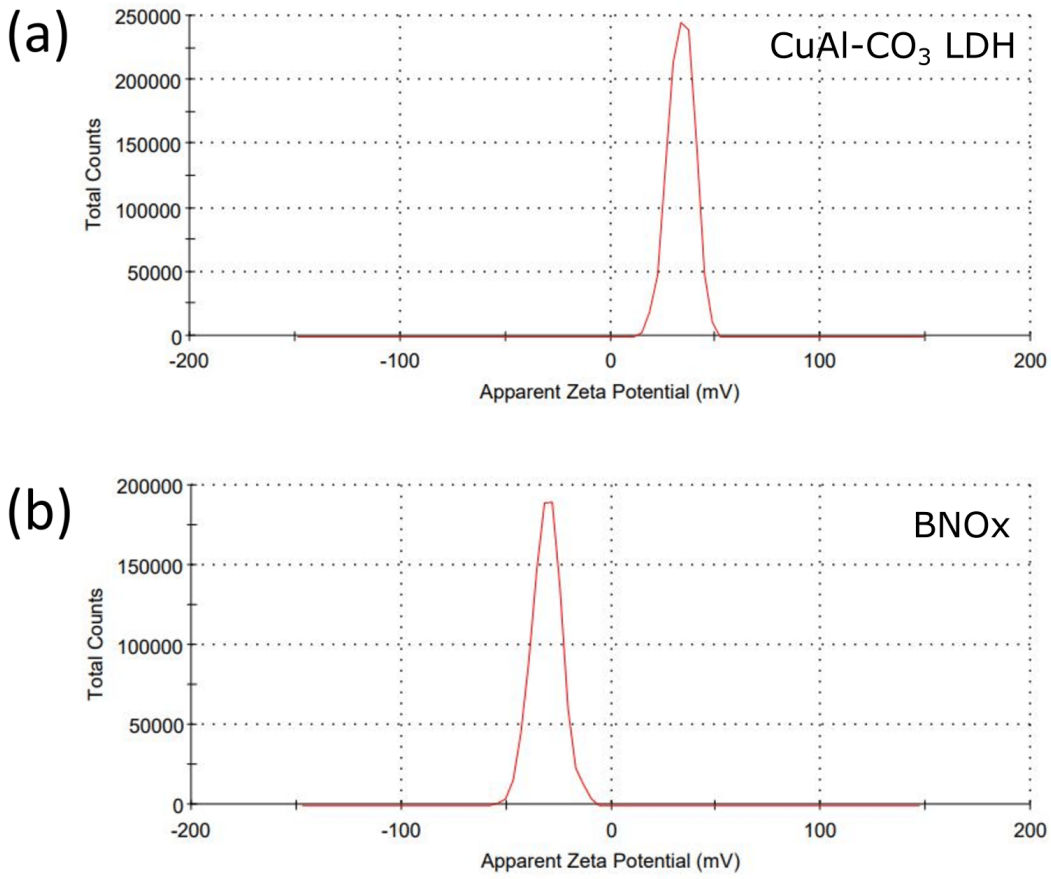


Figure 4.1: Zeta potential distributions of (a) CuAl-$CO_3$ LDH and (b) BNOx nanosheets. Data acquired using MP $H_2O$ as solvent (pH 7).

A number of different compositions were tested for the formation of the nanocomposite, the details of which are presented in Appendix C. An optimal ratio of 20:80 LDH/BNOx by mass was determined, as this level of LDH loading should be theoretically high enough to induce photocatalysis, but low enough to maintain the integrity and high performance previously reported for BNOx-based NF membranes. The LDH/BNOx nanocomposite was prepared by sonication for 24h, and the membranes were prepared *via* the common vacuum filtration technique, as described in our previous reports, and detailed in the Materials and Methods section.[10,21] The resulting nanocomposite and membranes

were characterised by pXRD, FT-IR, SEM, TEM, HAADF-STEM, EDX, EELS, mercury porosimetry and zeta potential. Figure 4.2 shows a comparison between the pXRD patterns of the two components of the membrane, and the membrane itself.

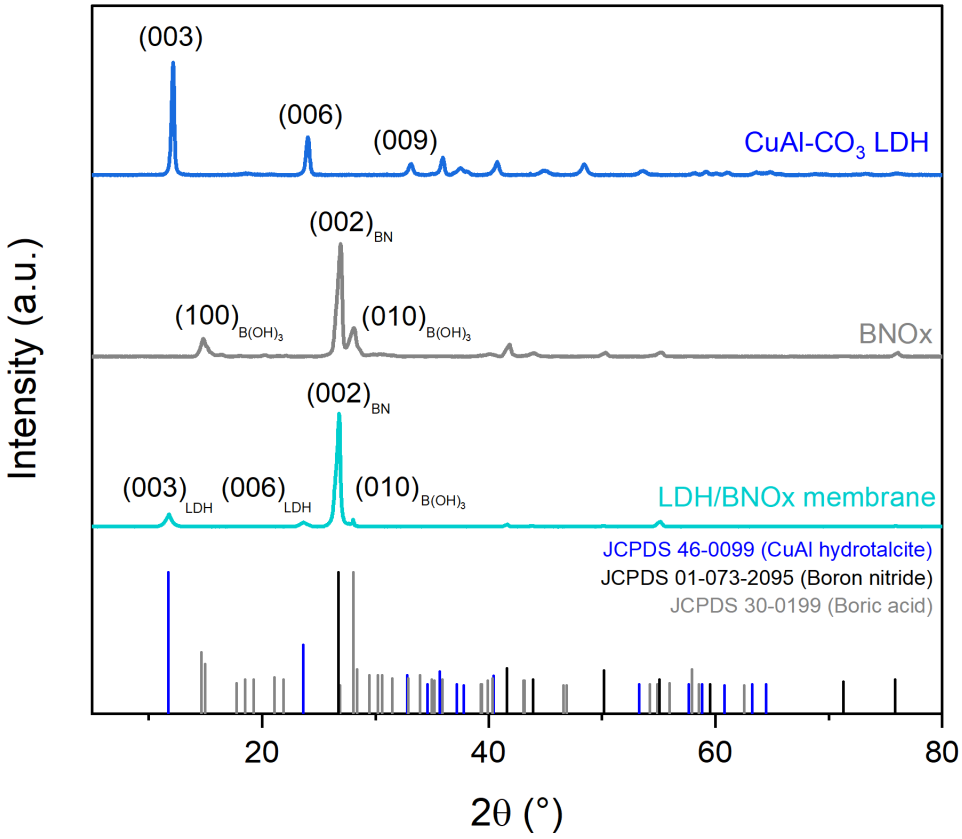


Figure 4.2: pXRD patterns of CuAl-$CO_3$ LDHs (blue), BNOx (grey) and LDH/BNOx nanocomposite (turquoise). pXRD reference patterns are provided for CuAl hydrotalcite, boron nitride, and boric acid.

The most prominent reflections observed from the membrane sample are the CuAl-$CO_3$ LDH (003) reflection at $2\theta = 12.1\ ^\circ$, the BN (002) reflection at $2\theta = 26.8\ ^\circ$, and the $B(OH)_3$ (010) reflection at $2\theta = 28.0\ ^\circ$.[21,41] All observed pXRD reflections in the membrane sample can be indexed to the characteristic reflections of CuAl-$CO_3$ LDH (JCPDS 46-0099), and BNOx (JCPDS 01-073-2095 for boron nitride, and JCPDS 30-0199 for boric acid ($B(OH)_3$)) - with no presence of any undesirable side products.

FT-IR was also conducted on the sample, as shown in Figure 4.3. The FT-IR spectrum of the membrane contains peaks characteristic of both BNOx and CuAl-$CO_3$ LDH. The B-N stretch (750 $cm^{-1}$) and B-N-B bend (1250-1500 $cm^{-1}$) can be observed, with the B-N-B bend broadening and losing detail due to overlap with the CuAl-$CO_3$ LDH $v_3$ $CO_3^{2-}$ stretch (1350 $cm^{-1}$). Additionally, there is a broad O-H stretch from roughly 3000-3600 $cm^{-1}$ due to the overlap of the BNOx O-H band at 3000-3200 $cm^{-1}$ and the CuAl-$CO_3$ LDH O-H stretch centred at 3400 $cm^{-1}$.[22,42]

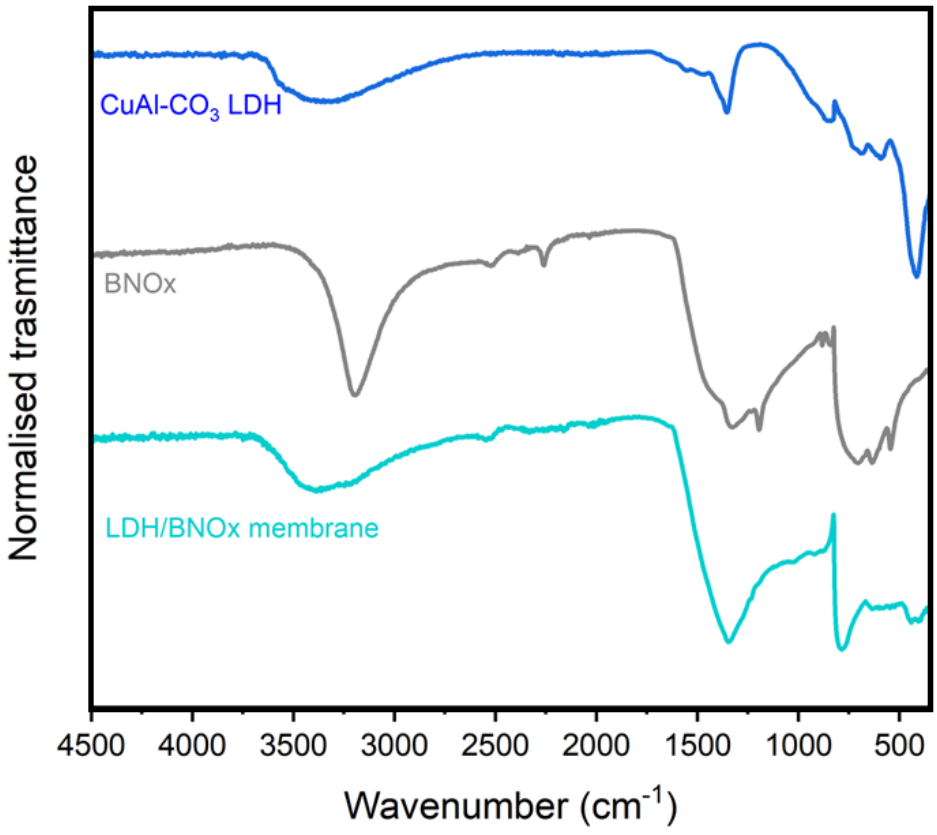


Figure 4.3: FT-IR spectra of CuAl-$CO_3$ LDH (blue), BNOx (grey) and LDH/BNOx nanocomposite (turquoise).

Top-view and cross-sectional SEM imaging was conducted to determine the morphological profile of the membranes, as shown in Figure 4.4. It is evident from SEM imaging that the membranes exhibit a very uniform, porous profile, with no obvious layering

or separation of the two materials observed.

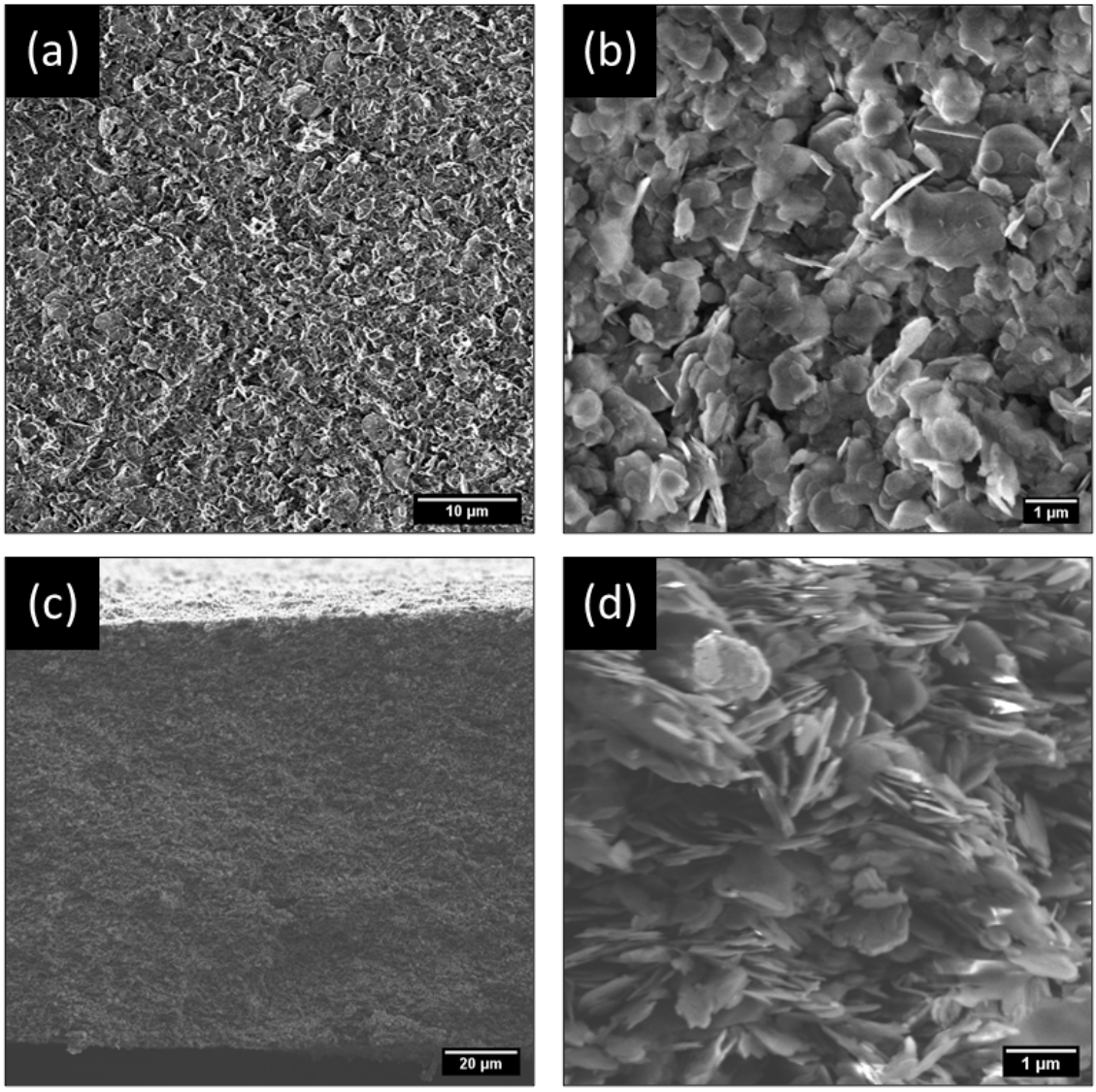


Figure 4.4: SEM images of hybrid membranes: (a,b) Top-view and (c,d) cross-sectional images of LDH/BNOx membranes. Lower magnification images (a,c) show general uniformity of membranes, and higher magnification (b,d) shows finer membrane structure consisting of networks of nanosheets.

Additional top-view and cross-section SEM images are shown in Appendix C (Figure C4). These membranes have a remarkably similar morphological profile to previously reported BNOx membranes, with a calculated mean thickness of 121 $\pm$ 8 µm. The thickness distribution is also provided in Appendix C (Figure C5).

From the SEM images, it is apparent that there is a uniform dispersion of larger and smaller populations of nanosheets. Size distribution analysis of the lateral sizes of nanosheets in the membrane structure was performed, revealing a mean lateral size of 0.85 μm and a large standard deviation of 0.38 μm (Appendix C, Figure C6). Furthermore, sheets sampled through size distribution analysis range widely in lateral size from 0.19 to 2.09 μm. This is indicative of a large, broad distribution consisting of smaller and larger flakes. Additionally, TEM imaging was performed on exfoliated BNOx by Dr. Tigran Simonian, as shown in Figure 4.5, and suggests that the larger, irregular rounded flakes present in the membrane are representative of BNOx nanosheets, with an average lateral size of 0.95 ± 0.32 μm, and flake sizes ranging from 0.43 to 1.90 μm (Appendix C, Figure C8). Additional TEM images of BNOx are provided in Appendix C (Figure C7).

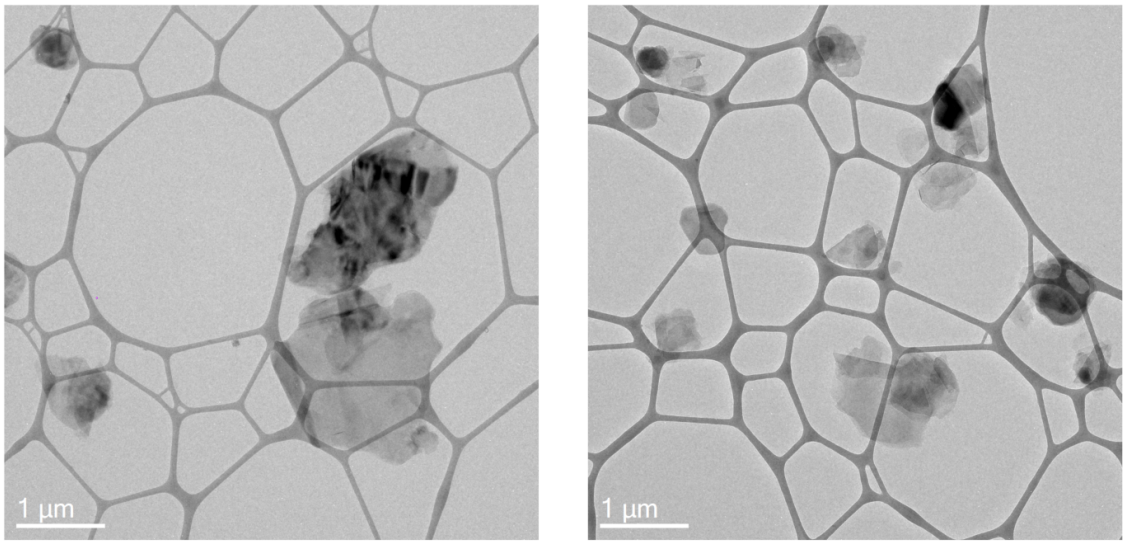


Figure 4.5: TEM images of exfoliated BNOx nanosheets.

This indicates that a sizable population of smaller sheets in the membrane are representative of CuAl-$CO_3$ LDH nanosheets, which is in line with expectations based on our previous reports.[41] This broad particle size distribution is an expected consequence of using liquid phase exfoliation in water, without further post-processing steps for size selection.[15,43]

To further confirm the composition of the LDH/BNOx nanocomposite, HAADF-STEM was conducted in combination with EDX and EELS mapping by Dr. Tigran Simonian, and confirms the presence of both individual CuAl-$CO_3$ LDH and BNOx nanosheets in the nanocomposite, as shown in Figure 4.6. The EDX and EELS spectra are provided in Appendix C (Figures C9 and C10)

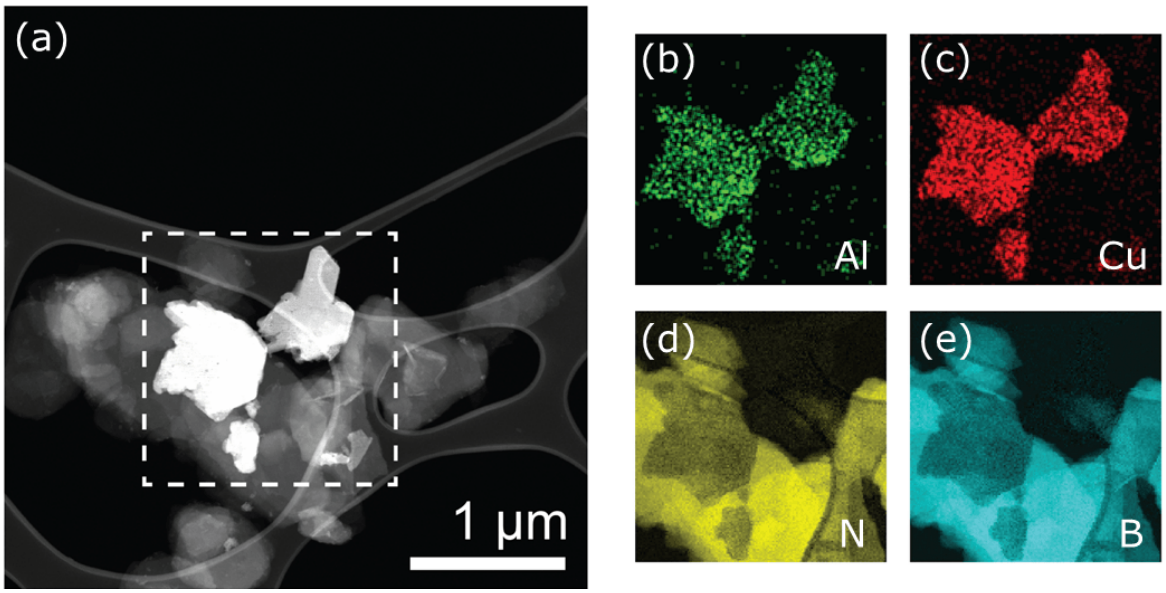


Figure 4.6: (a) HAADF-STEM image (a) of LDH/BNOx nanocomposite. Dashed box in (a) is area under analysis in (b)-(e). Elemental mapping of Al (b) and Cu (c) *via* EDX, and N (d) and B (e) *via* EELS. Scale bar in (b)-(e) is same as in (a).

Mercury porosimetry was conducted on the LDH/BNOx membrane sample to investigate the porosity of the membranes, in the approximate 10 nm to 10 µm range, as shown in Figure 4.7. Figure 4.7 (a) shows the intrusion of mercury into the sample as a function of pore diameter. At initial low pressures, the rate of intrusion is constant. As the pressure builds, mercury is forced into increasingly smaller pores, with an uptake occurring at the 4 µm mark. A gradual filling of pores then occurs to approximately 600 nm. At this point, a second distinct stage of filling is observed, almost linearly, to 150 nm. This region is significant, accounting for approximately 0.25 cc/g or 38.5% of the total pore volume (0.65 cc/g). A third and final stage of filling occurs at 150 nm, with a steep rise in the

curve due to rapid intrusion, before gradually plateauing out at 15 nm, with no further intrusion occurring as all pores are fully filled. The resultant pore size distribution, shown in Figure 4.7 (b), reveals that the vast majority of pores are less than 1 μm in size. Pores in the 10-200 nm range dominate the material, with a sharp peak at approximately 100 nm indicating a high concentration of pores within a narrow size range.

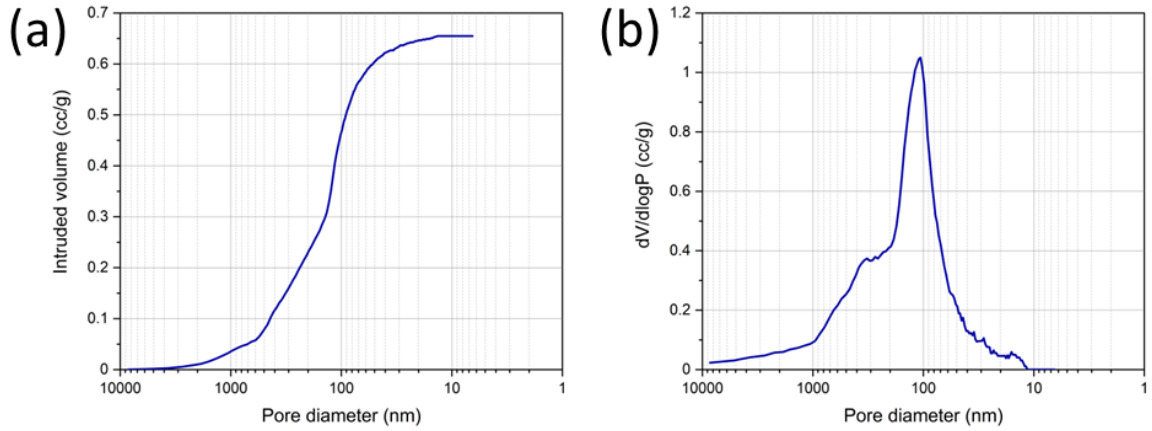


Figure 4.7: (a) Mercury intrusion and (b) pore size distribution of the LDH/BNOx membrane sample.

The porosimetry data is in good agreement with the morphologies observed in the SEM images in Figure 4.4, where porosity is observed between the flakes. Broadly speaking, there are strong similarities between the LDH/BNOx membranes developed here, and BN and BNOx-based membranes previously developed by our group.[10,21] In particular, a BN membrane exfoliated in *N*-methyl-2-pyrrolidone exhibited a total pore volume of 0.76 cc/g and a sharp pore size distribution peak at approximately 100 nm. Like that membrane, we consider the LDH/BNOx membrane developed here to be a low bulk density material with an open, interconnected porous network.

Thus, the combination of SEM, TEM, and mercury porosimetry confirms that the LDH nanosheets integrate well into the BNOx-based membranes, and therefore should not cause any major differences in NF performance.

### 4.3.2 Nanofiltration performance of LDH/BNOx nanocomposite membranes

Once it was confirmed that the LDH/BNOx nanocomposite could be used to produce uniform membranes of similar morphology and pore characteristics to previously reported BN and BNOx membranes, these membranes were assessed for their ability to remove water-soluble dyes from water. Two azo dyes (EB and MO), a triarylmethane dye (RhB) and a thiazine dye (MB) were tested, to examine the ability of the membranes to retain dyes of various sizes, charges (anionic vs. cationic) and functional groups. The dye retention performance of the membranes was tested by passing 20 mL aliquots of the dye through the membranes, and examining the difference in absorption of the feed and filtrate solutions, as per previous reports.[10,21] The UV-Vis absorption spectra of feeds and samples of permeates of all four dyes are shown in Figure 4.8. The absorbance values at $\lambda_{max}$ for each dye were recorded, and the retentions of each dye were calculated using Equation 2.2. The average retentions of each dye are shown in Table 4.1, along with the number of membranes evaluated in each case.

Table 4.1: Mean dye retention by nanocomposite membranes, and the number of membranes tested in each case.

| Dye tested | Mean retention (%) | No. of membranes tested |
|---|---|---|
| Evans Blue (15 μM) | 99.7 ± 0.4 | 8 |
| Methylene Blue (27 μM) | 99.9 ± 0.1 | 5 |
| Methyl Orange (50 μM) | 96.8 ± 3.1 | 11 |
| Rhodamine B (20 μM) | 97.4 ± 2.1 | 5 |

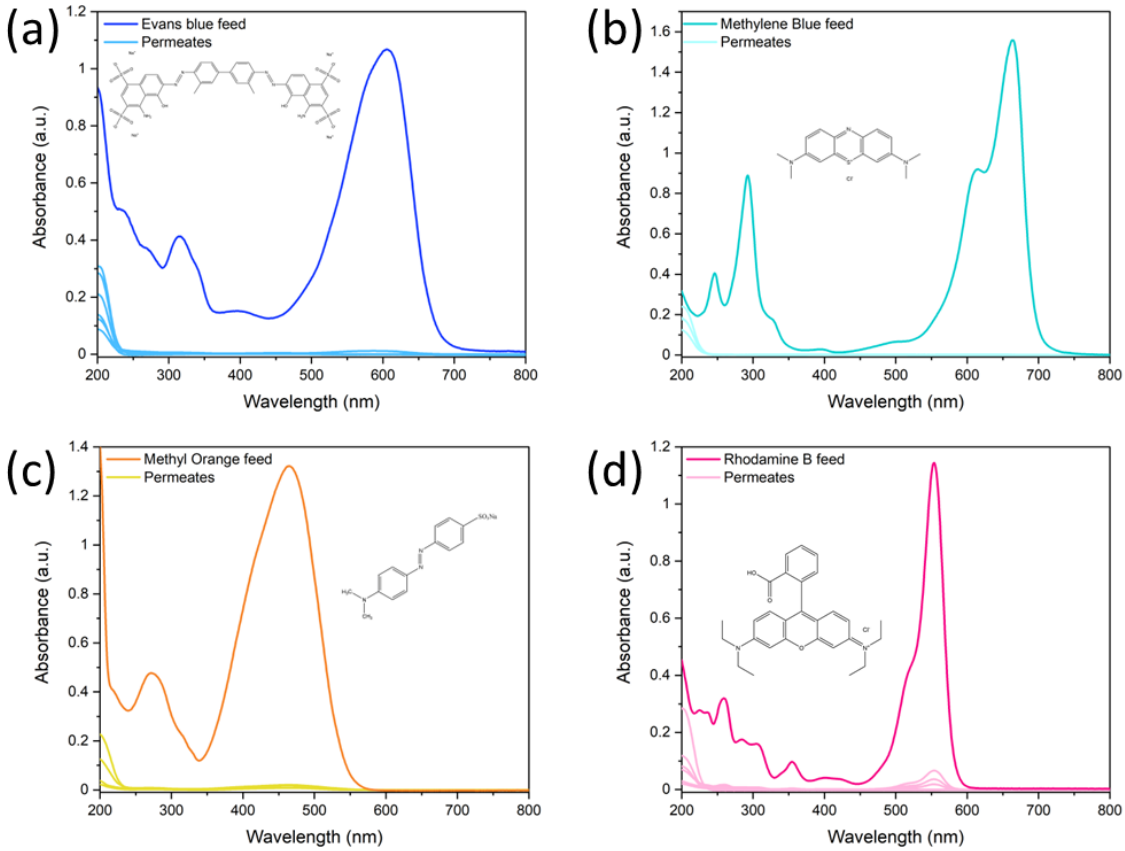


Figure 4.8: UV-Vis spectra demonstrating the retention of 20 mL of (a) Evans Blue (15 µM), (b) Methylene Blue (27 µM), (c) Methyl Orange (50 µM) and (d) Rhodamine B (20 µM) by LDH/BNOx NF membranes.

These retention values compare favourably with some of the best in literature for BN/BNOx-based membranes, as well as other 2D material-based membranes.[44,45] For example, amino-functionalised h-BN membranes showed excellent retention for larger molecules such as EB ($>$ 99%), but much lower values for smaller molecules such as MB MB (50.3%) and RhB (58.3%). However, the retention can be greatly improved to 94.1% for MB and $>$ 99% for RhB by increasing the membrane thickness.[18] GO membranes have been demonstrated to have dye rejection values of 98.4%, 98.9% and 86.4% for MO, MB and RhB respectively.[46] $WS_2$-based membranes exhibited retentions of 90% for EB.[47] It is therefore evident that the LDH/BNOx membranes reported exhibit exceptional retention

for larger dyes such as EB (dimensions: 1.2 nm x 3.1 nm), as well as smaller dyes such as MB (dimensions: 1.4 nm x 0.6 nm), and are in line with some of the best results reported in the literature.

The mechanism of dye removal from water by LDHs generally follows two schemes – incorporation of the dye into the LDH interlayer gallery *via* anion exchange, and dye adsorption to the nanosheet surface.[48] Carbonate-intercalated LDHs typically are the most stable sub-type, as the divalent carbonate anion is held strongly in the LDH interlayer, so adsorption *via* anion exchange in these LDHs is less commonly observed.[49] The dominant adsorption mechanism therefore is likely surface sorption. LDHs have a positive surface charge, so tend to preferentially adsorb anionic species through electrostatic interactions.

Interestingly, no clear trend can be observed between the charge of the dye and the retention in this case. It can be observed that EB (an anionic dye) and MB (a cationic dye) both exhibit exceptional retention of up to 100%, with marginally lower values obtained for MO (anionic) and RhB (cationic). This serves as further evidence that the introduction of LDHs into BNOx-based NF membranes has no significant impact on the NF performance. Our previous reports on BNOx NF membranes indicates the partial negative surface charge may have a small effect on the retention compared to pristine BN, resulting in marginally higher retention of cationic dyes.[21] However, the dominant retention mechanism observed is likely a result of the BNOx bonding and structure. Hexagonal BN is isostructural to graphene, with $sp^2$-hybridised alternating B and N atoms in a hexagonal arrangement, resulting in electron delocalisation and a resultant $\pi$-system. It has been reported that a major factor in the high retention values and high adsorption capacities of BN and BNOx towards dye molecules is due to $\pi$-$\pi$ interactions.[50,51] It is therefore evident here that BNOx is the material responsible for the high retention values in the LDH/BNOx nanocomposite membranes.

Another key measure of membrane performance is the water flux or permeance. While high retention capacity is a vital property of high-performance water purification membranes, it must be ensured that this does not compromise come at the cost of water transport across the membrane. In order to more accurately assess the suitability of our NF system for water purification, solvent flux studies were carried out on both the LDH/BNOx membranes, as well as the PVDF support. The results of the membrane flux studies are summarised in Table 4.2, with the PVDF template flux results shown in Appendix C (Table C2).

Table 4.2: Summary of water flux results of LDH/BNOx nanocomposite membranes on PVDF support.

| | *1st run* | *2nd run* | *3rd run* | **Average** |
|---|---|---|---|---|
| *Time (s)* | 44.87 | 47.20 | 46.40 | $\mathbf{46.16 \pm 0.97}$ |
| *Flux (L $m^2$ $h^{-1}$)* | 1672 | 1589 | 1616 | $\mathbf{1626 \pm 35}$ |

The hydrophilic PVDF template exhibited low resistance to water flow, as expected, with high flux values of 7360 ± 232 L $m^{-2}$ $h^{-1}$ at an operating pressure of 1 bar. The pure water permeance of the LDH/BNOx membranes on the PVDF support was measured to be 1626 ± 35 L $m^{-2}$ $h^{-1}$, which is slightly higher than previously reported BNOx membranes (1163 L $m^{-2}$ $h^{-1}$).[21] The water flux is very high for a membrane of this thickness, when compared with the literature. For example, these membranes exhibit water permeance rates comparable with amino-functionalised h-BN membranes with 0.4 μm thickness (1500 L $m^{-2}$ $h^{-1}$) reported by Chen *et al.*[18] Das *et al.* reported 0.35 μm-thick non-functionalised h-BN/PVDF membranes with flux rates of 1240 L $m^{-2}$ $h^{-1}$.[52] Furthermore, the LDH/BNOx membranes reported here exhibit flow rates more than 230 times higher than commercially available NF270-400 membranes (7 L $m^{-2}$ $h^{-1}$ $bar^{-1}$ or 23.8L $m^{-2}$ $h^{-1}$ @ 3.4 bar).[53] The highly efficient flow rate reported here can be attributed to the larger pore size observed for LDH/BNOx membranes compared to their pristine BNOx counterparts, as discussed previously in Section 4.3.1.

### 4.3.3 Adsorption behaviour of LDH/BNOx nanocomposite membranes

An analysis of the adsorption behaviour of the nanocomposite membranes was conducted to better understand the membrane retention mechanism. UV-Vis spectra showing the adsorption of each of the dyes over time is shown in Figure 4.9.

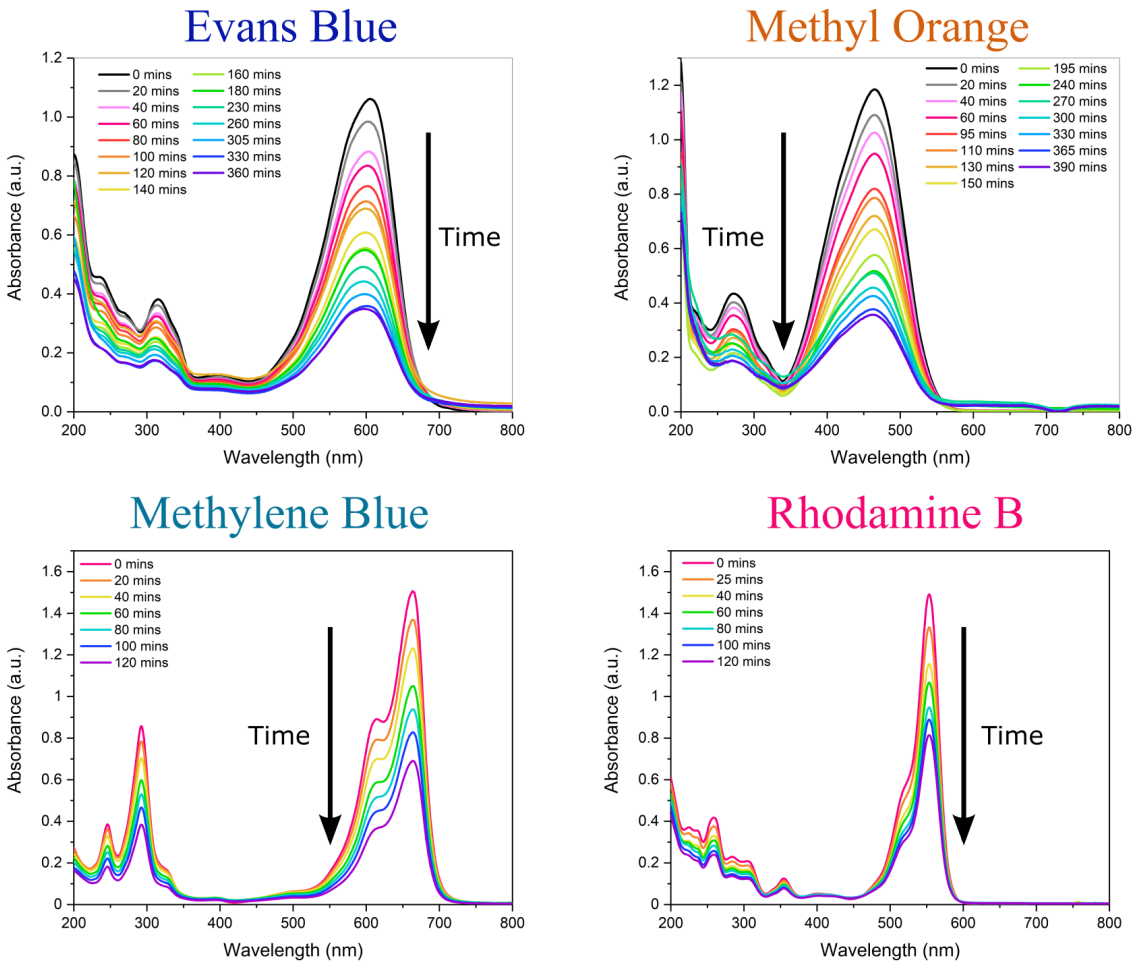


Figure 4.9: UV-Vis absorbance spectra demonstrating adsorption of EB, MO, MB and RhB on LDH/BNOx nanocomposite membranes over time.

Adsorption of dyes on many nanomaterials, including both BN and LDHs, is often best described by the pseudo-second-order (PSO) kinetic model.[54,55] Here, we observe two distinct adsorption behaviours in the case of these nanocomposite membranes, which are seemingly dependent on the charge of the dyes. The anionic dyes (EB and MO) follow an expected PSO adsorption model, as shown in Figure 4.10 (a,b)

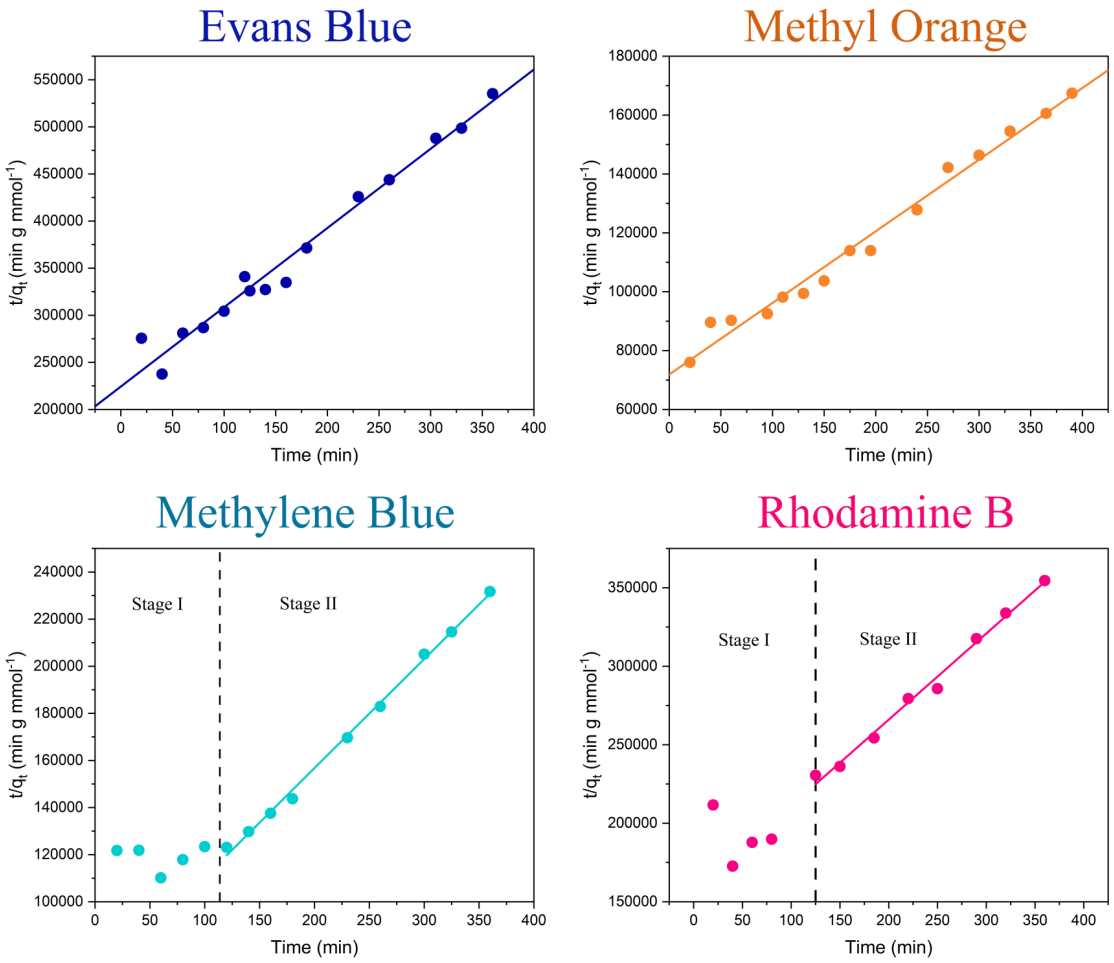


Figure 4.10: Pseudo-second-order models for adsorption of EB, MO, MB and RhB on LDH/BNOx nanocomposite membranes.

LDHs typically have a stronger adsorption capacity for anionic dyes due to attractive electrostatic interactions. However, here we observe the rate remaining constant over the

experiment in the case of the anionic dyes, whereas a change in rate would generally be expected as more LDH sites are occupied. This reaffirms the point that the π-π interactions between the BNOx and the dyes dominate over the electrostatic forces in the retention process, and serves as an explanation as to why there is no observable trend between the charge of the dyes and the retention of the membrane.

However, for the cationic dyes (MB and RhB), we see a deviation from simple PSO-type adsorption behaviour, as shown in Figure 4.10 (c,d). The observed adsorption data for MB and RhB can be split into two "stages" – stage I with fluctuating values and no clear correlation to the PSO model, and a stage II which fits nicely to the PSO model. To gain further insight into this charge-dependant adsorption behaviour, the intra-particle diffusion (IPD) model was applied to the adsorption of all four dyes by the nanocomposite, as shown in Figure 4.11.[56,57]

For anionic dyes (EB and MO), the data is observed to fit the linear intra-particle diffusion model, with high $R^2$ values. According to the IPD model, if the straight line plot of $q_t$ vs $t^{0.5}$ does not pass through the origin, then IPD is not the rate limiting step.[58,59] It can be observed for all dyes that none of the lines pass through the origin, indicating another adsorption process occurring in conjunction with IPD. This is likely the π-π interactions previously discussed, as well as electrostatic interactions between the dyes and the nanocomposite.

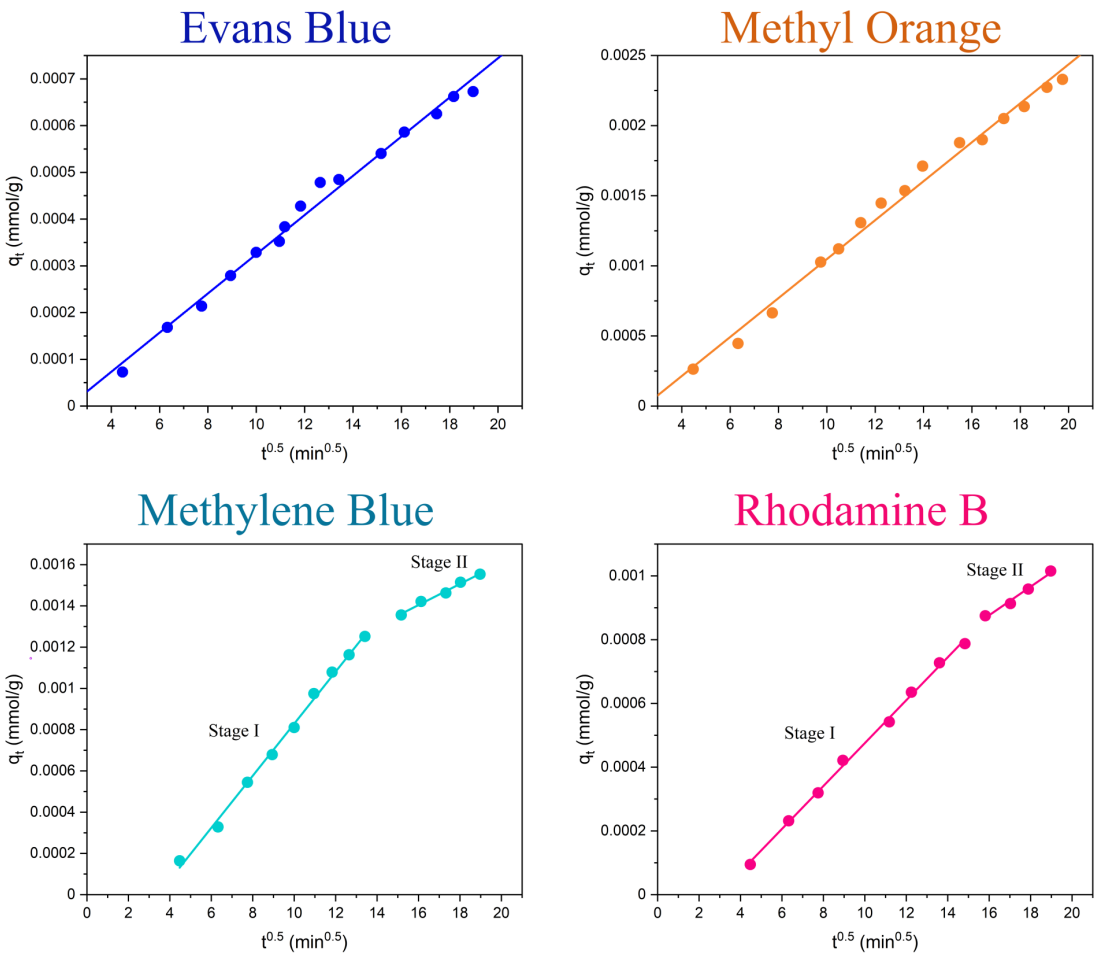


Figure 4.11: Intra-particle diffusion kinetic models for adsorption of EB, MO, MB and RhB on LDH/BNOx nanocomposite membranes.

However, for the cationic dyes (MB and RhB), a multi-linear adsorption profile can be observed. This is particularly evident in the case of MB. It is once again clear that two distinct adsorption processes occur, denoted stages I and II. Stage I is a sharper region and represents rapid surface adsorption. Stage II can be characterised by a smaller slope and the slower diffusion of the dyes into the pores of the membrane. The fitting parameters obtained from modelling the adsorption data with both the PSO and IPD kinetic models are presented in Tables 4.3 and 4.4, respectively.

Table 4.3: Parameters obtained from fitting PSO model to adsorption of dyes by LDH/BNOx nanocomposites

| **Dye** | $\mathbf{k_{PSO}}$ **(g mmol$^{-1}$ min$^{-1}$)** | $\mathbf{q}_e$ **(mmol g$^{-1}$)** | $\mathbf{R}_{PSO}{}^2$ |
|---|---|---|---|
| EB | 3.516 | 0.0012 | 0.9748 |
| MO | 0.823 | 0.0041 | 0.9843 |
| MB | 3.3339 | 0.0022 | 0.9972 |
| RhB | 1.924 | 0.0018 | 0.9914 |

Table 4.4: Parameters obtained from fitting IPD model to adsorption of dyes by LDH/BNOx nanocomposites

| **Dye** | $k_1$ **(mmol g$^{-1}$ min$^{-0.5}$)** | $\mathbf{R}_1{}^2$ | $k_2$ **(mmol g$^{-1}$ min$^{-0.5}$)** | $\mathbf{R}_2{}^2$ |
|---|---|---|---|---|
| EB | 4.193 x $10^{-5}$ | 0.9901 | - | - |
| MO | 1.389 x $10^{-4}$ | 0.9909 | - | - |
| MB | 1.262 x $10^{-4}$ | 0.9964 | 5.112 x $10^{-5}$ | 0.9880 |
| RhB | 6.432 x $10^{-5}$ | 0.9979 | 4.480 x $10^{-5}$ | 0.9841 |

We propose that this two-stage adsorption process arises for adsorption of cationic dyes due to the composition of the nanocomposites. Zeta potential measurements of the LDH/BNOx nanocomposite, as shown in Figure 4.12, indicate a partial negative surface charge ($\zeta_{LDH/BNOx}$ = -8.12 mV). A larger proportion of partially negatively charged BNOx than LDH in the nanocomposite attracts the cationic dyes to the surface faster, followed by a slow diffusion into the pores and retention by $\pi$-$\pi$ interactions, resulting in two distinct rates arising from the IPD model.

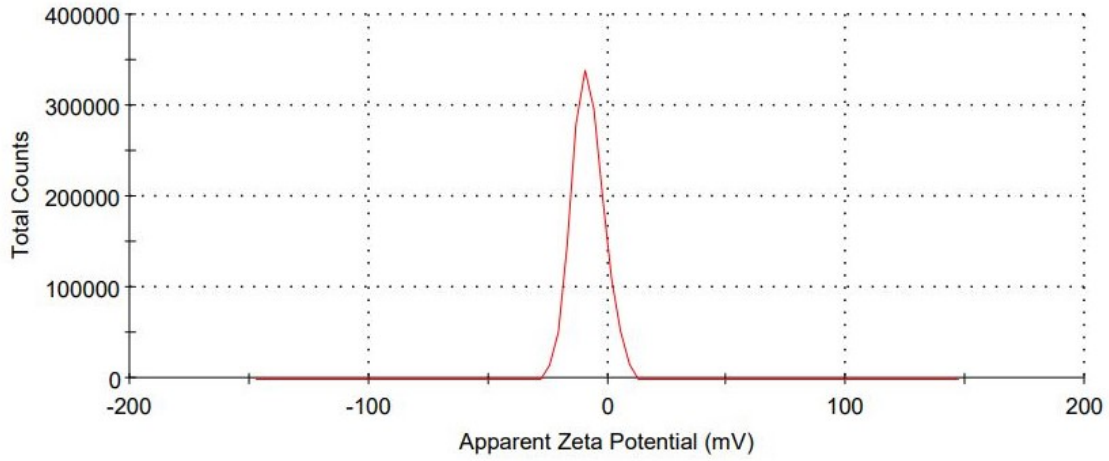


Figure 4.12: Zeta potential distribution of LDH/BNOx nanocomposite. Data acquired using MP $H_2O$ as solvent (pH 7).

### 4.3.4 Photocatalytic degradation of dyes by LDH/BNOx nanocomposite membranes

The excellent retention values of these membranes are in line with our previous reports, as well as other reports for similar systems in literature, and present an efficient route to water purification. However, a main drawback of pristine BN and BNOx-based membranes is fouling. The adsorption of the aforementioned dyes by the membranes leads to saturation of the BNOx nanosheets and blockage of the pores, which in turn results in lower retention values and flow rates over time, limiting their reusability. A potential method to overcome this key issue is the integration of photocatalysts in these membranes. Transition metal-containing LDHs have been previously reported to be promising photocatalysts for a variety of reactions, including photodegradation of water soluble dyes such as methyl orange and malachite green.[31,60–62] Therefore it was decided to exploit this property, and test the anti-fouling capabilities of these LDH-containing membranes using a simple, low-cost household

visible light source.

10 µL of 30% w/w $H_2O_2$ was used to boost the catalytic activity, the reasons for which will be discussed in Section 4.3.5.[63] The photocatalytic performance of the LDH/BNOx nanocomposite membranes for the degradation of EB, MB, MO and RhB was monitored using UV-Visible spectroscopy. Briefly, pristine membranes were submerged in the dye solution, the $H_2O_2$ was added, they were exposed to light, and aliquots were taken every 10 minutes for UV-Vis analysis. Figure 4.13 shows the reduction in the maximum absorbances as a result of decolourisation of the solutions, due to degradation of each of the dyes.

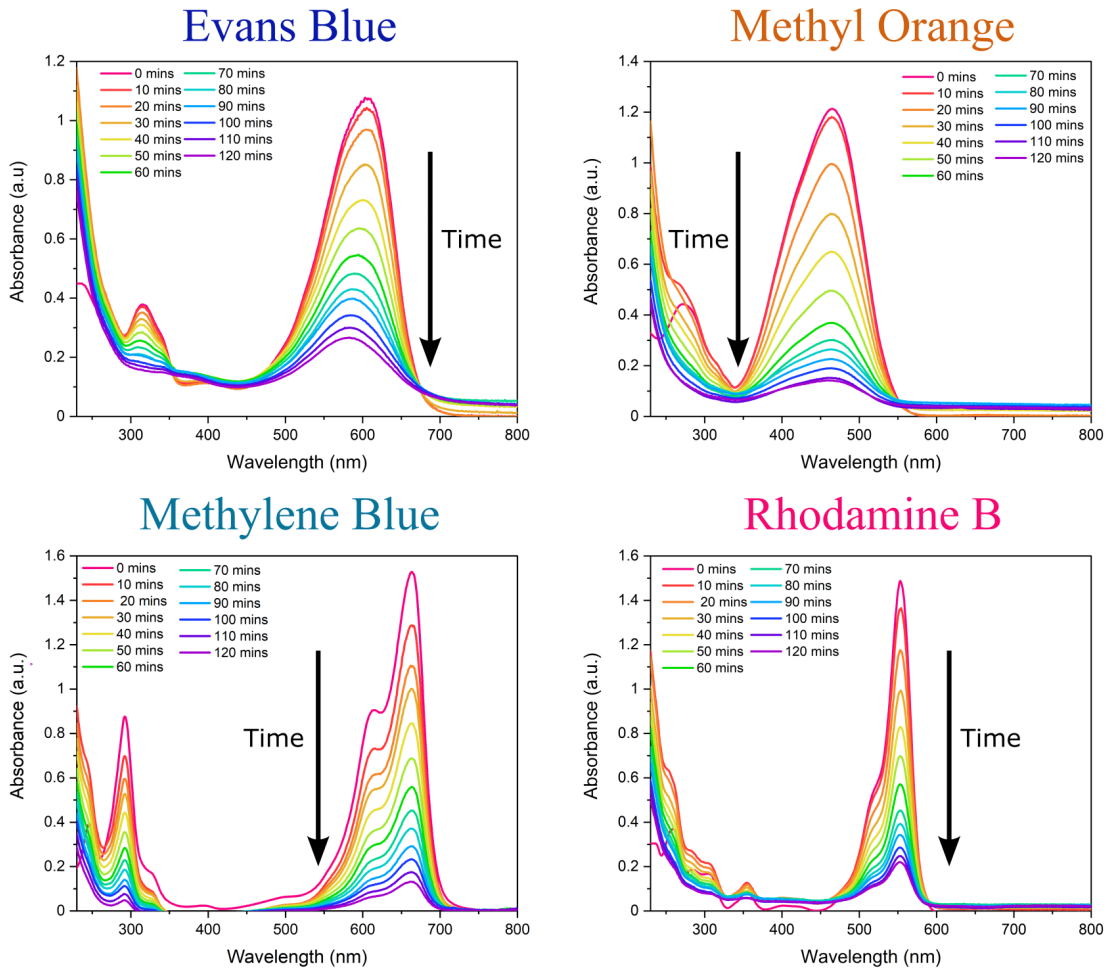


Figure 4.13: Reduction in UV-Vis absorbance of EB, MO, MB and RhB by visible-light photodegradation in presence of LDH/BNOx membrane catalysts and 10 µL of $H_2O_2$ (30 % w/w).

It can be observed that each of the dyes is degraded significantly over a 120-minute time frame, with the best result being achieved for MB. It is also important to highlight the significance of the result of degradation of EB by these nanocomposites, as reports of the visible-light photodegradation of EB are difficult to find. While there are numerous reports in the literature on the use of LDHs for adsorption-driven removal of EB from wastewater, to the best of our knowledge, this is the first report of EB degradation using a LDH-based photocatalyst.[33–35]

Photographs of membrane samples after filtration and after photodegradation are shown in Figure 4.14. The membranes can be seen to return completely to their original pale blue colour after the photodegradation process. The best results for each of the dyes are presented here, however each experiment was conducted in triplicate – the results of the other runs are shown in Appendix C (Figure C11 and Table C3)

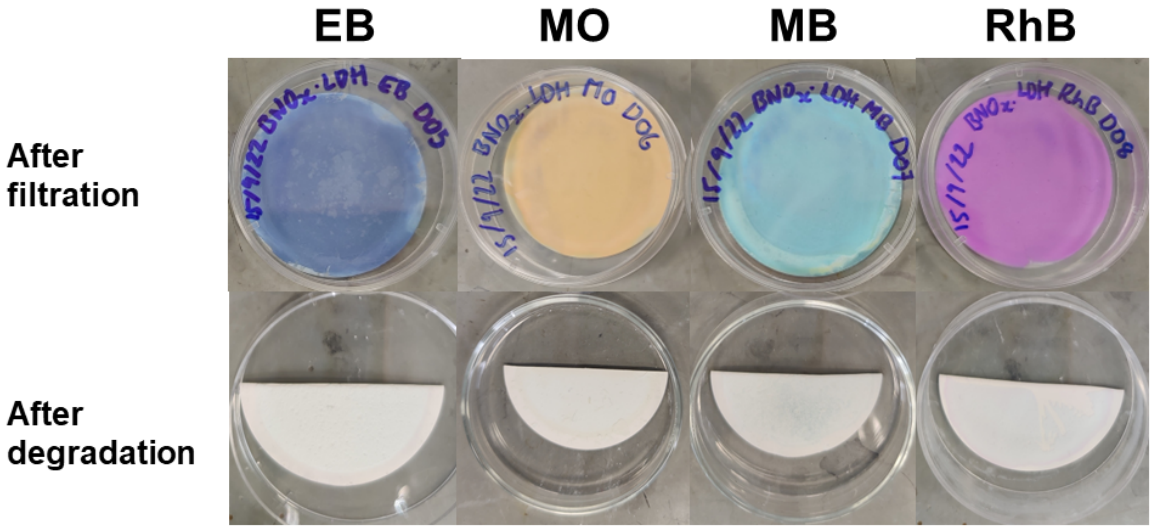


Figure 4.14: Pictures of membranes before (top) and after (bottom) photodegradation using 10 μL $H_2O_2$ (30% w/w) and a 5W COB LED.

The dye photodegradation process was modelled by PFO kinetics. The kinetics of organic dye degradation is often best described by the Langmuir-Hinshelwood model, which at low dye concentrations - as we have here - can be simplified to a PFO model.[64] The

apparent PFO rates for the best run of each dye, as well as average rates, are summarised in Figure 4.15 and in Table 4.5.

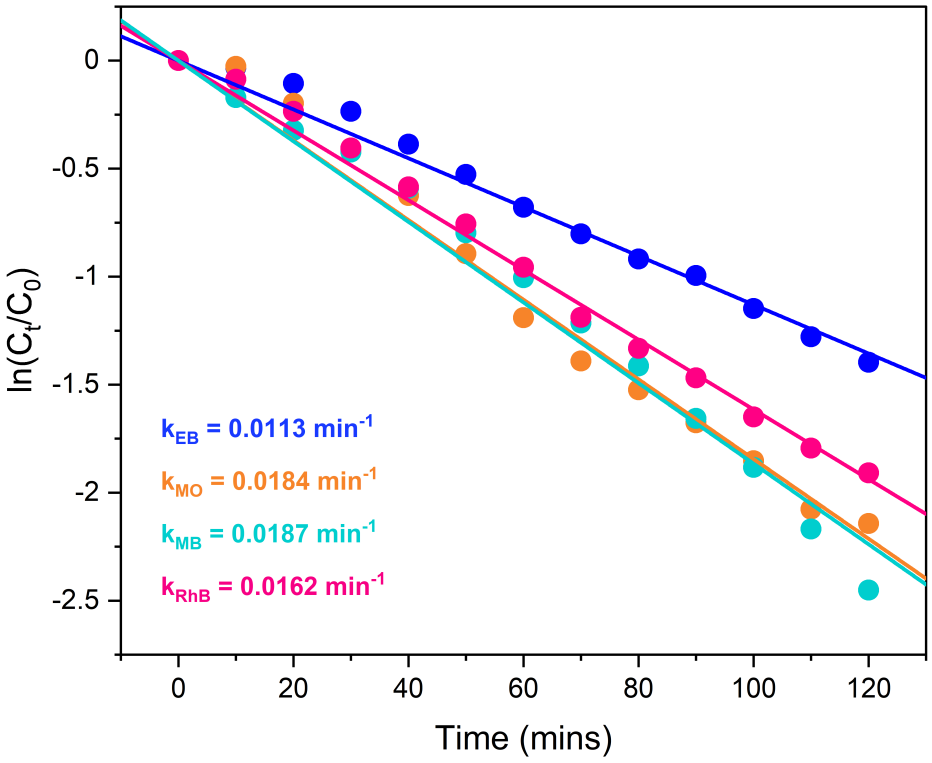


Figure 4.15: PFO models for degradation of EB (dark blue), MO (orange), MB (turquosie) and RhB (fuschia).

Table 4.5: Degradation extents at t = 120 mins, and PFO model rate constants for degradation of dyes by LDH/BNOx nanocomposite membranes.

| **Dye** | **Degradation %** | **Best $k_1$ ($min^{-1}$)** | $R_1^2$ | **Average $k_1$ ($min^{-1}$)** |
|---|---|---|---|---|
| EB | 75 | 0.0113 | 0.9950 | 0.0091 ± 0.0019 |
| MO | 88 | 0.0184 | 0.9949 | 0.0131 ± 0.0040 |
| MB | 91 | 0.0187 | 0.9934 | 0.0174 ± 0.0021 |
| RhB | 85 | 0.0162 | 0.9980 | 0.0151 ± 0.0008 |

The PFO degradation rate constants obtained for the LDH/BNOx catalytic membrane compare favourably to similar systems reported in the literature. For example, a Co-based LDH synthesised in water, using 40 μL of $H_2O_2$ in the photodegradation process, had a calculated rate constant of 3.5 x $10^{-3}$ $min^{-1}$ for degradation of RhB.[65] Nayak *et al.* synthesised MgCr LDH nanoplatelets for sunlight-driven degradation of RhB in the absence of $H_2O_2$, and calculated the rate constant to be 0.015 $min^{-1}$.[66] Although their light harvesting capabilities are superior, it is preferred to avoid the use of Cr-containing LDHs in water treatment applications if possible, as leaching of $Cr^{3+}$ and $Cr^{6+}$ is a potential hazard depending on the experimental conditions.[40] Ahmed *et al.* reported PFO rate constants of 0.01 $min^{-1}$ for visible-light degradation of MO by NiAl LDH photocatalysts.[28] It is clear therefore that the LDH/BNOx membrane developed here is comparable with existing LDH-based photocatalysts for organic pollutant degradation. Furthermore, the obtained rates of photodegradation for the LDH/BNOx are also comparable to more traditional UV-active metal oxide photocatalysts, such as $TiO_2$ (0.0102 $min^{-1}$ for MO)[67] and ZnO (0.008 $min^{-1}$ for MO)[68], although heterojunctions of the two metals or exotic morphologies tend to outperform our nanocomposite, without the need for $H_2O_2$.[69] Therefore, the degradation rates presented here are significant, with the added benefit of visible light activity.

Control experiments were conducted in the absence of catalyst, and showed insignificant extents of dye degradation in comparison with the photocatalytic nanocomposite membrane, as shown in Figure 4.16. It is clear in the case of EB, MO and RhB that photolysis in the presence of $H_2O_2$ and the absence of catalyst is minimal. A non-negligible degree of photolysis was observed in the case of MB, where roughly 20% of the dye was degraded in the absence of catalyst in 120 minutes. However, this was to be expected, as aqueous solutions of Methylene Blue are prone to photobleaching in the presence of visible light.[70] Nevertheless, the presence of the catalyst in this case clearly results in a more rapid degradation of the dye.

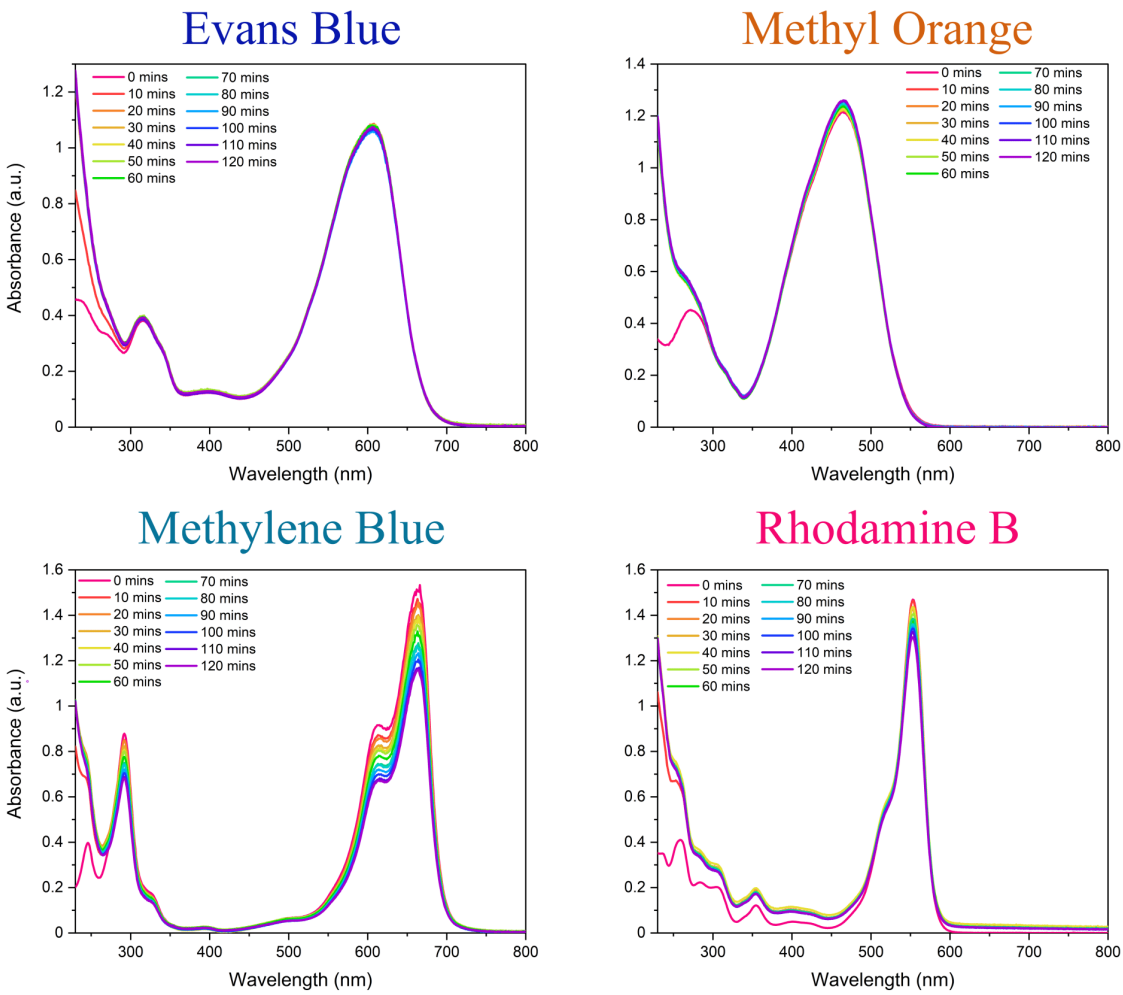


Figure 4.16: Photodegradation control experiment of dyes using 10µµL $H_2O_2$ (30% w/w), a 5W COB LED, and no photocatalytic membrane.

While the removal of the dyes by photodegradation allows for the material to be reused, the membrane itself suffers from mechanical failure, due in part to the generation of gas bubbles under illumination. SEM imaging of the membranes after photodegradation reveals partial exfoliation of the membranes, as well the generation of spherical cavities due to evolution of gases during the reaction (Figure 4.17).

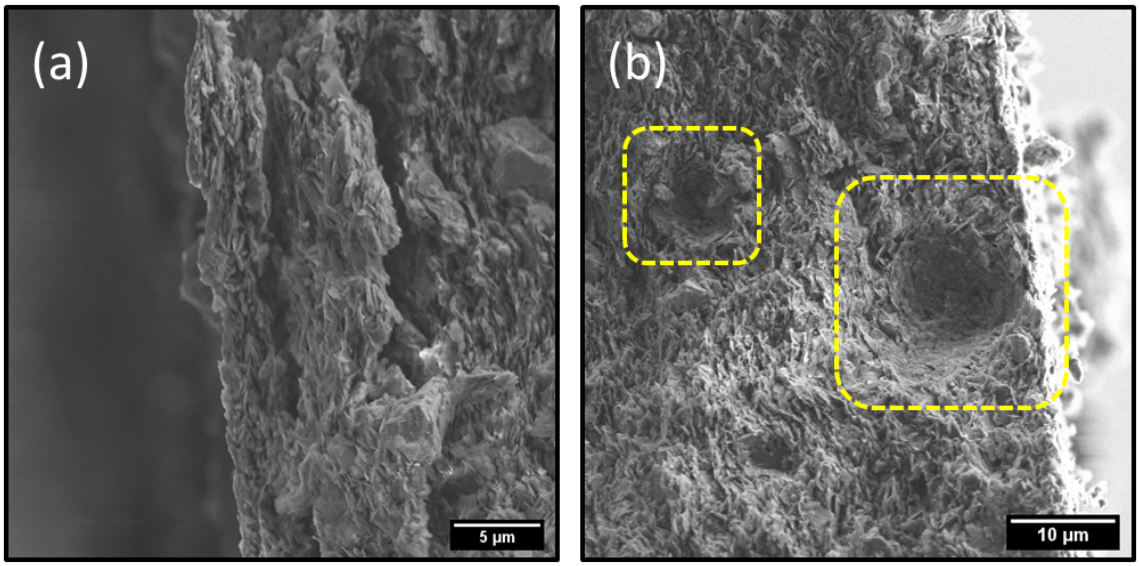


Figure 4.17: SEM images depicting (a) exfoliation of membrane and (b) formation of micro-bubble shaped cavities in membrane during photodegradation process.

Despite the excellent retention, flux, and catalytic activity of these membranes, it is evident that further research is needed to address the mechanical integrity and ensure the device itself is reusable - not just the material it consists of. Chemical cross-linking of the nanosheets within the membrane would be one of the best strategies to address the issues with mechanical stability. Nevertheless, the efficient and rapid visible-light photodegradation of the dyes in these high-retention, high-flux membranes is an exciting and promising result in the search for efficient NF membranes that are resistant to fouling.

### 4.3.5 Proposed photodegradation mechanism

Bulk h-BN is an indirect wide bandgap semiconductor, with reported bandgap values in the deep UV ($\sim$ 6 eV).[71] While an indirect-to-direct bandgap transition has been theorised on reducing the thickness of h-BN from few-layer to monolayer, the band-gap value remains large (6.46 eV). Photocatalysis has been observed in BN, however it is achieved through introduction of defects, and using UVC illumination.[72] For these reasons, it is unlikely that there is any significant contribution from BNOx to the visible-light photocatalytic activity observed in this study. The source of photocatalytic degradation can be primarily assigned to the presence of CuAl-$CO_3$ LDH in the nanocomposite in this case.

UV-Vis absorption spectra of LDHs can provide key information on their suitability as visible light photocatalysts.[24] Due to the intense light scattering exhibited by 2D nanosheets in solution, it is necessary to carry out the UV-Vis in solid state using DR UV-Vis to identify the key absorption features.[73] The DR UV-Vis spectrum of CuAl-$CO_3$ LDHs reveals two main absorption features – the first centred around 475 nm, which can be attributed to $O^{2-}$ to $Cu^{2+}$ ligand to metal charge transfer, and the second at 700 nm, associated with $Cu^{2+}$ $d-d$ transitions, as described in earlier chapters. These significant absorption features in the visible region, as shown in Figure 4.18, indicate the CuAl-$CO_3$ LDH is a good candidate for visible-light photocatalysis.

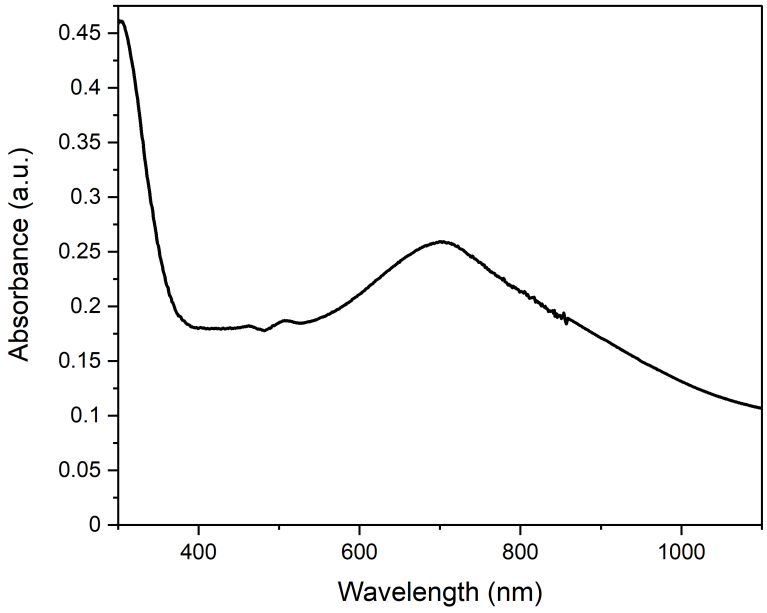


Figure 4.18: DR UV-Vis spectrum of CuAl-$CO_3$ LDHs.

As LDHs function as doped semiconductors, photocatalysis in LDHs is commonly accepted to be due to formation of electron-hole pairs as a result of light absorption. This behaviour has been well described by Baliarsingh *et al.*, as well as Xia *et al.* for a variety of LDHs, and we propose a similar mechanism for our system.[60,74] Photogenerated holes ($h^+$) react with water in the aqueous dye solution to form hydroxyl radicals ($^\bullet$OH). The photoexcited electrons ($e^-$) react with oxygen adsorbed on the LDH surface from dissolved oxygen in solution, forming superoxide radicals ($O_2^{\bullet-}$) (Equations 4.1 and 4.2).

$$h^+ + \mathrm{H_2O} \rightarrow 2\mathrm{H}^+ + 2\,{}^\bullet\mathrm{OH} \tag{4.1}$$

$$e^- + \mathrm{O_2} \rightarrow \mathrm{O_2^{\bullet-}} \tag{4.2}$$

$O_2^{\bullet-}$ radicals can be protonated to form hydroperoxyl radicals ($HO_2^\bullet$). $H_2O_2$ is

generated by the formation and combination of $HO_2^{\bullet}$ radicals. The reaction between photoexcited electrons and $H_2O_2$ produces more $^{\bullet}OH$ radicals which, along with $O_2^{\bullet-}$, are reactive oxygen species, resulting in degradation of the dyes (Equations 4.3 - 4.5).[60]

$$O_2^{\bullet-} + H^+ \rightarrow HO_2^{\bullet} \tag{4.3}$$

$$2HO_2^{\bullet} \rightarrow H_2O_2 + O_2 \tag{4.4}$$

$$H_2O_2 + e^- \rightarrow {}^{\bullet}OH + OH^- \tag{4.5}$$

Apparent photocatalysis reaction rates in LDHs are limited by both electron-hole pair generation, as well as separation and carrier mobilities.[61,75] $CO_3^{2-}$ intercalation in LDHs is reported to suppress the electron-hole recombination to an extent, thus increasing the apparent reaction rates, however high rates of degradation of dyes under visible-light illumination by pristine binary LDHs, particularly CuAl LDHs, is still rarely reported.[60,76] To overcome this hurdle, 10 μL of 30% (w/w) $H_2O_2$ were added to the solution, which is much less than previous reports for similar systems.[77] The addition of $H_2O_2$ to $Cu^{2+}$-based photocatalytic systems may improve the photocatalytic performance *via* two routes. Firstly, $H_2O_2$ acts as an electron acceptor, reducing the electron-hole recombination rate, thus enhancing the visible-light-driven generation of $^{\bullet}OH$ and $O_2^{\bullet-}$. Secondly, $Cu^{2+}$-containing solids can also drive the catalytic decomposition of $H_2O_2$ to generate $^{\bullet}OH$ radicals *via* Fenton-like redox processes (Equations 4.6 and 4.7).[78,79]

$$Cu^{2+} + H_2O_2 \rightarrow Cu^+ + HO_2^{\bullet} + OH^- \tag{4.6}$$

$$Cu^+ + H_2O_2 \rightarrow Cu^{2+} + {}^{\bullet}OH + OH^- \tag{4.7}$$

In this system, much lower rates of degradation are observed in the absence of

$H_2O_2$. This was demonstrated using RhB where 58% of RhB is seen to be removed from solution after 120 minutes, compared to 85% removal upon addition of $H_2O_2$ (Appendix C, Figure C12). Furthermore, it is difficult to separate the contributions of adsorption and photodegradation processes in the absence of $H_2O_2$ as roughly 45% of RhB is adsorbed at that same point in time in dark conditions. To gain insights into the catalytic mechanism, the terephthalic acid (TA) probe technique was used to monitor the formation of $^{\bullet}$OH radicals. TA is a highly sensitive $^{\bullet}$OH radical probe, reacting to form a fluorescent product – hydroxyterephthalic acid (hTA), which can be monitored using photoluminescence spectroscopy (PL).[80,81] Under excitation with 315 nm light, hTA has a characteristic emission band centred around 420 nm, and the intensity of this emission band while used in this context in photocatalytic systems is representative of more efficient generation of $^{\bullet}$OH radicals. PL emission spectra were recorded for four different environments – TA + LDH/BNOx + dark, TA + LDH/BNOx + dark + $H_2O_2$, TA + LDH/BNOx + light, and TA + LDH/BNOx + light + $H_2O_2$, as shown in Figure 4.19.

It can be observed that in the absence of light and $H_2O_2$, there is no measurable emission that is characteristic of the presence of hTA, meaning there is little-to-no $^{\bullet}$OH radical generation in these conditions. Upon addition of $H_2O_2$, the appearance of a significant emission peak can be observed in dark conditions, confirming that the LDH/BNOx acts as a Fenton-type catalyst. Exposure to light in the absence of $H_2O_2$ results in the generation of a low intensity emission peak, which is to be expected, as generation of $^{\bullet}$OH radicals by LDHs is limited by electron-hole recombination.

The most intense signal is observed when the LDH/BNOx catalyst is exposed to light in the presence of $H_2O_2$, resulting in the formation of more $^{\bullet}$OH radicals through both Fenton-type reactions, as well as from photoexcited electrons and photogenerated holes. Based on these experimental observations, we propose that the catalytic mechanism is a synergistic process, with contributions from $Cu^{2+}$-based photo-Fenton-type chemistry, as

well as the semiconducting behaviour of CuAl-$CO_3$ LDHs.

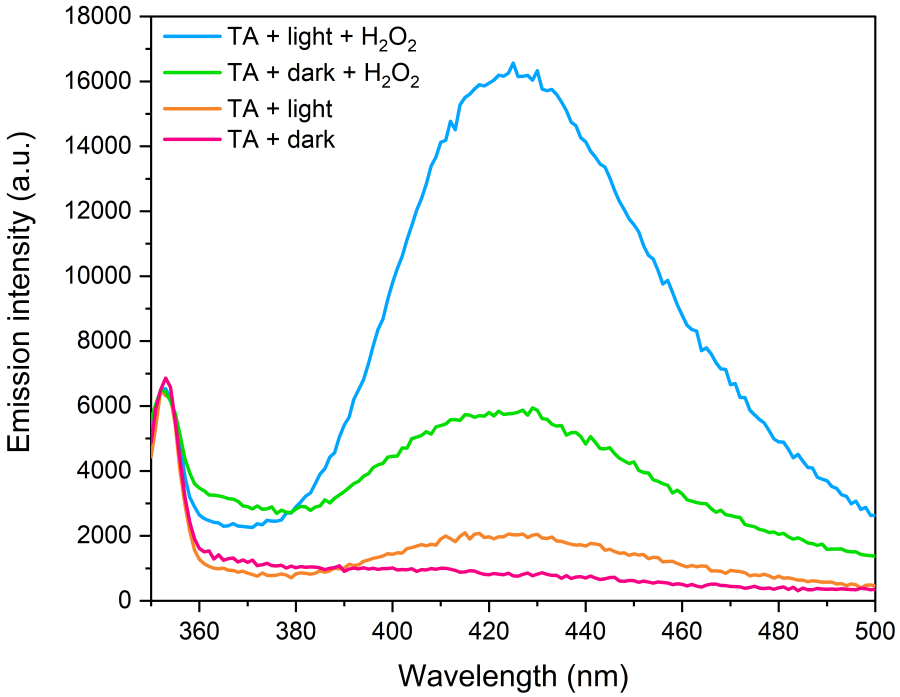


Figure 4.19: Photoluminescence emission spectra of hydroxyterephthalic acid generated using LDH/BNOx catalyst.

•OH radicals are expected to initiate degradation of these dyes by disrupting the chromophores, *via* azo bond cleavage in EB and MO, and ring opening mechanisms in the case of RhB and MB. UV-Vis provides indirect evidence of this proposal in the case of EB – a diazo dye - as a decrease in UV-Vis absorbance intensity is accompanied by a significant blue shift $\lambda_{max}$ from 608 nm to 580 nm (Figure 4.13). This is indicative of a reduction in the extent of conjugation due to reduction and subsequent cleavage of the azo bond.[82] Tentative proposed mechanisms of the initial steps of degradation of each of the dyes are shown in Figure 4.20, based on experimental observations for EB, as well as evidence in the literature for similar systems for degradation of the other dyes.[83–86]

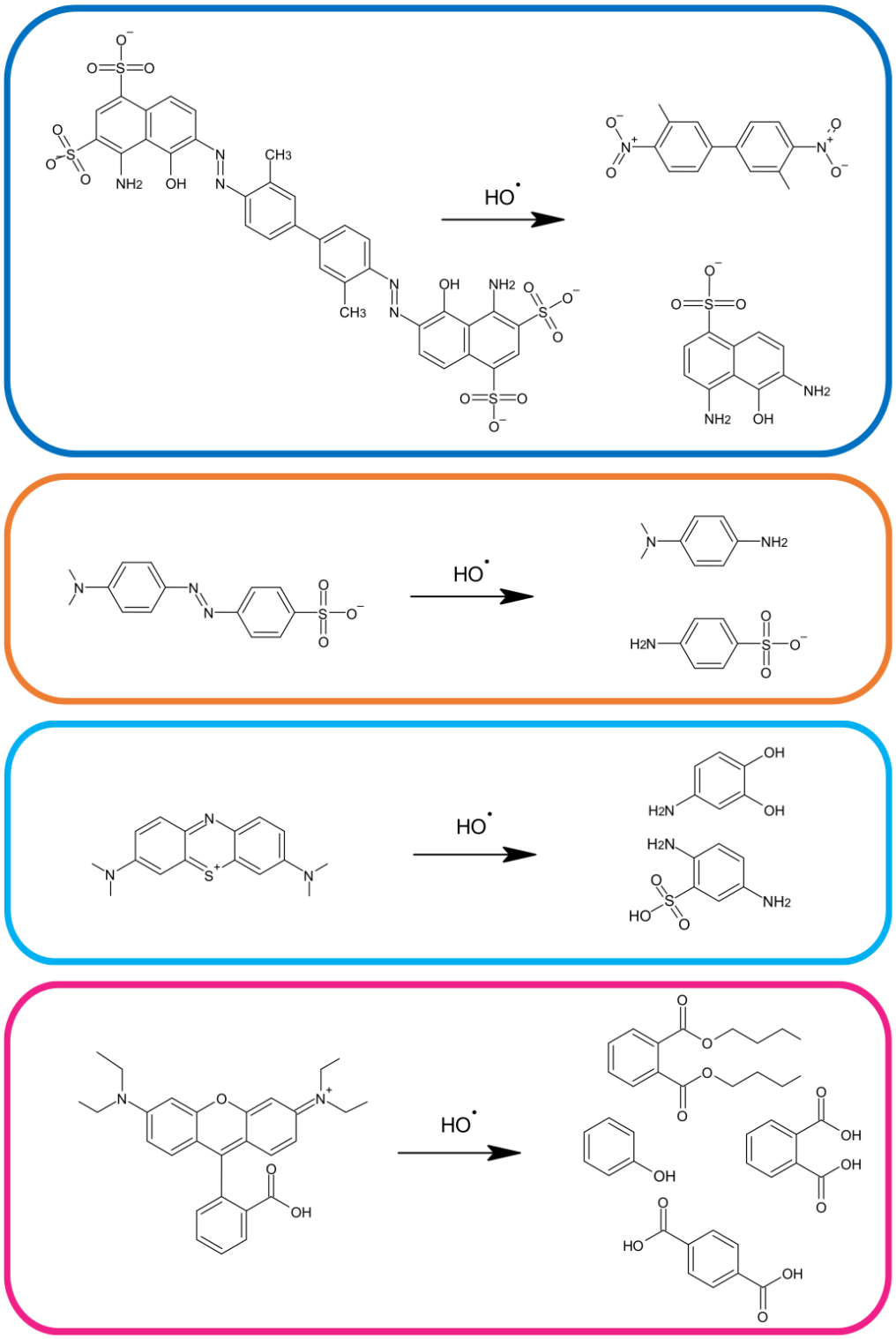


Figure 4.20: Proposed mechanisms of initial degradation steps of (from top to bottom) EB, MO, MB and RhB by hydroxyl radicals.

## 4.4 Conclusions

Thus, we have produced a novel, electrostatically stabilised CuAl-$CO_3$ LDH/BNOx nanocomposite through a mixture of top-down and bottom-up synthetic techniques. This nanocomposite was used to develop novel, high-performance LDH/BNOx membranes for advanced NF applications. The membranes have been produced using a multi-step process, including co-precipitation, liquid-phase exfoliation, and vacuum filtration techniques. The excellent NF performance of these membranes was demonstrated, with up to almost 100% dye retention being achieved for multiple water-soluble dyes with varying sizes and charges. The dye retention results, as well as solvent flux, are in line with some of the best reported to date. Furthermore, the membranes have demonstrated excellent photocatalytic degradation and removal of dyes under visible-light ambient conditions. This approach should enable us to address the critical membrane fouling problem, allowing for regeneration and re-use of the membranes. These results are summarised graphically in Figure 4.21. However, currently our membranes are fragile and require the presence of the Durapore PVDF membrane filter template as a substrate for mechanical stability. Our future work will involve the improvement of the mechanical stability of membranes by chemical cross-linking of the nanosheets, to produce membranes with higher mechanical integrity. Nevertheless, we believe this work represents a significant step forward in advanced nanofiltration technologies, and playing our part in achieving UN SDG6. We also believe that our approach to use 2D nanomaterials with opposite surface charges to produce electrostatically stabilised 2D nanocomposites opens up new exiting opportunities in development of new membrane materials with a broad range of important applications.

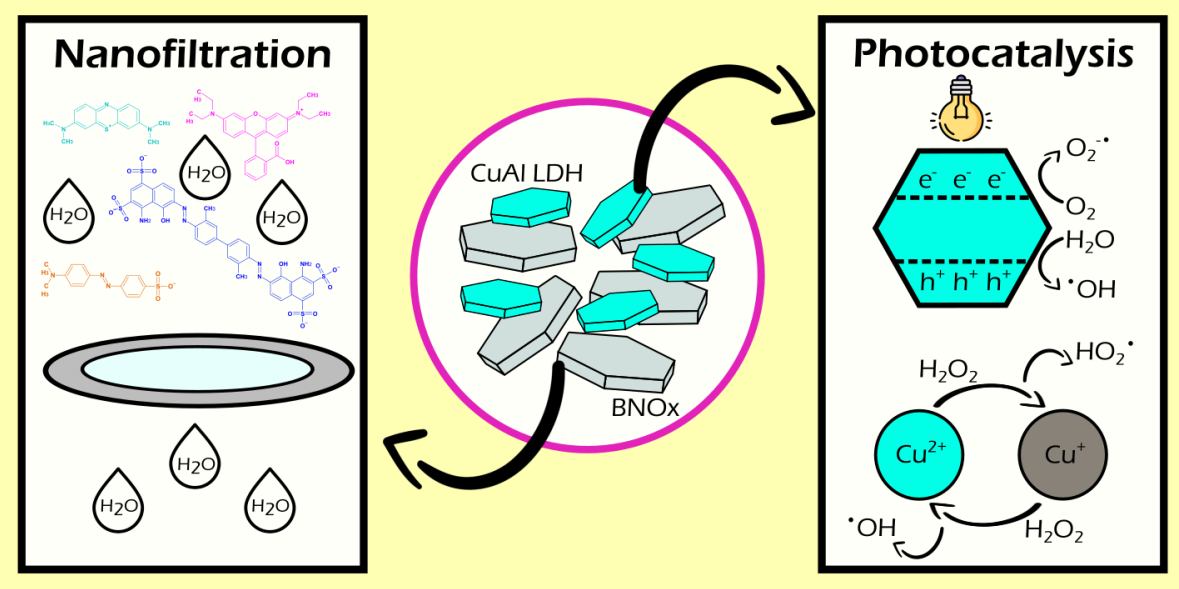


Figure 4.21: Graphical summary of the main outcomes of this body of work.

# References


(1) *Progress on household drinking water, sanitation and hygiene I 2000-2017*; tech. rep.; New York: United Nations Children's Fund (UNICEF) and World Health Organisation, 2019.

(2) Kishor, R.; Purchase, D.; Saratale, G. D.; Saratale, R. G.; Ferreira, L. F. R.; Bilal, M.; Chandra, R.; Bharagava, R. N. *Journal of Environmental Chemical Engineering* **2021**, *9*, 105012.

(3) Imran, M.; Crowley, D. E.; Khalid, A.; Hussain, S.; Mumtaz, M. W.; Arshad, M. *Reviews in Environmental Science and Biotechnology* **2015**, *14*, 73–92.

(4) Khatri, J.; Nidheesh, P. V.; Anantha Singh, T. S.; Suresh Kumar, M. *Chemical Engineering Journal* **2018**, *348*, 67–73.

(5) McMullan, G.; Meehan, C.; Conneely, A.; Kirby, N.; Robinson, T.; Nigam, P.; Banat, I. M.; Marchant, R.; Smyth, W. F. *Applied Microbiology and Biotechnology* **2001**, *56*, 81–87.

(6) Lellis, B.; Fávaro-Polonio, C. Z.; Pamphile, J. A.; Polonio, J. C. *Biotechnology Research and Innovation* **2019**, *3*, 275–290.

(7) Morshed, M. N.; Al Azad, S.; Deb, H.; Shaun, B. B.; Shen, X. L. *Journal of Water Process Engineering* **2020**, *33*, 101062.

(8) Srivastava, S.; Sinha, R.; Roy, D. *Aquatic Toxicology* **2004**, *66*, 319–329.

(9) García Doménech, N.; Purcell-Milton, F.; Gun'ko, Y. K. *Materials Today Communications* **2020**, *23*, 100888.

(10) García Doménech, N.; Purcell-Milton, F.; Arjona, A. S.; García, M.-L. C.; Ward, M.; Cabré, M. B.; Rafferty, A.; McKelvey, K.; Dunne, P.; Gun'ko, Y. K. *Nanomaterials* **2022**, *12*, 473.

(11) Vrijenhoek, E. M.; Hong, S.; Elimelech, M. *Journal of Membrane Science* **2001**, *188*, 115–128.

(12) Yang, L.; Zhang, X.; Rahmatinejad, J.; Raisi, B.; Ye, Z. *Journal of Membrane Science* **2023**, *670*, 121355.

(13) Jhaveri, J. H.; Murthy, Z. V. *Desalination* **2016**, *379*, 137–154.

(14) Chen, X.; Qiu, M.; Ding, H.; Fu, K.; Fan, Y. *Nanoscale* **2016**, *8*, 5696–5705.

(15) Sun, L.; Huang, H.; Peng, X. *Chemical Communications* **2013**, *49*, 10718.

(16) Coogan, Á.; Gun'ko, Y. K. *Materials Advances* **2021**, *2*, 146–164.

(17) Homaeigohar, S.; Elbahri, M. *NPG Asia Materials 2017 9:8* **2017**, *9*, e427–e427.

(18) Chen, C.; Wang, J.; Liu, D.; Yang, C.; Liu, Y.; Ruoff, R. S.; Lei, W. *Nature Communications* **2018**, *9*, 1–8.

(19) Fatima, J.; Shah, A. N.; Tahir, M. B.; Mehmood, T.; Shah, A. A.; Tanveer, M.; Nazir, R.; Jan, B. L.; Alansi, S. *Frontiers in Environmental Science* **2022**, *10*, 210.

(20) Zhang, J.; Li, Z.; Zhan, K.; Sun, R.; Sheng, Z.; Wang, M.; Wang, S.; Hou, X. *ELECTROPHORESIS* **2019**, *40*, 2029–2040.

(21) García Doménech, N.; Coogan, Á.; Purcell-Milton, F.; Casasín García, M. L.; Sanz Arjona, A.; Brunet Cabré, M.; Rafferty, A.; Mckelvey, K.; Dunne, P. W.; Gun'ko, Y. K. *Nanoscale Advances* **2022**, *4*, 4895–4904.

(22) Andriani, Y.; Song, J.; Lim, P. C.; Seng, D. H. L.; Lai, D. M. Y.; Teo, S. L.; Kong, J.; Wang, X.; Zhang, X.; Liu, S. *Ceramics International* **2019**, *45*, 4909–4917.

(23) Arrabito, G.; Bonasera, A.; Prestopino, G.; Orsini, A.; Mattoccia, A.; Martinelli, E.; Pignataro, B.; Medaglia, P. G. *Crystals* **2019**, *9*, 361.

(24) Silva, C. G.; Bouizi, Y.; Fornés, V.; García, H. *Journal of the American Chemical Society* **2009**, *131*, 13833–13839.

(25) Yu, J.; Yu, F.; Yuen, M. F.; Wang, C. *Journal of Materials Chemistry A* **2021**, *9*, 9389–9430.

(26) Hobbs, C.; Jaskaniec, S.; McCarthy, E. K.; Downing, C.; Opelt, K.; Güth, K.; Shmeliov, A.; Mourad, M. C.; Mandel, K.; Nicolosi, V. *npj 2D Materials and Applications* **2018**, *2*, 1–10.

(27) Miao, P.; Zhao, J.; Shi, R.; Li, Z.; Zhao, Y.; Zhou, C.; Zhang, T. *ACS ES and T Engineering* **2022**, *2*, 1088–1102.

(28) Ahmed, M. S.; Khan, M. S. J.; Khan, S. B.; Akhtar, K.; Bakhsh, E. M.; Khalil, A.; Khan, S. A.; Asiri, A. M.; Kamal, T. *Applied Nanoscience* **2022**, *12*, 3597–3606.

(29) Saliba, D.; El Jamal, S. E.; Jonderian, A.; Ammar, M.; Hmadeh, M.; Al-Ghoul, M. *RSC Advances* **2020**, *10*, 43066–43074.

(30) Yang, Z.; Wang, F.; Zhang, C.; Zeng, G.; Tan, X.; Yu, Z.; Zhong, Y.; Wang, H.; Cui, F. *RSC Advances* **2016**, *6*, 79415–79436.

(31) Khodakarami, M.; Dehghan, G.; Rashtbari, S.; Amini, M. *Applied Catalysis A: General* **2024**, *670*, 119563.

(32) Mittal, J. *Journal of Environmental Management* **2021**, *295*, 113017.

(33) Shamim, M.; Dana, K. *International Journal of Environmental Science and Technology* **2018**, *15*, 1275–1284.

(34) Kefif, F.; Ezziane, K.; Bahmani, A.; Bettahar, N.; Mayouf, S. *Bulletin of Materials Science* **2019**, *42*, 1–11.

(35) Saiah, F. B. D.; Su, B. L.; Bettahar, N. *Journal of Hazardous Materials* **2009**, *165*, 206–217.

(36) Berner, S.; Araya, P.; Govan, J.; Palza, H. *Journal of Industrial and Engineering Chemistry* **2018**, *59*, 134–140.

(37) Mallakpour, S.; Behranvand, V. In *Layered Double Hydroxide Polymer Nanocomposites*, Thomas, S., Daniel, S., Eds.; Woodhead Publishing Series in Composites Science and Engineering; Woodhead Publishing: Cambridge, UK, 2020, pp 781–803.

(38) Tajuddin, M. H.; Yusof, N.; Wan Azelee, I.; Wan Salleh, W. N.; Ismail, A. F.; Jaafar, J.; Aziz, F.; Nagai, K.; Razali, N. F. *Frontiers in Chemistry* **2019**, *7*, 429057.

(39) Wei, C.; Yan, X.; Zhou, Y.; Xu, W.; Gan, Y.; Zhang, Y.; Zhang, N. *Crystals* **2022**, *12*, 1713.

(40) Radha, A. V.; Kamath, P. V. *Bulletin of Materials Science* **2004**, *27*, 355–360.

(41) Coogan, Á.; Hughes, L.; Purcell-Milton, F.; Cardiff, S.; Nicolosi, V.; Gun'ko, Y. K. *The Journal of Physical Chemistry C* **2022**, *126*, 18980–18987.

(42) Tanaka, T.; Kameshima, Y.; Nishimoto, S.; Miyake, M. *Analytical Methods* **2012**, *4*, 3925–3927.

(43) Backes, C.; Szydłowska, B. M.; Harvey, A.; Yuan, S.; Vega-Mayoral, V.; Davies, B. R.; Zhao, P. L.; Hanlon, D.; Santos, E. J.; Katsnelson, M. I.; Blau, W. J.; Gadermaier, C.; Coleman, J. N. *ACS Nano* **2016**, *10*, 1589–1601.

(44) Xu, M.; Tang, Q.; Liu, Y.; Shi, J.; Zhang, W.; Guo, C.; Liu, Q.; Lei, W.; Chen, C. *ACS Applied Materials and Interfaces* **2023**, *15*, 12524–12533.

(45) Sajid, M.; Sajid Jillani, S. M.; Baig, N.; Alhooshani, K. *Chemosphere* **2022**, *287*, 132140.

(46) Jee, H.; Jang, J.; Kang, Y.; Eisa, T.; Chae, K. J.; Kim, I. S.; Yang, E. *Membranes* **2022**, *12*, 402.

(47) Sun, L.; Ying, Y.; Huang, H.; Song, Z.; Mao, Y.; Xu, Z.; Peng, X. *ACS Nano* **2014**, *8*, 6304–6311.

(48) Darmograi, G.; Prelot, B.; Layrac, G.; Tichit, D.; Martin-Gassin, G.; Salles, F.; Zajac, J. *Journal of Physical Chemistry C* **2015**, *119*, 23388–23397.

(49) Sasai, R.; Sato, H.; Sugata, M.; Fujimura, T.; Ishihara, S.; Deguchi, K.; Ohki, S.; Tansho, M.; Shimizu, T.; Oita, N.; Numoto, M.; Fujii, Y.; Kawaguchi, S.; Matsuoka, Y.; Hagura, K.; Abe, T.; Moriyoshi, C. *Inorganic Chemistry* **2019**, *58*, 10928–10935.

(50) Itskou, I.; L'Hermitte, A.; Marchesini, S.; Tian, T.; Petit, C. *Accounts of Materials Research* **2023**, *4*, 143–155.

(51) Chen, T.; Li, M.; Liu, J. *Crystal Growth and Design* **2018**, *18*, 2765–2783.

(52) Das, R.; Solís-Fernández, P.; Breite, D.; Prager, A.; Lotnyk, A.; Schulze, A.; Ago, H. *Chemical Engineering Journal* **2021**, *420*, 127721.

(53) Nanofiltration (NF) `https://www.dupont.com/water/technologies/nanofiltration-nf.html` (accessed 05/02/2023).

(54) Bangari, R. S.; Yadav, A.; Awasthi, P.; Sinha, N. *Colloids and Surfaces A: Physicochemical and Engineering Aspects* **2022**, *634*, 127943.

(55) Rathee, G.; Awasthi, A.; Sood, D.; Tomar, R.; Tomar, V.; Chandra, R. *Scientific Reports 2019 9:1* **2019**, *9*, 1–14.

(56) Weber Jr., W. J.; Morris, J. C. *Journal of the Sanitary Engineering Division* **1963**, *89*, 31–59.

(57) Sekine, T.; Nakatani, K. *Langmuir* **2002**, *18*, 694–697.

(58) Pholosi, A.; Naidoo, E. B.; Ofomaja, A. E. *South African Journal of Chemical Engineering* **2020**, *32*, 39–55.

(59) Hou, T.; Zhang, H.; He, D.; Liu, Q.; Zhang, Z.; Xiao, L.; Li, W.; Barnes, M. *RSC Advances* **2018**, *8*, 36858–36868.

(60) Baliarsingh, N.; Parida, K. M.; Pradhan, G. C. *Industrial and Engineering Chemistry Research* **2014**, *53*, 3834–3841.

(61) Mohapatra, L.; Parida, K. *Journal of Materials Chemistry A* **2016**, *4*, 10744–10766.

(62) Ahmed, N.; Shibata, Y.; Taniguchi, T.; Izumi, Y. *Journal of Catalysis* **2011**, *279*, 123–135.

(63) Yuan, X.; Li, W. *Applied Clay Science* **2017**, *138*, 107–113.

(64) Abderrazek, K.; Najoua, F. S.; Srasra, E. *Applied Clay Science* **2016**, *119*, 229–235.

(65) Fazal, H.; Iqbal, A.; Cao, Y.; Zai, J.; Ali, N.; Zhang, Y.; Wu, X.; Zhang, X.; Qian, X. *CrystEngComm* **2021**, *23*, 1234–1242.

(66) Nayak, S.; Parida, K.; Dumitru Pavel, O. *Catalysts* **2021**, *11*, 1072.

(67) Al-Qaradawi, S.; Salman, S. R. *Journal of Photochemistry and Photobiology A: Chemistry* **2002**, *148*, 161–168.

(68) Shahat, M. A.; Ghitas, A.; El-Hossary, F. M.; El-Rahman, A. M. A. *IOP Conference Series: Materials Science and Engineering* **2022**, *1269*, 012010.

(69) Zha, R.; Nadimicherla, R.; Guo, X. *Journal of Materials Chemistry A* **2015**, *3*, 6565–6574.

(70) Nassar, S. J. M.; Wills, C.; Harriman, A. *ChemPhotoChem* **2019**, *3*, 1042–1049.

(71) Cassabois, G.; Valvin, P.; Gil, B. *Nature Photonics* **2016**, *10*, 262–266.

(72) Duan, L.; Wang, B.; Heck, K.; Guo, S.; Clark, C. A.; Arredondo, J.; Wang, M.; Senftle, T. P.; Westerhoff, P.; Wen, X.; Song, Y.; Wong, M. S. *Environmental Science and Technology Letters* **2020**, *7*, 613–619.

(73) Harvey, A.; Backes, C.; Boland, J. B.; He, X.; Griffin, A.; Szydlowska, B.; Gabbett, C.; Donegan, J. F.; Coleman, J. N. *Nature Communications* **2018**, *9*, 1–11.

(74) Xia, S. J.; Liu, F. X.; Ni, Z. M.; Xue, J. L.; Qian, P. P. *Journal of Colloid and Interface Science* **2013**, *405*, 195–200.

(75) Chen, Z. R.; Zhu, Y. Q.; Xu, S. M.; Zhao, Y.; Peng, Q.; Yan, H. *Journal of Materials Chemistry A* **2021**, *9*, 20466–20482.

(76) Eriksen, T. E.; Lind, J.; Merényi, G. *Radiation Physics and Chemistry* **1985**, *26*, 197–199.

(77) Li, J.; Zhang, S.; Chen, Y.; Liu, T.; Liu, C.; Zhang, X.; Yi, M.; Chu, Z.; Han, X. *RSC Advances* **2017**, *7*, 29051–29057.

(78) Yang, Z. Z.; Zhang, C.; Zeng, G. M.; Tan, X. F.; Wang, H.; Huang, D. L.; Yang, K. H.; Wei, J. J.; Ma, C.; Nie, K. *Journal of Materials Chemistry A* **2020**, *8*, 4141–4173.

(79) Bokare, A. D.; Choi, W. *Journal of Hazardous Materials* **2014**, *275*, 121–135.

(80) Page, S. E.; Arnold, W. A.; McNeill, K. *Journal of Environmental Monitoring* **2010**, *12*, 1658–1665.

(81) Myilsamy, M.; Mahalakshmi, M.; Murugesan, V.; Subha, N. *Applied Surface Science* **2015**, *342*, 1–10.

(82) Chung, K. T. *Mutation Research/Reviews in Genetic Toxicology* **1983**, *114*, 269–281.

(83) Kapoor, R. T.; Danish, M.; Singh, R. S.; Rafatullah, M.; Abdul, A. K. *Journal of Water Process Engineering* **2021**, *43*, 102255.

(84) Wang, S.; Jia, Y.; Song, L.; Zhang, H. *ACS Omega* **2018**, *3*, 18456–18465.

(85) Wang, Q.; Tian, S.; Ning, P. *Industrial and Engineering Chemistry Research* **2014**, *53*, 643–649.

(86) Antonin, V. S.; Garcia-Segura, S.; Santos, M. C.; Brillas, E. *Journal of Electroanalytical Chemistry* **2015**, *747*, 1–11.

# Chapter 5

# Lanthanide-Doped Layered Double Hydroxide Nanostructures for Chemo-sensing

## 5.1 Introduction

Since the turn of the century, the use of nanomaterials for novel sensing platforms has emerged as an area of significant interest, due to the diverse range of applications ranging from biomedical imaging, to food quality control, to environmental monitoring.[1–3] This surge in interest is evidenced by the steady growth in the number of publications referencing 'nano' and 'sensing' in recent years (Figure 5.1).

In particular, layered 2D materials might offer unique advantages as sensing platforms, which can primarily be attributed to them having higher surface-to-volume ratios than their 0D, 1D and 3D counterparts. This distinct property enables a substantial increase

in the available surface area for interaction with specific analytes, often leading to a marked improvement in detection limits. Moreover, ongoing progress and advancements in solution processing techniques for 2D materials holds great promise for the future of sensing technology, facilitating the straightforward printing of nanosensing platforms.[4–7]

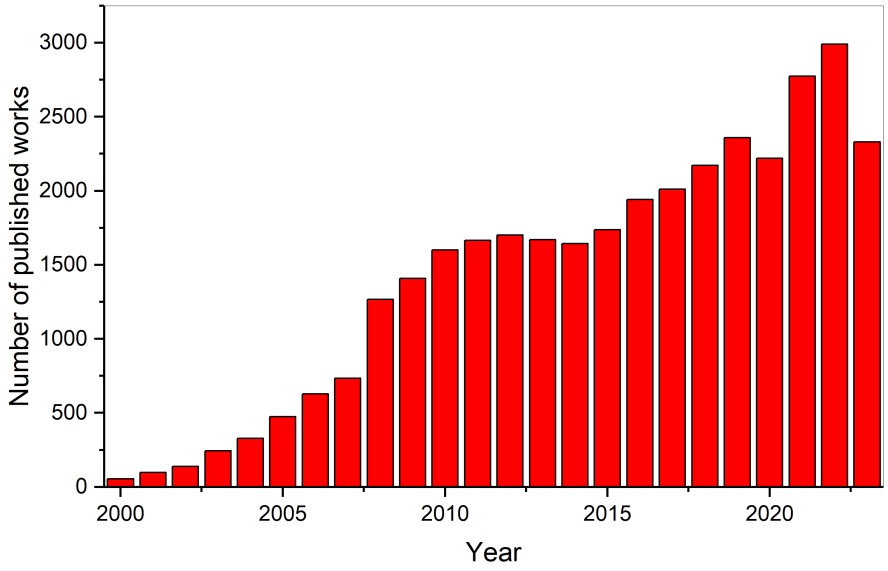


Figure 5.1: Number of publications mentioning both 'nano' and 'sensing' either in titles, or as keywords from the years 2000-2023 inclusive. Data was obtained from Scopus.

Among the multiple sensing approaches exploited in the nano-world, including colorimetric, acoustic, electrochemical and magnetic, luminescent sensing offers significant advantages, including high sensitivity and rapid detection times.[8–12] Rare-earth-based luminescent materials are highly attractive options, given their unique photophysical properties including characteristic narrow emission bands, long luminescent lifetimes, and large Stokes shifts which enables them to be used in sensing across wide electromagnetic spectral ranges.[13] While rare-earth-based materials, specifically lanthanides, offer many exciting opportunities in the world of sensing, the challenge of locating, extracting and purifying lanthanides from ore deposits means researchers ought to proceed with caution when considering the scalability of such technologies.[14] Therefore, doping of nanomaterials

with rare-earth elements is of considerable importance, facilitating the exploitation of their unique properties, while minimising overuse of these resources.[15,16]

While previous environmental-based work presented in this thesis concerned the removal of organic molecules, in particular dyes, from water, inorganic materials such as heavy metal oxyanions are perhaps an even more prevalent source of both airborne and water-borne pollution, with developing nations being disproportionally affected.[17,18] The presence of the dichromate anion ($Cr_2O_7^{2-}$), a source of hexavalent chromium (Cr(VI)), in wastewater, is of particular concern to both humans, as well as the broader ecosystem, as brought into the public eye by the 2000 film '*Erin Brockovich*'.[19] Dichromate pollution, originating primarily from industrial processes, is a matter of the utmost concern. Cr(VI) is highly toxic and carcinogenic to humans, with prolonged exposure leading to respiratory distress and disease, major skin irritation, and most worryingly, carcinogenesis.[20,21] Furthermore, the increasing prevalence of Cr(VI) in water sources can have detrimental effects on our ecosystems, contaminating crucial water resources, severely impacting the balance of aquatic life, and entering the human food chain. Thus, it is clear that accurate and reliable detection and monitoring of dichromate levels in water is necessary for safeguarding human, animal, and plant health.

Layered rare-earth hydroxides have recently emerged as a promising new class of luminescent 2D materials, demonstrating their effectiveness in pollutant sensing applications.[22–24] While there are numerous articles on the use of LDHs for the adsorptive removal of anionic pollutants from water, surprisingly, the utilisation of rare-earth-doped LDHs for this purpose remains largely unexplored, to the best of our knowledge.[25–28] This oversight is noteworthy, given the potential advantages they may offer over their pure rare-earth hydroxide counterparts. This includes simpler, milder and greener synthetic routes, as well as avoiding the overconsumption of rare-earth elements, while still retaining the distinctive optical properties that make rare-earth hydroxides so valuable in sensing

applications.

This important avenue of research is closely aligned with the UN Sustainable Development Goals (SDGs), most notably SDG6, which relates to clean water and sanitation, as well as SDG15, which strives for the protection of ecosystems and prevention of land degradation and biodiversity loss. The exploration of the untapped potential of rare-earth doped LDHs in pollutant sensing is just one of the many ways in which we, as materials scientists, can contribute to a more sustainable and environmentally conscious future.[29]

## 5.2 Aims of this work

The main aim of this research was to synthesise a range of photoluminescent, rare-earth doped LDHs *via* room-temperature co-precipitation synthetic procedures, investigate their photophysical properties, and explore their potential sensing applications. More specifically, the goal was to produce phosphorescent $Eu^{3+}$ and $Tb^{3+}$-doped MAl LDHs (where M = $Zn^{2+}/Mg^{2+}$), denoted MgAlEu, MgAlTb, ZnAlEu and ZnAlTb LDHs. The materials were initially characterised via pXRD and SEM, and the undoped MgAl and ZnAl LDHs were also studied using the same techniques to determine any potential impact of doping on the resultant structure and morphology. Then, photophysical analysis, including excitation and emission measurements, as well as lifetime measurements, were conducted using photoluminescence (PL) spectroscopic techniques. Finally, we planned to test the resultant materials for use as sensors for the detection of a common pollutant of concern – the dichromate anion ($Cr_2O_7^{2-}$) - by monitoring the change in PL emission of the LDHs in the presence of various concentrations of $Cr_2O_7^{2-}$. We also aimed to provide some insights

into the dominant quenching mechanism of the LDH-chromate sensing system, as well as a demonstration of the potential economic benefits of using rare-earth-doped LDHs.

## 5.3 Results and discussion

### 5.3.1 Synthesis and characterisation of lanthanide-doped LDHs

MAlEu, and MAlTb LDHs (where M = $Mg^{2+}/Zn^{2+}$) were synthesised *via* a two-step, room-temperature co-precipitation procedure, using a modification of the published procedure from Chen *et al.*, as described in Section 2.4.[30] Briefly, sodium carbonate was used as the carbonate source for anion intercalation, sodium hydroxide was used as the precipitating base, and a molar ratio of $M^{2+}$:$Al^{3+}$:$Ln^{3+}$ = 1:0.5:0.1 was used, where $Ln^{3+}$ = $Eu^{3+}$ or $Tb^{3+}$. Analysis of the true doping level, as well as the homogeneity of the lanthanide cations throughout the LDH framework *via* EDX and ICP-MS is the subject of future work. The resultant materials exhibited the characteristic red and green emission typical to $Eu^{3+}$ and $Tb^{3+}$, respectively, under UV radiation, as shown in Figure 5.2.

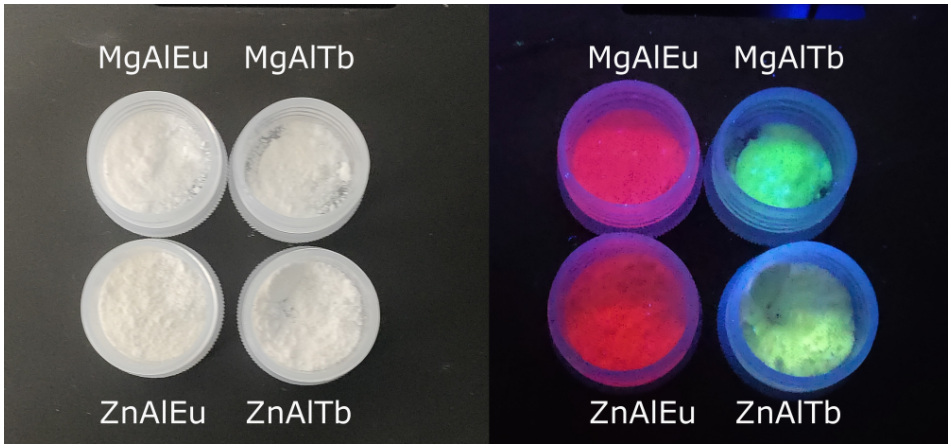


Figure 5.2: Images of lanthanide-doped LDHs in daylight (left) and under 280 nm UV illumination (right).

The characteristic emission colours from the resultant materials confirmed the presence of $Eu^{3+}$ and $Tb^{3+}$ in the samples. However, to ensure that doping had taken place, rather than the formation of a mixture of emissive and non-emissive phases, as well as to confirm that the lanthanide doping did not disrupt or inhibit the formation of the hydrotalcite phases, pXRD was conducted on the undoped and doped samples, as shown in Figure 5.3.

pXRD indicates that, in all cases, the LDH phases were the sole crystalline products resulting from the synthesis, with all the diffraction peaks present being fully indexed to the rhombohedral (space group: R-3m) MgAl hydrotalcite structure (PDF: 89-0460) with a 2:1 Mg:Al ratio, and rhombohedral ZnAl hydrotalcite (PDF: 48-1021) with a 2:1 Zn:Al ratio. The characteristic (003), (006) and (012) reflections are present at 2θ values of 11.6°, 23.2° and 34.6° respectively for MgAl LDH, and 11.8°, 23.7° and 34.7° for ZnAl LDH.[31,32] Furthermore, no lanthanide-containing impurity phases, such as oxides or hydroxides, could be observed in the acquired pXRD patterns, confirming successful doping of the lanthanide ions into the structure and complete formation of the hydrotalcite phase. However, there are some distinct differences in the pXRD diffraction patterns between the MgAl LDH and the ZnAl LDH samples.

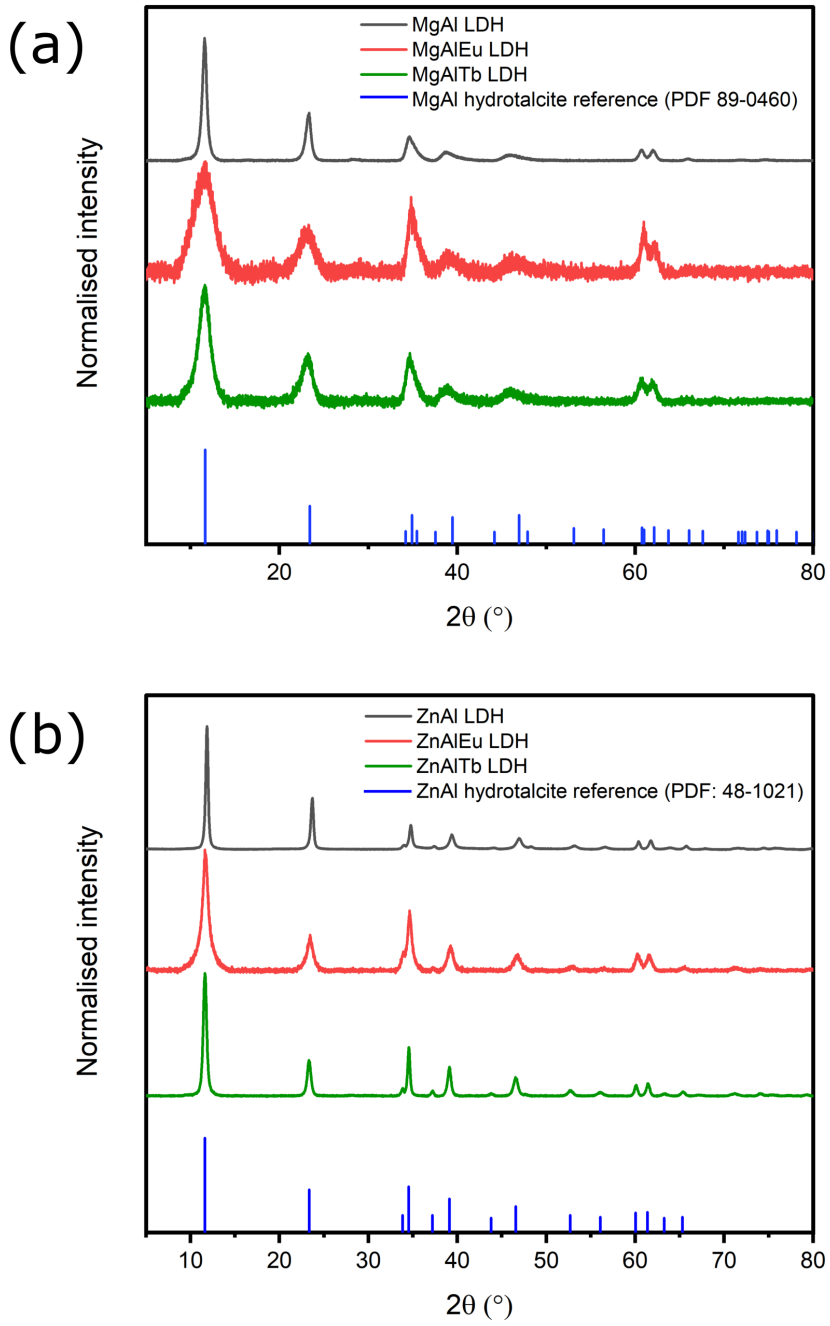


Figure 5.3: pXRD patterns comparison of Eu-doped (red), Tb-doped (green) and undoped (grey) samples of (a) MgAl LDH and (b) ZnAl LDH. Reference pXRD patterns for MgAl and ZnAl hydrotalcite are shown in blue.

When comparing doped and undoped samples of MgAl LDH, no change in the 2θ position of the (003) diffraction peak can be observed, as shown in Figure 5.4, which indicates no lattice expansion along the *c*-direction of the rhombohedral unit cell. This serves as an indication that there is no intercalation of lanthanide-containing complexes into the LDH interlayer, and instead that the lanthanide ions are being integrated into the metal hydroxide sheets *via* replacement of either the $Mg^{2+}$ or $Al^{3+}$ species.

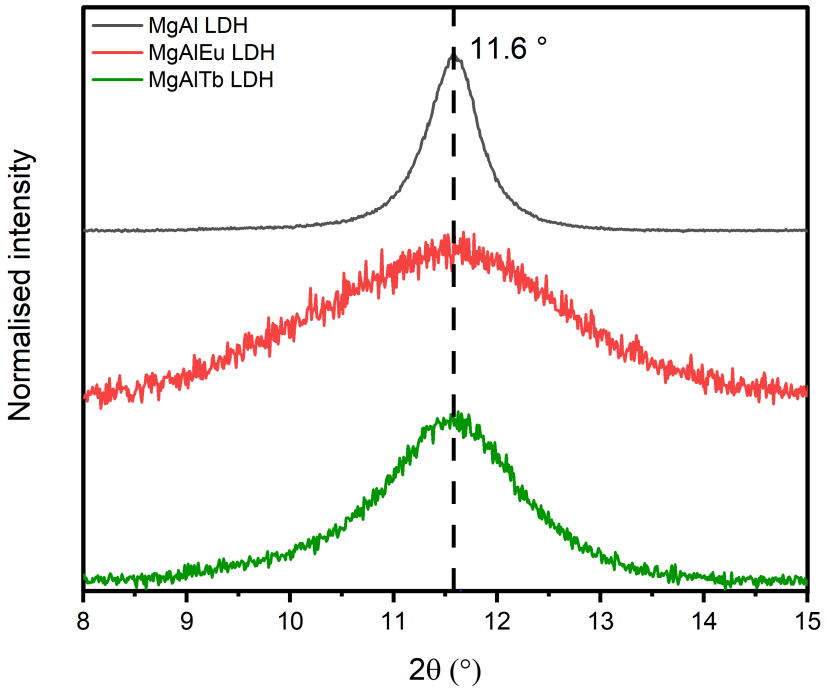


Figure 5.4: pXRD pattern of doped and undoped MgAl LDHs in the region of the (003) hydrotalcite reflection, showing significant peak broadening, but no peak shift.

However, it is evident from the obtained diffraction data (Figure 5.3 (a) and 5.4) that there is a significant peak broadening of the doped samples compared with the undoped samples. Furthermore, the Eu-doped sample exhibits substantially more peak broadening than the Tb-doped sample. To understand this phenomenon, it is necessary to analyse the crystallite sizes of the doped and undoped samples.

Typically, narrower and sharper peaks are indicative of a larger crystallite size, or a material with higher crystallinity. Consequently, peak broadening is a common indicator of a reduction in crystallite size in a material. The crystallite sizes can be estimated using the Scherrer equation (Equation 5.1):

$$D = \frac{K\lambda}{\beta cos\theta} \tag{5.1}$$

where $D$ is the crystallite size, $K$ is the shape factor (typically taken as 0.89 although it is highly dependent on the shape of the crystallites), $\lambda$ is the wavelength of the X-ray source (Cu $K_\alpha = 1.54$ Å), $\beta$ is the FWHM of the given diffraction peak (in radians), and $\theta$ is the Bragg angle. The crystallite sizes were estimated by analysis and averaging of the (003) and (006) diffraction peaks, with the results shown in Table 5.1. Scherrer crystallite analysis was conducted using Bruker DIFFRAC.EVA V6.1.

Table 5.1: Summary of Scherrer crystallite analysis of undoped and doped MgAl LDHs from pXRD patterns.

| | **MgAl** | **MgAlEu** | **MgAlTb** |
|---|---|---|---|
| $\beta_{\mathbf{003}}$ | 0.575° | 2.654° | 1.461° |
| $\mathbf{D_{003}}$ | 13.8 nm | 3.0 nm | 5.4 nm |
| $\beta_{\mathbf{006}}$ | 0.674° | 1.604° | 1.151° |
| $\mathbf{D_{006}}$ | 11.9 nm | 5.0 nm | 7.0 nm |
| $\mathbf{D_{avg}}$ | 12.85 nm | 4.0 nm | 6.2 nm |

Peak broadening arises in pXRD patterns from crystal lattice imperfections, which can be caused by a variety of reasons, including reduction in crystallite size, distortion of the crystal lattice, and structural defects such as dislocations and stacking faults.[33] In particular, for small crystals, a reduced crystallite size is the dominant factor in pXRD peak

broadening.[34] To determine if the peak broadening could be attributed to a reduction in crystallite size in this case, SEM was conducted on the MgAl doped and undoped samples to examine their size and morphology, as shown in Figure 5.5.

Samples were prepared for SEM *via* two methods: as powders adhered to sticky carbon tape, as well through drop-casting material on TEM grids. SEM images corresponding to both preparation methods are shown in Figure 5.5. It can be observed that clusters of small nanoparticles were formed *via* the co-precipitation approach. The particles appear to be anisotropic, an observation which is particularly evident for MgAlEu LDHs and which is consistent with reports of lanthanide-doped MgAl LDHs from Gunawan *et al.*[35]

The pristine MgAl LDH nanoparticles are estimated to lie in the size range of 20-140 nm, with an average size of (72 $\pm$ 20) nm, which was deduced from a preliminary size distribution analysis (Appendix D, Figure D1 (c)). This size is roughly in line with literature reports of MgAl LDHs nanoplatelets synthesised *via* hydrothermal approaches and co-precipitation approaches.[36–38] The SEM analysis reveals a slight decrease in particle size for MgAlEu LDHs (approx. (65 $\pm$ 20) nm), and a slight increase in particle size for MgAlTb LDHs (approx. (82 $\pm$ 29) nm), the results of which can be found in Appendix D (Figure D1 (a,b)). This is consistent with the pXRD observations of peak broadening. The introduction of large cationic dopants such as $Eu^{3+}$ and $Tb^{3+}$ in LDH host matrices can result in a distortion of the octahedral coordination of the metal centres, restricting the growth of larger crystalline domains.[39] The LDH matrix may be slightly more tolerant to $Tb^{3+}$ doping due to its smaller ionic radius (92 pm) when compared with $Eu^{3+}$ (95 pm), resulting in a lesser degree of pXRD peak broadening due to a more complete crystallisation of the $Tb^{3+}$-doped species than their $Eu^{3+}$-doped counterparts.

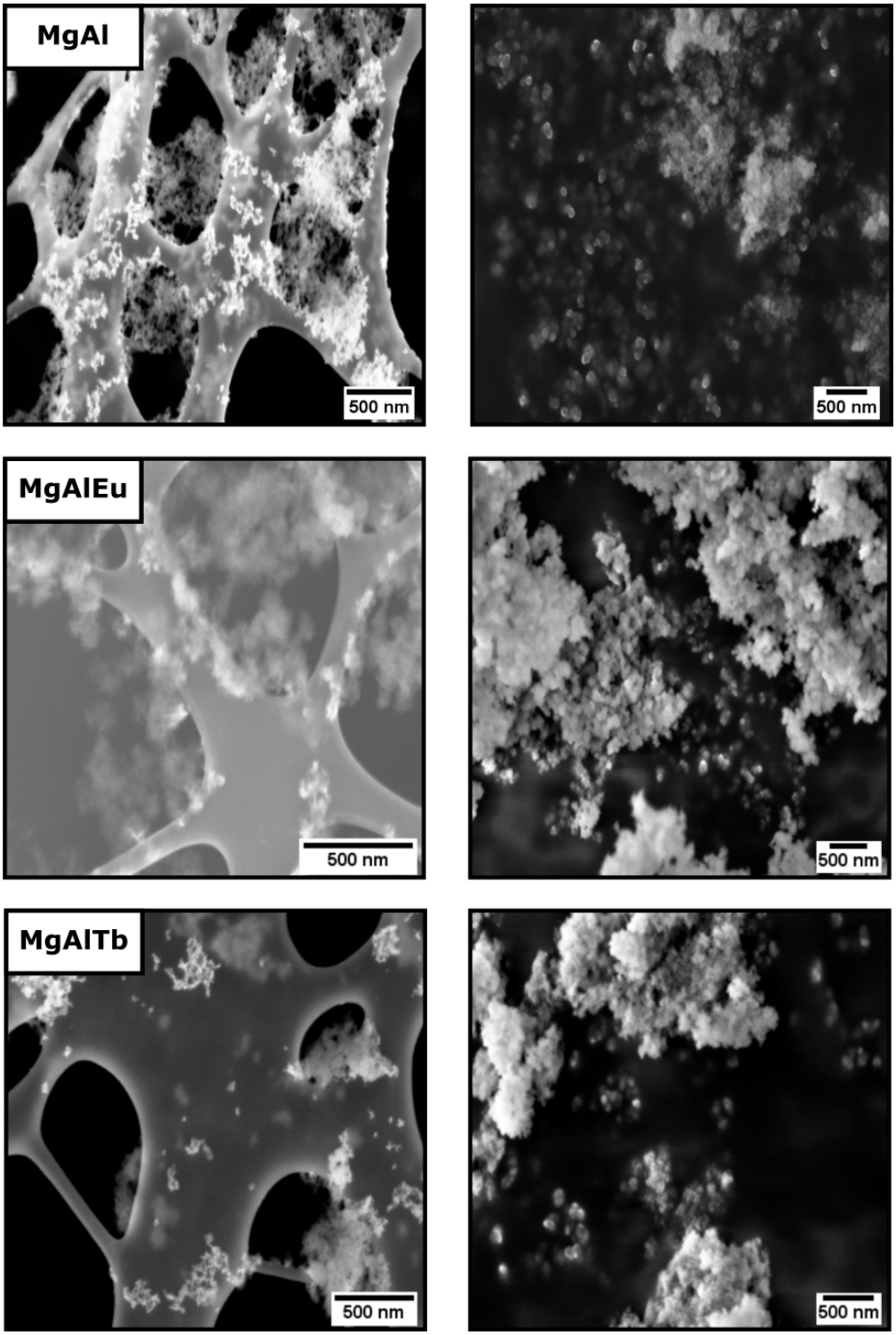


Figure 5.5: SEM images of MgAl (top), MgAlEu (middle) and MgAlTb (bottom) LDH nanosheets. Images acquired on drop-cast colloidal suspensions on TEM grids (left) and of powders on carbon tape (right).

However, it is evident that TEM would be the preferred imaging technique for these samples. Due to the small sizes of the nanoparticles formed in both doped and undoped MgAl LDHs, TEM imaging would undoubtedly result in a more accurate size analysis, which is the subject of future work. Nevertheless, from the SEM analysis it can be deduced that the likely origin of the broad peaks in the pXRD patterns of the doped MgAl LDH samples is due to the formation of very small nanocrystallites, as opposed to nanosheets with lateral sizes of $>$ 100 nm.

The same pXRD and SEM analysis was conducted on undoped and doped ZnAl LDH samples. There are some similarities between the doped MgAl and ZnAl LDH pXRD patterns. In particular, the ZnAl LDHs follow a similar peak broadening trend to MgAl LDH, in that $Eu^{3+}$-doping results in much more pronounced peak broadening than $Tb^{3+}$-doping. However, there are also some noticeable differences between the materials. In contrast to the MgAl LDHs, a slight shift of the (003) pXRD diffraction peak to lower values of 2θ can be observed in the case of doped ZnAl LDHs, as shown in Figure 5.6.

This shift to lower 2θ means that there is an increase in the $d_{003}$ spacing in the doped versus undoped ZnAl LDHs, and similar observations have been recently reported for ZnAlEu LDHs by Pastor *et al.*[40] Furthermore, peak broadening in the doped ZnAl LDH samples is much less pronounced than was observed for the MgAl LDH. This indicates that the metal hydroxide sheets are expanding to accommodate the lanthanide dopants, leading to an expansion of the rhombohedral unit cell along the *c*-direction. Scherrer analysis was conducted on the doped and undoped ZnAl LDH samples, as was conducted for their MgAl counterparts, the results of which are summarised in Table 5.2.

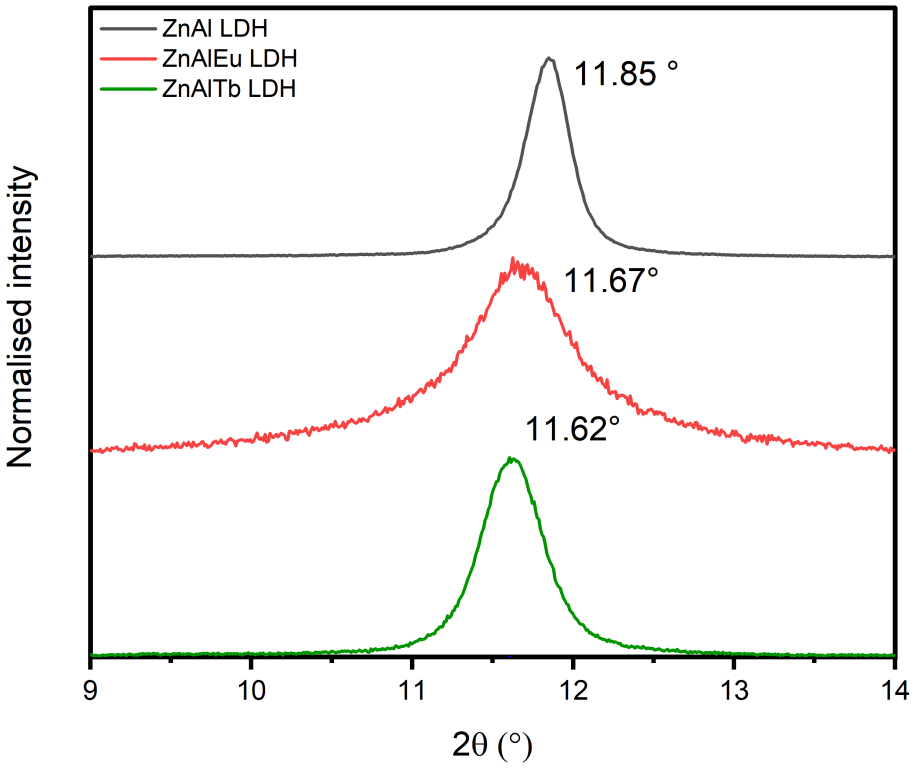


Figure 5.6: pXRD pattern in the region of the (003) hydrotalcite reflection, with slight peak shift, along with peak broadening, observed for doped ZnAl LDHs.

Table 5.2: Summary of Scherrer crystallite analysis of undoped and doped ZnAl LDHs from pXRD patterns.

| | **ZnAl** | **ZnAlEu** | **ZnAlTb** |
|---|---|---|---|
| $\beta_{003}$ | 0.320° | 0.764° | 0.445° |
| $\mathbf{D_{003}}$ | 25.0 nm | 10.4 nm | 17.9 nm |
| $\beta_{006}$ | 0.343° | 0.748° | 0.451° |
| $\mathbf{D_{006}}$ | 23.7 nm | 10.8 nm | 17.9 nm |
| $\mathbf{D_{avg}}$ | 24.4 nm | 10.6 nm | 17.9 nm |

SEM was also conducted on the doped and undoped ZnAl LDH samples, as shown in Figure 5.7. It can be observed that, in contrast to MgAl LDH formation, the co-precipitation synthesis of ZnAl LDHs resulted in the formation of uniform hexagonal nanoplates, with an average lateral size of (217 $\pm$ 56) nm, consistent with previous reports.[40] Both ZnAlEu and ZnAlTb LDHs also crystallised in the form of nanosheets, with $Eu^{3+}$ and $Tb^{3+}$ doping seemingly following the same trend in crystallite size as was demonstrated previously for MgAl LDHs. ZnAlEu and ZnAlTb LDH nanosheets were calculated to have average lateral sizes of (125 $\pm$ 48) nm and (277 $\pm$ 101) nm, respectively. The size distribution analyses can be found in Appendix D (Figure D2). For larger crystallites however, the peak broadening is more typically ascribed to micro-strain rather than reduction in crystallite size, which is consistent with expansion of the unit cell to accommodate the lanthanide dopants. As was discussed previously for MgAl LDHs, the slightly smaller ionic radius of $Tb^{3+}$ is more easily accommodated in the ZnAl LDH host matrix than $Eu^{3+}$, resulting in less strain and distortion of the crystal, and thus less peak broadening.[41,42]

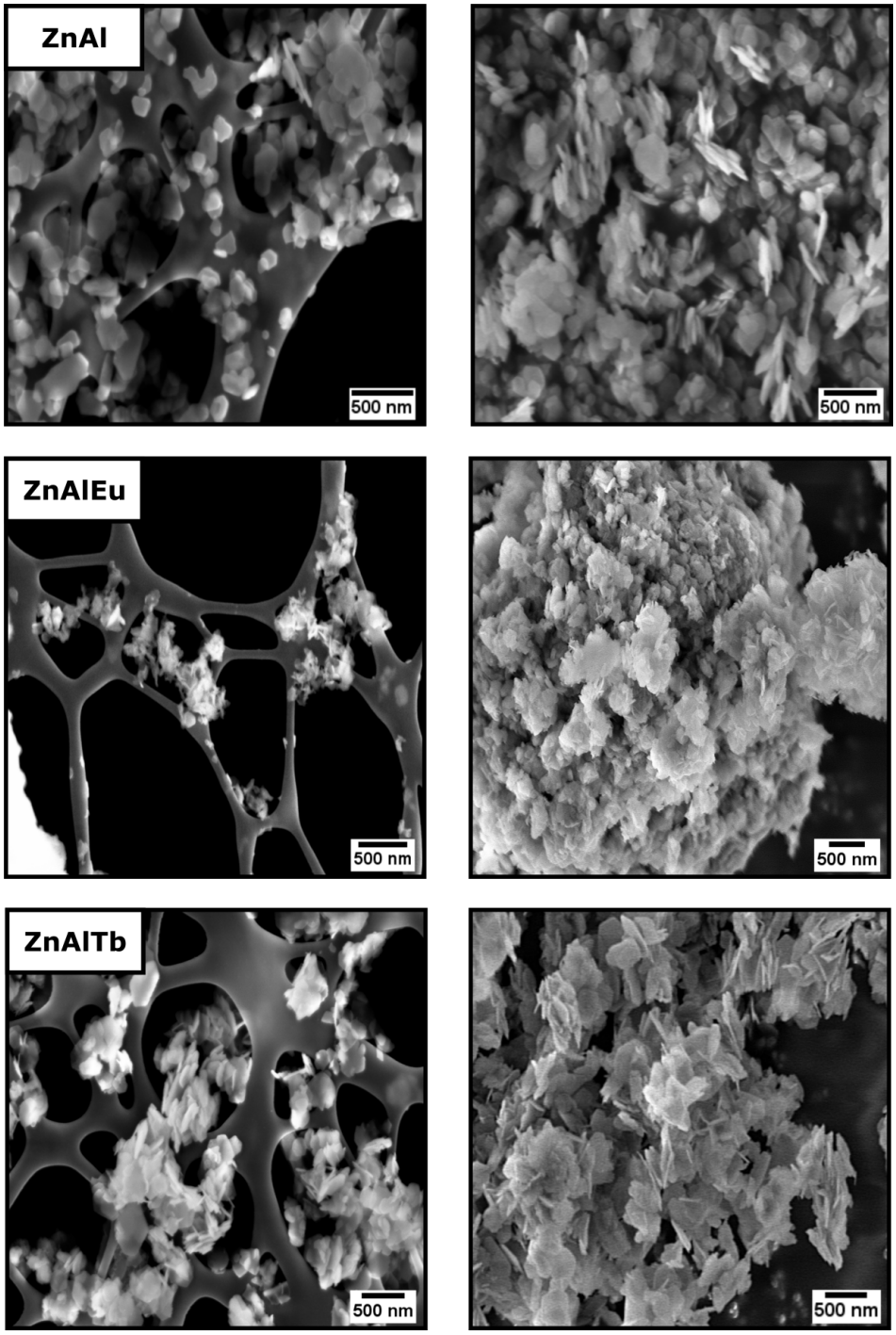


Figure 5.7: SEM images of ZnAl (top), ZnAlEu (middle) and ZnAlTb (bottom) LDH nanosheets. Images acquired on drop-cast colloidal suspensions on TEM grids (left) and of powders on carbon tape (right).

## 5.3.2 Photophysical characterisation of lanthanide-doped LDHs

### $Eu^{3+}$-doped MgAl and ZnAl LDHs

Following confirmation of the successful formation of the MgAl and ZnAl LDH phases, photophysical characterisation of the resultant materials were conducted using photoluminescence spectroscopy (PL). Figure 5.8 (a) and (b) show the PL excitation and emission spectra of MgAlEu and ZnAlEu LDH.

The excitation spectra for both LDHs were measured using an emission wavelength ($\lambda_{em}$) of 615 nm and, despite the clear differences in crystallinity and morphology, are almost identical. The excitation spectra both contain a cluster of sharp peaks in the observed region as a result of *f-f* transitions in $Eu^{3+}$, which has an electronic configuration of [Xe]$4f^6$.[43] The intensity of this cluster in the 200-300 nm region is enhanced compared to most other $Eu^{3+}$-doped systems, as it overlaps with the broad absorption band of MgAl and ZnAl LDHs.[44] The emission spectra were measured using an excitation wavelength ($\lambda_{ex}$) of 270 nm, in the region of the $O^{2-}$ to $Eu^{3+}$ charge transfer band.[45] The emission spectra contain two sharp emission peaks at approximately 593 nm and 615 nm, associated with the $^5D_0$ – $^7F_1$ and $^5D_0$ – $^7F_2$ transitions of $Eu^{3+}$ ions, respectively.

The ratio of the emission intensities associated with these transitions can provide information on the local environment of the $Eu^{3+}$ cation within the LDH host crystal. The $^5D_0$ – $^7F_1$ transition is a partially allowed magnetic dipole transition, whereas the $^5D_0$ – $^7F_2$ transition is a forced electric dipole transition.[46,47] The $^5D_0$ – $^7F_2$ transition is often referred to as a 'hypersensitive transition', as it is sensitive to its environment, and its intensity is commonly reported to increase with decreasing symmetry of the $Eu^{3+}$ site within the host crystal.[48]

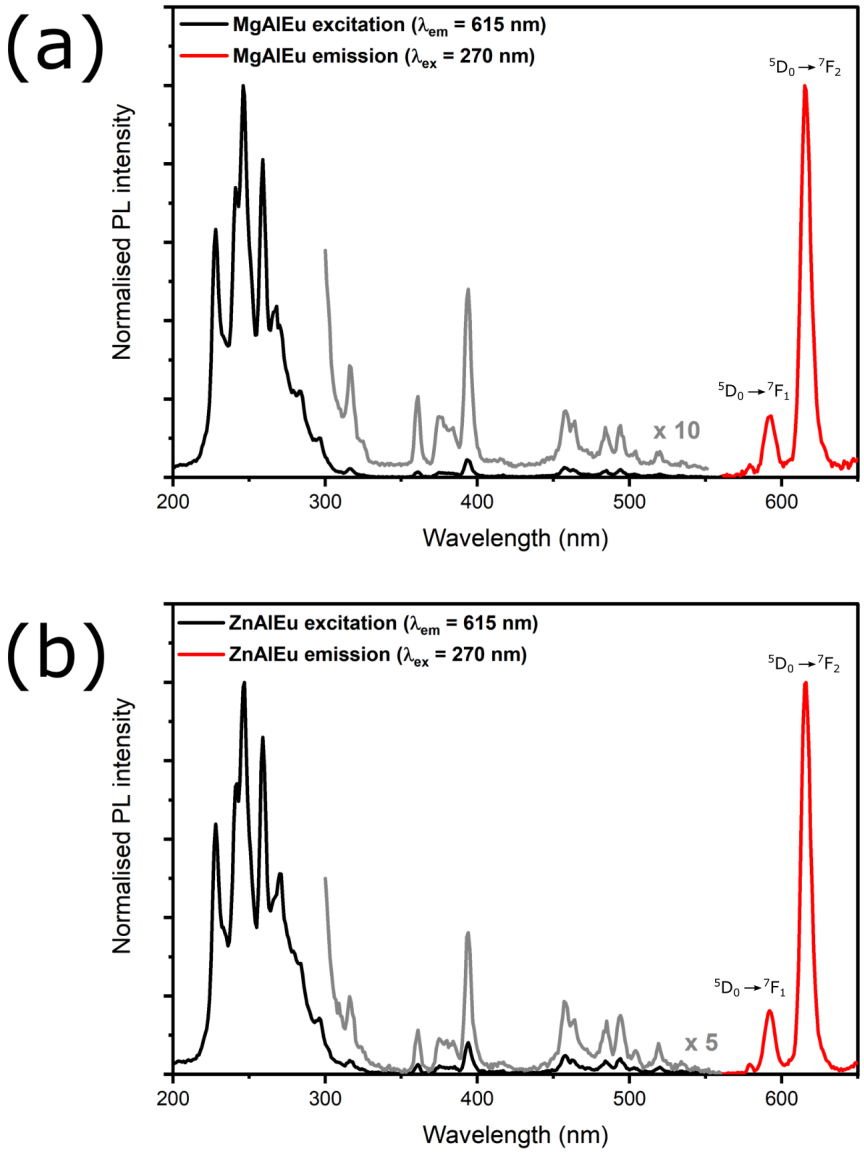


Figure 5.8: PL excitation and emission spectra of (a) MgAlEu and (b) ZnAlEu LDHs.

Thus, the asymmetry ratio $R_{21}$, as presented in Equation 5.2, can be used to infer some information about the symmetry of the $Eu^{3+}$ coordination environment.[47,49]

$$R_{21} = \frac{I(^5D_0 - {}^7F_2)}{I(^5D_0 - {}^7F_1)} \tag{5.2}$$

where I($^5D_0 \rightarrow {}^7F_J$) represents the peak intensity of that given electronic transition. Typically, high values of $R_{21}$ can often indicate that there is a large deviation from $Eu^{3+}$ centrosymmetric geometry. By applying Equation 5.2 and extracting the peak intensities from the PL emission data, $R_{21}$ for MgAlEu LDH and ZnAlEu LDH were calculated to be 5.24 and 5.65, respectively. This indicates that the $Eu^{3+}$ dopant exists in a low symmetry, non-centrosymmetric environment, with slightly lower symmetry observed in the case of ZnAlEu LDHs. This high asymmetry ratio, and thus low symmetry bonding environment, has previously been reported for $Eu^{3+}$-doped ZnAl LDHs intercalated by carbonate ions.[50]

While the local coordination of the metal centres in LDHs is described in the ideal case as octahedral, the distinct difference in cationic radii may result in the distortion of the edge-sharing octahedra in the LDH structure, leading to the high asymmetry ratio. In fact, a number of articles have reported a 10-fold coordination environment, with no centre of inversion, for the $Eu^{3+}$ dopant in similar inorganic structures.[51–53] To further investigate any potential differences in the $Eu^{3+}$ doping between MgAl and ZnAl LDHs, the phosphorescent lifetimes of both species were investigated.

The phosphorescence decay curves of both the MgAlEu and ZnAlEu LDHs exhibit very similar profiles and indeed at a first glance look near identical, as shown in Figure 5.9 (a). Upon closer inspection there are only minor differences in the decay profiles of both species, as shown in Figure 5.9 (b).

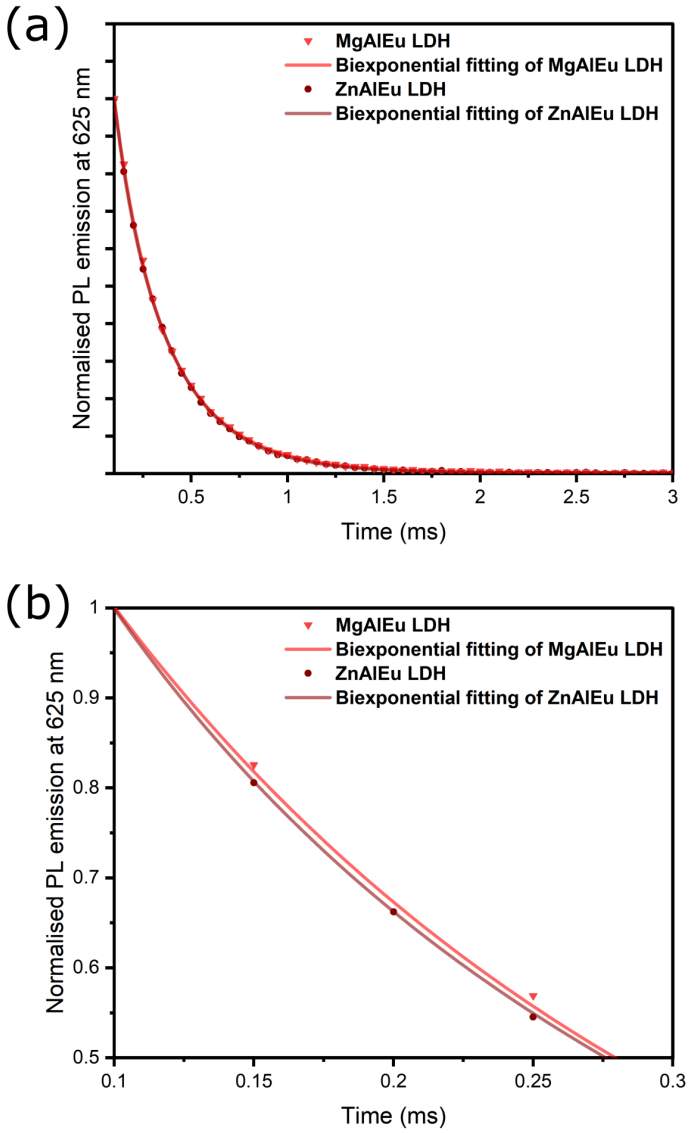


Figure 5.9: (a) Phosphorescence decay curves of MgAlEu and ZnAlEu LDH. (b) Close-up of 0 – 0.3 ms region of decay curve, showing slight differences in the decay profiles.

The data were fitted using biexponential decay models, the results of which give two distinct lifetimes, a short-lived ($\tau_1$) and long-lived ($\tau_2$) component, according to Equation 5.3:

$$y = A_1 e^{-\frac{t}{\tau_1}} + A_2 e^{-\frac{t}{\tau_2}} \tag{5.3}$$

where $A_1$ and $A_2$ are fitting parameters and are related to the relative PL intensity. This method is commonly applied for $Eu^{3+}$-doped inorganic systems, to represent that the $Eu^{3+}$ cation can occupy two distinct sites in the inorganic host lattice, leading to two distinct lifetimes. This behaviour has been reported for $Eu^{3+}$-doped LDHs, metal carbonates, and other inorganic systems.[40,54] For completeness, the data were also fitted using mono-exponential decay models for comparison, the results of which can be found in Appendix D (Figures D3,D5). The average lifetime ($\tau_{avg}$) can be obtained from the biexponential decay model using Equation 5.4, and the results are summarised in Table 5.3.

$$\tau_{avg} = \frac{A_1\tau_1^2 + A_2\tau_2^2}{A_1\tau_1 + A_2\tau_2} \tag{5.4}$$

Table 5.3: PL decay lifetimes and parameters from biexponential fitting of MgAlEu and ZnAlEu LDH decay.

| | $\mathbf{A_1}$ | $\tau_1$ **(ms)** | $\mathbf{A_2}$ | $\tau_2$ **(ms)** | $\tau_{\mathbf{avg}}$ **(ms)** |
|---|---|---|---|---|---|
| **MgAlEu** | 0.5350 | 0.1418 | 0.9997 | 0.3252 | 0.29 |
| **ZnAlEu** | 0.4213 | 0.0794 | 1.2291 | 0.2967 | 0.28 |

As phosphorescent lifetimes are highly dependent on the crystal field environment, and the $Eu^{3+}$ dopant exists in sites with similar asymmetry in both MgAlEu and ZnAlEu LDHs as evidenced by the asymmetry ratio calculated from the emission spectra, similar lifetimes in both materials are to be expected. ZnAlEu LDH exhibits a slightly shorter lifetime (0.28 ms) than MgAlEu LDH (0.29 ms). The slightly decreased lifetime of ZnAlEu LDH may

be attributed to a minor decrease in the symmetry of the $Eu^{3+}$ site compared to MgAlEu LDH, which is commonly reported for $Eu^{3+}$-doped systems and $Eu^{3+}$-centered complexes.[55] However, this change in lifetime is negligible, with any observable differences between both $Eu^{3+}$-doped samples being in the short and long lifetime components, $\tau_1$ and $\tau_2$. Lifetimes on the order of 0.3 ms, or 300 μs, are in line with reports of $Eu^{3+}$-doped complexes and nanomaterials in the literature.[56–58]

### $Tb^{3+}$-doped MgAl and ZnAl LDHs

PL excitation and emission measurements were conducted on both MgAlTb and ZnAlTb LDHs, as shown in Figure 5.10 (a) and (b), respectively. The excitation spectra were measured from 200 – 450 nm using the $^5D_4$ – $^7F_5$ emission band at 544 nm, and the emission spectra were recorded from 450-650 nm, using an excitation wavelength of 226 nm.

The excitation spectra of both MgAlTb and ZnAlTb LDHs contain a number of sharp peaks. The peaks in the 220-250 nm region can be attributed to excitation of electrons from $4f$ to $5d$ orbitals in $Tb^{3+}$ (i.e. [Xe]$4f^8 \rightarrow$ [Xe]$4f^7 5d^1$), whereas the lower intensity bands present at longer wavelengths (i.e. from 300 nm onwards), can be attributed to forbidden $f - f$ transitions in $Tb^{3+}$.[59] Excitation at 226 nm leads to the generation of a number of sharp emission peaks in the 450 – 650 nm region, corresponding to the $^5D_4$ – $^7F_J$ transitions, more specifically the $^5D_4$ – $^7F_6$, $^7F_5$, $^7F_4$ and $^7F_3$ transitions at 489 nm, 544 nm, 587 nm and 617 nm, respectively.[60] It is clear that the dominant peak is at 544 nm, leading to the green emission exhibited by these materials.

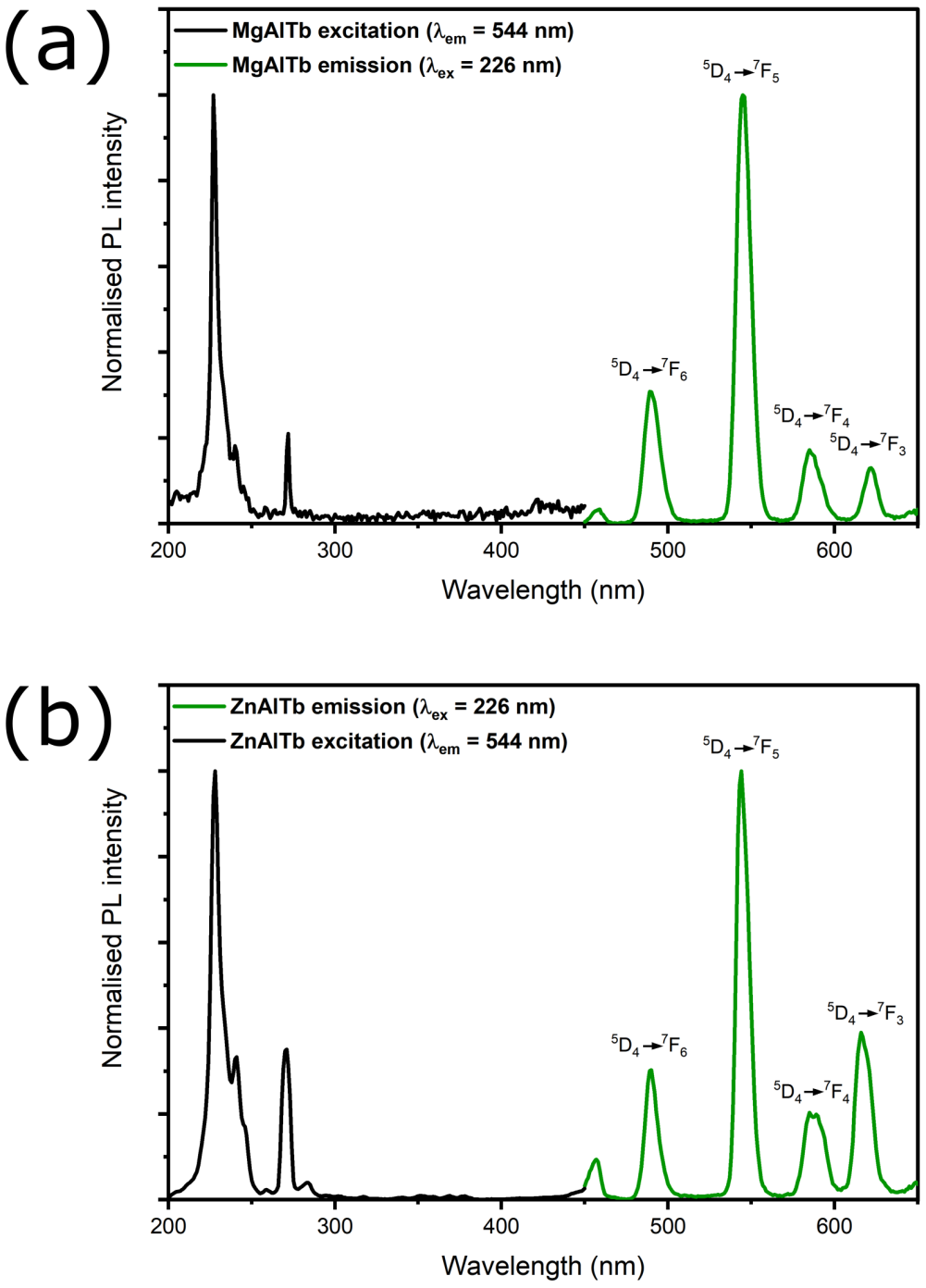


Figure 5.10: Normalised PL excitation and emission spectra for (a) MgAlTb and (b) ZnAlTb LDHs, obtained using excitation and emission wavelengths of 226 nm and 544 nm, respectively.

While some reports detail the use of an asymmetry ratio, analogous to that of $Eu^{3+}$, to describe the symmetry of the $Tb^{3+}$ site, this method is not widely used, and thus will not be discussed here. Instead, it more common to say that, in a general sense, the intensity of the $^5D_4$ – $^7F_5$ transition, located at 544 nm in our materials, is an indicator of the $Tb^{3+}$ site asymmetry as this particular transition is hypersensitive to its surroundings.[30,61] In both MgAlTb LDH and ZnAlTb samples, the $^5D_4$ – $^7F_5$ transition is by far the most intense emission peak, once again indicating a low symmetry environment, similar to the $Eu^{3+}$-doped case.

To further investigate any potential differences in the $Tb^{3+}$ doping between MgAl and ZnAl LDHs, the phosphorescent lifetimes of both species were investigated, as shown in Figure 5.11. The decay data were fitted using biexponential decay models, as was conducted previously for $Eu^{3+}$-doped LDHs inorganic systems. For completeness, the data were also fitted using mono-exponential decay models, the results of which can be found in Appendix D (Figures D4, D6). In contrast to $Eu^{3+}$-doped LDHs, the $Tb^{3+}$-doped LDHs have noticeably different decay profiles.

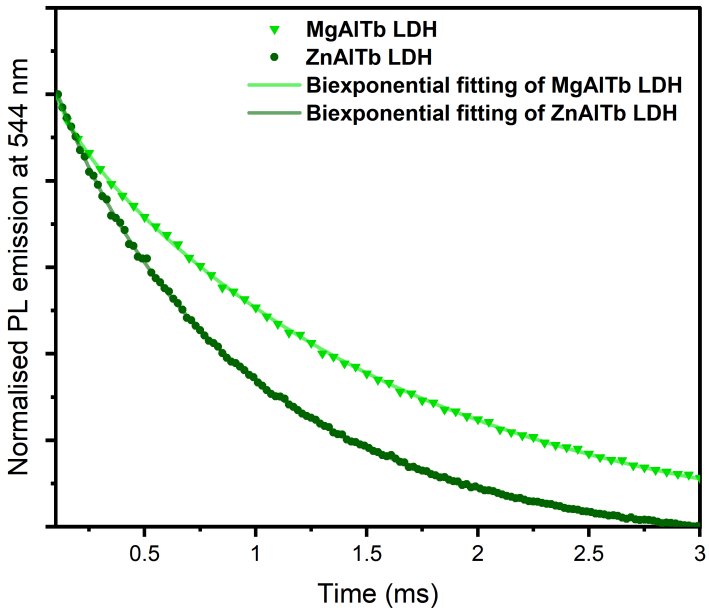


Figure 5.11: Phosphorescence decay curves of MgAlTb and ZnAlTb LDH.

It can be observed that the MgAlTb sample has a significantly longer phosphorescent lifetime than ZnAlTb LDH, and were calculated to be 1.53 ms and 0.96 ms, respectively. The results of the biexponential decay fitting are summarised in Table 5.4.

Table 5.4: PL decay lifetimes and parameters from biexponential fitting of MgAlTb and ZnAlTb LDH decay.

| | $\mathbf{A_1}$ | $\tau_1$ **(ms)** | $\mathbf{A_2}$ | $\tau_2$ **(ms)** | $\tau_{\mathbf{avg}}$ **(ms)** |
|---|---|---|---|---|---|
| **MgAlTb** | 0.1707 | 0.0979 | 1.0404 | 1.5421 | 1.53 |
| **ZnAlTb** | 0.1432 | 0.2234 | 1.0753 | 0.9781 | 0.96 |

To understand this noticeable change in lifetime, it may be useful to revisit the emission spectra of both samples. It can be observed that the $^5D_4$ – $^7F_3$ transition at 617 nm has a much higher intensity in the case of ZnAlTb LDHs when compared to MgAlTb

LDHs. This enhancement of the emission peak in the orange-red region is responsible for the slightly more yellow emission observed in ZnAlTb LDHs under the UV-lamp (Figure 5.2.) As the luminescent lifetimes were calculated by monitoring the decay of the emission over time at 544 nm, specifically monitoring the $^5D_4$ – $^7F_5$ relaxation, then it is likely that the observed shorter lifetime in ZnAlTb LDH is due to more efficient relaxation to the $^7F_3$ level. The increased prominence of the $^5D_4$ – $^7F_3$ transition in ZnAlTb LDH compared to MgAlTb not only contributes to the shortened lifetime, but also manifests as a noticeable shift in the colour of the emission, transitioning from a true green to a more yellow-green hue. This is depicted in the CIE chromaticity diagram (Figure 5.12), which was produced using the emission spectra of the lanthanide doped LDHs. The origin of the anomalous enhancement of the $^5D_4$ – $^7F_3$ transition in these ZnAlTb nanoplates is currently unknown. These phosphorescent lifetimes on the order of a few ms are common MgAlTb LDHs intercalated with sensitiser anions, as reported by Gunawan *et al.* (1.3 ms)[35], as well as for other $Tb^{3+}$ doped inorganic materials including carbon dots[62], and $KSr_{1-x}PO_4$ phosphors.[63]

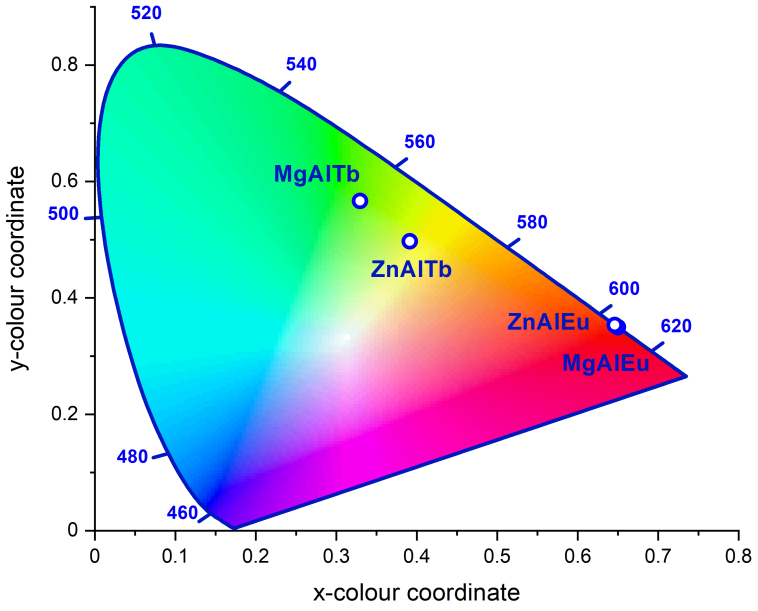


Figure 5.12: Chromaticity diagram of all phosphorescent LDHs produced in this work.

### 5.3.3 Lanthanide-doped LDHs for luminescent 'turn-off' sensing of dichromate ions

#### Initial quenching tests

Following structural, morphological and photophysical characterisation, all four luminescent LDH samples – namely MgAlEu, MgAlTb, ZnAlEu, and ZnAlTb LDHs - were tested for potential applications in luminescent 'turn-off' sensing, in which successful sensing is characterised by quenching of the luminescence in the presence of the test analyte. Dichromate ($Cr_2O_7^{2-}$) was chosen as a test analyte in this case, as it is a source of hexavalent chromium (Cr(VI)), a prevalent environmental pollutant whose accidental consumption can

lead to serious consequences for human health.[20] The initial testing conditions were as follows: 10 mg of LDH was placed in 10 mL of 2 mM $Na_2Cr_2O_7$ solution and sonicated for 10 minutes (equivalent to 432 ppm of $Cr_2O_7^{2-}$). The PL emission spectra were measured in the presence and absence of $Cr_2O_7^{2-}$ to determine the effect of the pollutant on the emission of the LDHs. It was observed that, in all four cases, near 100% quenching of the lanthanide luminescence by $Cr_2O_7^{2-}$ was observed at this concentration, as shown in Figure 5.13. Full emission spectra of all rare-earth doped LDHs in the presence of 2 mM $Cr_2O_7^{2-}$ can be found in Appendix D (Figures D7-D10).

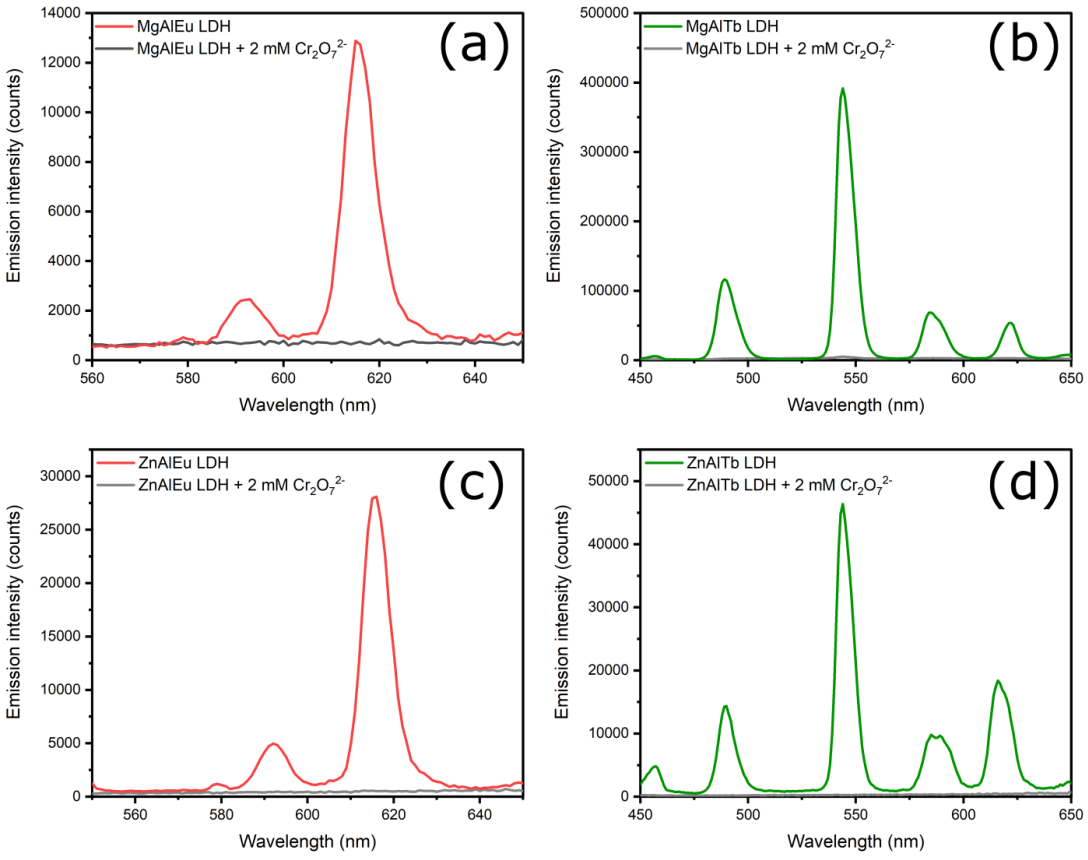


Figure 5.13: PL emission of (a) MgAlEu, (b) MgAlTb, (c) ZnAlEu and (d) ZnAlTb LDH in presence (grey) and absence (coloured) of $Cr_2O_7^{2-}$.

### Concentration-dependent studies and estimation of detection limits

The relationship between the concentration of the quencher and the extent of quenching was examined using PL spectroscopy. Briefly, 10 mg of MgAlEu LDH was mixed with 10 mL of $Na_2Cr_2O_7$ aqueous solution, of varying concentrations from 1 mM down to 0.01 mM. The concentration dependency of the emission is shown in Figure 5.14. (a) and (b).

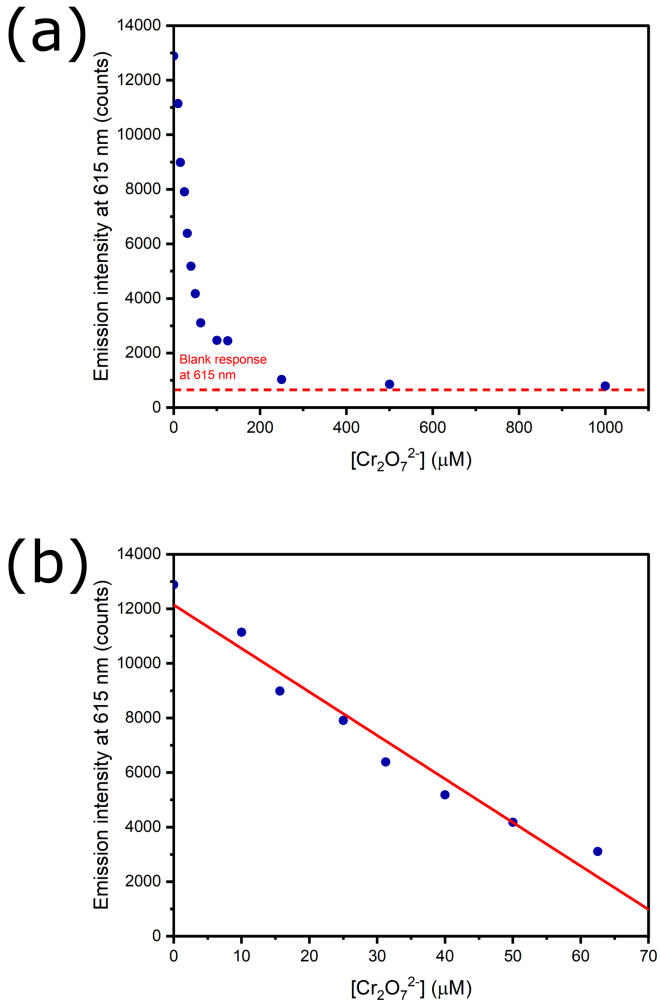


Figure 5.14: Dependence of the emission intensity of MgAlEu LDH on the concentration of $Cr_2O_7^{2-}$ present for (a) the entire concentration range tested, and (b) in the low concentration region.

It is worth noting that the only MgAlEu LDHs were the subject of this study, with similar studies on the other LDH compositions being subject to future work. It can be observed that in the low-concentration regime, the emission intensity decreases approximately linearly with increasing dichromate concentration, according to Equation 5.5, obtained from linear regression analysis in OriginLab:

$$\mathrm{y} = -159.46\mathrm{x} + 12142.28 \tag{5.5}$$

where $y$ is the emission intensity, and $x$ is the concentration of dichromate (in μM). Due to time constraints, this concentration-dependent study was only conducted once, and further datapoints and repetitions of are required to verify the linearity of the quenching response with respect to concentration. This concentration-dependent emission curve can be used to estimate the sensor's limit of detection (LOD). LOD is often calculated using the slope of the emission-concentration calibration curve, and the standard deviation of measurements of a 'blank' sample, according to Equation 5.6, known as the '3σ method':[64]

$$LOD = \frac{3.3\sigma_{blank}}{|k|} \tag{5.6}$$

where $\sigma_{blank}$ is the standard deviation of the emission intensity of blank measurements, and $k$ is the slope of the emission vs. concentration plot. It should be mentioned that, in the case of luminescent 'turn-off' sensors, the 'blank' sample contains the sensing material, but no analyte.

8 PL emission measurements were taken of the blank sample (MgAlEu LDH in the absence of quencher), resulting in mean ($\mu_{blank}$) and $\sigma_{blank}$ values of 12015 counts and 624

counts, respectively. Taking $k$ as 159.46 from Equation 5.5 yields a LOD of 12.9 μM, or 2.8 ppm, using the $3\sigma$ method. However, a number of articles on sensing are critical of the $3\sigma$ approach, and many established researchers in the field instead prefer alternative methods to LOD calculations. One such method to more accurately assess the LOD is by using the limit of blank (LOB), as shown in Equation 5.7:[65]

$$\mathrm{LOB} = \mu_{blank} + 1.645\sigma_{blank} \tag{5.7}$$

where $\mu$ is the mean, and $\sigma$ is the standard deviation of the response. Using the same values of $\mu_{blank}$ and $\sigma_{blank}$ as above yields a LOB of 13041 counts. The LOD can be related to the LOB according to Equation 5.8:

$$\mathrm{LOD} = \mathrm{LOB} + 1.645\sigma_{low} \tag{5.8}$$

where $\sigma_{low}$ is the standard deviation of the response in a low concentration sample.

Taking $\sigma_{low}$ as the error in the $y$-intercept of the calibration curve in the low-concentration regime, the LOD is approximately 13685 counts. This LOD value can be converted from counts to $Cr_2O_7^{2-}$ concentration using Equation 5.5, giving a theoretical LOD of 10.4 μM or approximately 2.2 ppm. Due to the similarity in the results of the two different LOD calculation approaches, it is therefore very likely that the detection limit of the MgAlEu LDH for chromate sensing lies somewhere in the region of 10-13 μM, or 2-3 ppm. It is important to stress that this LOD is just an initial estimate, and multiple repetitions as well as more datapoints in the region of the anticipated LOD would be required to more accurately assess the LOD, which are subject to future work along with LOD calculations

for the other LDH sensing systems.

While many recently reported $Eu^{3+}$-based anionic sensors have reported LODs down to the parts per billion (ppb) range, these new low-ppm range $Eu^{3+}$-doped MgAl LDHs have estimated detection limits that are comparable to a number of reported Eu-based sensors for Cr(VI)-containing anions, despite having a relatively low doping fraction (6.25% mol $Eu^{3+}$), as well as a very simple room-temperature and ambient pressure synthetic approach. For example, pure layered europium hydroxide sensors for dichromate were reported with a LOD of 1.2 μM.[24] Liu *et al.* reported $Eu^{3+}$-based metal-organic complexes with LOD values of down to 16 μM for chromate ($CrO_4^-$). Another report of a solvothermally-synthesised $Eu^{3+}$-centred metal-organic complex exhibited LOD values of 1.07 ppm for chromate and dichromate.[66] Furthermore, these sensors have comparable LODs to non-luminescent LDH-based colourimetric anionic sensors, such as the detection of $F^-$ by MgAl LDH (12.9 μM)[67]

**Insights into sensing mechanism - static vs. dynamic quenching**

A number of experimental investigations were conducted to investigate the dominant quenching mechanism in our lanthanide-LDH based sensing systems. While there are a number of specific quenching mechanisms, they can generally be described as static or dynamic processes. Static quenching can be described as the complexation between the luminescent material (the donor) and a quencher (the acceptor) to form a non-emissive, or less-emissive, ground-state complex. Dynamic quenching, which can encompass FRET, Dexter, as well as collisional quenching, can generally be described as the result of energy transfer between donor and acceptor.[68–71] All of our investigations into the quenching mechanism were conducted using MgAlEu LDH initially, with tests on the other LDH samples being subject to future work.

Initially, UV-Vis absorption spectroscopy was conducted on the quencher, $Cr_2O_7^{2-}$, to assess its absorption profile. It can be observed that the absorption spectrum of $Na_2Cr_2O_7$ has significant overlap with the MgAlEu LDH excitation spectrum, as shown in Figure 5.15 (a). Therefore, it is likely that the $Cr_2O_7^{2-}$ ions are directly absorbing photons from the excitation source, leading to a reduction in the number of photons reaching the $Eu^{3+}$ dopant, thus hindering the formation of the excited state and its subsequent relaxation through emission.

Furthermore, there is a noticeable red-shift in the $Cr_2O_7^{2-}$-associated UV-Vis absorption bands after mixing with MgAlEu LDH, as shown in Figure 5.15 (b). As LDHs have a partial positive surface charge, one of their most common applications is as adsorbents for anionic pollutants, including $Cr_2O_7^{2-}$ . In our case, $Cr_2O_7^{2-}$ is indeed strongly adsorbed on the surface of the LDH after 10 minutes of mixing, and is not removed even after multiple rounds of centrifugation at 15,000 rpm. Adsorption has been reported to cause a redshift in UV-Vis absorption bands of the adsorbate, in a phenomenon known as the adsorption-induced absorbance redshift, and is a result of interactions between the electronic states of $Cr_2O_7^{2-}$ and MgAlEu LDH.[72] Adsorption of quencher molecules onto the surface of luminescent nanomaterials would constitute a static quenching process. Therefore, both of these UV-Vis observations are indicators of 'turn-off' sensing *via* static quenching.

However, the spectral overlap as shown in Figure 5.15 (b) could equally be indicative of an energy transfer process, which would constitute a dynamic quenching mechanism. Therefore, further studies on the luminescent lifetime, as well as the concentration dependence of the quenching, are required to gain a clearer insight into whether static or dynamic quenching is the dominant mechanism in this sensing system.

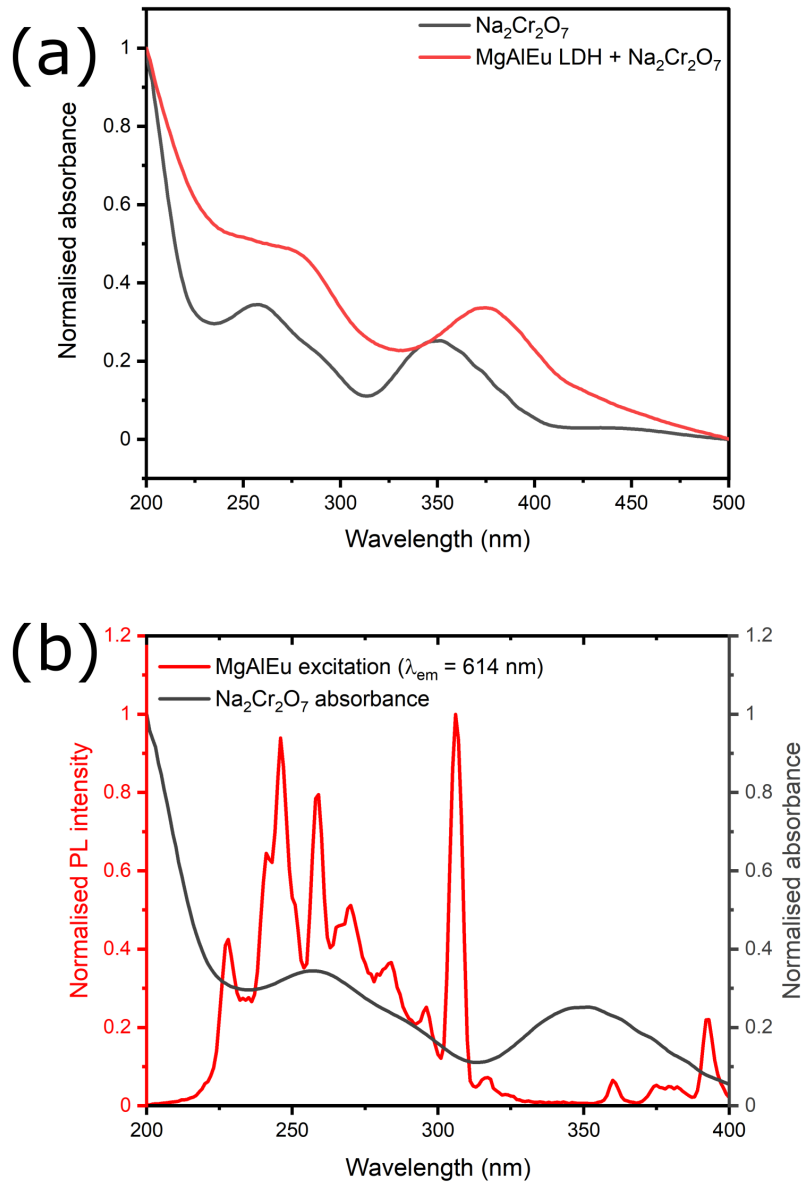


Figure 5.15: (a) Spectral overlap of MgAlEu LDH PL excitation (red) and $Na_2Cr_2O_7$ absorbance (black). (b) Adsorption-induced absorbance redshift of $Na_2Cr_2O_7$.

A Stern-Volmer plot was produced, to gain some initial insights into the quenching mechanism. The Stern-Volmer equation describes the kinetics of luminescence quenching, i.e. describes partially quenched luminescence as a function of the concentration of a

quencher molecule.[73] The Stern-Volmer equation is presented in Equation 5.9:

$$\frac{I_0}{I} = 1 + K_{SV}[Q] \tag{5.9}$$

where $I_0$ is the emission intensity in the absence of a quencher, $I$ is the fluorescence intensity in the presence of the quencher, $K_{SV}$ is the Stern-Volmer quenching constant, represented by the slope of the graph of $\frac{I_0}{I}$ versus $[Q]$, and $[Q]$ is the concentration of the quencher molecule. As shown in Figure 5.16, the Stern-Volmer plot does not follow a simple linear trend, but instead an upward curvature is observed.

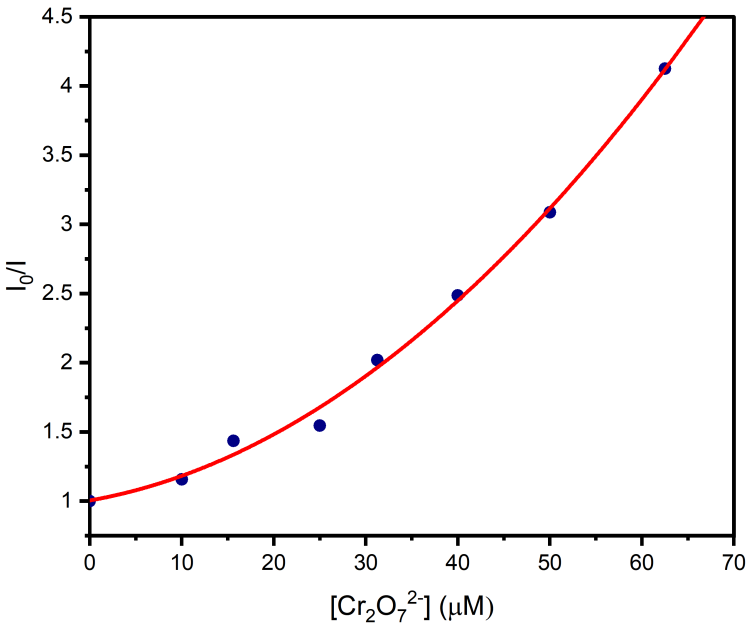


Figure 5.16: Stern-Volmer plot of phosphorescence quenching of MgAlEu LDH by low concentrations of $Cr_2O_7^{2-}$.

While a good amount of useful data can be extracted from a Stern-Volmer plot (for example limits of detection and quenching constants), it alone is not sufficient to tell us

whether a quenching mechanism is static, dynamic, or a combination of the two. Typically, a linear Stern-Volmer plot indicates that the quenching mechanism is *either* static *or* dynamic, whereas a non-linear Stern-Volmer plot that displays noticeable curvature is indicative of a more complex scenario involving an interplay between both static and dynamic mechanisms. However, this is not always the case, and quite often curved Stern-Volmer plots can arise even in cases of purely static quenching.[74–76] To further distinguish between static and dynamic processes, it is common to compare the lifetimes in the absence and the presence of the quencher, as shown in Figure 5.17. It can be observed that, in the MgAlEu LDH/chromate system, the phosphorescence lifetimes remain unchanged, with the only observed difference between the decay curves in the presence and absence of the quencher being in the emission intensities.

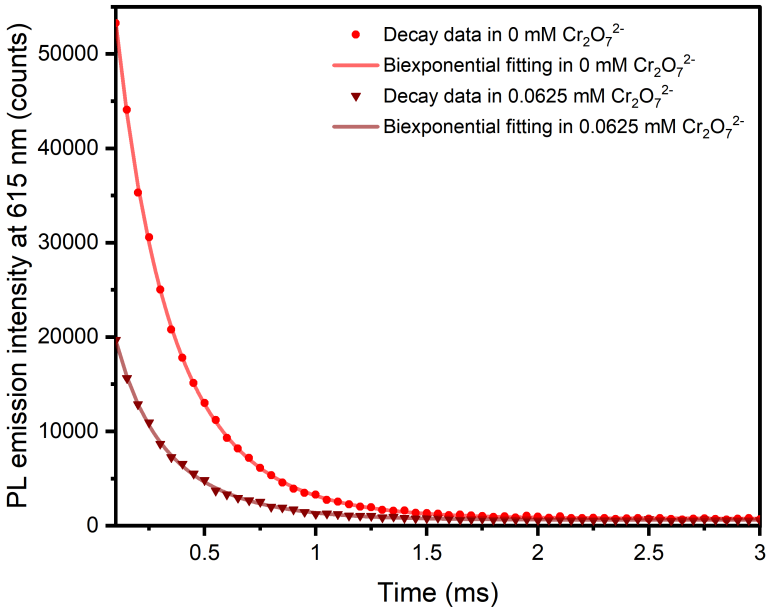


Figure 5.17: Comparison of phosphorescence decay of MgAlEu LDH in presence and absence of $Cr_2O_7^{2-}$ quencher.

Dynamic quenching processes involve a quencher molecule coming into close proximity with a luminophore in its excited state. In this regime, the excited state is deactivated via energy transfer from the luminophore to the quencher, which results in the luminophore returning to its ground state faster, and thus effectively reducing the lifetime. Therefore, if dynamic quenching is occurring, then the measured luminescence lifetime should be shorter in the presence of the quencher, than its absence.[68] In contrast, in the static quenching regime, the system can be assumed to form a non-emissive ground state complex, hindering the formation of the excited state and thus the apparent lifetime does not change, only the apparent emission intensity.

The luminescent lifetimes of MgAlEu LDH in both the presence and absence of $Cr_2O_7^{2-}$ quencher were calculated using Equation 5.4 as mentioned previously, the results of which are summarised in Table 5.5.

Table 5.5: Biexponential fitting parameters and average lifetime of MgAlEu LDHs in presence and absence of quencher.

| $Cr_2O_7^{2-}$ | $A_1$ | $\tau_1$ *(ms)* | $A_2$ | $\tau_1$ *(ms)* | $\tau_{\mathbf{avg}}$ **(ms)** |
|---|---|---|---|---|---|
| 0 | 26920 | 0.1376 | 54010 | 0.3217 | **0.29 ± 0.04** |
| 0.0625 | 11310 | 0.1106 | 20030 | 0.3057 | **0.27 ± 0.04** |

It appears that there is a negligible change in PL lifetime of the MgAlEu LDH in the presence of the quencher compared to in its absence. However, to ensure there is no real change in the lifetimes, it is important to consider any uncertainty in the calculations and fitting models. The following (quite lengthy) expression for estimating the error in luminescence lifetime can be derived from the uncertainty propagation formulae for addition, multiplication, division and exponents respectively, as shown in Equation 5.10 and derived in Appendix D:

$$\delta\tau_{avg} = \tau_{avg}\sqrt{\left(\frac{\delta A_1^2\tau_1^4 + 2A_1^2\tau_1^2\delta\tau_1^2 + \delta A_2^2\tau_2^4 + 2A_2^2\tau_2^2\delta\tau_2^2}{(A_1\tau_1^2 + A_2\tau_2^2)^2}\right) + \left(\frac{\tau_1^2\delta A_1^2 + A_1^2\delta\tau_1^2 + \tau_2^2\delta A_2^2 + A_2^2\delta\tau_2^2}{(A_1\tau_1 + A_2\tau_2)^2}\right)} \tag{5.10}$$

where $\delta$x is the relatively uncertainty in variable $x$, obtained from fitting in OriginLab.

It is evident therefore that, when the uncertainty in the measurements is taken into consideration, there is no discernible change in the luminescent lifetime in the presence of the quencher compared to in its absence. Therefore, the experimental evidence points towards a static quenching mechanism. The lack of change in luminescent lifetime, in addition to the spectral overlap of the absorption of Cr(VI) and the excitation of $Eu^{3+}$, as well as the absorption-induced redshift in chromate anion absorbance, supports that the mode of sensing is due to static quenching, and more specifically is a result of the inner filter effect of Cr(VI)-containing ions.[24,77,78]

### 5.3.4 Advantages of lanthanide doping over lanthanide-based materials - a brief comparative cost analysis

There are a number of recent reports which detail the use of rare-earth hydroxides as novel sensing platforms.[22–24,79,80] While these sensors exhibit high sensitivities and low limits of detection, it is important to consider how feasible the scalability of these sensing platforms are, particularly in terms of cost, as well as abundance of these elements in the earth's crust. Rare-earth elements are incredibly expensive for a number of reasons, including the difficulty in sourcing lanthanide-contain. However, the name 'rare-earth element' does not come from their abundance (in fact, europium and terbium are more abundant than gold and silver), but instead from their dispersion throughout the Earth's crust. Rare-earth containing minerals

are typically not found in high concentration clusters or deposits, meaning they are difficult to mine, and thus their supply is scarce. Furthermore, the isolation of rare-earth elements from ores involves complex, multi-step extraction processes such as ion exchange, solvent extraction, and electrolysis. These are the predominant reasons for the high prices of these materials, as summarised in Table 5.6. It is worth noting that these prices were obtained from common chemical vendors such as Sigma Aldrich and Fisher Scientific, whereas on an industrial scale, these prices would undoubtedly be significantly lower.

Table 5.6: Prices per 100g, and metal percentage Earth abundances for the synthetic precursors used in this chapter.

| **Reagent** | **Price per 100 g (to nearest €)** | **Abundance of metal in Earth's crust** |
|---|---|---|
| $MgCl_2.6H_2O$ | €6 | 2.33% |
| $Al(NO_3)_3.9H_2O$ | €14 | 8.23% |
| $Zn(NO_3)_2.6H_2O$ | €13 | 0.007% |
| $Tb(NO_3)_3.6H_2O$ | €2002 | 0.0002% |
| $Eu(NO_3)_3.6H_2O$ | €2318 | 0.00012% |
| NaOH | €18 | 2.36% |
| $Na_2CO_3$ | €5 | 2.36% |

Pure rare-earth hydroxides are typically synthesised using standard precipitation reactions, as shown in Equation 5.11, where Ln denotes the lanthanide species (either europium or terbium in this instance).

$$\mathrm{Ln(NO_3)_3.6H_2O + 3NaOH \rightarrow Ln(OH)_3 \downarrow + 3NaNO_3 + 6H_2O} \tag{5.11}$$

Taking this into consideration, and assuming a 100% yield of the rare-earth hydroxide from the salt precursor, the cost of the metal salts precursors required to produce 100 g of $Eu(OH)_3$ and $Tb(OH)_3$ would be approximately €5100 and €4330, respectively. This can

then be compared to the estimated cost it would require to produce 100 g of rare-earth doped LDHs. While determining the empirical formula of a given composition of LDH is difficult, for the purposes of a rough cost estimate, we will assume that the stoichiometric coefficients correspond to that of the initial molar ratios used (i.e. ($M^2$:$Al^{3+}$:$Ln_{3+}$ = 1:0.5:0.1). The general equation for the formation of an LDH with this stoichiometry, using the precursors used throughout this chapter, are given in Equations 5.12 and 5.13.

$$\frac{5}{8}\mathrm{MgCl_2.6H_2O} + \frac{5}{16}\mathrm{Al(NO_3)_3.9H_2O} + \frac{1}{16}\mathrm{Ln(NO_3)_3.6H_2O} + 2\mathrm{NaOH} + \frac{3}{16}\mathrm{Na_2CO_3} \rightarrow \mathrm{Mg_{0.625}Al_{0.3125}Ln_{0.0625}(OH)_2(CO_3)_{0.1875}.mH_2O} \downarrow \tag{5.12}$$

$$\frac{5}{8}\mathrm{Zn(NO_3)_2.6H_2O} + \frac{5}{16}\mathrm{Al(NO_3)_3.9H_2O} + \frac{1}{16}\mathrm{Ln(NO_3)_3.6H_2O} + 2\mathrm{NaOH} + \frac{3}{16}\mathrm{Na_2CO_3} \rightarrow \mathrm{Zn_{0.625}Al_{0.3125}Ln_{0.0625}(OH)_2(CO_3)_{0.1875}.mH_2O} \downarrow \tag{5.13}$$

As before, based on the assumption of 100% yield of the LDH, the masses of each metal salt precursor required to form 100 g of the LDH can be calculated, and thus estimate the overall cost can be estimated. These are summarised in Table 5.7 and 5.8 for doped MgAl and ZnAl LDHs, respectively.

This cost analysis reveals significant reductions in raw material expenses when utilising Eu- and Tb-doped LDHs instead of $Eu(OH)_3$ and $Tb(OH)_3$. Specifically, the use of Eu-doped LDHs as sensors could result in cost savings of up to 83% for MgAlEu LDH and 87% for ZnAlEu LDH compared to the $Eu(OH)_3$. Similarly, savings of up to 82% and 86% for MgAlTb and ZnAlTb, respectively, can be achieved compared to the alternative use of $Tb(OH)_3$. Therefore, by substituting rare earth hydroxides for rare earth-doped layered

double hydroxides, significant reductions in cost can be achieved, which bodes well for the scalability of lanthanide-based environmental sensing devices using LDHs as the matrix.

Table 5.7: Cost breakdown of producing 100 g of rare earth-doped MgAl LDHs

| **LDH type** | **Reagent** | **Mass required** | **Cost** | **Total cost of 100 g** |
|---|---|---|---|---|
| MgAlEu | $MgCl_2.6H_2O$ | 161.2 g | €9.70 | €874.80 |
| | $Al(NO_3)_3.9H_2O$ | 149.6 g | €20.90 | |
| | $Eu(NO_3)_3.6H_2O$ | 35.6 g | €824.50 | |
| | NaOH | 102.1 g | €18.40 | |
| | $Na_2CO_3$ | 25.4 g | €1.30 | |
| MgAlTb | $MgCl_2.6H_2O$ | 161.2 g | €9.70 | €769.20 |
| | $Al(NO_3)_3.9H_2O$ | 148.7 g | €20.80 | |
| | $Tb(NO_3)_3.6H_2O$ | 35.9 g | €719.10 | |
| | NaOH | 101.5 g | €18.30 | |
| | $Na_2CO_3$ | 25.2 g | €1.30 | |

Table 5.8: Cost breakdown of producing 100 g of rare earth-doped ZnAl LDHs

| **LDH type** | **Reagent** | **Mass required** | **Cost** | **Total cost of 100 g** |
|---|---|---|---|---|
| ZnAlEu | $Zn(NO_3)_2.6H_2O$ | 178.7 g | €23.20 | €674.80 |
| | $Al(NO_3)_3.9H_2O$ | 112.7 g | €15.80 | |
| | $Eu(NO_3)_3.6H_2O$ | 26.8 g | €621.00 | |
| | NaOH | 76.9 g | €13.80 | |
| | $Na_2CO_3$ | 19.1 g | €1.00 | |
| ZnAlTb | $Zn(NO_3)_2.6H_2O$ | 177.9 g | €23.10 | €596.20 |
| | $Al(NO_3)_3.9H_2O$ | 112.2 g | €15.70 | |
| | $Tb(NO_3)_3.6H_2O$ | 27.1 g | €542.60 | |
| | NaOH | 76.6 g | €13.80 | |
| | $Na_2CO_3$ | 19.0 g | €1.00 | |

## 5.4 Conclusions

In summary, in this chapter we have explored the immense potential of rare-earth-doped layered double hydroxides as luminescent sensing platforms for wastewater analysis applications. $Eu^{3+}$ and $Tb^{3+}$-doped MgAl and ZnAl LDHs were successfully synthesised *via* a room temperature co-precipitation approach. The crystallinity and phase purity of the resultant materials were analysed *via* pXRD, which, along with SEM imaging, provided some interesting and important insights into the influence of lanthanide doping on the structure of these materials.

Photophysical analysis of the resultant LDHs confirmed successful doping due to the presence of the distinct emission spectra of lanthanide ions. The observed spectral features, as well as analysis of the luminescent lifetimes, allowed us to gain useful information on the local coordination environments of the rare-earth dopants.

This part of our work also detailed the application of rare-earth-doped LDHs as luminescent 'turn-off' sensors for dichromate, a prevalent environmental pollutant of considerable health and ecological concern. A near-complete quenching of lanthanide luminescence was observed down to a concentration of around 200 μM. A concentration-dependent study of the luminescence quenching in the 0-70 μM range revealed a linear relationship between emission intensity and chromate concentration. This facilitated the calculation of detection limits down to around 10 μM or 2 ppm.

A combination of UV-Vis and concentration-dependent PL spectroscopic analysis were used to investigate the quenching mechanism. The absence of discernible changes in luminescent lifetime in the presence of the quencher, coupled with significant spectral overlap and adsorption-induced red shifting of the dichromate absorbance, pointed towards a static quenching mechanism, attributed to an inner filter effect.

Lastly, a comparative cost analysis highlighted the economic viability of employing rare-earth-doped LDHs in environmental sensing applications. The substantial reduction in raw material costs when compared with rare-earth hydroxides highlights the potential scalability of these materials for more widespread sensing devices. A graphical summary of the work conducted in this chapter is shown in Figure 5.18. We believe this research will serve as an important contribution to the field of environmental nanosensing, showcasing the potential of rare-earth-doped LDHs as robust and cost-effective sensing platforms, while simultaneously addressing urgent challenges outlined in the UN Sustainable Development Goals.

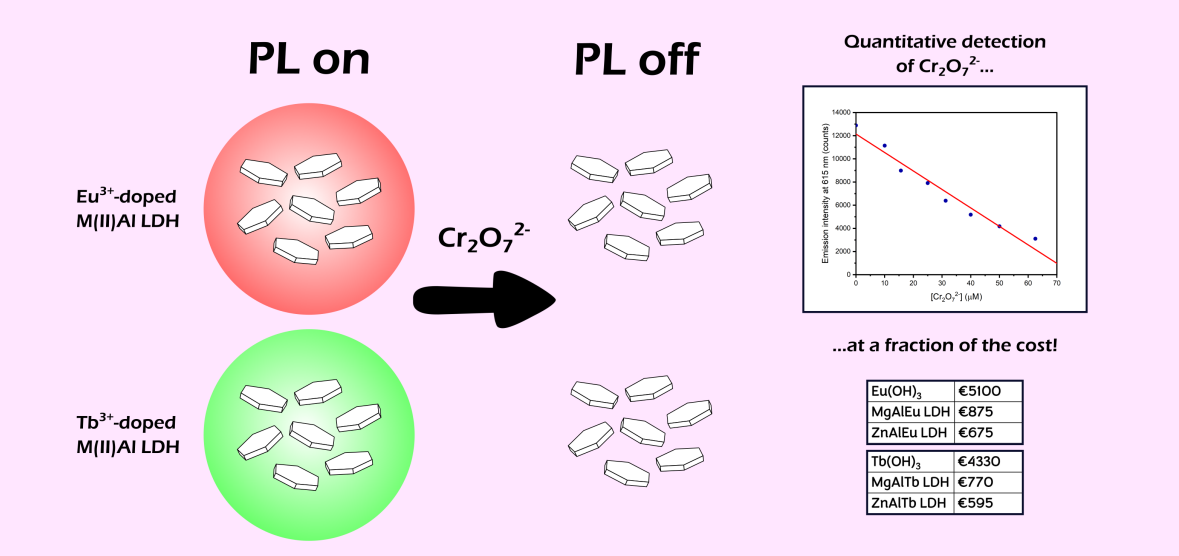


Figure 5.18: Graphical summary highlighting the main outcomes of this body of work.

# References


(1) Altug, H.; Oh, S. H.; Maier, S. A.; Homola, J. *Nature Nanotechnology* **2022**, *17*, 5–16.

(2) Su, S.; Wu, W.; Gao, J.; Lu, J.; Fan, C. *Journal of Materials Chemistry* **2012**, *22*, 18101–18110.

(3) Kumar, V.; Guleria, P.; Mehta, S. K. *Environmental Chemistry Letters* **2017**, *15*, 165–177.

(4) He, P.; Brent, J. R.; Ding, H.; Yang, J.; Lewis, D. J.; O'Brien, P.; Derby, B. *Nanoscale* **2018**, *10*, 5599–5606.

(5) Song, O.; Rhee, D.; Kim, J.; Jeon, Y.; Mazánek, V.; Söll, A.; Kwon, Y. A.; Cho, J. H.; Kim, Y. H.; Sofer, Z.; Kang, J. *npj 2D Materials and Applications* **2022**, *6*, 1–12.

(6) Sui, X.; Rangnekar, S. V.; Lee, J.; Liu, S. E.; Downing, J. R.; Chaney, L. E.; Yan, X.; Jang, H. J.; Pu, H.; Shi, X.; Zhou, S.; Hersam, M. C.; Chen, J. *Advanced Materials Technologies* **2023**, 2301288.

(7) Chen, M.; Cui, D.; Wang, N.; Weng, S.; Zhao, Z.; Tian, F.; Gao, X.; He, K.; Chiang, C. T.; Albawardi, S.; Alsaggaf, S.; Aljalham, G.; Amer, M. R.; Zhou, C. *ACS Applied Nano Materials* **2023**, *6*, 3236–3244.

(8) Munawar, A.; Ong, Y.; Schirhagl, R.; Tahir, M. A.; Khan, W. S.; Bajwa, S. Z. *RSC Advances* **2019**, *9*, 6793–6803.

(9) Liu, Y.; Lv, X.; Zhang, X.; Liu, L.; Xie, J.; Chen, Z. *Spectrochimica Acta Part A: Molecular and Biomolecular Spectroscopy* **2020**, *239*, 118497.

(10) Zhu, C.; Yang, G.; Li, H.; Du, D.; Lin, Y. *Analytical Chemistry* **2015**, *87*, 230–249.

(11) Okada, S.; Bartelle, B. B.; Li, N.; Breton-Provencher, V.; Lee, J. J.; Rodriguez, E.; Melican, J.; Sur, M.; Jasanoff, A. *Nature Nanotechnology* **2018**, *13*, 473–477.

(12) Guan, W.; Zhou, W.; Lu, J.; Lu, C. *Chemical Society Reviews* **2015**, *44*, 6981–7009.

(13) Aulsebrook, M. L.; Graham, B.; Grace, M. R.; Tuck, K. L. *Coordination Chemistry Reviews* **2018**, *375*, 191–220.

(14) Binnemans, K.; Jones, P. T. *Journal of Sustainable Metallurgy* **2015**, *1*, 29–38.

(15) Donnelly, F. C.; Purcell-Milton, F.; Dunne, P. W.; Rulikowska, A.; Alguacil, V.; Gun'ko, Y. K. *Materials Today Communications* **2019**, *20*, 100590.

(16) Zheng, B.; Fan, J.; Chen, B.; Qin, X.; Wang, J.; Wang, F.; Deng, R.; Liu, X. *Chemical Reviews* **2022**, *122*, 5519–5603.

(17) Nordborg, M.; Arvidsson, R.; Finnveden, G.; Cederberg, C.; Sörme, L.; Palm, V.; Stamyr, K.; Molander, S. *Environmental Impact Assessment Review* **2017**, *62*, 110–114.

(18) Heavy Metals — UNDRR `https://www.undrr.org/hips-cluster/heavy-metals` (accessed 10/09/2023).

(19) Banks, S. *Environs: Environmental Law and Policy Journal* **2002**, *26*, 219–252.

(20) Sharma, P.; Singh, S. P.; Parakh, S. K.; Tong, Y. W. *Bioengineered* **2022**, *13*, 4923–4938.

(21) Costa, M. *Critical Reviews in Toxicology* **1997**, *27*, 431–442.

(22) Liang, J.; Ma, R.; Sasaki, T. *Dalton Transactions* **2014**, *43*, 10355–10364.

(23) Bai, M.; Liu, X.; Sakai, N.; Ebina, Y.; Jia, L.; Tang, D.; Sasaki, T.; Ma, R. *Journal of Physical Chemistry Letters* **2021**, *12*, 10135–10143.

(24) Liu, W.; Zhang, J.; Yin, X.; He, X.; Wang, X.; Wei, Y. *Materials Chemistry and Physics* **2021**, *266*, 124540.

(25) Kim, Y.; Son, Y.; Bae, S.; Kim, T. H.; Hwang, Y. *Nanomaterials* **2022**, *12*, 1384.

(26) Wang, X.; Zhou, W.; Wang, C.; Chen, Z. *New Journal of Chemistry* **2018**, *42*, 9463–9471.

(27) Gumus, Z. P.; Erbas, Z.; Soylak, M. *Analytical Letters* **2023**, *57*, 1646–1665.

(28) Suh, M. J.; Weon, S.; Li, R.; Wang, P.; Kim, J. H. *Environmental Science and Technology* **2020**, *54*, 9106–9115.

(29) Sustainable Development Goals launch in 2016 `https://www.un.org/sustainabledevelopment/blog/2015/12/sustainable-development-goals-kick-off-with-start-of-new-year/` (accessed 11/26/2023).

(30) Chen, Y.; Bao, Y.; Wang, X. *Journal of Fluorescence* **2016**, *26*, 813–820.

(31) Zhang, J.; Xie, X.; Li, C.; Wang, H.; Wang, L. *RSC Advances* **2015**, *5*, 29757–29765.

(32) Chen, Y.; Zhou, S.; Li, F.; Li, F.; Chen, Y. *Journal of Luminescence* **2011**, *131*, 701–704.

(33) Ungár, T. *Scripta Materialia* **2004**, *51*, 777–781.

(34) Langford, J. I.; Wilson, A. J. C. *Journal of Applied Crystallography* **1978**, *11*, 102–113.

(35) Gunawan, P.; Xu, R. *Journal of Physical Chemistry C* **2009**, *113*, 17206–17214.

(36) Qiao, X. G.; Dugas, P. Y.; Prevot, V.; Bourgeat-Lami, E. *Polymer Chemistry* **2020**, *11*, 3195–3208.

(37) Dong, H.; Chen, M.; Rahman, S.; Parekh, H. S.; Cooper, H. M.; Xu, Z. P. *Applied Clay Science* **2014**, *100*, 66–75.

(38) Chen, B.; Sun, Q.; Wang, D.; Zeng, X. F.; Wang, J. X.; Chen, J. F. *Industrial and Engineering Chemistry Research* **2020**, *59*, 2960–2967.

(39) Teixeira, A.; Morais, A.; Silva, I.; Breynaert, E.; Mustafa, D. *Crystals* **2019**, *9*, 153.

(40) Pastor, A.; Chen, C.; de Miguel, G.; Martín, F.; Cruz-Yusta, M.; O'Hare, D.; Pavlovic, I.; Sánchez, L. *Chemical Engineering Journal* **2023**, *471*, 144464.

(41) Stokes, A. R.; Wilson, A. J. *Proceedings of the Physical Society* **1944**, *56*, 174.

(42) Zhao, Y.; Li, J. G.; Fang, F.; Chu, N.; Ma, H.; Yang, X. *Dalton Transactions* **2012**, *41*, 12175–12184.

(43) Janicki, R.; Kdziorski, A.; Mondry, A. *Physical Chemistry Chemical Physics* **2016**, *18*, 27808–27817.

(44) Xu, S. M.; Pan, T.; Dou, Y. B.; Yan, H.; Zhang, S. T.; Ning, F. Y.; Shi, W. Y.; Wei, M. *Journal of Physical Chemistry C* **2015**, *119*, 18823–18834.

(45) Blanco-Gutierrez, V.; Demourgues, A.; Jubera, V.; Gaudon, M. *Journal of Materials Chemistry C* **2014**, *2*, 9969–9977.

(46) Tanner, P. A. *Chemical Society Reviews* **2013**, *42*, 5090–5101.

(47) Kolesnikov, I. E.; Povolotskiy, A. V.; Mamonova, D. V.; Kolesnikov, E. Y.; Kurochkin, A. V.; Lähderanta, E.; Mikhailov, M. D. *Journal of Rare Earths* **2018**, *36*, 474–481.

(48) Bondzior, B.; Dereń, P. J. *Journal of Luminescence* **2018**, *201*, 298–302.

(49) Blasse, G.; Grabmaier, B. C., *Luminescent Materials*; Springer-Verlag: Berlin, Germany, 1994.

(50) Morais, A. F.; Silva, I. G. N.; Ferreira, B. J.; Teixeira, A. C.; Sree, S. P.; Terraschke, H.; Garcia, F. A.; Breynaert, E.; Mustafa, D. *Chemical Communications*, 13571–13574.

(51) Yang, R.; Jiang, P.; Gao, W.; Cong, R.; Yang, T. *Journal of Solid State Chemistry* **2019**, *276*, 173–180.

(52) Balda, R.; Fernández, J.; García, A. J.; Imbusch, G. F. *Journal of Luminescence* **1998**, *76-77*, 551–554.

(53) Morais, A. F.; Silva, I. G.; Lima, B. C.; Garcia, F. A.; Mustafa, D. *ACS Omega* **2020**, *5*, 23778–23785.

(54) Liu, M.; Kang, M.; Chen, K.; Mou, Y.; Sun, R. *Applied Physics A: Materials Science and Processing* **2018**, *124*, 1–10.

(55) Shavaleev, N. M.; Eliseeva, S. V.; Scopelliti, R.; Bünzli, J. C. G. *Inorganic Chemistry* **2015**, *54*, 9166–9173.

(56) Kumar, V.; Tiwari, S. P.; Etefa, H. F.; Jule, L. T.; Ntwaeaborwa, O. M.; Swart, H. C. *Journal of Luminescence* **2022**, *250*, 119085.

(57) Wang, M.; Hu, C.; Su, Q. *Biosensors* **2022**, *12*, 131.

(58) Shen, Y.; Xu, S.; He, D. *PLOS ONE* **2015**, *10*, e0129689.

(59) Verma, R. K.; Kumar, K.; Rai, S. B. *Solid State Sciences* **2010**, *12*, 1146–1151.

(60) Wang, J.; Zakrzewski, J. J.; Zychowicz, M.; Xin, Y.; Tokoro, H.; Chorazy, S.; ichi Ohkoshi, S. *Angewandte Chemie International Edition* **2023**, *62*, e202306372.

(61) Neto, A. N. C.; Kasprzycka, E.; Souza, A. S.; Gawryszewska, P.; Suta, M.; Carlos, L. D.; Malta, O. L. *Journal of Luminescence* **2022**, *248*, 118933.

(62) Vostrikova, A. M.; Kokorina, A. A.; Demina, P. A.; German, S. V.; Novoselova, M. V.; Tarakina, N. V.; Sukhorukov, G. B.; Goryacheva, I. Y. *Scientific Reports* **2018**, *8*, 1–8.

(63) Weng, M. H.; Yang, R. Y.; Peng, Y. M.; Chen, J. L. *Ceramics International* **2012**, *38*, 1319–1323.

(64) Liu, Q. R.; Liu, B.; Qiu, M. M.; Miao, W. N.; Xu, L. *Journal of Solid State Chemistry* **2022**, *311*, 123138.

(65) Armbruster, D. A.; Pry, T. *The Clinical Biochemist Reviews* **2008**, *29*, S49.

(66) Liu, J.; Ji, G.; Xiao, J.; Liu, Z. *Inorganic Chemistry* **2017**, *56*, 4197–4205.

(67) Jia, Y.; Li, Z.; Shi, W. *Sensors and Actuators B: Chemical* **2013**, *188*, 576–583.

(68) Webber, S. E. *Photochemistry and Photobiology* **1997**, *65*, 33–38.

(69) Dworak, L.; Reuss, A. J.; Zastrow, M.; Rück-Braun, K.; Wachtveitl, J. *Nanoscale* **2014**, *6*, 14200–14203.

(70) Murphy, C. B.; Zhang, Y.; Troxler, T.; Ferry, V.; Martin, J. J.; Jones, W. E. *Journal of Physical Chemistry B* **2004**, *108*, 1537–1543.

(71) Lakowicz, J. R. *Principles of Fluorescence Spectroscopy* **1983**, 257–301.

(72) Liu, C.; Chung, S. Y.; Lee, S.; Weiss, S.; Neuhauser, D. *Journal of Chemical Physics* **2009**, *131*, 174705.

(73) Gehlen, M. H. *Journal of Photochemistry and Photobiology C: Photochemistry Reviews* **2020**, *42*, 100338.

(74) Ciotta, E.; Prosposito, P.; Pizzoferrato, R. *Journal of Luminescence* **2019**, *206*, 518–522.

(75) Keizer, J. *J. Am. Chem. Soc* **1983**, *105*, 1494–1498.

(76) Peak, D.; Werner, T. C.; Dennin, R. M.; Baird, J. K. *The Journal of Chemical Physics* **1983**, *79*, 3328–3335.

(77) Chen, S.; Yu, Y. L.; Wang, J. H. *Analytica Chimica Acta* **2018**, *999*, 13–26.

(78) Tang, S.; You, X.; Fang, Q.; Li, X.; Li, G.; Chen, J.; Chen, W. *Sensors* **2019**, *19*, 228.

(79) Tian, C.; Wang, L.; Luan, F.; Fu, X.; Zhuang, X.; Chen, L. *Chemical Communications* **2019**, *55*, 12479–12482.

(80) Li, J.; Gu, Q.; Heng, H.; Wang, Z.; Jin, H.; He, J. *Spectrochimica Acta Part A: Molecular and Biomolecular Spectroscopy* **2022**, *272*, 120969.

# Chapter 6

# Conclusions and Future Work

## 6.1 Conclusions

This thesis represents a comprehensive exploration of the properties and potential applications of selected two-dimensional nanomaterials, with a particular focus on layered double hydroxide (LDH)-based nanomaterials. The results presented here contribute unique insights into the synthesis, structural and functional properties, as well as potential applications of these nanomaterials.

The room-temperature, aqueous, synthetic approaches employed throughout this project proved to be very efficient, resulting in the preparation of a variety of LDH and LDH-derived nanomaterials. Firstly, chemical co-precipitation was used to synthesise CuAl-$CO_3$ LDHs. Two different approaches, a modified-co-precipitation and post-synthetic functionalisation, were explored for chirality induction in CuAl-$CO_3$ LDHs. These approaches resulted in the formation of numerous LDH-derived chiroptically active nanostructures. Most notably, the phenylalanine post-synthetic functionalisation in the presence of a base

resulted in the formation of unique chiral CuO superstructures, which have shown *g*-factors 2 orders of magnitude higher than anticipated for ligand-induced chirality. A combination of characterisation techniques including pXRD, CD and SEM revealed the assembly of CuO nanosheets into superstructures, driven by phenylalanine $\pi$-$\pi$ interactions, as the origin of significant optical activity enhancement. This innovative approach to produce chiral 2D nanomaterials opens avenues for applications in chiral sensing and asymmetric catalysis.

Building upon this foundation, the next part of our project was focused on the preparation of a novel electrostatically stabilized CuAl-$CO_3$ LDH/BNOx nanocomposite designed for advanced nanofiltration (NF) applications. The nanocomposite, which was produced using a combination of top-down and bottom-up synthetic techniques, exhibited promising performance in nanofiltration membranes, achieving up to 100% retention of various water-soluble dyes, as well as state-of-the-art solvent flux rates. A combination of SEM and mercury porosimetry, as well as adsorption studies, were used to elucidate the structural origins of these excellent nanofiltration properties. Additionally, the inclusion of LDHs in these membranes resulted in the demonstration of efficient photocatalytic degradation of dyes under visible-light conditions, most notably serving as the first example of Evans Blue degradation by a LDH-based photocatalyst. While the current membranes require additional substrate support for mechanical stability, ongoing efforts aim to enhance their mechanical integrity through chemical cross-linking of nanosheets. This work marks a significant step forward in user-friendly and affordable nanofiltration technologies, contributing valuable insights for potential applications in water treatment, aligned closely with UN SDG 6. It is also anticipated that the merging of these two projects, and thus formation of chiral CuO/BNOx nanocomposite membranes, may be of significant interest for applications in chiral separation.

The final body of work presented in this thesis explores the synthesis and characterisation of lanthanide-doped MgAl and ZnAl-based LDHs *via* two-step chemical

co-precipitation approaches. Photophysical and structural characterisation, using pXRD and PL respectively, reveals interesting and useful information on the local coordination environments of the $Eu^{3+}$ and $Tb^{3+}$ cations in the LDH matrices, which deserves further study on how the coordination impacts the photophysical properties. A preliminary study of the luminescent sensing capabilities of the LDHs was conducted, revealing that all LDHs synthesised in this work were capable of luminescent 'turn-off' chemo-sensing of dichromate ions. A more in-depth study on the MgAlEu LDH sensing capabilities allowed for the determination of dichromate detection limits down to the low ppm range, as well as revealed the origin of luminescent sensing through a static quenching approach. This research showcases the potential of lanthanide-doped LDHs for environmental sensing applications, supported by a comparative cost analysis, which emphasizes the economic viability of these materials, suggesting scalability for widespread sensing devices. Once again, this research is very closely aligned with UN SDG 6.

In summary, this body of work underscores the multifunctional potential of layered double hydroxides. By seamlessly integrating material synthesis, detailed characterization, and application insights, this research contributes to the ever-evolving field of materials science, and highlights the pivotal role layered double hydroxides may have as multifunctional materials across various domains, including energy science, environmental, and pharmaceutical applications.

## 6.2 Preliminary studies and future work

While several substantial strides have been made in this research, there are still some aspects of the project that are require further studies in order to bring these research directions to full completion. Furthermore, this project has revealed numerous new avenues of research in these materials which warrant exploration. In our future research endeavours, we aim to pursue the following specific avenues of research, to expand the applications of layered double hydroxides in nanoscience and nanotechnology.

1) The post-synthetic functionalisation of LDHs with chiral molecules will be further explored, and expanded to other LDHs and chiral molecules, to determine whether this approach can be generalised in order to obtain other chiral metal oxides. Furthermore, we aim to experiment with the synthetic parameters in the modified co-precipitation approach to see if it is possible to induce chirality while maintaining the LDH crystal structure.

2) Subsequently, the obtained chiral metal oxides will be mixed with BN and BNOx to make new types of chiral membranes. These membranes will be tested for potential applications in enantiomeric separation, to see if the chiral morphology of the obtained structures have any impact on their efficacy as chiral filters.

3) The main future avenue of research on the LDH/BNOx nanocomposite membranes will involve improving their mechanical and structural integrity, i.e., reducing their fragility. This is to ensure the entire membranes themselves are reusable, and not just the material that makes up the membrane. The main avenue of research we aim to explore in this regard in chemical cross-linking, which will require further functionalisation of the BN or BNOx nanosheets.

4) In addition to improving the mechanical integrity in order to ensure membrane reusability, other LDH compositions will be tested as potential photocatalysts for integration into BNOx-based membranes, to assess their feasibility as anti-fouling agents. Furthermore, we believe the introduction of other co-catalysts, with lower electron-hole recombination rates, in conjunction with LDHs may improve the photodegradation efficiency, and potentially eliminate the need for hydrogen peroxide, thus enhancing the sustainability and green chemical nature of this process.

5) TEM imaging of the lanthanide-doped and undoped MgAl and ZnAl LDH is required for a more in-depth analysis of their morphology. Furthermore, EDX elemental mapping, as well as ICP-MS, is required to reveal the true level of doping in these materials, as well as examine the homogeneity of the doping, and how this may impact the photophysical properties of these materials.

6) A full study on the sensing of dichromate ions will be conducted using MgAlTb, ZnAlEu and ZnAlTb LDHs, as was carried out for MgAlEu LDHs, to clearly determine their limits of detection. Furthermore, the sensing of other anionic pollutants in water including phosphate, arsenate, fluoride, sulfide, and nitrate, among other anions, will be explored.

7) The post-synthetic functionalisation of lanthanide-doped luminescent LDHs with chiral ligands will be explored as potential novel CPL light emitters.

8) Finally, we aim to explore the potential of introducing other functionalities, for example magnetic LDHs, containing Ni, Co or Fe, and the combination with other properties including luminescence and chirality to produce multimodal LDH nanosheets.

In regard to the future research avenues highlighted above, a number of preliminary results have already been obtained in some of these projects, particularly in relation to points 1, 4 and 8 above, which are quite promising, and are shown below.

**Expansion of chirality induction to other ligands and LDH compositions**

A CD spectroscopic study of post-synthetic treatment of LDHs with various chiral ligands was conducted. Firstly, a number of alternative chiral ligands were tested with CuAl-$CO_3$ LDH, to see if the transformation to chiral CuO was possible. The other chiral molecules tested were mandelic acid (MA), dibenzoyl tartaric acid (DBTA), lactic acid (LA), tartaric acid (TA), and cysteine (Cys). CD spectroscopic analysis found that MA and DBTA did result in the induction of chirality using CuAl LDH, resulting in signals in the same regions as for CuO-Phe, but with much lower CD intensities, as shown in Figure 6.1 (a) and (b). Interestingly, functionalisation with both L- and D-DBTA resulted in the same CD signal, rather than mirror images of one another. It is possible that both enantiomers are being immobilised in the interlayer via both carboxyl groups, resulting in the same CD signal, which is an interesting and unusual phenomenon that warrants further study. However, additional characterisation needs to be conducted on these materials to determine whether chiral superstructures were formed, and whether the LDH to CuO phase transformation occurred.

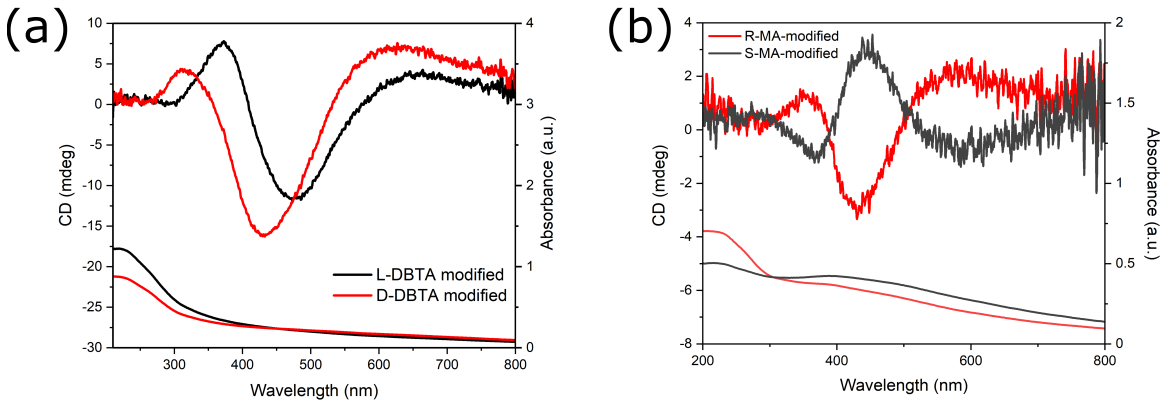


Figure 6.1: CD and UV-Vis spectra of (a) L- and D-DBTA treated CuAl LDH, and (b) R- and S-MA-treated CuAl LDH.

The other chiral molecules that were tested (LA, TA and Cys) did not produce any CD signal in the treated CuAl LDHs. Interestingly, the only molecules that have worked to date have been those containing phenyl rings, i.e., Phe, DBTA, and MA. Whereas, the non-aromatic chiral ligands have been unable to produce a CD signal thus far. This seems to support our theory that $\pi$-$\pi$ interactions between adjacent phenyl rings on the surfaces of the nanosheets causes chiral assembly and thus enhancement of the optical activity.

Furthermore, some other LDH compositions were tested with a number of chiral molecules. MgAl LDH was treated with Phe, glutamic acid (Glu) and proline (Pro), and no chiroptical activity was produced in any of these cases. However, CuCr LDH treated with L-Phe resulted in a significant broad CD signal spanning from 500-800 nm, as shown in Figure 6.2 (a), with tests with the opposite enantiomer being the subject of future work. The observed CD signal is in the region of one of the DR UV-Vis absorption bands of CuCr LDH, which can be attributed to $Cr^{3+}$ d-d transitions (Figure 6.2 (b)).

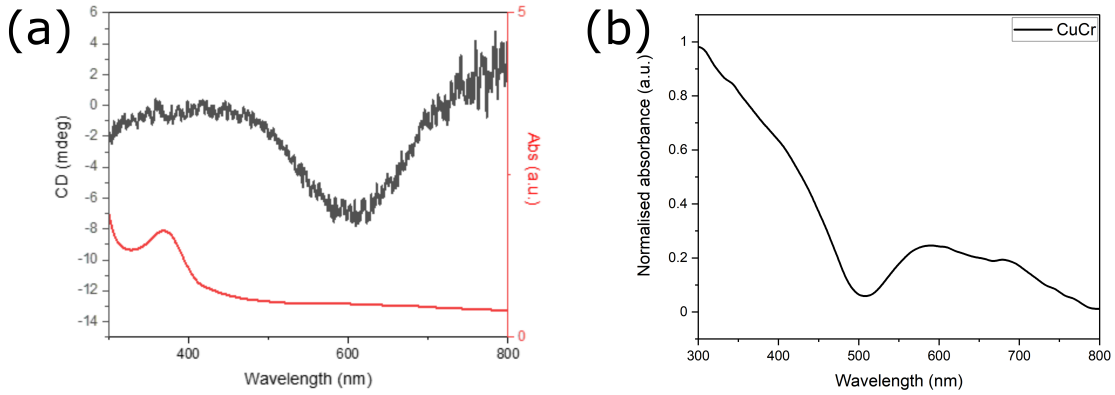


Figure 6.2: (a) CD and liquid-phase UV-Vis spectra of L-Phe-treated CuCr LDH. (b) Solid-state UV-Vis spectrum of L-Phe-treated CuCr LDH.

Interestingly, it seems that there is another trend unveiling here, in that transition metal ions need to be present in the LDH matrix for chiroptical activity to be induced, although further studies are needed on this. Therefore, based on these observations, the

future plan is to investigate the formation of chiral metal oxides or LDHs by choosing chiral ligands with $\pi$-systems, as well as transition metal-containing LDHs.

### Photocatalysis in other LDH compositions

Due to the strong absorption observed by CuCr LDHs across the visible spectrum, as shown previously in Figure 6.2 (b), it was decided to test Cr-containing LDHs for the photocatalytic degradation of methylene blue (MB) dye, as an alternative to CuAl LDHs. CuCr, CoCr and ZnCr LDHs were synthesised through co-precipitation approaches, as have been discussed in detail throughout this thesis. pXRD analysis is still to be conducted on the other materials, however pXRD of ZnCr LDH revealed that the synthesis resulted in the formation of mixed-metal-oxides (MMOs), rather than the hydroxide phase, as shown in Figure 6.3.

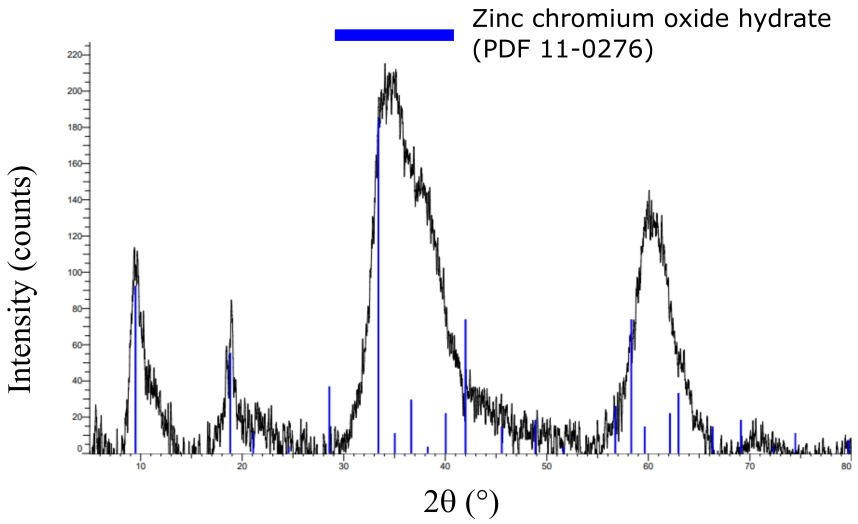


Figure 6.3: pXRD pattern of ZnCr MMO product. Reference pattern of ZnCr MMO is shown in blue.

MMOs are also widely reported as effective photocatalysts, therefore it was decided to test the ZnCr oxide product for photocatalytic degradation of MB, also using hydrogen peroxide as was previously conducted for CuAl LDHs. ZnCr MMOs were initially left in the dark in MB solution for 120 minutes, after which 20 μL of $H_2O_2$ was added and exposed to visible light. Aliquots were taken every 15 minutes for UV-Vis analysis. However, UV-Vis analysis shows that, while there is significant degradation of MB within that timeframe, it is accompanied by the release of $Cr^{6+}$, as shown by the emergence of the distinctive peaks at 270 nm and 390 nm (Figure 6.4.) Therefore, the use of Cr-containing LDHs or MMOs for degradation of the dyes was not pursued further, due to the structural instability of the materials in oxidising environments, leading to the leaching of hexavalent chromium into the system.

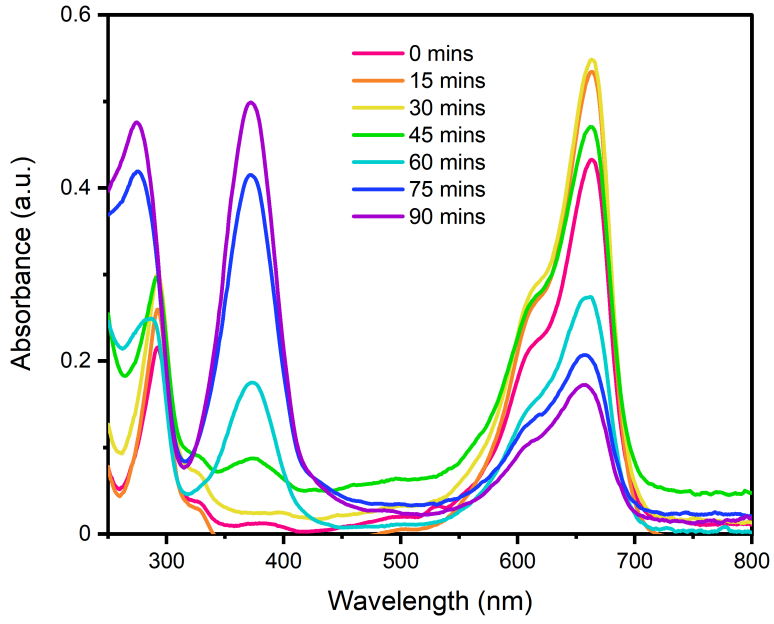


Figure 6.4: Photodegradation of methylene blue over time by ZnCr MMO, accompanied by release of $Cr^{6+}$.

### Magnetic NiCo LDHs

Magnetic NiCo LDHs intercalated and stablilised by citrate were synthesised *via* a co-precipitation approach using sodium borohydride as the precipitating agent, resulting in the formation of a black material, that showed a significant response to a magnet. Vibrating sample magnetometry (VSM) revealed a curve with no hysteresis, but very low saturation magnetisation, which are the characteristics of paramagnetic behaviour (Figure 6.5). Furthermore, TEM analysis of the resulting material revealed the formation of very small, ultrathin nanosheets using this approach, as shown in Figure 6.6.

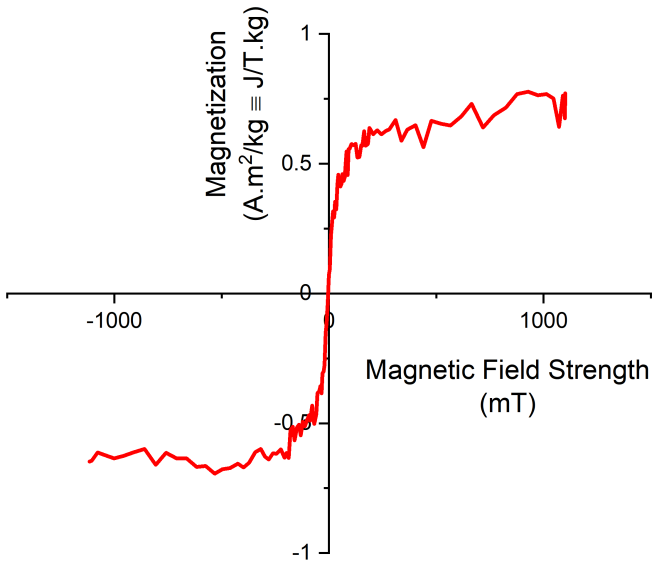


Figure 6.5: VSM curve of NiCo LDHs, showing no hysteresis and low saturation magnetisation.

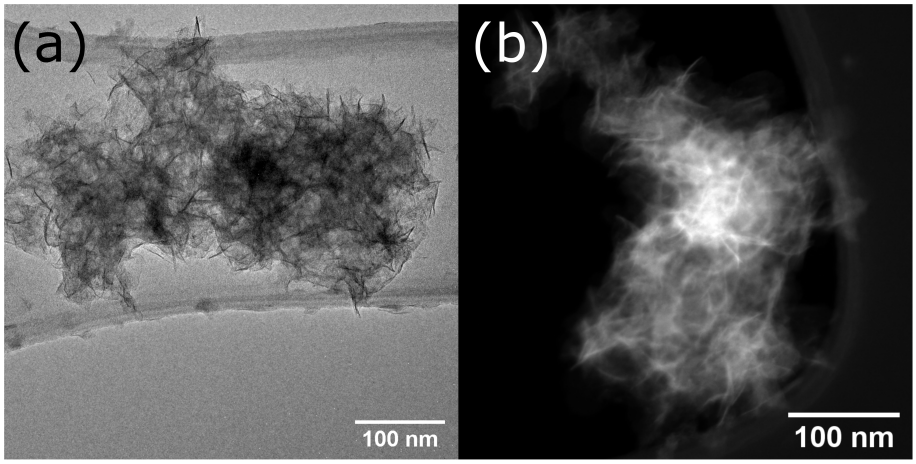


Figure 6.6: (a) TEM and (b) HAADF-STEM image of potential NiCo LDH nanostructures.

However, pXRD analysis revealed the low crystallinity of the resulting material, and thus it was not clear at all if the LDH phase had formed (Figure 6.7 (a)). Interestingly, when the material was kept in ethanol, it remained black and magnetic, however when transferred to water, it turned green and lost its magnetism. Furthermore, after the transition to the green material, there were some pXRD reflections present indicative of the formation of the NiCo LDH phase, albeit still with very low crystallinity (Figure 6.7 (b)). Therefore, it seems that this approach forms an amorphous, magnetic NiCo oxide precursor, and subsequent hydration of this phase leads to the formation of a non-magnetic hydroxide phase. This interesting phenomenon warrants further study and is the subject of future research projects.

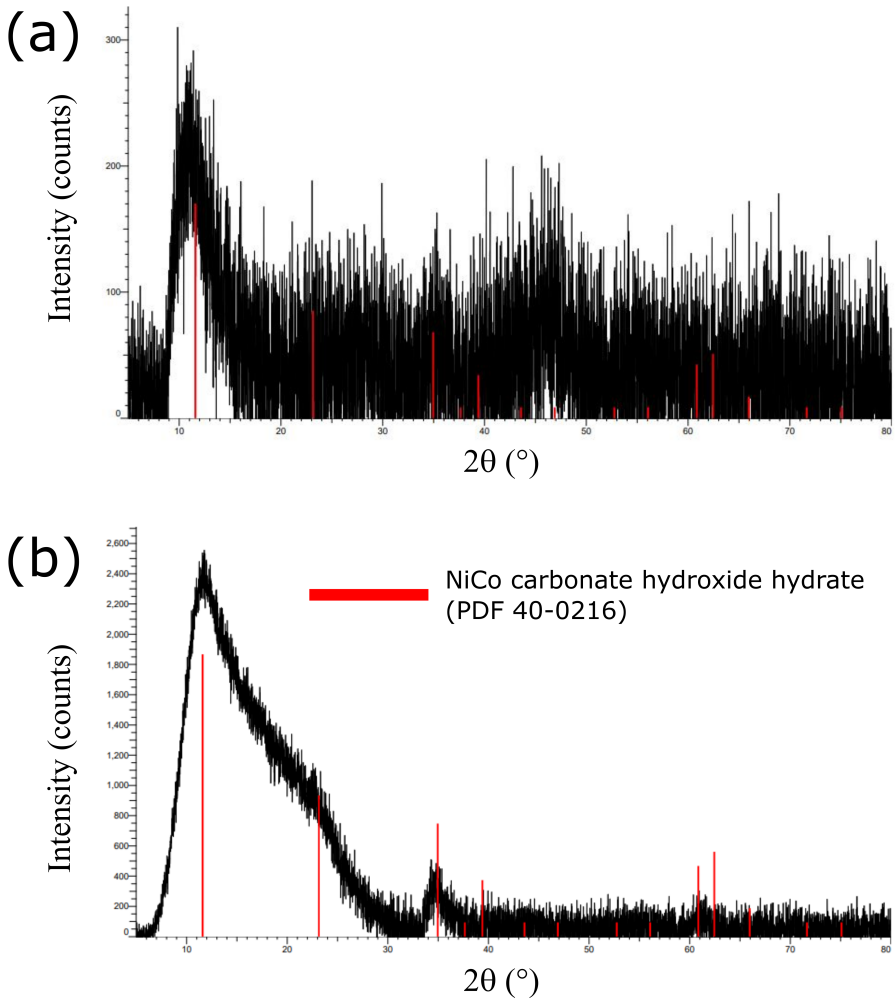


Figure 6.7: pXRD patterns of NiCo LDH product (a) before and (b) after hydration. Reference pattern of NiCo LDH is shown in red.

# Appendix A

## Derivation of the ellipticity and g-factor equations for circular dichroism spectroscopy

The interference of a left-handed and right-handed circularly polarised light wave travelling with the same phase and amplitude will result in a linearly polarised wave. However, when those waves have different amplitudes, as would be the case after interacting with a chiral molecule, the resultant wave is elliptically polarised, as shown in Figure A1.

A typical CD output is given in terms of ellipticity ($\theta$), which can be defined in terms of the magnitudes od the electric field vectors of the left- ($E_l$) and right- ($E_r$) handd circularly polarised light waves. As shown in Figure A2 and Equation A1, this is a simple trigonometric expression.

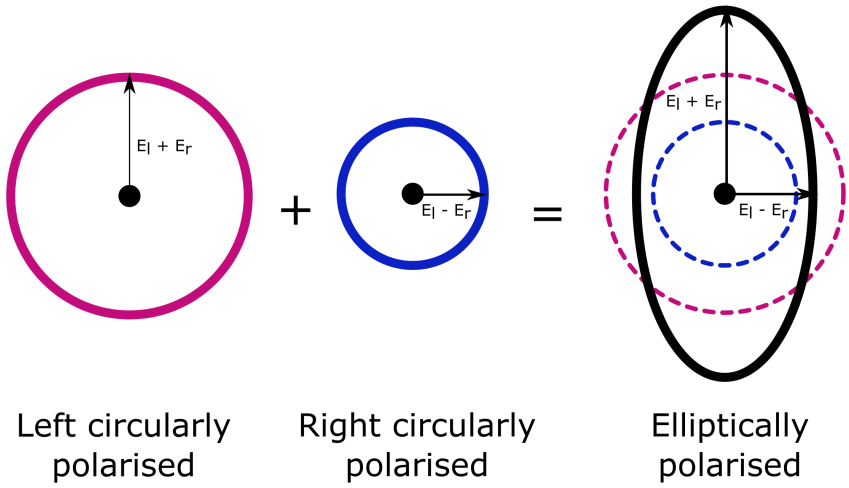


Figure A1: Interference of left- and right-circularly polarised light waves to produce an elliptically polarised wave.

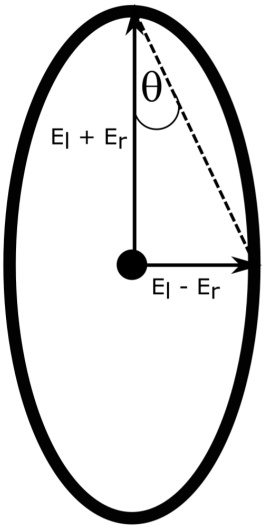


Figure A2: Trigonometric expression for ellipticity.

$$tan\theta = \frac{E_l - E_r}{E_l + E_r} \tag{A1}$$

where θ is expressed in units of radians (rad). However, in the limit of small θ, tanθ ≈ θ, therefore the above expression can be simplified to give Equation A2.

$$\theta = \frac{E_l - E_r}{E_l + E_r} \tag{A2}$$

As the intensity $(I)$ of an electromagnetic wave is proportional to the square of the magnitude of the electric field vector $(E)$, i.e. $I \propto |E|^2$), then Equation A2 can be rewritten as:

$$\theta = \frac{I_l^{1/2} - I_r^{1/2}}{I_l^{1/2} + I_r^{1/2}} \tag{A3}$$

Additionally, intensity is related to absorbance $(A)$ *via* the Beer-Lambert law, which is given in its logarithmic form in Equation A4

$$I = I_0 e^{-Aln10} \tag{A4}$$

Combining Equations A3 and A4 gives us an expression for ellipticity in terms of the absorbance of left- and right-handed circularly polarised light, as shown in Equation A5.

$$\theta = \frac{e^{-\frac{A_l}{2}ln10} - e^{-\frac{A_r}{2}ln10}}{e^{-\frac{A_l}{2}ln10} + e^{-\frac{A_r}{2}ln10}} \tag{A5}$$

This expression can be recognised as a hyperbolic tangent function of the form $-tanh(\frac{x-y}{2})$, in which $x = \frac{A_l}{2}ln10$ and $y = \frac{A_r}{2}ln10$. By using this modified expression, and recognising that $\Delta A = A_l - A_r$, we can gain a simple expression for ellipticity in terms of $\Delta A$, as shown in Equation A6.

$$\theta(rad) = tanh(\frac{\Delta Aln10}{4}) \tag{A6}$$

In the limit of small $x$, $tanh(x) \approx x$. Therefore, for small values of $\Delta A$, as is typically observed in circular dichroism, Equation A6 for ellipticity can be further simplified to give Equation A7.

$$\theta(rad) = \frac{\Delta Aln10}{4} \tag{A7}$$

However, CD spectrometers typically report an output in units of millidegrees (mdeg). Therefore, to convert from ellipticity in units of rad to units of mdeg, Equation A8 can be applied.

$$\theta(mdeg) = 1000 \text{ x } \frac{180}{\pi} \text{ x } \frac{\Delta Aln10}{4} \tag{A8}$$

Multiplying out all numerical terms gives the following expression for ellipticity in terms of millidegrees:

$$\theta(mdeg) \approx 32980\Delta A \tag{A9}$$

This derivation thus proves the origin of the CD conversion factor given in Section 2.6.3. Furthermore, this allows the $g$-factor to be calculated directly from the CD ellipticity output, according to Equation A10.

$$g = \frac{\Delta A}{A} = \frac{\theta}{32980A} \tag{A10}$$

# Appendix B

## Additional data for Chapter 3

This Appendix contains extra information and data from Chapter 3. It includes size distribution histograms obtained from analysis of TEM images, additional spectroscopic data such as CD, UV-Vis and FT-IR, EDX spectra, and additional SEM and STEM images.

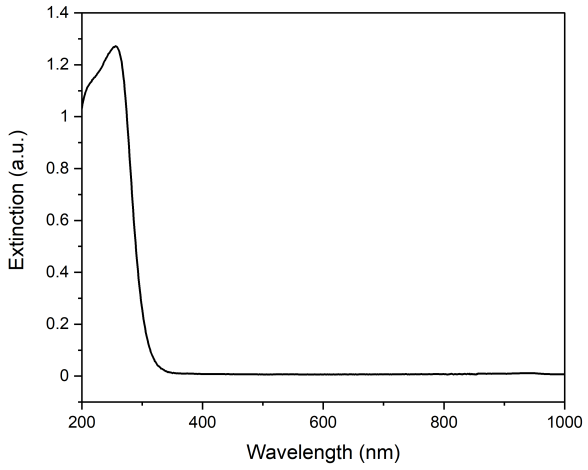


Figure B1: Diffuse reflectance UV-Vis exctinction spectrum of VWR super premium micorscope slide - the solid support for all DR UV-Vis analysis in this thesis.

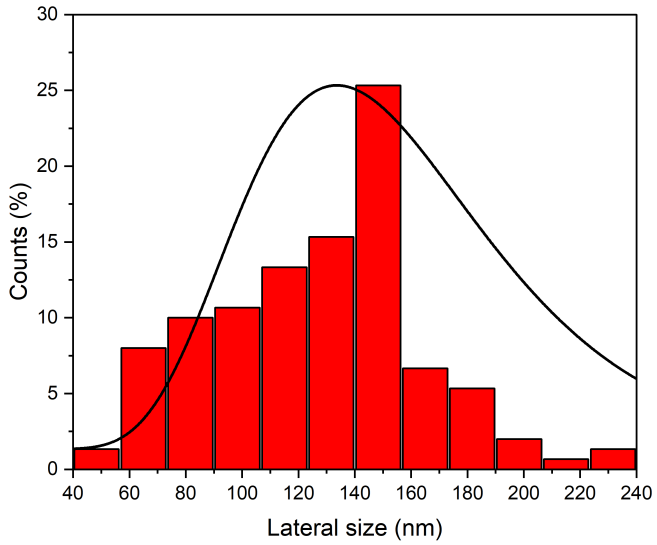


Figure B2: Size distribution analysis of CuAl-$CO_3$ LDH nanosheets, as evaluated from TEM images.

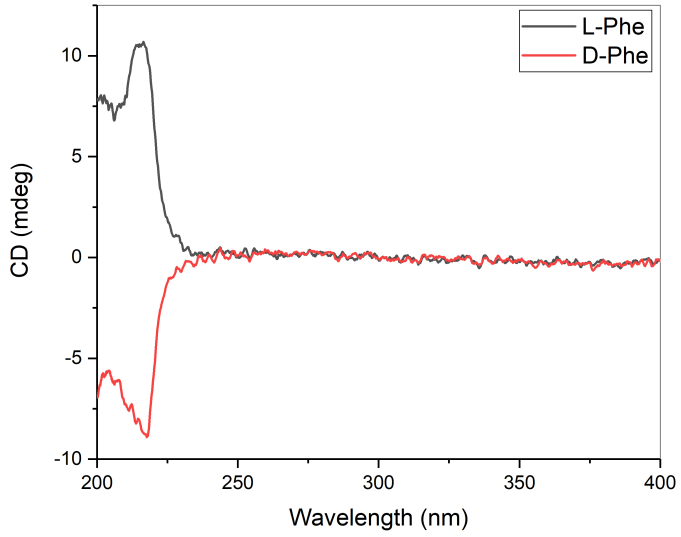


Figure B3: CD spectra of L-Phe (black) and D-Phe (red), acquired using MP water as solvent.

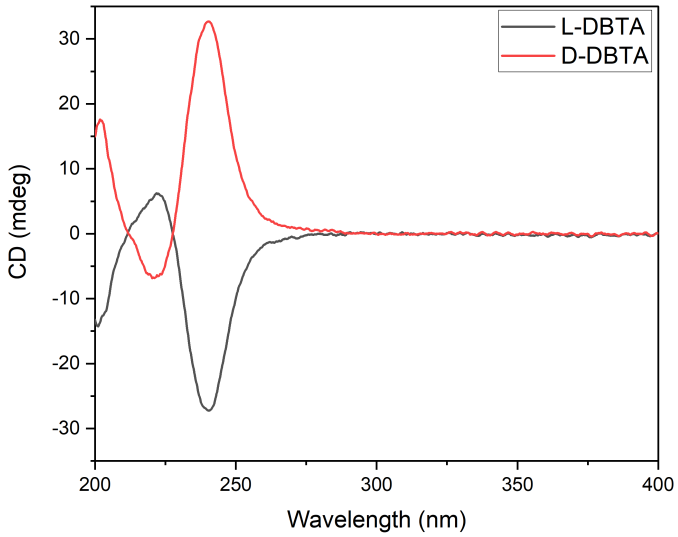


Figure B4: CD spectra of L-DBTA (black) and D-DBTA (red), acquired using MP water as solvent.

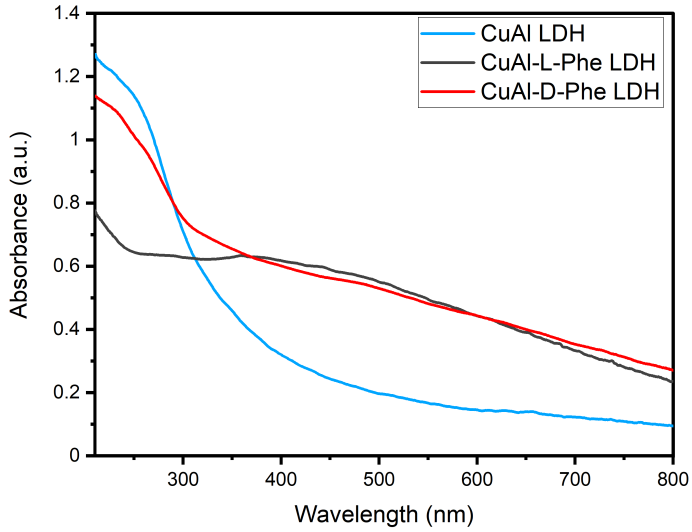


Figure B5: UV-Vis absorption spectra of CuAl LDH (blue), CuO-L-Phe (black) and CuO-D-Phe (red), acquired using ethanol as solvent.

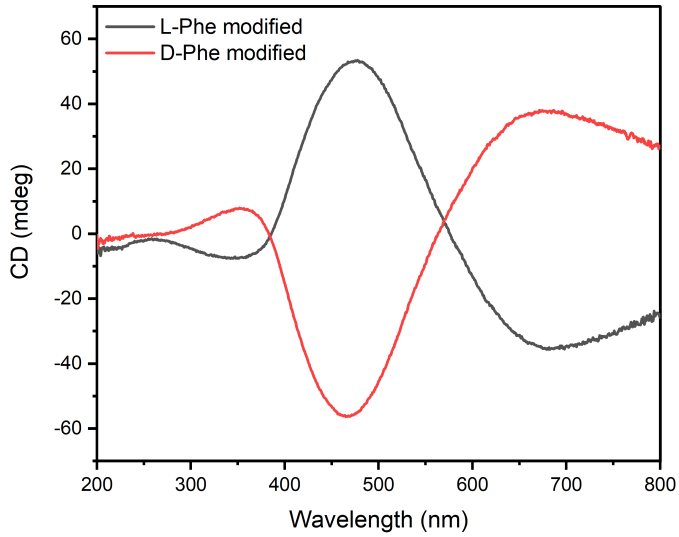


Figure B6: CD spectra of CuO-L-Phe (black) and CuO-D-Phe (red), acquired using MP water as solvent.

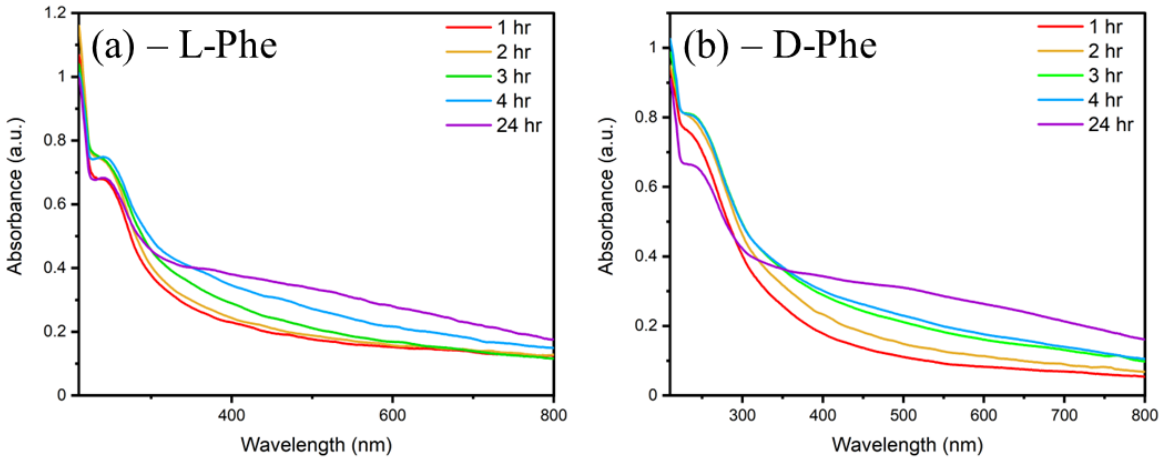


Figure B7: Time-dependent UV-Vis absorption spectra, obtained during formation of (a) CuO-L-Phe and (b) CuO-D-Phe.

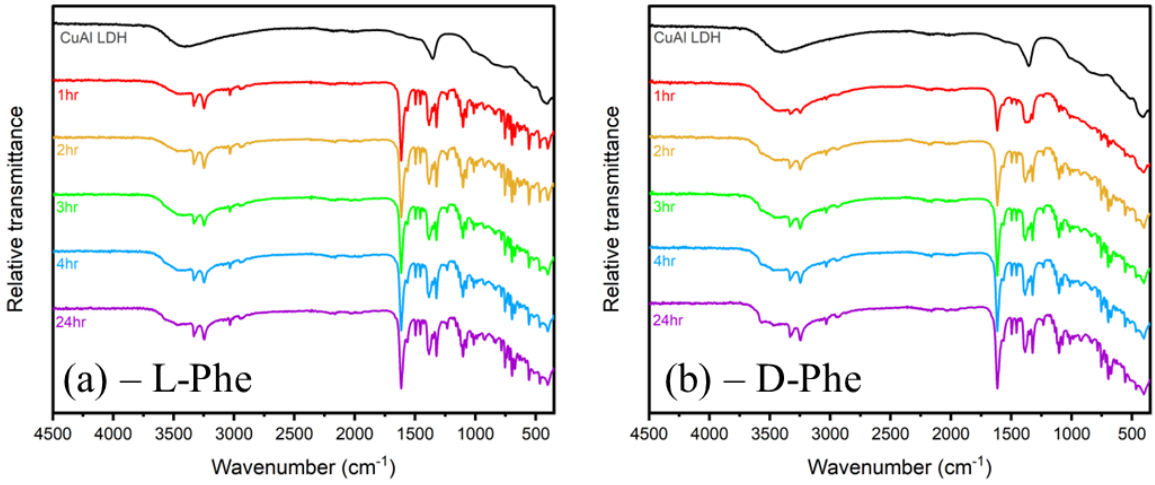


Figure B8: Time-dependent FT-IR spectra, obtained during formation of (a) CuO-L-Phe and (b) CuO-D-Phe.

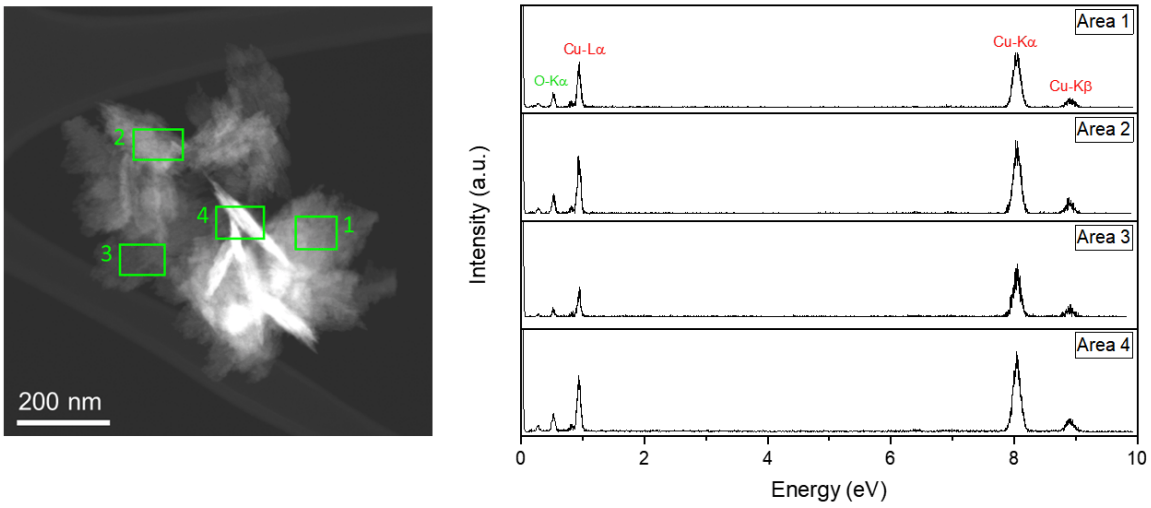


Figure B9: STEM image and corresponding EDX spectra of areas under analysis in a sample of CuO-L-Phe.

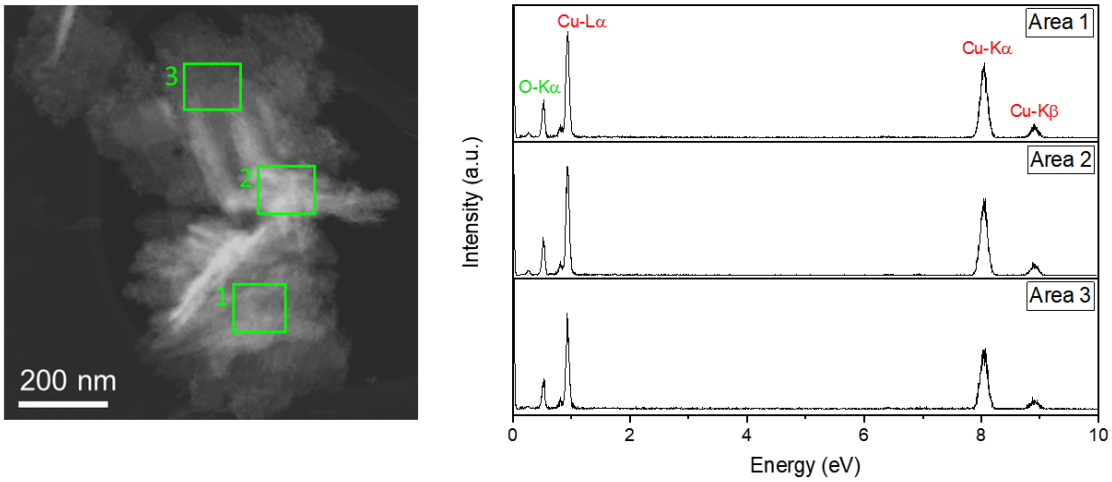


Figure B10: STEM image and corresponding EDX spectra of areas under analysis in a sample of CuO-D-Phe.

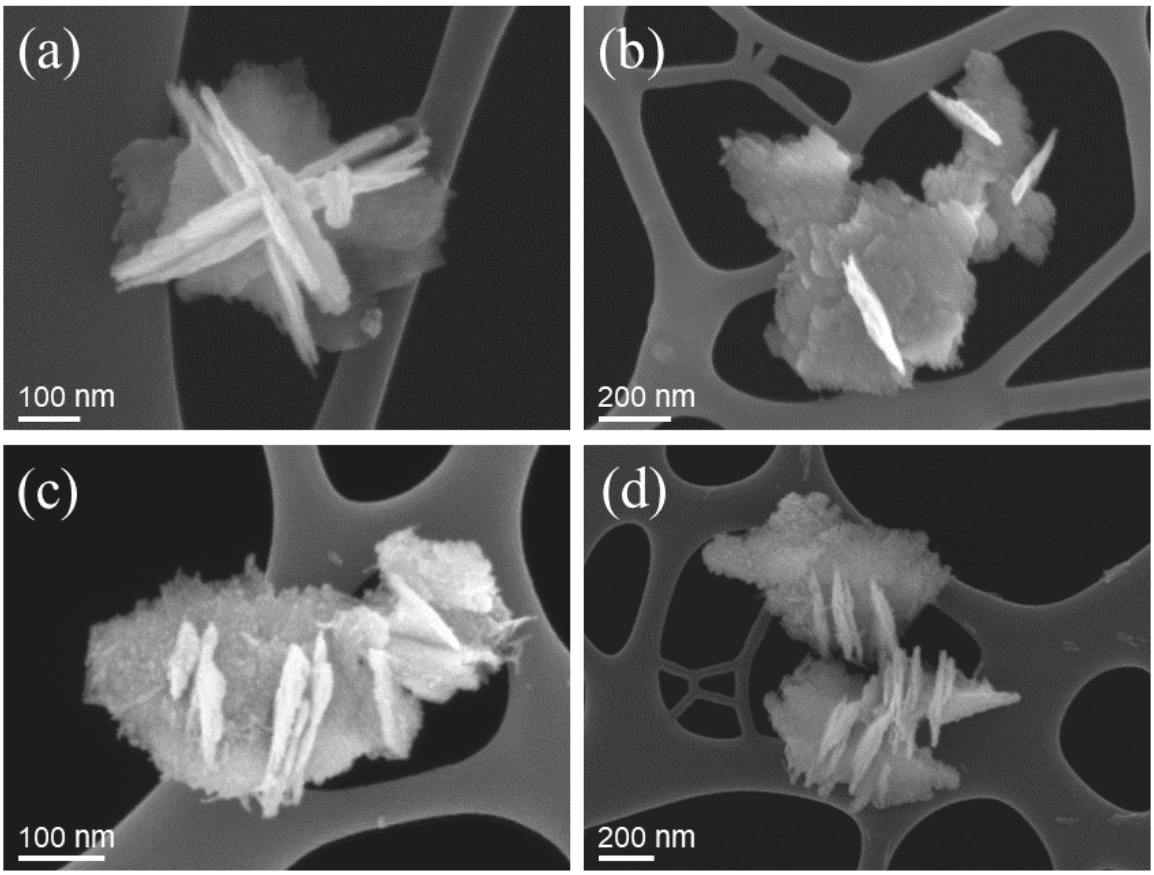


Figure B11: Additional SEM images of (a,b) CuO-L-Phe and (c,d) CuO-D-Phe nanosheet clusters.

# Appendix C

## Additional data for Chapter 4

### Compositional optimisation of LDH/BNOx nanocomposite

Membranes were prepared from a variety of compositions of LDHs. Their retentions were tested for Evans Blue and it was observed that high retentions were observed for all samples, as shown in Table C1. The UV-Vis spectra of the feed and filtrates are shown in Figure C1.

Table C1: 15 μM Evans Blue retention values of LDH/BNOx nanocomposite membranes with various compositions.

| LDH/BNOx composition by mass | Average retention (%) | No. of samples |
|---|---|---|
| 20:80 | 99 | 3 |
| 30:70 | 100 | 1 |
| 40:60 | 100 | 1 |
| 50:50 | 100 | 2 |

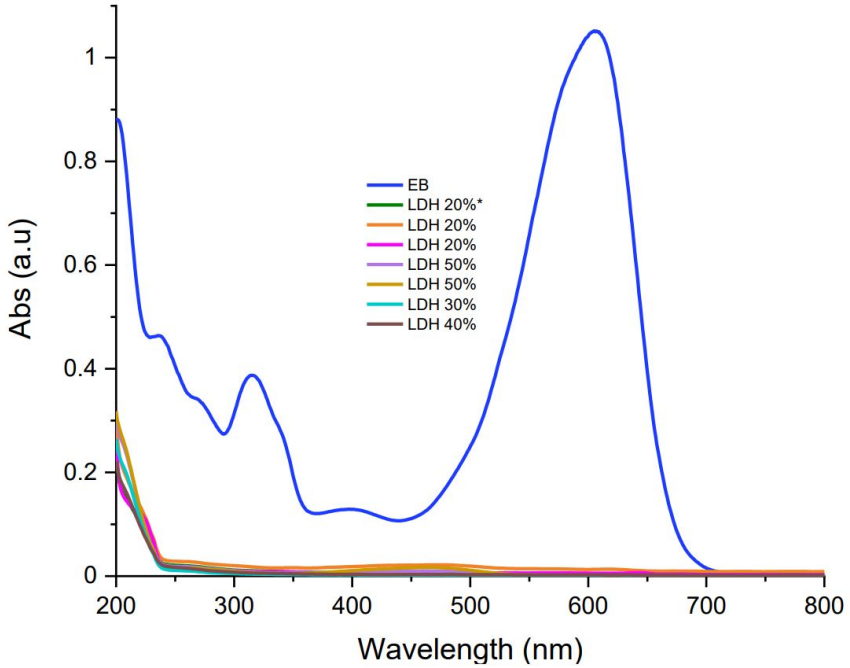


Figure C1: UV-Vis spectra of the retention of 20 mL of 15 μM Evans Blue by LDH/BNOx nanocomposite membranes of various compositions.

However, for LDH loading above 20%, two problems were encountered. The first was that the mechanical stability of the membranes suffered, due to significant shrinking of LDHs after drying, as a large amount of water can be incorporated into their interlayer. This resulted in mechanical failure of membranes prepared with a CuAl-$CO_3$ LDH mass loading of 30% or above, as shown in Figure C2.

The second problem encountered was the formation of undesired side products. At 50% mass loading of LDH, the formation of copper (II) oxide was observed by a colour change from light blue to brown, and was confirmed by pXRD, as shown in Figure C3. Therefore, it was decided to proceed with the 20:80 LDH/BNOx membranes, as they did not impact the mechanical stability of existing LDH side products, and were reliable and reproducible, not resulting in the formation of side products.

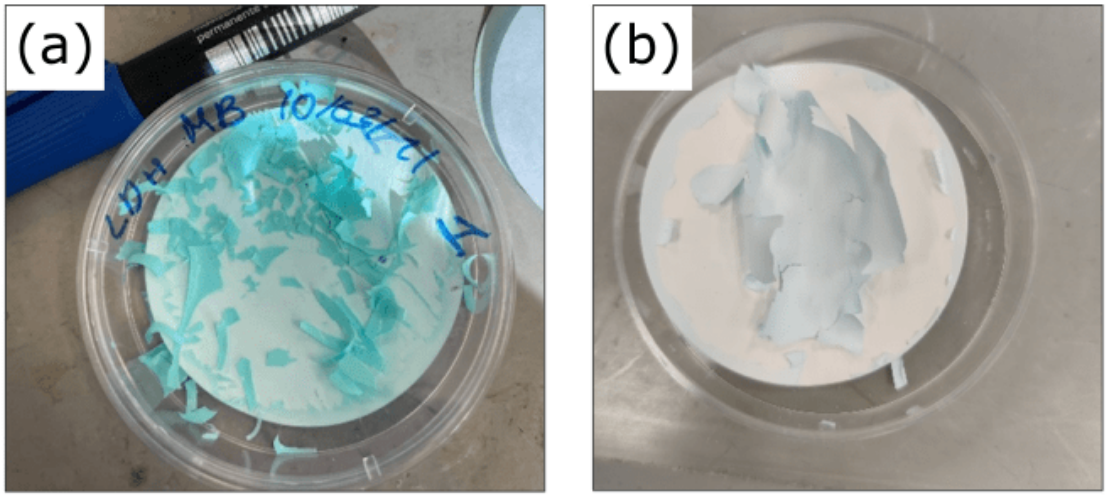


Figure C2: (a) Pure CuAl-$CO_3$ LDH membrane and (b) 30:70 LDH/BNOx membrane, both showing mechanical failure.

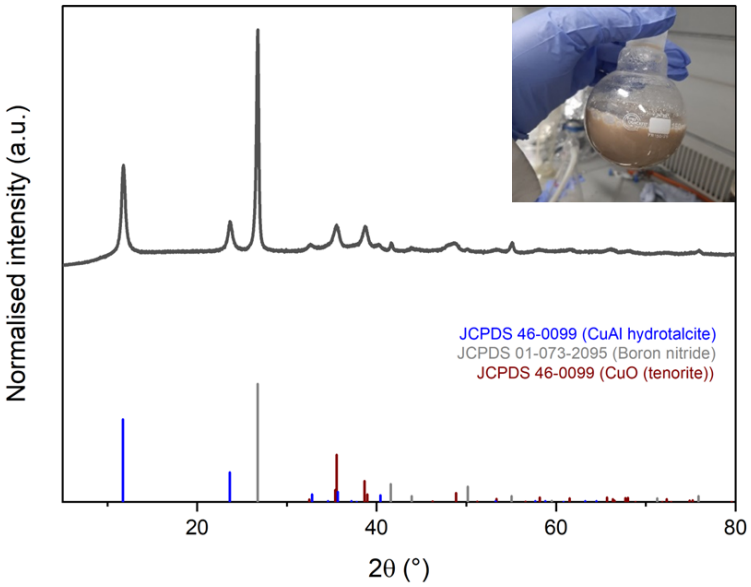


Figure C3: pXRD pattern of 50:50 LDH/BNOx nanocomposite membranes. Brown colour change is shown in inset.

## SEM, TEM and particle size distributions

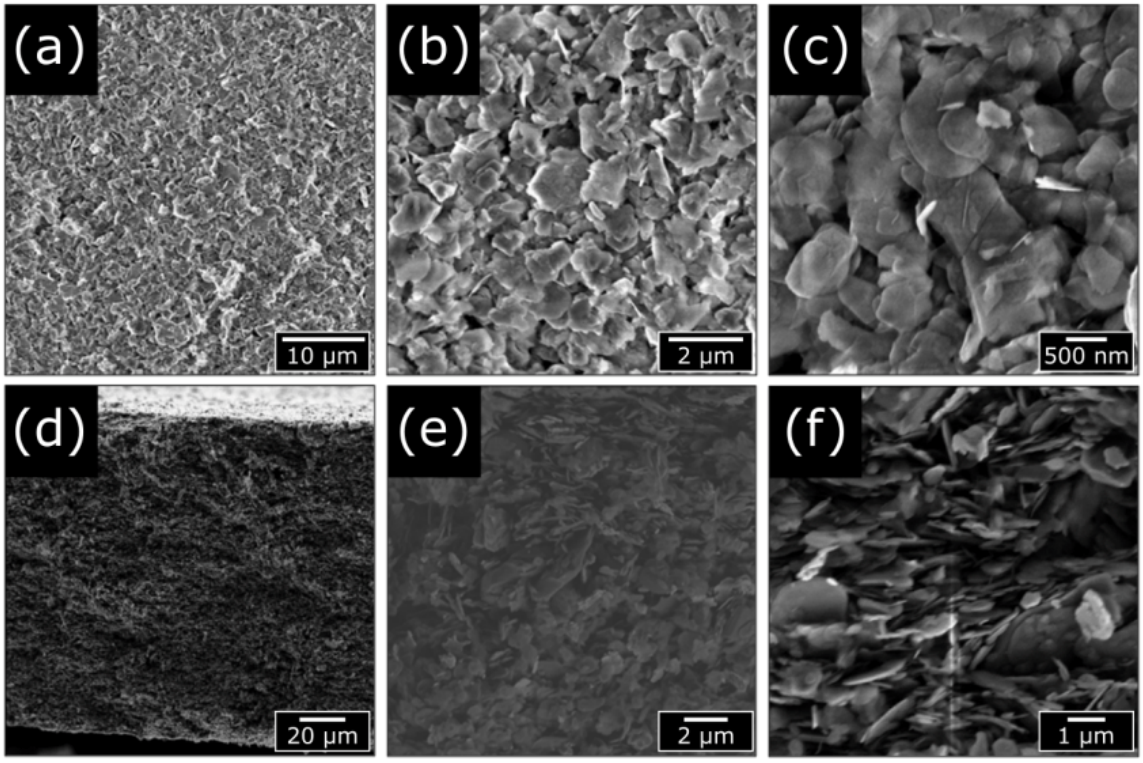


Figure C4: Additional top-view (a,b,c) and cross-sectional (d,e,f) SEM images of 20:80 LDH/BNOx membranes.

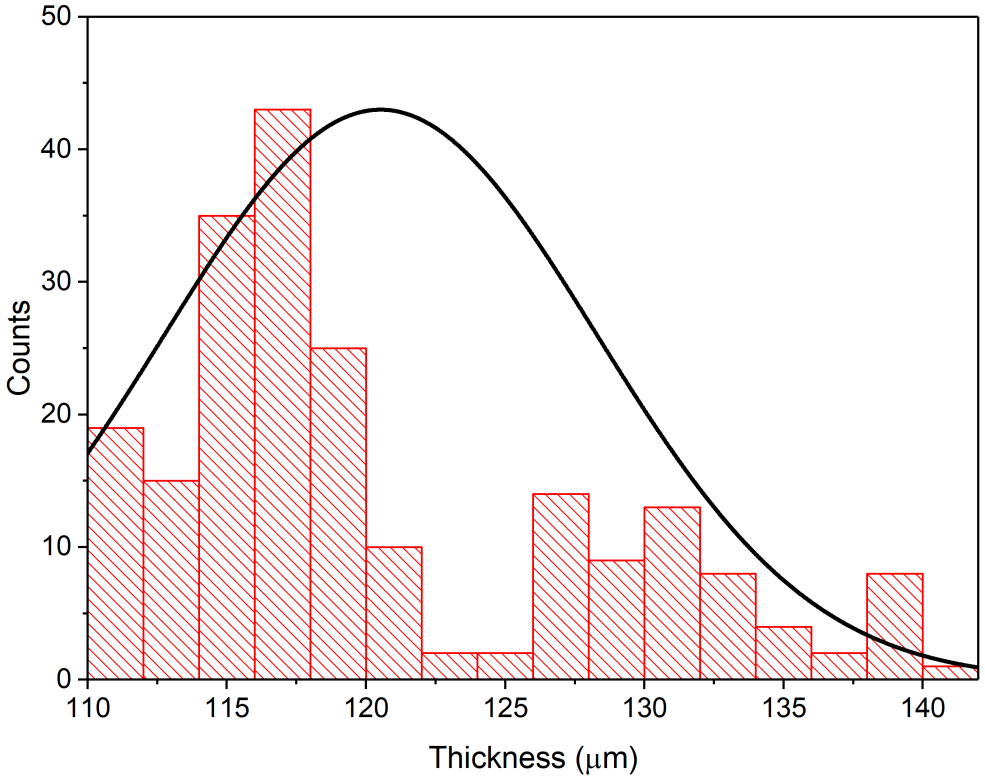


Figure C5: Distribution of LDH/BNOx membrane thickness across multiple membrane samples, as evaluated from SEM images.

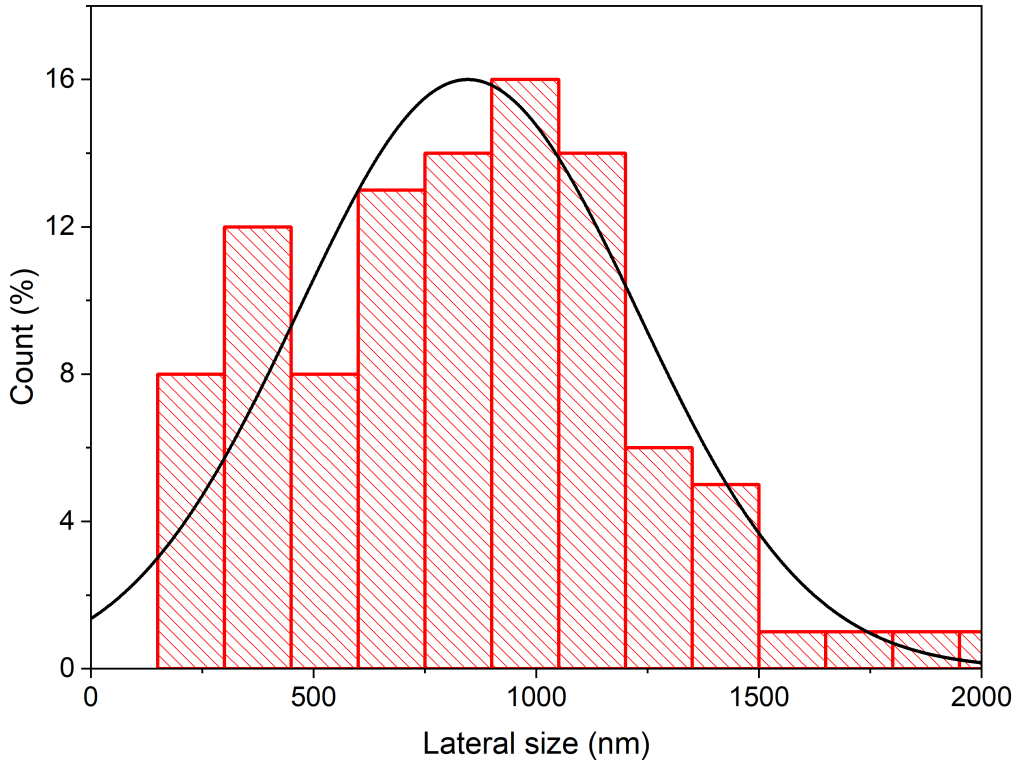


Figure C6: Distribution of LDH and BNOx flake sizes within membranes, as evaluated from SEM images.

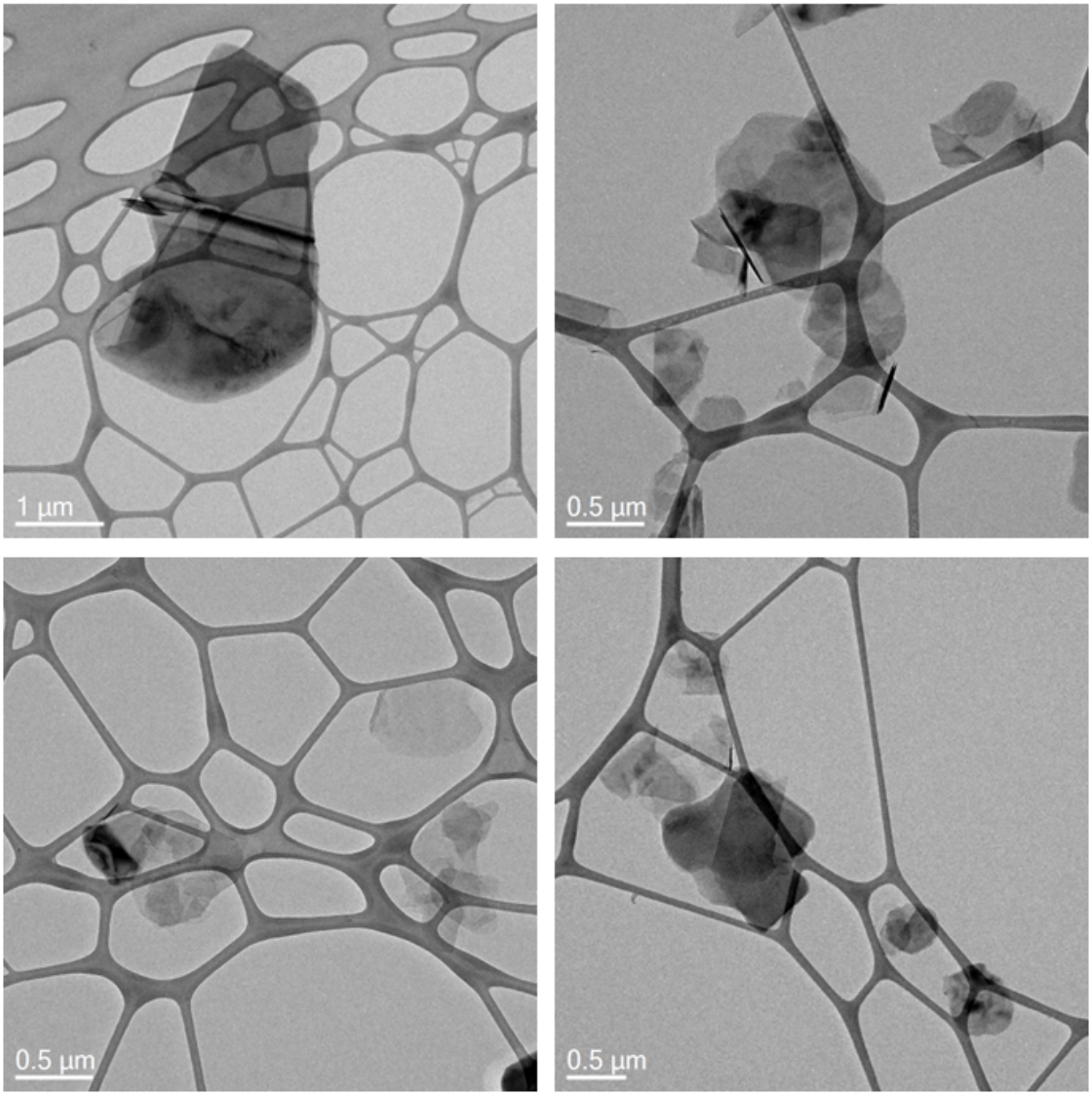


Figure C7: TEM images of exfoliated BNOx nanosheets.

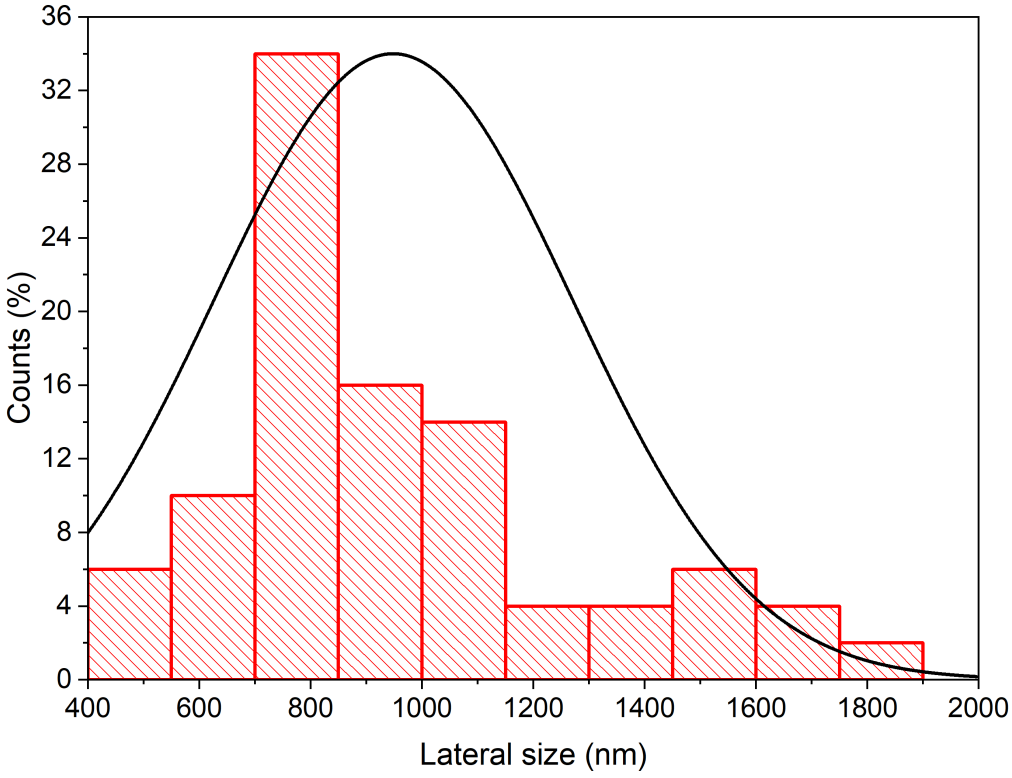


Figure C8: Particle size distribution of exfoliated BNOx nanosheets, as evalutated from TEM images.

## EDX and EELS spectra

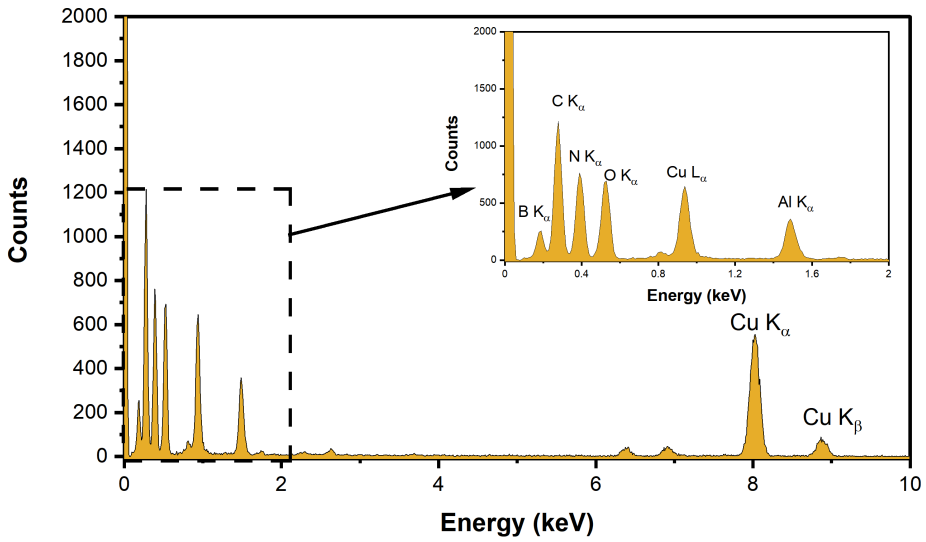


Figure C9: EDX spectrum of CuAl LDH/BNOx nanocomposite. Inset: portion of the spectrum from 0-2keV to show assignmenets of characteristic transitions.

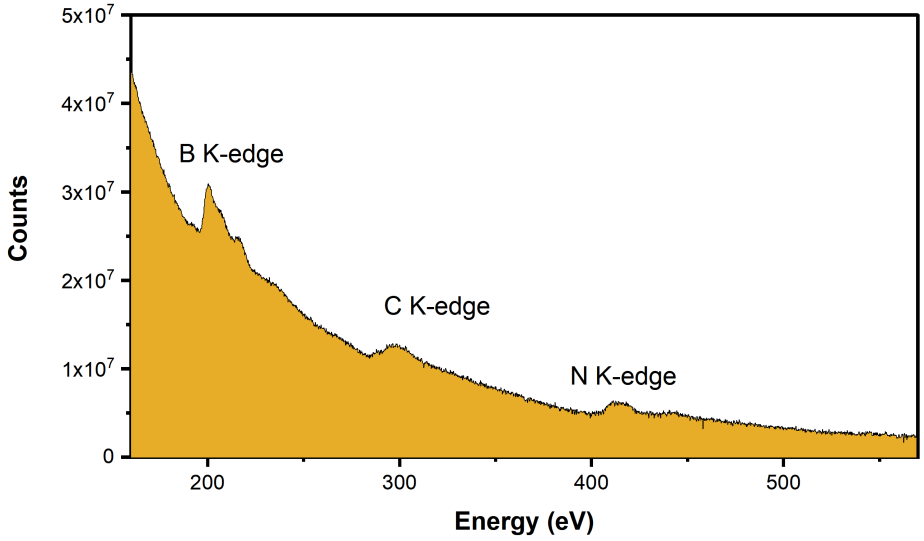


Figure C10: Integrated EELS spectrum of CuAl LDH/BNOx nanocomposite showing the B, N and C K-edges.

## Additional data on membrane performance

Table C2: Summary of water flux results of pristine PVDF support.

| | *1st run* | *2nd run* | *3rd run* | **Average** |
|---|---|---|---|---|
| *Time (s)* | 10.36 | 10.48 | 9.76 | $\mathbf{10.20 \pm 0.31}$ |
| *Flux (L $m^2$ $h^{-1}$)* | 7239 | 7156 | 7684 | $\mathbf{7360 \pm 232}$ |

Table C3: Pseudo-first-order kinetic paramters of 2nd and 3rd runs of photodegradation experiments.

| | **1st run** | | **2nd run** | |
|---|---|---|---|---|
| **Dyes** | **$k_1$ ($min^{-1}$)** | **$R_1^2$** | **$k_1$ ($min^{-1}$)** | **$R_1^2$** |
| Evans Blue | 0.0063 | 0.9962 | 0.0095 | 0.9963 |
| Methyl Orange | 0.0094 | 0.9991 | 0.0115 | 0.9984 |
| Methylene Blue | 0.0187 | 0.9934 | 0.0145 | 0.9991 |
| Rhodamine B | 0.0148 | 0.9968 | 0.0143 | 0.9990 |

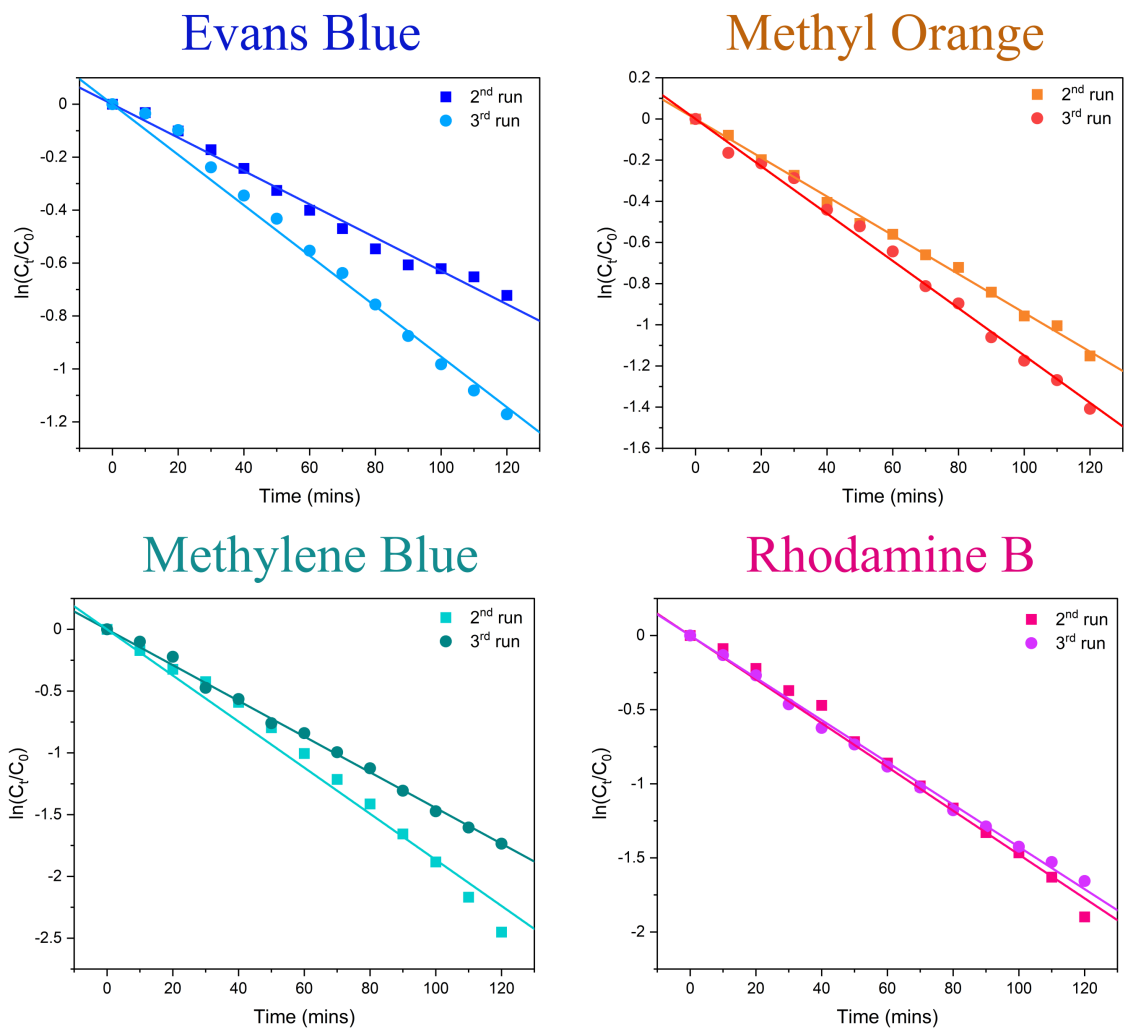


Figure C11: PFO kinetic modelling of 2nd and 3rd runs of photodegradation of EB, MO, MB and RhB by LDH/BNOx nanocomposite membranes.

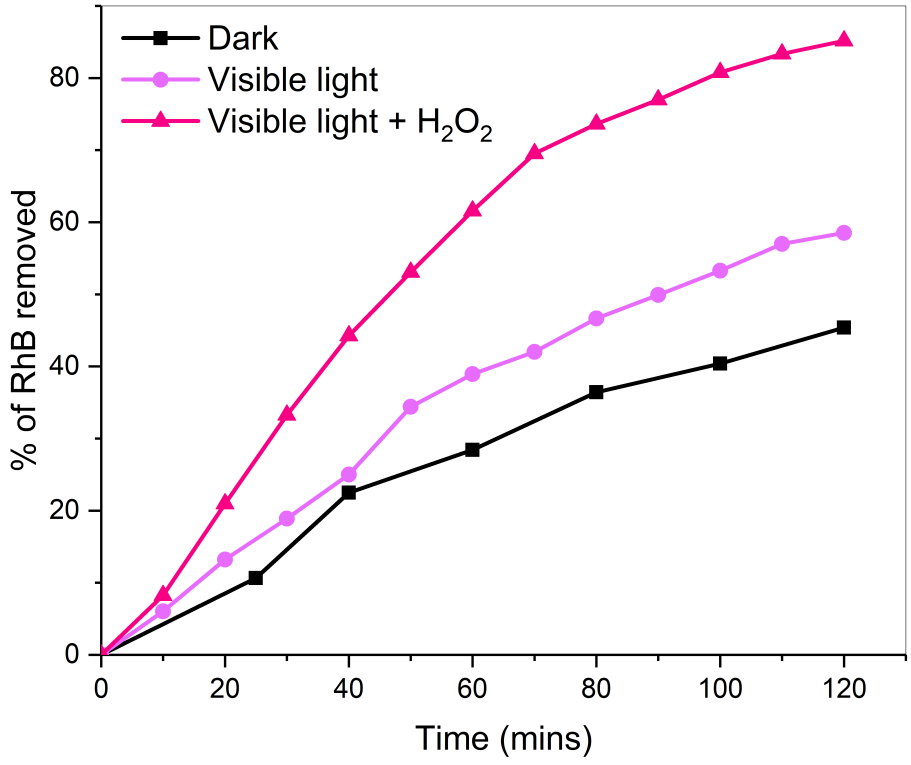


Figure C12: Removal of RhB from solution by LDH/BNOx membrane under dark conditions (black), visible light in the absence of $H_2O_2$ (purple), and light in the presence of $H_2O_2$ (fuschia).

# Derivations of kinetics models used in Chapter 4

## Langmuir-Hinshelwood kinetics for dye degradation

The Langmuir-Hinshelwood model is most commonly used for describing the kinetics of dye degradation by means of heterogeneous catalysis. The process can be thought of as a single molecular species $A$ in liquid phase, which adsorbs on a surface, reacts, and the resulting product $P$ does not adsorb, according to Equation C1.

$$A_{(l)} \rightarrow A_{(ads)} \rightarrow P_{(l)} \tag{C1}$$

The reaction rate $r$ for such a process is given by Equation C2:

$$r = k\theta \tag{C2}$$

where $k$ is the rate constant, and $\theta$ is the surface coverage of $A$, given by Equation C3,

$$\theta = \frac{K_{ads}C}{1 + K_{ads}C} \tag{C3}$$

where $K_{ads}$ is the rate constant for adsorption of $A$ on the surface, and $C$ is the concentration of reactant $A$. Combining Equations C2 and C3 then gives us the non-linear Langmuir-Hinshelwood rate equation, as shown in Equation C4.

$$r = \frac{kK_{ads}C}{1 + K_{ads}C} \tag{C4}$$

In the above regime, there are two limiting scenarios, which both depend on $C$. The first limiting scenario occurs when $C$ is large, then $\theta \approx 1$, and the process can be modelled as a zero-order process, where $r \approx k$. The second limiting scenario occurs when $C$ is small, and so is relevant for the work presented in Chapter 4 of this thesis, as the concentrations of dyes used were in the μM range. When $C$ is small, then $K_{ads}C << 1$, and thus Equation C4 can be simplified to give Equation C5.

$$r \approx kK_{ads}C \tag{C5}$$

This can then be further simplified by combining the rate constants to give Equation C6,

$$r \approx k_1 C \tag{C6}$$

which can be recognised as a pseudo-first-order (PFO) rate equation, where $k_1 = kK_{ads}$ and is the apparent PFO rate constant. To obtain a linear equation for analysis, one can separate the variables and integrate Equation C6, as shown below in Equations C7-9,

$$r = -\frac{dC}{dt} = k_1 C \tag{C7}$$

$$\int \frac{1}{C} dC = -\int k_1 dt \tag{C8}$$

$$ln(C) = -k_1 t + c \tag{C9}$$

where $c$ is a constant. Using the boundary conditions of $C = C_0$ at $t = 0$ leads to Equation C10, which is recognisable as the linear form of the PFO integrated rate law.

$$ln\left(\frac{C_0}{C_t}\right) = k_1 t \tag{C10}$$

For photodegradation processes that obey Langmuir-Hinshelwood kinetics, a plot of $ln\left(\frac{C_0}{C_t}\right)$ versus $t$ gives a straight line with slope $k_1$, the apparent PFO rate constant.

## Pseudo-second-order models for dye adsorption

### The non-linear pseudo-second-order rate equation

Pseudo-second-order (PSO) kinetic models are often used to describe adsorption of molecules on the surfaces of nanomaterials. The differential PSO rate equation is shown in Equation C11.

$$\frac{dq_t}{dt} = k_2(q_2 - q_t)^2 \tag{C11}$$

where $q_t$ is the amount of adsorbate adsorbed at time $t$, and is often given in units of (mg/g) or (mmol/g), $q_2$ is the maximum theoretical adsorbed amount at equilibrium, and $k_2$ is the PSO rate constant. The integrated rate equation can be obtained according to the steps below in Equations C12-15.

$$\frac{1}{(q_2 - q_t)^2}dq \;=\; k_2 dt \tag{C12}$$

$$u = q_2 - q_t \text{ and } du = -dq \tag{C13}$$

$$-\int \frac{1}{u^2}du \;=\; k_2 \int dt \tag{C14}$$

$$\frac{1}{q_2 - q_t} = kt + c \tag{C15}$$

Using the boundary conditions of $q_t = 0$ at $t = 0$, $c$ is found to be $\frac{1}{q_2}$, which when substituted into the above equation, followed by some slight rearranging, gives Equation C16.

$$q_t = q_2 - \frac{q_2}{k_2 t q_2 + 1} \tag{C16}$$

Equation C16 can be rewritten in a simpler form to give an expression that may be recognised as the non-linear PSO integrated rate equation, as shown in Equation C17.

$$q_t = \frac{k_2 q_2^2 t}{k_2 q_2 t + 1} \tag{C17}$$

This non-linear form may be used as presented to perform non-linear fitting on adsorption datsets. However, it is often simpler and more visually accessible in kinetic studies to perform fitting using linear equations. In this regard, four linear PSO equations can be derived from the non-linear expression, termed Type I, II, III and IV, shown in Equations C18 through C21, respectively, as shown below.

$$\frac{t}{q_t} = \frac{t}{q_2} + \frac{1}{k_2 q_2^2} \tag{C18}$$

$$\frac{1}{q_t} = \left(\frac{1}{k_2 q_2^2}\right)\frac{1}{t} + \frac{1}{q_2} \tag{C19}$$

$$q_t = q_2 - \left(\frac{1}{k_2 q_2}\right)\frac{q_t}{t} \tag{C20}$$

$$\frac{q_t}{t} = k_2 q_2^2 - k_2 q_2 q_t \tag{C21}$$

In this work, the linear Type I PSO equation was used, however for completeness, it will be demonstrated in the next subsection how to obtain all four linear equations from manipulation of Equation C17.

**Deriving the linear forms of the pseudo-second-order rate equation**

The simplest linear form to obtain from the non-linear PSO rate equation (C17) is the Type IV equation, as shown in Equation C21. One can multiply both sides of Equation C17 by $k_2tq_2 + 1$ to obtain Equation C22.

$$k_2q_2q_tt + q_t = k_2tq_2^2 \tag{C22}$$

The above equation can then be rearranged slightly, and grouped in terms of $t$ to obtain Equation C23.

$$q_t = t(k_2q_2^2 - k_2q_2q_t) \tag{C23}$$

Dividing across both sides of Equation C23 by $t$ results in Equation C24, which can be recognised as the PSO linear Type IV equation, shown previously in Equation C21. For adsorption data that follows PSO kinetics, a plot of $\frac{q_t}{t}$ on the y-axis vs $q_t$ on the x-axis should result in a linear graph, with slope = -$k_2q_2$, and intercept = $k_2q_2^2$.

$$\text{Type IV:} \qquad \frac{q_t}{t} = k_2q_2^2 - k_2q_2q_t \tag{C24}$$

The Type III form can be obtained easily from the Type IV equation. A slight rearranging of Equation C24 results in Equation C25.

$$k_2 q_2 q_t = k_2 q_2^2 - \frac{q_t}{t} \tag{C25}$$

Dividing across both sides of Equation C25 by $k_2 q_2$ results in Equation C26, which can be recognised as the linear Type III form of the PSO rate equation, as shown previously in Equation C20. For adsorption data that follows PSO kinetics, a plot of $q_t$ on the y-axis vs $\frac{q_t}{t}$ on the x-axis should result in a linear graph, with slope $= -\frac{1}{k_2 q_2}$, and intercept $= q_2$.

$$\text{Type III:} \qquad q_t = q_2 - \left(\frac{1}{k_2 q_2}\right) \frac{q_t}{t} \tag{C26}$$

To obtain the Type II equation, the first step is to invert both sides of the non-linear PSO equation, as shown in Equation C17, to obtain Equation C27.

$$\frac{1}{q_t} = \frac{k_2 q_2 t + 1}{k_2 q_2^2 t} \tag{C27}$$

The fraction on the right hand side of Equation C27 can be split into partial fractions to obtain Equation C28.

$$\frac{1}{q_t} = \frac{k_2 q_2 t}{k_2 q_2^2 t} + \frac{1}{k_2 q_2^2 t} \tag{C28}$$

Equation C28 then simplifies down to Equation C29, which can be recognised as the linear Type II form of the PSO rate equation, as shown previously in Equation C19. For adsorption data that follows PSO kinetics, a plot of $\frac{1}{q_t}$ on the y-axis vs $\frac{1}{t}$ on the x-axis should result in a linear graph, with slope $= \frac{1}{k_2 q_2^2}$ , and intercept $= \frac{1}{q_2}$.

$$\text{Type II:} \qquad \frac{1}{q_t} = \frac{1}{q_2} + \left(\frac{1}{k_2 q_2^2}\right)\frac{1}{t} \tag{C29}$$

The Type I equation can be found by simply multiplying across Equation C29 by $t$ to obtain Equation C30. For adsorption data that follows PSO kinetics, a plot of $\frac{t}{q_t}$ on the y-axis vs $t$ on the x-axis should result in a linear graph, with slope $= \frac{1}{q_2}$ , and intercept $= \frac{1}{k_2 q_2^2}$.

$$\text{Type I:} \qquad \frac{t}{q_t} = \frac{t}{q_2} + \frac{1}{k_2 q_2^2} \tag{C30}$$

# Appendix D

## Additional data for Chapter 5

This Appendix contains extra information and data from Chapter 5. It includes size distribution histograms obtained from analysis of SEM images, additional PL decay graphs, additional data from quenching experiments, as well as a derivation of the error formula presented in Chapter 5.

## Size distribution of LDHs

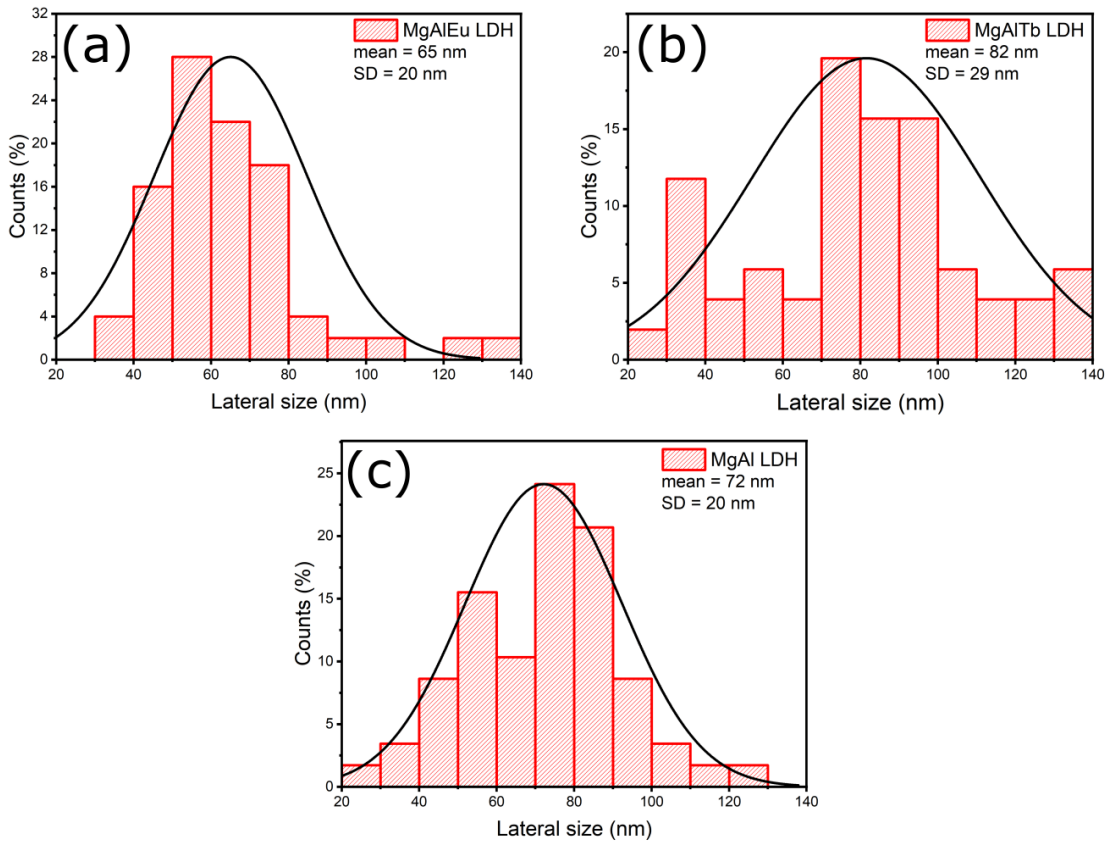


Figure D1: Size distributions of (a) MgAlEu LDH, (b) MgAlTb LDH, and (c) pristine MgAl LDH, from analysis of SEM images.

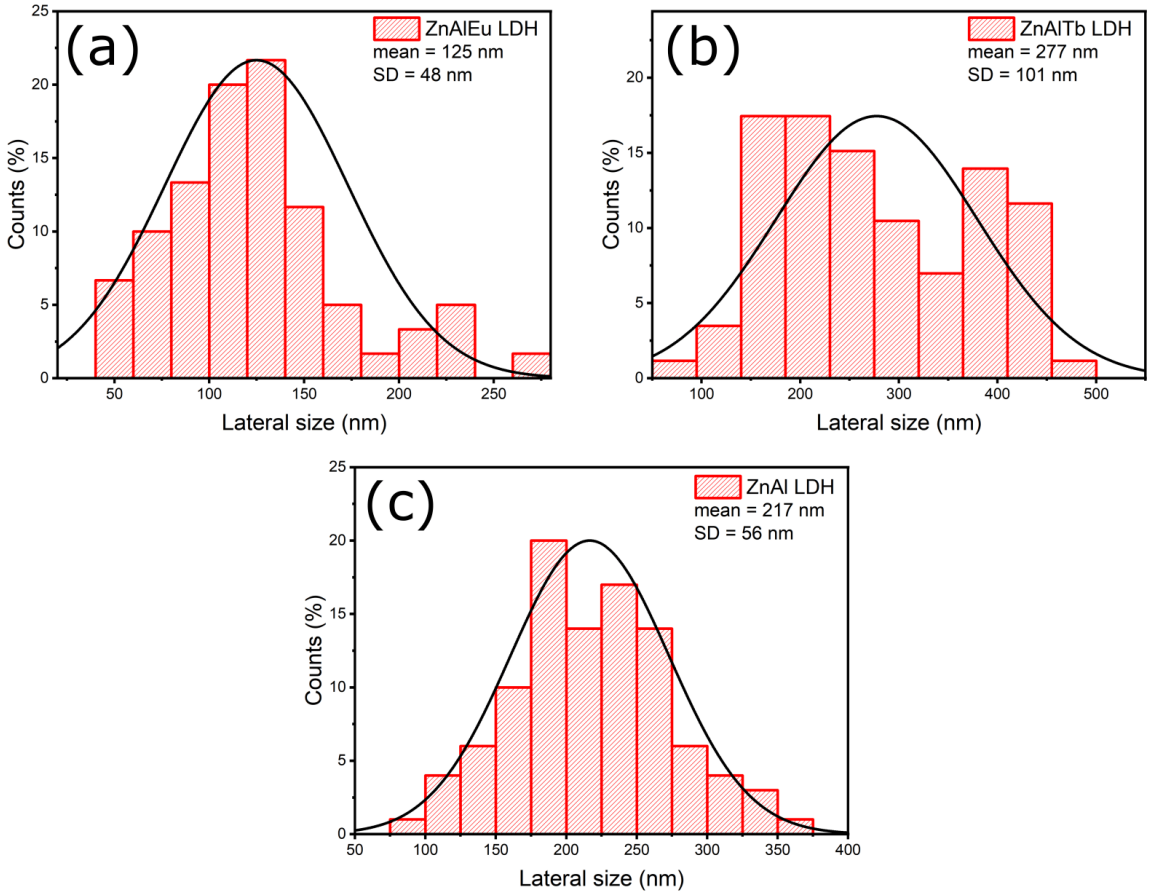


Figure D2: Size distributions of (a) ZnAlEu LDH, (b) ZnAlTb LDH, and (c) pristine ZnAl LDH, from analysis of SEM images.

## Phosphorescent lifetimes of lanthanide-doped LDHs

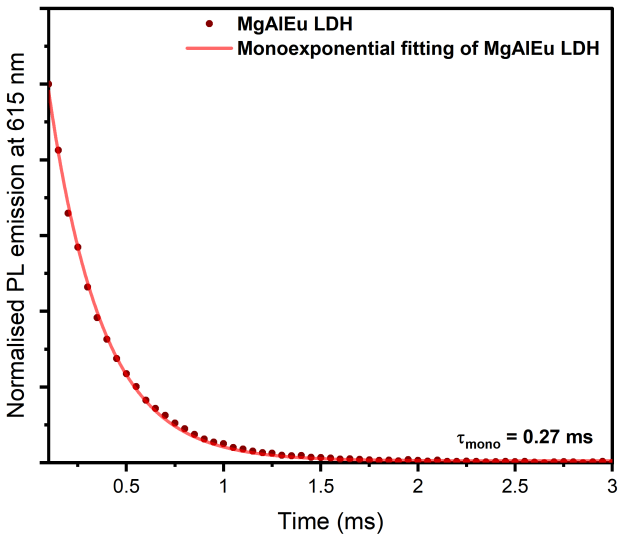


Figure D3: Phosphorescence decay of MgAlEu LDH, fitted using a monoexponential decay model, yielding a lifetime of 0.27 ms.

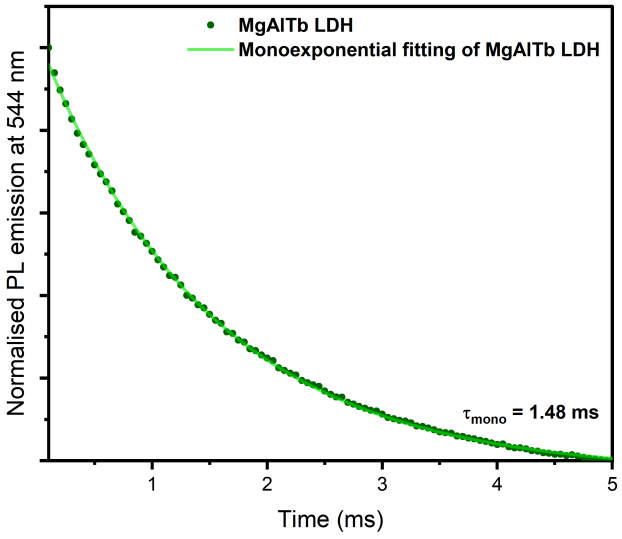


Figure D4: Phosphorescence decay of MgAlTb LDH, fitted using a monoexponential decay model, yielding a lifetime of 1.48 ms.

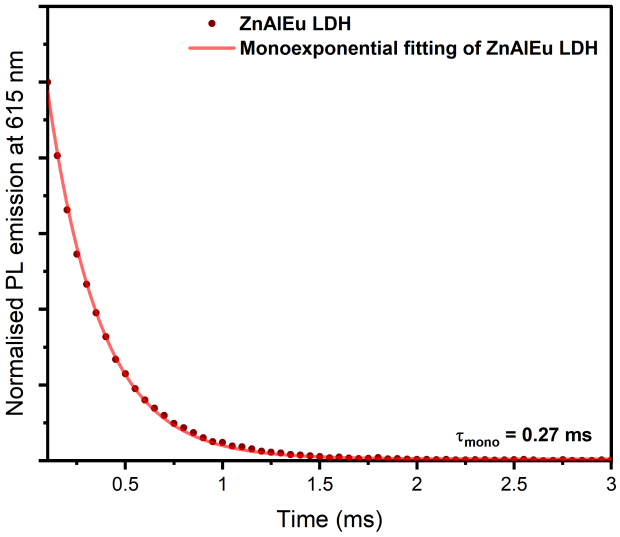


Figure D5: Phosphorescence decay of ZnAlEu LDH, fitted using a monoexponential decay model, yielding a lifetime of 0.27 ms.

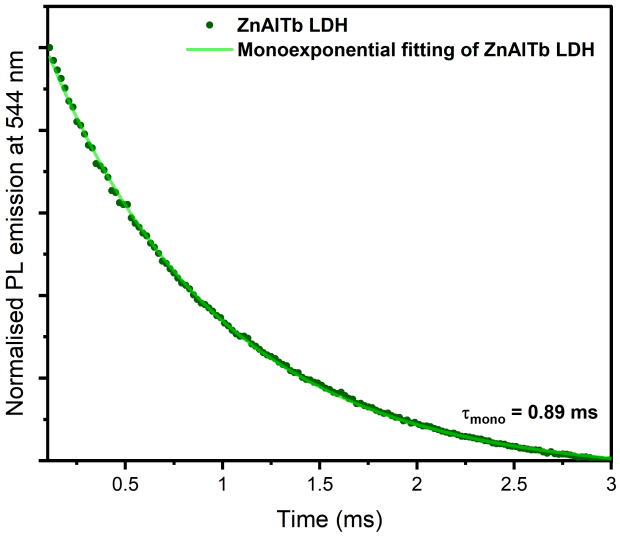


Figure D6: Phosphorescence decay of ZnAlTb LDH, fitted using a monoexponential decay model, yielding a lifetime of 0.89 ms.

## Emission spectra of chromate-quenched lanthanide-doped LDHs

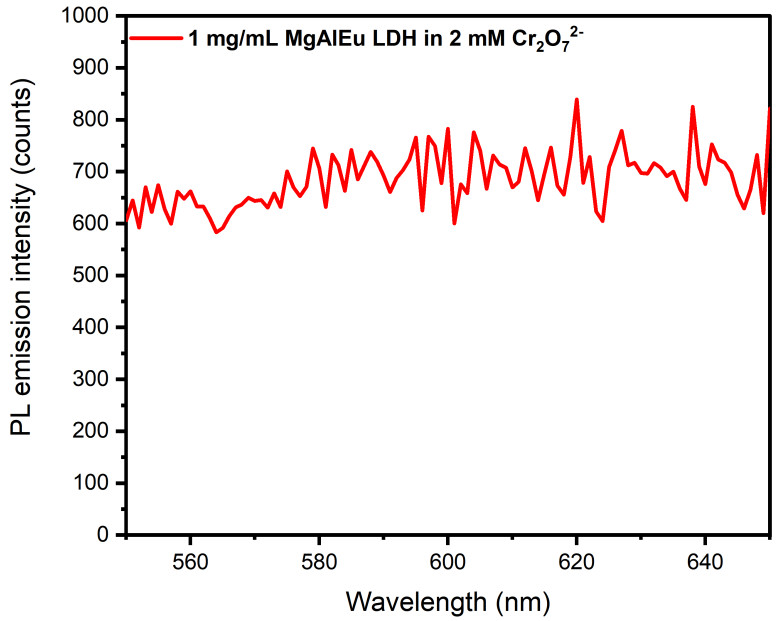


Figure D7: PL emission spectrum of 1 mg/mL colloidal dispersion of MgAlEu LDH in 2 mM $Cr_2O_7^{2-}$.

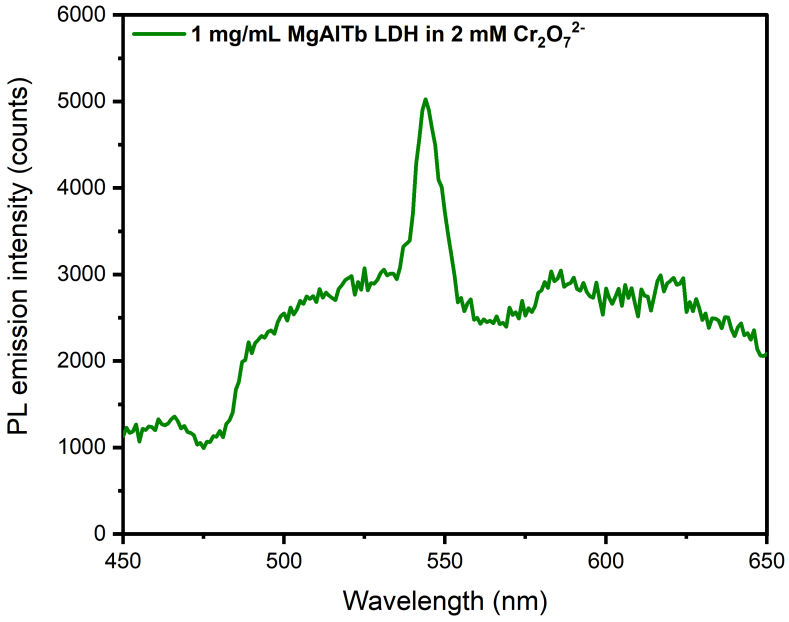


Figure D8: PL emission spectrum of 1 mg/mL colloidal dispersion of MgAlTb LDH in 2 mM $Cr_2O_7^{2-}$.

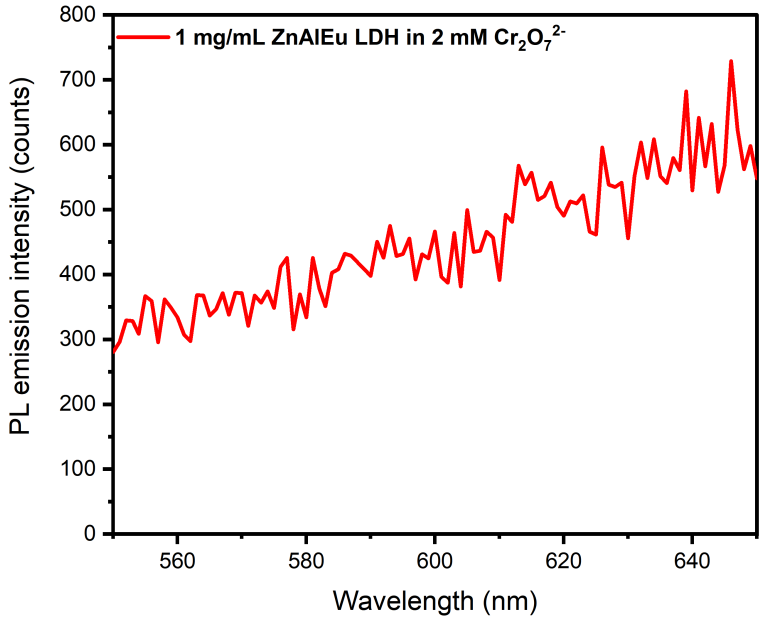


Figure D9: PL emission spectrum of 1 mg/mL colloidal dispersion of ZnAlEu LDH in 2 mM $Cr_2O_7^{2-}$.

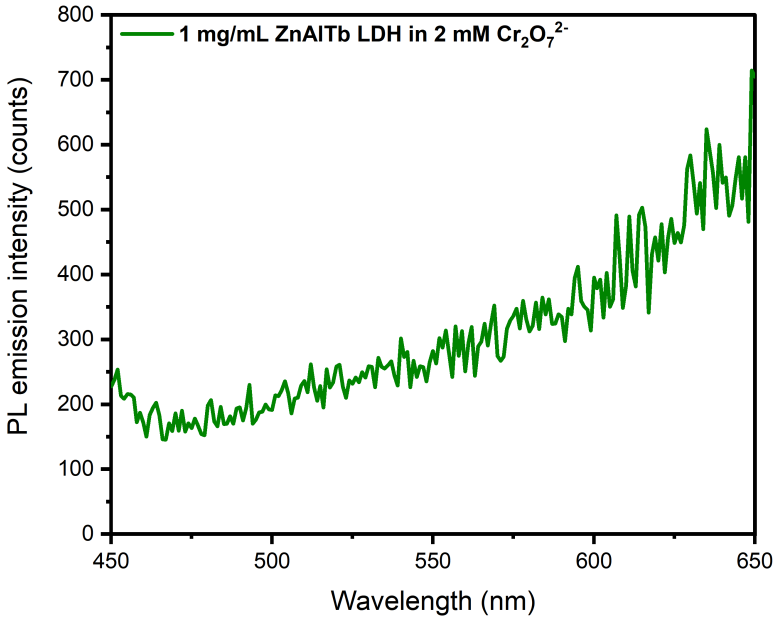


Figure D10: PL emission spectrum of 1 mg/mL colloidal dispersion of ZnAlTb LDH in 2 mM $Cr_2O_7^{2-}$.

## Derivation of error propagation formula for biexponential lifetime fitting

The general error propagation formulae for addition, multiplication and division are given in Equations D1 to D3, respectively.

$$z = x + y \qquad \delta_z = \sqrt{(\delta_x)^2 + (\delta_y)^2} \tag{D1}$$

$$z = x * y \qquad \delta_z = z\sqrt{(\frac{\delta_x}{x})^2 + (\frac{\delta_y}{x})^2} \tag{D2}$$

$$z = \frac{x}{y} \qquad \delta_z = z\sqrt{(\frac{\delta_x}{x})^2 + (\frac{\delta_y}{x})^2} \tag{D3}$$

The equation for calculating the average lifetime from a biexponential decay fit is given in Equation D4.

$$\tau_{avg} = \frac{A_1\tau_1^2 + A_2\tau_2^2}{A_1\tau_1 + A_2\tau_2} \tag{D4}$$

Therefore, substituting Equation D4 in to D3 allows us to devise an expression for the error or uncertainity in the average lifetime ($\delta(\tau_{avg})$), according Equation D5.

$$\delta(\tau_{avg}) = \tau_{avg}\sqrt{(\frac{\delta(A_1\tau_1^2 + A_2\tau_2^2)}{A_1\tau_1^2 + A_2\tau_2^2})^2 + (\frac{\delta(A_1\tau_1 + A_2\tau_2)}{A_1\tau_1 + A_2\tau_2})^2} \tag{D5}$$

Then, using the error propaation rules for addition and multiplication, we can derive individual error expressions for all of the individual terms in Equation D5, according to Equations D6-D9.

$$\delta(A_1\tau_1^2) = A_1\tau_1^2\sqrt{(\frac{\delta A_1}{A_1})^2 + 2(\frac{\delta(\tau_1)}{\tau_1})^2} \tag{D6}$$

$$\delta(A_2\tau_2^2) = A_2\tau_2^2\sqrt{(\frac{\delta A_2}{A_2})^2 + 2(\frac{\delta(\tau_2)}{\tau_2})^2} \tag{D7}$$

$$\delta(A_1\tau_1) = A_1\tau_1\sqrt{(\frac{\delta A_1}{A_1})^2 + (\frac{\delta(\tau_1)}{\tau_1})^2} \tag{D8}$$

$$\delta(A_2\tau_2) = A_2\tau_2\sqrt{(\frac{\delta A_2}{A_2})^2 + (\frac{\delta(\tau_2)}{\tau_2})^2} \tag{D9}$$

The above terms now enable us to derive error expressions for the both numerator and demoninator in Equation D4. according to Equations D10 and D11.

$$\delta(A_1\tau_1^2 + A_2\tau_2^2) = \sqrt{A_1^2\tau_1^4(\frac{\delta(A_1^2)}{A_1^2} + 2\frac{\delta(\tau_1^2)}{\tau_1^2}) + A_2^2\tau_2^4(\frac{\delta(A_2^2)}{A_2^2} + 2\frac{\delta(\tau_2^2)}{\tau_2^2}} \tag{D10}$$

$$\delta(A_1\tau_1 + A_2\tau_2) = \sqrt{A_1^2\tau_1^2(\frac{\delta(A_1^2)}{A_1^2} + \frac{\delta(\tau_1^2)}{\tau_1^2}) + A_2^2\tau_2^2(\frac{\delta(A_2^2)}{A_2^2} + \frac{\delta(\tau_2^2)}{\tau_2^2}} \tag{D11}$$

The expressions in Equations D10 and D11 can then be further expanded to give Equations D12 and D13, respectively.

$$\delta(A_1\tau_1^2 + A_2\tau_2^2) = \sqrt{\delta(A_1^2)\tau_1^4 + 2A_1^2\tau_1^2\delta(\tau_1^2) + \delta(A_2^2)\tau_2^4 + 2A_2^2\tau_2^2\delta(\tau_2^2)} \tag{D12}$$

$$\delta(A_1\tau_1 + A_2\tau_2) = \sqrt{\delta(A_1^2)\tau_1^2 + A_1^2\delta(\tau_1^2) + \delta(A_2^2)\tau_2^2 + A_2^2\delta(\tau_2^2)} \tag{D13}$$

Finally, these expressions can be now be substitued into Equation D5 to give the final expression for the uncertainty in a luminescent lifetime measurement, calculated using biexponential fitting parameters.

$$\delta\tau_{avg} = \tau_{avg}\sqrt{(\frac{\delta A_1^2\tau_1^4 + 2A_1^2\tau_1^2\delta\tau_1^2 + \delta A_2^2\tau_2^4 + 2A_2^2\tau_2^2\delta\tau_2^2}{(A_1\tau_1^2 + A_2\tau_2^2)^2}) + (\frac{\tau_1^2\delta A_1^2 + A_1^2\delta\tau_1^2 + \tau_2^2\delta A_2^2 + A_2^2\delta\tau_2^2}{(A_1\tau_1 + A_2\tau_2)^2})} \tag{D14}$$